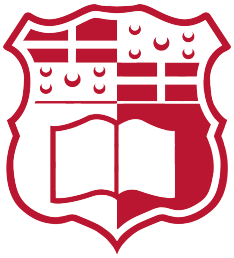

# Cosmological Constraints on Physics Beyond General Relativity


**Rebecca Briffa**

Supervised by Prof. Jackson Levi Said

Co-supervised by Prof. Celia Escamilla-Rivera

Institute of Space Science and Astronomy

Faculty of Science

University of Malta

L-Università ta' Malta



WWW.UM.EDU.MT

*First edition, January 9, 2025*

L-Università ta' Malta

**FACULTY/INSTITUTE/CENTRE/SCHOOL**_____
**DECLARATION OF AUTHENTICITY FOR DOCTORAL STUDENTS**

Student's Code rbri0028

Student's Name & Surname Rebecca Briffa

Course PhD

Title of Dissertation/Thesis
Cosmological Constraints on Physics Beyond General Relativity

**(a) Authenticity of Thesis/Dissertation**

I hereby declare that I am the legitimate author of this Thesis/Dissertation and that it is my original work.

No portion of this work has been submitted in support of an application for another degree or qualification of this or any other university or institution of higher education.

I hold the University of Malta harmless against any third party claims with regard to copyright violation, breach of confidentiality, defamation and any other third party right infringement.

**(b) Research Code of Practice and Ethics Review Procedure**

I declare that I have abided by the University's Research Ethics Review Procedures. Research Ethics & Data Protection form code SCI-2024-00030.

☑ As a Ph.D. student, as per Regulation 66 of the Doctor of Philosophy Regulations, I accept that my thesis be made publicly available on the University of Malta Institutional Repository.

□ As a Doctor of Sacred Theology student, as per Regulation 17 (3) of the Doctor of Sacred Theology Regulations, I accept that my thesis be made publicly available on the University of Malta Institutional Repository.

□ As a Doctor of Music student, as per Regulation 26 (2) of the Doctor of Music Regulations, I accept that my dissertation be made publicly available on the University of Malta Institutional Repository.

□ As a Professional Doctorate student, as per Regulation 54 of the Professional Doctorate Regulations, I accept that my dissertation be made publicly available on the University of Malta Institutional Repository.

[redacted]
Signature of Student

REBECCA BRIFFA
Name in Full (in Caps)

30/09/2024
Date

# Publications

The following papers have been published during my studies:

- **R. Briffa**, S. Capozziello, J. Levi Said, J. Mifsud and E. N Saridakis. Constraining Teleparallel Gravity through Gaussian Proccesses. *Classical and Quantum Gravity*,38(5):055007, 2020. doi:110.1088/1361-6382/abd4f5.

- **R. Briffa**, C. Escamilla Riviera, J. Levi Said, J. Mifsud and N. Pullicino. Impact of $H_0$ priors on $f(T)$ late time cosmology.*The European Physical Journal Plus*, 137(5):532, 2022. doi:10.1140/epjp/s13360-022-02725-4.

- **R. Briffa**, C. Escamilla Riviera, J. Levi Said and J. Mifsud. $f(T, B)$ Gravity in the late Universe. *Physics of the Dark Universe*. 39 (2023), 101153. doi: 10.1016/j.dark.2022.101153i.

- **R. Briffa**, C. Escamilla-Rivera, J. Levi Said, J. Mifsud, Constraints on $f(T)$ cosmology with Pantheon+, *Monthly Notices of the Royal Astronomical Society*, 522(4): 6024, 2023. doi:10.1093/mnras/stad1384.

- **R. Briffa**, C. Escamilla-Rivera, J. Levi Said, J. Mifsud. Growth of structures using redshift space distortion in $f(T)$ cosmology. *Monthly Notices of the Royal Astronomical Society*. 528(2):2711, 2024. doi:10.1093/mnras/stae103.

- R. Sandoval-Orozco, C. Escamilla-Rivera, **R. Briffa**, J. Levi Said, J. Mifsud. $f(T)$ cosmology in the regime of quasar observations., *Physics of the Dark Universe*, 45(2024):101407, 2024. doi:10.1016/j.dark.2023.101407.

- D.A Gomes, **R. Briffa**, A. Kozak, J. Levi Said, M. Saal M, A. Wojnar. Cosmological constraints of Palatini $f(\mathcal{R})$ gravity. *Journal of Cosmology and Astroparticle Physics*. 01(2024):011, 2024. doi:10.1093/mnras/stae103.

- R. Sandoval-Orozco, C. Escamilla-Rivera, **R. Briffa**, J. Levi Said. Testing $f(T)$ cosmologies with HII Hubble diagram and CMB distance priors, *Physics of the Dark Universe*, 4(2024):101641, 2024. doi:10.1016/j.dark.2024.101641.

*For those who believe in the pursuit of knowledge and understanding*

*"The more I learn, the more I realise how much I don't know."*
*- Albert Einstein*

# Acknowledgements

I am writing this with tears streaming down my face. Whether they are tears of joy, I cannot say, but I would like to believe they are. I can hardly believe I've finished, and it feels like the perfect moment to thank and acknowledge the people who have made this journey bearable and possible.

First and foremost, I would like to express my deepest gratitude to my supervisor. Without him, I wouldn't have been able to begin this journey, let alone complete it. He made me believe that this was something within my reach and that I was capable of achieving it. For that, I am profoundly thankful to Prof. Jackson Levi Said for supporting me throughout this journey and helping me believe in myself. Your guidance and words of encouragement will forever be something I am grateful for.

I would also like to extend my thanks to Dr. Jurgen Mifsud, who has been an invaluable sounding board for my ideas and discussions along the way, always ready to offer help when I needed it. For this, I am truly grateful. Additionally, a heartfelt thanks to Prof. Celia Escamilla-Rivera, who has always been there to offer advice, research updates, and invaluable feedback.

To the wonderful people in the lab: thank you for being such an important part of this journey. I've never been much of a morning person, but your presence made it worth getting up and heading to the lab each day. Your words of encouragement never ceased, and through the ups and downs, you were always there to cheer me on or lift me up. A special thank you to Julian Bonello, who has been a constant source of chocolate and snacks whenever the need arose (which was often, and by now, I owe you more chocolates than I can count). To Denis Cutajar, Miguel Zammit, and Xandru Mifsud, thank you for always being there with advice and support. Your wisdom has left a lasting impact on my life, and for that, I am deeply grateful.

I would also like to thank Maria Caruana, who has been by my side for over a decade and with whom I started this journey. We've always supported each other, and your words of encouragement have meant the world to me. A special thanks also goes to Connor Sant Fournier, Andrew Finch, Federico Cilia, and Jonathan Farrugia. To all of you, I extend my deepest thanks (and apologies for my singing, drumming, humming, and relentless Christmas songs).

Words cannot fully express my gratitude to the special people in my life. My aunt Maryanne and uncle Alexander have been my pillars of strength, and without their love and unwavering support, I wouldn't be here today. I am also incredibly thankful to my in-laws, Noel and Rosanne, whose steadfast support gave me the strength to continue.

To my big brother Roberto and his partner Deborah, your love and support have been instrumental in pushing me through this journey. Your passion for everything you do has inspired me to be more passionate in my own work. The interest you've shown in my work was always appreciated, and I have always wanted to share this journey

with you. Thank you both for your unwavering support and for always looking out for me.

Lastly, my deepest and greatest thanks go to my partner, Leon, who has been by my side for the better part of my life. You have been my rock, listening to me talk about this journey for far too long, putting up with my complaints, shenanigans and tears. Yet, you have always supported me and given me the strength to finish strong. Your interest in the things I do has always amazed me, and I hope I can be just as interested in the things you love. Thank you, Leon. I only hope I've made you proud.

# Abstract

The standard cosmological model, ΛCDM, has long been successful in explaining the Universe's evolution. However, as observational precision has advanced, significant tensions, such as the Hubble tension and the $S_{8,0}$ tension, have emerged, challenging the model's validity and hinting at the potential need for theories beyond General Relativity. Among these alternatives, Teleparallel Gravity, where gravity is described through torsion rather than curvature, offers a promising avenue. In particular, the Teleparallel Equivalent of General Relativity (TEGR) is considered, a formulation that replicates General Relativity's field equations but uses the torsion scalar $T$ as the primary contributor to the gravitational Lagrangian. To explore the potential of this framework in addressing these tensions, generalised functions such as $f(T)$ and $f(T, B)$ gravity models are investigated. Consequently, in this work a comprehensive suite of cosmological datasets are utilised. The Pantheon compilation of Type Ia Supernovae (SNe Ia) provides precise luminosity distance measurements, constraining the expansion history. Cosmic Chronometers (CC) data offer model-independent estimates of the Hubble parameter based on differential age dating of galaxies. Baryon Acoustic Oscillations (BAO) measurements probe the imprint of sound waves in the early Universe, refining constraints on the late-time expansion. Redshift Space Distortions (RSD) trace the growth of cosmic structures, offering insights into large-scale structure formation. Additionally, the BICEP/Keck BB-spectrum enables exploration of primordial gravitational waves, shedding light on early Universe physics. Alongside these datasets advanced techniques like Gaussian Processes (GPs) for reconstructing the arbitrary function, and Markov Chain Monte Carlo (MCMC) for constraining the parameters of these models are employed. The results establish $f(T)$ gravity as a promising alternative to ΛCDM, capable of addressing persistent tensions such as $H_0$ and $S_{8,0}$. The models provide observationally consistent solutions for late-time cosmic acceleration, the growth of structures, and primordial gravitational waves. These findings present the most comprehensive constraints on $f(T)$ gravity to date, underscoring its potential as a viable framework and enhance our understanding of the Universe's evolution, offering valuable insights into the late- and early-time Universe. As a result, this work contributes to the growing body of research exploring alternatives to ΛCDM and highlighting the potential of modified gravity models as viable solutions.

# Contents

# List of Figures

# List of Tables

# List of Abbreviations

**2dFGRS** 2-degree Field Galaxy Redshift Survey

**6dFGS** 6df Galaxy Survey

**AIC** Akaike Information Criteria

**BAO** Baryon Acoustic Oscillations

**BIC** Bayesian Information Criteria

**BICEP** Background Imaging of Cosmic Extragalactic Polarization

**BOSS** Baryon Oscillation Spectroscopic Survey

**CC** Cosmic Chronometers

**CDM** Cold Dark Matter

**CHP** Carnegie Hubble Program

**CLASS** Cosmic Linear Anistropy Solving System

**CMB** Cosmic Microwave background

**COBE** Cosmic Background Explorer

**DESI** Dark Energy Spectroscopic Instrument

**eBOSS** Extended Baryon Oscillation Spectroscopic Survey

**EoS** Equation of State

**FLRW** Friedmann-Leîmaitre-Roberston-Walker

**GAMA** Galaxy and Mass Assembly

**GaPP** Gaussian Process in Python

**GP** Gaussian Process

**GR** General Relativity

**GW** Gravitational Waves

**HST** Hubble Space Telescope

**HiCLASS** Horndeski in the Cosmic Linear Anistropy Solving System

**HW** H0LiCOW

**JWST** James Webb Space Telescope

**KiDS** Kilo-Degree Survey (KiDS-1000)

**LSS** Large Scale Structure

**MCMC** Markov Chain Monte Carlo

**MCT** Multi-Cycle Treasury

**PN** Pantheon Compilation data set

**PN+** Pantheon+ Compilation data set

**PN+& SH0ES** Pantheon+ Compilation data set

**RSD** Redshift Space Distortion

**SNe Ia** Supernovae of Type Ia

**SDSS** Sloan Digital SKy Survey

**TEGR** Teleparallel Equivalent of General Relativity

**TG** Teleparallel Gravity

**TRGB** Tip of the Red Giant Branch

**WiggleZ** WiggleZ Dark Energy Survey

**WMAP** Wilkinson Microwave Anisotropy Probe

# 1

# Introduction

Recent decades have witnessed immense advancements in cosmology, a field focused on the origin, evolution, and eventual fate of the Universe. Technological progress and new observational discoveries have profoundly changed our understanding of the cosmos. At the heart of this exploration is the study of the fundamental forces of nature—gravity, electromagnetism, the strong nuclear force, and the weak nuclear force— with gravity emerging as both intriguing and mysterious.

Isaac Newton's "Philosophiæ Naturalis Principia Mathematic" [23] provided a foundational description of gravity as a force following an inverse square law. While this model successfully explained many aspects of planetary motion, it faced limitations, such as the discrepancy in the prediction of Mercury's orbit. Albert Einstein addressed these limitations with his theory of General Relativity (GR) in 1915 [24], proposing that gravity results from the curvature of spacetime. This theory was confirmed by key observations, including the bending of light during the 1919 solar eclipse [25] and accurate measurement of Mercury's precession [26]. These findings helped establish GR as a viable theory of gravity.

In turn, Einstein's GR led to the development of a model describing an isotropic and homogeneous Universe, explored independently by Friedmann [27], Robertson [28], Lemaître [29], and Walker [30]. However, these solutions to Einstein's equations pointed to an expanding Universe. Believing this to be a mistake, Einstein attempted to modify his theory by introducing a cosmological constant to account for a static Universe, which was the prevailing assumption at the time [31].

Later on, Edwin Hubble's 1929 discovery of an expanding Universe [32] overturned the previously accepted model of a static Universe. Through his observations, Hubble found that galaxies are receding from Earth at speeds proportional to their distance, providing compelling evidence that the Universe is expanding. This relationship led to the formulation of the Hubble constant, $H_0$, which quantifies the rate at which the Universe is expanding,

overturning the previously accepted model of a static Universe .

To build on Hubble's discovery of an expanding Universe, a significant breakthrough in the late 1990s revealed that the Universe is not only expanding, but that its expansion is accelerating. This observation was made by two independent groups: the Supernova Cosmological Project [33] and the High-z Supernova Search Team [34] revealed that the Universe's expansion is accelerating. This unexpected acceleration, contrary to gravity's attractive nature, led to the introduction of dark energy—a form of energy with negative pressure [35, 36]. One simple candidate for dark energy is the cosmological constant, $\Lambda$, which drives this acceleration with an exerted negative pressure.

At the same time, astrophysical observations of galaxy rotation curves suggested the presence of dark matter, a non-baryonic matter component that interacts only through gravity, as it has never been directly detected and thus, is assumed to interact with baryons solely through gravitational effects [37]. Despite no direct detection, dark matter accounts for the discrepancies observed in galaxy dynamics [36]. Cold Dark Matter (CDM), referring to slow-moving particles relative to light, remains the leading candidate in addressing the inconsistency between measured and predicted velocities of galaxy rotation curves [35].

Together, dark energy and CDM form the $\Lambda$CDM model, the cornerstone of modern cosmology. This model describes a flat, homogeneous, and isotropic Universe, where dark energy drives cosmic acceleration and CDM accounts for the unseen matter shaping galaxies [38]. As the simplest and most successful framework, $\Lambda$CDM provides the most comprehensive explanation of the Universe's large-scale structure and evolution.

Considered as the standard model of cosmology, $\Lambda$CDM can describe the Universe using only six free parameters: the densities of dark matter and baryons, the scalar spectral index, the amplitude of curvature fluctuations, the angular diameter distance to the sound horizon at last scattering, and the reionisation optical depth. By setting these parameters, it is possible to derive other cosmological quantities, including the Hubble constant [39]. The Hubble constant is a crucial metric for measuring the rate of the Universe's expansion [40].

This relatively simple model has achieved remarkable success in describing the Universe, encompassing its evolution from the Big Bang to the present epoch [39]. The story begins with the Big Bang, which marks the origin of the Universe in an extremely hot and dense state [41]. It is also assumed, that almost immediately, the Universe underwent a period of rapid exponential expansion known as inflation. During this phase, the Universe expanded at a staggering rate, smoothing out initial quantum fluctuations and resolving key issues like the horizon problem (which refers to the question of why regions of the Universe that are far apart appear to have the same temperature and properties, despite being too distant to have exchanged information since the Big Bang) and flatness problem (the Universe appears to be nearly flat, requiring extremely precise initial conditions in the early Universe

to maintain this flatness over time) [42]. This inflationary period set the initial conditions for the large-scale structure of the Universe [43].

As inflation subsided, the Universe entered the radiation-dominated era. During this time, the Universe was filled with a hot, dense plasma of particles and photons [35]. Approximately 380,000 years after the Big Bang, the Universe cooled enough for protons and electrons to combine and form neutral hydrogen atoms—a process called recombination [44]. This cooling allowed photons to travel freely through space, resulting in the Cosmic Microwave background (CMB), a faint glow of radiation that provides a snapshot of the Universe at this early stage. Discovered in 1965 [45, 46], the CMB remains one of the most significant pieces of evidence for the early Universe, offering insights into the Universe's infancy and its subsequent evolution.

Following the release of the CMB, the Universe entered the matter-dominated era. During this phase, matter became the dominant component, leading to the formation of galaxies and large-scale cosmic structures [35]. In the past few billion years, the Universe has transitioned into a dark energy-dominated era [41, 34, 33]. This phase defines the current state of cosmic evolution, where dark energy plays a crucial role in the accelerated expansion the Universe.

Beyond its role as a cosmic snapshot, the CMB encodes critical information about the early Universe in the form of density fluctuations—tiny variations in temperature that serve as the seeds of all the structure in the Universe today, from galaxies to galaxy clusters [44]. The detailed study of these fluctuations has been significantly advanced by experiments such as the Cosmic Background Explorer (COBE) [47], the Wilkinson Microwave Anisotropy Probe (WMAP) [13], and Planck [15, 16], which have provided precise measurements of cosmological parameters like the mean density of the Universe, expansion rate, and distribution of baryonic matter, dark matter, and dark energy .

Inflation also predicts the existence of primordial Gravitational Waves (GW), which are ripples in spacetime generated during the early Universe and therefore, carry valuable information about the Universe's earliest moments. While direct detection remains elusive at current stage due to the sensitivity limits of current detectors like LIGO-Virgo [48], indirect evidence may be found through the effect of primordial GWs on the polarisation spectrum of the CMB. Experiments such as BICEP2 [49], Keck Array [50] and BICEP3 [51] have placed constraints on primordial GWs amplitudes by analysing CMB polarisation data, offering potential insights into these primordial waves .

These detailed investigations into the early Universe, including the study of GWs and CMB fluctuations, have contributed to the refinement of the $\Lambda$CDM model plus inflation cosmology. According to this model, the Universe is composed of three primary components: dark energy, which constitutes about 68% of the total energy density; CDM, which

accounts for approximately 27%; and baryonic matter, which makes up the remaining 5% and includes all baryonic matter and observable structures such as stars, galaxies, and other luminous objects [16, 44] . The accuracy of this model in matching cosmological observations is impressive. However, despite its success, the ΛCDM model faces significant challenges that continue to engage the scientific community. One key issue include the nature of dark energy and dark matter. Despite extensive and precise measurements over decades, no direct or indirect evidence for these exotic particles has been conclusively found [52, 53, 54, 55]. This lack of definitive detection leaves many fundamental questions unanswered, especially since dark energy and dark matter are believed to constitute approximately 95% of the total energy density of the Universe. Consequently, the true nature of these constituents remains one of the most significant unknowns within the ΛCDM model [39].

Another significant challenge to the ΛCDM model is the Hubble tension [18, 40, 22, 56, 57, 58], an unresolved discrepancy in the measurements of the current Universe's expansion rate. The Hubble constant, $H_0$, which defines this rate, has been determined through various methods. In theory, these methods should yield the same value; however, they have produced conflicting results, leaving cosmologists with the challenge of determining which measurement is correct. This discrepancy has sparked intense debate and ongoing research into potential new physics.

Historically, late-time measurements based on the cosmic distance ladder [59, 60, 2, 4] and early-time measurements inferred from the CMB [10, 15, 16, 14] have provided these different values for the Hubble constant. For example, data from the CMB, primarily from the Planck satellite, suggest a lower value of the Hubble constant, while local, more direct methods, such as those using Cepheid variables and Supernovae of Type Ia (SNe Ia), indicate a higher value.

Over the years, this tension between the measurements has become increasingly pronounced as technological advancements and statistical refinements improved precision, with the discrepancy reaching a level of $5\sigma$, making it highly unlikely that this difference is a mere statistical anomaly. To illustrate the growing tension, Fig. 1.1, sourced from Ref. [18], shows the Hubble constant as a function of publication date, using the two different methods. The orange error bars represent values from the distance ladder, particularly from SH0ES [1, 2, 3, 4, 5, 6, 7] and Carnegie Hubble Program (CHP) [8], while the purple error bars show indirect measurements from CMB data, including results from the WMAP [9, 10, 11, 12, 13] and Planck collaborations [14, 15, 16]. The most recent measurements diverge significantly, with a difference exceeding $5\sigma$.

This growing gap suggests that our understanding of cosmological parameters may require refinement or, perhaps, point to new physics beyond the ΛCDM model. Addressing the Hubble tension is critical for resolving fundamental questions about the Universe's

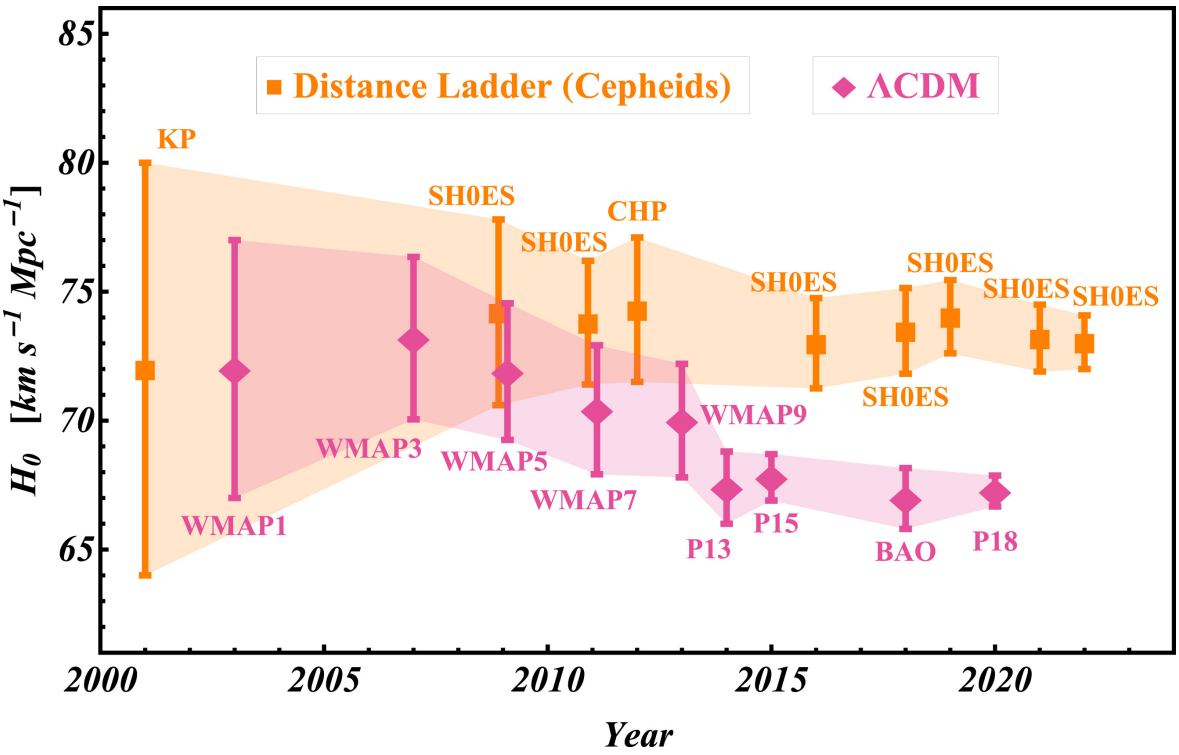


Figure 1.1: The graph illustrates the Hubble constant as a function of publication date, using two measurement methods: direct measurements from the late Universe, primarily from SH0ES [1, 2, 3, 4, 5, 6, 7] and CHP [8] projects, shown in orange, and indirect measurements derived from early-Universe data based on CMB observations from WMAP [9, 10, 11, 12, 13], Planck [14, 15, 16], and BAO [17] collaborations, shown in purple. The latest data exhibits a disagreement greater than $5\sigma$. Sourced from Ref. [18].

structure and its evolution.

In addition to the Hubble tension, another significant discrepancy in cosmology is the $S_{8,0}$ tension [61, 62]. Like the Hubble constant, $S_{8,0}$ is a key cosmological parameter that describes the clustering of matter and how matter is distributed across large-scale structures in the Universe [18]. Specifically, $S_{8,0}$ is a parameter that combines two key measurements: the amplitude of matter fluctuations (how much matter clumps together) and the total matter density of the Universe [63].

Similar to the Hubble tension, early-time measurements based on the CMB, such as those from the Planck satellite, suggest a higher value for $S_{8,0}$ than late-time measurements, including weak gravitational lensing and galaxy clustering surveys [61, 64, 62]. This tension has also grown more prominent as data collection and precision improve, indicating that, much like the Hubble tension, the chances of it being a statistical fluke are increasingly slim.

Therefore, the ΛCDM model can be interpreted as a first-order approximation of the re-

alistic and practical Universe, which still, needs to be fully appreciated. However, both the $H_0$ and $S_{8,0}$ tensions point to potential gaps in our current understanding of the standard cosmological model, suggesting that either unknown systematic errors are at play, or new physics beyond the standard $\Lambda$CDM framework might be required to explain these discrepancies [57, 63, 65, 66, 18, 40, 56].

The scientific community has explored numerous approaches to address these cosmological tensions, both from observational and theoretical perspectives. On the observational front, the James Webb Space Telescope (JWST) has provided a new avenue to examine the Hubble tension with unprecedented precision. However, early findings from JWST have so far reinforced the existence of the tension rather than resolving it [67, 68].

From a theoretical standpoint, the idea that new physics may alleviate these discrepancies is an exciting prospect, particularly given that the Hubble tension is not the only challenge to the $\Lambda$CDM model—or to GR itself [65, 66, 69, 70]. One promising avenue of exploration involves modified gravity, where extensions or alternatives to GR could offer new insights. Numerous theories have been proposed in the literature, often motivated by phenomena that GR struggles to fully explain, as well as by the desire to reconcile gravity with quantum mechanics [66]. In reality modifications to GR had started to formulate immediately after Einstein's field equations had been published, with the intention of unifying gravity with electromagnetism [69, 71]. Nevertheless, in the current context, modifying Einstein's GR implies that corrections on the gravity content of the cosmological model will be considered.

One intriguing possibility gaining significant traction in recent years is Teleparallel Gravity (TG) [65, 66]. Unlike GR, which describes gravity through spacetime curvature, TG replaces curvature with torsion as the mechanism responsible for generating the gravitational field. This shift in geometric interpretation opens new pathways for addressing both the Hubble and $S_{8,0}$ tensions and may offer a viable alternative framework to describe the evolution of the Universe. Additionally, TG enhances interpretability by emphasising torsion, which facilitates the natural inclusion of extra degrees of freedom and its capability to define a local energy-momentum tensor, thereby addressing a significant challenge inherent in GR [72].

A key formulation within TG is the Teleparallel Equivalent of General Relativity (TEGR), which maintains the same field equations as GR, ensuring consistency with classical gravitational phenomena while offering a new perspective. In TEGR, gravity is not seen as the result of curved spacetime but as a result from torsion in a flat spacetime.

In TEGR, spacetime is equipped with a "Teleparallel connection" and a torsion scalar $T$, in which the former has zero curvature but non-zero torsion [72, 66, 73, 74]. This torsion captures the gravitational interaction, essentially describing how mass and energy twist space-

time, creating the effects that are observed as gravity. The underlying structure allows TEGR to not only reproduce the successes of GR but also explore new modifications to the theory.

This reimagining of gravity opens the door to further extensions of TEGR that aim to resolve key cosmological issues, such as the nature of dark energy or the current expansion rate of the Universe. As a bridge between classical GR and modified gravity models, TEGR has become an active area of research, particularly for those investigating possible alternatives to the standard ΛCDM paradigm. By reinterpreting gravity in terms of torsion, TEGR serves as a foundational step toward more generalised theories of gravity. One natural extension of TEGR is through generalising the action to an arbitrary function of the torsion scalar, $f(T)$. This modification, known as $f(T)$ gravity, has recently gained considerable attention for its potential to explain various astronomical observations, including the accelerated expansion of the Universe, without invoking dark energy [73, 75, 76, 77, 78, 79].

A notable advantage of $f(T)$ gravity lies in its ability to generate second-order equations of motion. These equations depend only on the Hubble parameter, $H(z)$, and its first derivative, which simplifies the theory's mathematical structure and makes it well-suited for non-parametric reconstruction approaches. In this work, such approaches will be explored to analyse the functional form of $f(T)$. Additionally, cosmological observations will be utilised to test if the proposed $f(T)$ can be used to explain the accelerating cosmic expansion without dark energy.

In GR, the curvature scalar can be decomposed into a torsion term and a boundary term, the latter of which does not affect the dynamics at the Lagrangian level. However, this decomposition allows for the construction of a more generalised model, where both the torsion scalar and the boundary term contribute when extended to an arbitrary function, $f(T, B)$ [80, 81, 82, 83, 84]. The boundary term, responsible for fourth-order derivatives, complements the torsion scalar's second-order contributions, offering a richer and more versatile gravitational framework. This extended $f(T, B)$ model provides a promising avenue for developing new gravitational theories, potentially resolving longstanding issues in cosmology and astrophysics.

This leads to a critical question: Are these extended TG theories viable when tested against recent cosmological datasets? This study aims to address that question by assessing the cosmological dynamics of these two classes of theories, focusing primarily on late-time behaviour, but also considering their effects on the amplitude of density fluctuations and primordial GWs. The central objective is to identify viable cosmological models that align with current observational data while also providing potential solutions to tensions and discrepancies emerging between different datasets.

In this work, two main approaches are employed. The first approach leverages Gaussian Process (GP), which enable a model-independent reconstruction of the arbitrary function's

behaviour within these theories. This technique is particularly valuable for exploring models beyond ΛCDM, as it allows for the construction of cosmological models without imposing predefined parametrisations, offering a flexible means to detect deviations from the standard model of cosmology.

The second approach adopts a more traditional framework using the Markov Chain Monte Carlo (MCMC) method to evaluate the viability of these models with current observational data, focusing on $f(T)$ and $f(T, B)$ gravity. This method is essential for testing the compatibility of these models with cosmological observations, particularly in studying the Universe's late-time acceleration and fluctuations. By constraining the model parameters and assessing their fit to the data, this analysis aims to identify which models best reflect the cosmological history of the Universe and offer a meaningful alternative to ΛCDM.

In summary, this work explores the potential of extended TG theories, specifically $f(T)$ and $f(T, B)$ models, as alternatives to the standard ΛCDM cosmology. These theories offer new insights into gravity through torsion rather than curvature, and may address significant cosmological challenges like the Hubble tension and the nature of dark energy. By using both model-independent techniques such as GPs and more traditional approaches like MCMC this research seeks to assess the viability of these models against recent observational data, focusing on their impact on late-time cosmic acceleration, density fluctuations, and primordial GWs. The ultimate aim is to identify cosmological models that not only fit current data but also shed light on unresolved tensions in modern cosmology.

The structure of this thesis is as follows: Chapter 2 provides an overview of the concepts of curvature and torsion, alongside discussions of GR and TEGR. This leads into an examination of the standard model of cosmology and its challenges, ultimately motivating the consideration of extended TG theories, such as $f(T)$ and $f(T, B)$ gravity.

Chapter 3 introduces the methodologies employed in this work, including the GP algorithm and the MCMC technique. A discussion of the data sets and $H_0$ priors follows, accompanied by a detailed explanation of the models used in the analysis of $f(T)$ gravity—the primary focus of this investigation—along with statistical metrics. Chapter 4 explores $f(T)$ gravity using GP, presenting the reconstruction results and accompanying statistical analysis. In Chapter 5, the MCMC technique is applied to constrain the $f(T)$ cosmological models introduced earlier, yielding parameter constraints and examining the resulting tensions.

Chapter 6 extends the analysis to the more generalised framework of $f(T, B)$ gravity, where new cosmological models are introduced and constrained using recent data. In Chapter 7, an updated data catalogue is employed to assess the impact on the cosmological models, with comparisons drawn between the widely-used Pantheon and Pantheon+ catalogues in the context of $f(T)$ gravity and the $H_0$ tension. Chapter 8 constrains the $f(T)$ cosmological models in terms of density fluctuations, providing further insights into $f(T)$ gravity in

relation to both the $H_0$ and $S_8$ tensions. In addition, Chapter 9 leverages a modified Boltzmann code integrated with the MCMC approach to constrain $f(T)$ gravity at late times, and also includes modifications to incorporate CMB BB-spectrum modes to constrain GWs and examine the effects of $f(T)$ on these parameters. Finally, Chapter 10 presents the conclusions of this work, summarising the key findings, their implications, and potential directions for future research.

N.B: throughout this work, unless otherwise stated, the reduced Planck unit system, $c = \hbar = 1$, will be used.

# 2

# Foundations of General Relativity and Teleparallel Gravity

Modern cosmology is built on the framework of GR, which describes gravity as the curvature of spacetime. Over the past century, GR has successfully explained a wide range of phenomena, from the motion of planets to the large-scale structure of the Universe. The ΛCDM model, based on GR, has become the standard model of cosmology, postulating that the Universe is dominated by dark energy, represented by the cosmological constant $\Lambda$, and CDM. This model has been highly successful in explaining many observations.

However, despite its success, challenges like the "Hubble tension" have raised questions about whether GR and ΛCDM provide a complete picture of the Universe. These tensions have motivated the exploration of extensions to GR, including modifications where gravity is described not by spacetime curvature but by torsion, as in TEGR.

In this formulation, which represents a less-explored competing geometry, gravity is attributed to the torsion of spacetime rather than curvature, opening the door to further modifications such as $f(T)$ gravity, where the Lagrangian is generalised to a function of the torsion scalar $T$. These extensions offer new avenues to address unresolved issues, including cosmic acceleration, without solely relying on the cosmological constant $\Lambda$. Further modifications, such as $f(T, B)$ gravity, which introduces a boundary term $B$, allow a richer dynamical framework by connecting torsion and curvature.

These extensions have significant implications for understanding the evolution of the Universe, density fluctuations and primordial GWs. These are a key observational features, which provide a powerful tool for testing these modified theories of gravity and assessing their viability in explaining the early Universe and the current cosmic tensions.

This chapter will explore these theoretical developments, beginning with the foundations of curvature and torsion, and will outline how extensions like $f(T)$ and $f(T, B)$ gravity

that aim to address the limitations of GR and ΛCDM.

## 2.1 | Notions of Curvature and Torsion

The motion of particles within the Universe is intrinsically linked to the geometry of spacetime. A fundamental aspect of understanding gravity involves defining a mathematical framework that describes gravitational effects through curvature or torsion. This is formalised through the concept of a manifold, denoted as $\mathcal{M}$. In this context, manifolds form the foundational framework upon which spacetime is modelled. A manifold can be regarded as a complex geometric space that locally resembles flat spacetime [19]. Therefore, the manifold appears to be a construction of locally sewed coordinate patches with real numbers [85].

Manifolds are classified according to their dimensions, which correspond to the number of coordinates required to specify a point on them. For example, a line is a 1-dimensional manifold, a surface like a sphere or plane is a 2-dimensional manifold, and our intuitive 3-dimensional space is an example of a 3-dimensional manifold. In the realm of GR, spacetime itself is modelled as a 4-dimensional manifold, incorporating three spatial dimensions and one temporal dimension.

While a manifold encompasses all the necessary information regarding the spatial and temporal coordinates, it does not specify how these coordinates are related. The relationships and geometries on a manifold are defined using the metric tensor $g_{\mu\nu}$, which encapsulates all the necessary information to describe the manifold's geometry [86, 20]. The metric tensor is a smooth function that varies from point to point on the manifold. In simple terms, it is a mathematical object that allows the calculation of the infinitesimal distance $ds$ between two nearby points in a manifold, given by

$$ds^2 = \sum_{\mu\nu=0}^{3} g_{\mu\nu} dx^\mu dx^\nu \equiv g_{\mu\nu} dx^\mu dx^\nu \,, \tag{2.1}$$

where $ds^2$ represents the line element and $dx^\mu$ and $dx^\nu$ are differential displacements of the coordinates [19]. For any given coordinate system, the metric tensor is represented as a matrix, and its form depends on the spacetime's characteristics [41]. It is important to note the use of the Einstein summation convention, where the summation sign is omitted. The first index is designated for time coordinates, while the remaining indices are for spatial coordinates. The metric tensor also has an inverse, and the relationship between the metric tensor and its inverse is given by the Kronecker delta $\delta^\mu_\sigma$ [87]

$$g^{\mu\nu} g_{\nu\sigma} = \delta^\mu_\sigma \,. \tag{2.2}$$

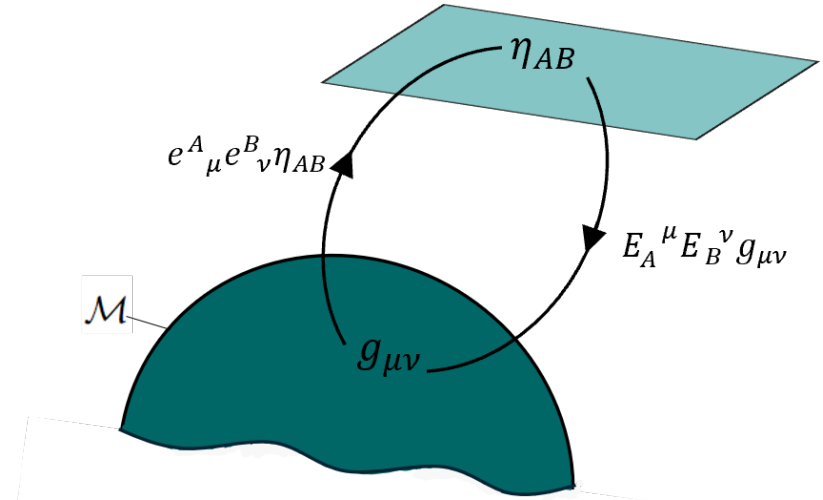


Figure 2.1: Illustration of the mapping from the global spacetime metric on the manifold to the local Minkowski metric in the local frame via tetrad contraction.

Although the metric tensor is fundamental in describing spacetime within a given coordinate system, there are cases where working in a locally flat or orthonormal frame (Minkowski spacetime) is advantageous. This is where the concept of tetrads comes into play as they provide a means to transition between local orthonormal bases and global coordinate systems. Tetrads $e^A{}_\mu$ enable the construction of the global metric from the local Minkowski metric and vice versa, as shown in Fig. 2.1 [72, 88]. The Minkowski metric $\eta_{AB}$ describes a flat spacetime (essentially the spacetime for special relativity) where there is no curvature due to gravity and is expressed $\eta_{AB} = \eta^{AB} = \text{diag}(-1, 1, 1, 1)$ [72, 89]. Using tetrads, the relationship between the general spacetime metric $g_{\mu\nu}$ and the local Minkowski metric is given by [66]

$$g_{\mu\nu} = e^A{}_\mu e^B{}_\nu \eta_{AB}\,, \qquad \eta_{AB} = E_A{}^\mu E_B{}^\nu g_{\mu\nu}\,, \tag{2.3}$$

where $E_A{}^\mu$ denotes the inverse of $e^A{}_\mu$. Greek indices $(\mu, \nu)$ refer to the general manifold, while Latin indices $(A, B)$ are used for the Minkowski space [73]. Additionally, the tetrads and their inverses satisfy the orthogonality condition [73, 90]

$$e^A{}_\mu E_B{}^\mu = \delta^A_B\,, \qquad e^A{}_\mu E_A{}^\nu = \delta^\nu_\mu\,. \tag{2.4}$$

In the same vein, the term tensor, in this case, arises from mathematical objects of identical name which have explicit transformation properties under a change of coordinates and are in general denoted as $T^{\mu_1 \ldots \mu_k}{}_{\nu_1 \ldots \nu_l}$. In theories of gravity, tensor formalism is a necessity as each term in the equations obeys certain transformation rules which removes another

layer of complexity when going from one coordinate basis to another [41, 87]. Tensors generalise the concept of vectors and scalar and provide a framework for describing physical quantities that transform is a specific way under coordinate changes. A tensor of $(\mu, \nu)$ is an object that $\mu$ contravariant indices (which are superscripts) and $\nu$ covariant indices (which are subscripts). For example the metric tensor can be though of rank-2 tensor that describes the geometry of spacetime. Tensors can be thought of as multi-dimensional arrays that encapsulate information about physics laws and relationships in a coordinate-independent manner. For instance, scalars (rank 0-tensors) and vectors (rank-q tensors) are special cases of tensors [91].

In addition, tensor contraction is an operation that reduces the rank of a tensor by summing over one contravariant and one covariant index. For instance, contracting the metric tensor $g_{\mu\nu}$ with its inverse $g^{\mu\sigma}$ yields the Kronecker delta $\delta^{\sigma}_{\nu}$

$$g^{\mu\sigma} g_{\sigma\nu} = \delta^{\mu}_{\nu}. \tag{2.5}$$

This operation is essential for simplifying expressions and for calculations involving tensors.

Another key operator, which will be used frequently, is the derivative with respect to the manifold, denoted as $\partial_\mu = \frac{\partial}{\partial x^\mu}$ [87]. In flat Minkowski spacetime, partial derivatives are generally sufficient for describing physical quantities. However, when extending to curved manifolds, partial derivatives no longer suffice because they do not account for the manifold's curvature. To properly describe differentiation on curved spacetime, the concept of covariant differentiation is introduced, ensuring the result remains a tensor and incorporates the curvature. Covariant differentiation uses the connection coefficients (Christoffel symbols) to account for the curvature of the manifold [31]. This makes partial derivatives inadequate in such cases, and a new operator—the covariant derivative—must be employed. For a general tensor, the covariant derivative is defined as follows [19]

$$\begin{aligned}\nabla_\sigma T^{\mu_1\cdots\mu_k}{}_{\nu_1\ldots\nu_l} = \partial_\sigma T^{\mu_1\cdots\mu_k}{}_{\nu_1\ldots\nu_l} + \widehat{\Gamma}^{\mu_1}{}_{\lambda\sigma} T^{\lambda\mu_2\cdots\mu_k}{}_{\nu_1\ldots\nu_l} + \widehat{\Gamma}^{\mu_2}{}_{\lambda\sigma} T^{\mu_1\lambda\ldots\mu_k}{}_{\nu_1\ldots\nu_l}\cdots \\ - \widehat{\Gamma}^{\lambda}{}_{\nu_1\sigma} T^{\mu_1\cdots\mu_k}{}_{\lambda\nu_2\ldots\nu_l} - \widehat{\Gamma}^{\lambda}{}_{\nu_2\sigma} T^{\mu_1\cdots\mu_k}{}_{\nu_1\lambda\ldots\nu_l}\cdots,\end{aligned} \tag{2.6}$$

where $\widehat{\Gamma}$ is called the general connection, which encapsulate the effects of geometry, depending on the type of theory used. The additional terms in the above equation characterises the geometry of spacetime in the manifold [85]. The exact mathematical definition of the general connection will be defined later as it will be dependant, as will be shown, on the type of geometry (theory) used.

When working with covariant derivatives involving Latin indices, the standard connection is replaced by the spin connection coefficients, denoted as $\widehat{\omega}^{A}{}_{B\mu}$. The covariant derivative of a general tensor in this context is expressed as follows [72]

$$\nabla_\sigma T^{A_1\ldots A_k}{}_{B_1\ldots B_l} = \partial_\sigma T^{A_1\ldots A_k}{}_{B_1\ldots B_l} + \widehat{\omega}^{A_1}{}_{C\sigma} T^{CA_2\ldots A_k}{}_{B_1\ldots B_l} + \widehat{\omega}^{A_2}{}_{C\sigma} T^{A_1C\ldots A_k}{}_{B_1\ldots B_l} + \ldots - \widehat{\omega}^{C}{}_{B_1\sigma} T^{A_1\ldots A_k}{}_{CB_2\ldots B_l} - \widehat{\omega}^{C}{}_{B_2\sigma} T^{A_1\ldots A_k}{}_{B_1C\ldots B_l} + \ldots . \tag{2.7}$$

When covariant derivatives of tensors are taken in these local frames, the spin connection $\widehat{\omega}^{A}{}_{B\mu}$ is introduced to account for the changes in these local frames from point to point in the curved spacetime. The way the basis vectors (or tetrads) "twist" and "turn" as they are moved through spacetime is essentially described by the spin connection [19, 90].

In the framework of GR and other gravity theories, the connection plays a crucial role in describing the motion of free-falling particles, whereas the metric defines the causal structure of spacetime. To characterise the degree of curvature associated with any given connection, the Riemann curvature tensor is used, which is defined as [20, 21, 87, 92]

$$\widehat{R}^{\rho}{}_{\sigma\mu\nu} = \partial_\mu \widehat{\Gamma}^{\rho}{}_{\nu\sigma} - \partial_\nu \widehat{\Gamma}^{\rho}{}_{\mu\sigma} + \widehat{\Gamma}^{\rho}{}_{\mu\lambda}\widehat{\Gamma}^{\lambda}{}_{\nu\sigma} - \widehat{\Gamma}^{\rho}{}_{\nu\lambda}\widehat{\Gamma}^{\lambda}{}_{\mu\sigma} . \tag{2.8}$$

The Riemann curvature tensor captures the intrinsic curvature of the manifold by quantifying how vectors change when parallel transported around a closed loop. In a flat spacetime, this transport would result in no change to the vector's direction. Conversely, in a curved spacetime, the vector will differ from its original orientation upon completing the loop. This deviation from flatness is precisely described by the Riemann tensor, providing a measure of the manifold's curvature. Therefore, in the case of a flat spacetime, the Riemann curvature tensor would be identically zero, $\widehat{R}^{\rho}{}_{\sigma\mu\nu} = 0$, indicating the absence of curvature [21, 66]. This concept is illustrated on the left-hand side of Fig. 2.2.

However, curvature is not the only geometric feature that can be examined. Another crucial aspect of spacetime geometry is torsion, which reveals additional structural properties of the manifold. Torsion is characterised by the twisting and rotational characteristics inherent to the manifold and is quantified by the torsion tensor. While the curvature tensor measures deviations from flatness, the torsion tensor provides insight into the twisting and rotational behaviour of the manifold. It is defined as [72, 19, 21]

$$\widehat{T}^{\lambda}{}_{\mu\nu} = \widehat{\Gamma}^{\lambda}{}_{\nu\mu} - \widehat{\Gamma}^{\lambda}{}_{\mu\nu} . \tag{2.9}$$

The torsion tensor quantifies how the connection deviates from being symmetric, thus providing a measure of the twisting within the manifold. This distinction is crucial in theories where torsion plays a significant role in gravitational interactions, such as in TG, where torsion is used to describe gravitational effects within a framework distinct from GR. The influence of torsion on spacetime geometry is illustrated in Fig. 2.2, where it is depicted as the non-closure of a parallelogram.

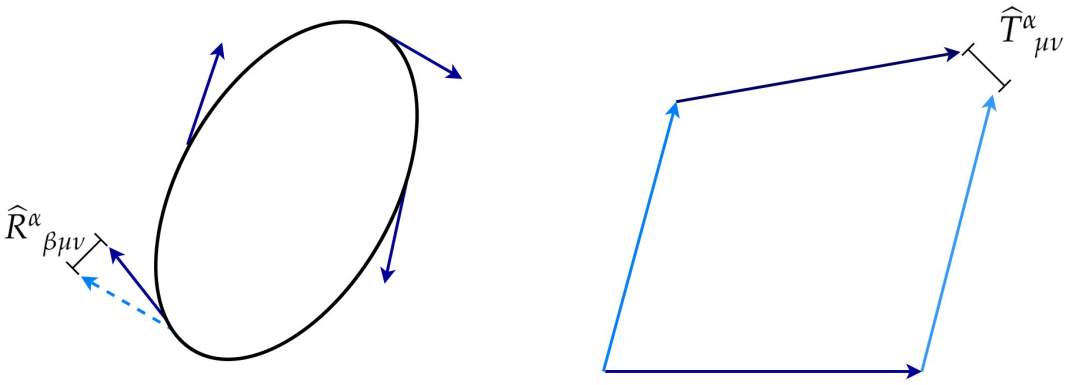


Figure 2.2: Left hand side shows the geometrical interpretation of the Riemann curvature tensor. If a vector is parallel transported along a closed loop, the end vector does not meet the original direction vector. The difference between the two vectors is a measure of the curvature. Right hand side illustrates the physical meaning of torsion, where the parallelogram does not close when two vectors are parallel transported along each other. The torsion tensor is the difference between the final two vectors. Illustrations based on [19, 20, 21]

In examining the geometric features of spacetime, it is important to note that the connections used in defining both the Riemann curvature tensor and the torsion tensor can vary depending on the theory of gravity. Each connection uniquely characterises different aspects of the manifold's geometry [72].

For the Riemann curvature tensor, the connection used is the Levi-Civita connection. This connection is defined specifically for a metric-compatible [1], torsion-free geometry, meaning $\widehat{T}^{\mu}{}_{\nu\sigma} = 0$ , and is given by [19]

$$\mathring{\Gamma}^{\sigma}{}_{\mu\nu} = \frac{1}{2} g^{\sigma\rho} \left( \partial_{\mu} g_{\rho\nu} + \partial_{\nu} g_{\rho\mu} - \partial_{\rho} g_{\mu\nu} \right) . \tag{2.10}$$

The Levi-Civita connection ensures that the metric tensor is preserved under parallel transport, and it plays a fundamental role in GR, where gravity is described purely through curvature with a vanishing torsion tensor, such that $\widehat{R}^{\mu}{}_{\nu\sigma\rho} \neq 0$ [19, 66].

In contrast, the teleparallel connection is used in TG and is characterised by a metric-compatibility and vanishing curvature, $\widehat{R}^{\mu}{}_{\nu\sigma\rho} = 0$. This connection is defined as [72, 93]

$$\Gamma^{\rho}_{\nu\mu} = E_A{}^{\rho} \partial_{\mu} e^A{}_{\nu} + E_A{}^{\rho} \omega^A{}_{B\mu} e^B{}_{\nu} , \tag{2.11}$$

where $\omega^A{}_{B\mu}$ accounts for the fictitious forces arising in inertial frames.

[1] Metric compatibility means that the metric tensor, which measures distances and angles, remains unchanged when vectors are parallel transported along any path in the manifold [21]

The teleparallel connection is designed to incorporate torsion ($\widehat{T}^{\mu}{}_{\nu\sigma} \neq 0$), which describes how spacetime deviates from being curvature-free. In this framework, gravitational effects are attributed to torsion rather than curvature, providing an alternative perspective to the traditional description of gravity in GR [19].

Both connections offer unique insights into the nature of gravity and the structure of spacetime, with the Levi-Civita connection focusing on curvature and the teleparallel connection emphasising torsion.[2]

In theories where torsion plays a significant role, such as in TG, additional tensors are introduced to describe and quantify the effects of torsion on the geometry of spacetime. Two such tensors are the contorsion tensor and the superpotential tensor.

The contorsion tensor quantifies how the connection deviates from being symmetric due to the presence of torsion In a spacetime with torsion, the connection is not symmetric, which means that the order in which you take the covariant derivative of a tensor affects the result. The contorsion tensor $K^{\sigma}{}_{\mu\nu}$ is defined as [66]

$$K^{\sigma}{}_{\mu\nu} := \Gamma^{\sigma}_{\mu\nu} - \mathring{\Gamma}^{\sigma}_{\mu\nu} = \frac{1}{2}\left(T_{\mu}{}^{\sigma}{}_{\nu} + T_{\nu}{}^{\sigma}{}_{\mu} - T^{\sigma}{}_{\mu\nu}\right) , \tag{2.12}$$

which can be seen to be described as the difference between the teleperallel and its counterpart of the Levi-Civita connection. Notably, this tensor can be expressed entirely in terms of torsion tensors, similar to how the Riemann tensor is formulated purely in terms of the Levi-Civita symbols.

The superpotential tensor is a construct that combines information about the contorsion tensor and the torsion tensor in a spacetime with torsion. It plays a role in various formulations of gravity, particularly in TG.

The superpotential tensor $S_{A}{}^{\mu\nu}$ is given by [66]

$$S_{A}{}^{\mu\nu} := \frac{1}{2}\left(K^{\mu\nu}{}_{A} - E_{A}{}^{\nu}T^{\alpha\mu}{}_{\alpha} + E_{A}{}^{\mu}T^{\alpha\nu}{}_{\alpha}\right) . \tag{2.13}$$

The superpotential tensor combines these contributions to give a measure that encapsulates how torsion and contorsion affect the spacetime structure. It is useful in formulating the action in TG theories and in understanding how torsion contributes to the overall geometry and dynamics of spacetime.

[2]The quantities calculated using the Levi-Civita connection are denoted with over-circles, while those calculated with the teleparallel connection are presented without this notation.

## 2.2 | Gravitational Frameworks: GR and TEGR

Having explored the concepts of torsion, contorsion, and the superpotential tensor, which are central to TG, it is now essential to examine how these geometric properties are incorporated into the gravitational actions of various theories.

Starting with GR, the geometry of spacetime is intricately linked to the distribution of matter in the Universe through the Einstein field equations [90]. These field equations can be derived from the principle of least action, a method that constructs the equations of motion from a scalar quantity known as the Lagrangian. This approach was first formalised by Hilbert in Ref. [94]. In GR, the action is referred to as the Einstein-Hilbert action, reflecting the collaborative efforts of both Einstein and Hilbert in its development [19].

The Lagrangian in GR is a scalar quantity. Therefore since gravity is described through the curvature of spacetime this scalar must be constructed from the Riemann curvature tensor, which encapsulates the curvature properties of spacetime. In GR, the relevant scalar is the Ricci scalar $\mathring{R} = \mathring{R}^{\mu}{}_{\mu}$, derived from the Ricci tensor $\mathring{R}_{\mu\nu} = \mathring{R}^{\alpha}{}_{\mu\alpha\nu}$ [41]. To account for the matter content of spacetime, the matter Lagrangian $\mathcal{L}_{\rm m}$ is introduced and added to the total Lagrangian.

Thus, the action for GR is expressed as an integral over spacetime of the Lagrangian density, encompassing both the curvature of spacetime and the matter fields [94, 72]

$$\mathcal{S}_{\rm GR} = \frac{1}{2\kappa^2}\int \mathrm{d}^4x\,\sqrt{-g}\mathring{R} + \int \mathrm{d}^4x\,\sqrt{-g}\mathcal{L}_{\rm m}\,, \tag{2.14}$$

where $g = \det(g_{\mu\nu})$, $\kappa^2 = 8\pi G$ is the metric determinant. As the metric tensor encodes all the information regarding gravitation, it represents the dynamical variable of the system.

By applying the principle of least action, one can derive the equations of motion for the system by varying the action leading to the Einstein field equations, which are the cornerstone of GR [95, 96]

$$\mathring{G}_{\mu\nu} \coloneqq \mathring{R}_{\mu\nu} - \frac{1}{2}\mathring{R}g_{\mu\nu} = \kappa^2\mathcal{T}_{\mu\nu}\,, \tag{2.15}$$

where $\mathring{G}_{\mu\nu}$ is the Einstein tensor, and $\mathcal{T}_{\mu\nu}$ is the stress-energy tensor. The Einstein tensor $\mathring{G}_{\mu\nu}$ encapsulates the curvature of spacetime due to the presence of matter and energy. It is constructed from the Ricci tensor $\mathring{R}_{\mu\nu}$. On the other hand, the stress-energy tensor $\mathcal{T}_{\mu\nu}$ characterises the density and flux of energy and momentum in spacetime, representing the matter constituents of the Universe [86]. This tensor includes contributions from all forms of matter, radiation, and any other forms of energy present in the Universe.

The Einstein field equations Eq. 2.15 thus relates the curvature of spacetime, encoded in the Einstein tensor $\mathring{G}_{\mu\nu}$, to the distribution of matter and energy, described by the stress-energy tensor $\mathcal{T}_{\mu\nu}$. These equations form the core of GR, governing how matter and energy

influence the curvature of spacetime, which in turn dictates the motion of matter and energy within the gravitational field. They are the feature of GR when Wheeler said "spacetime tells matter how to move, matter tells spacetime how to curve" [97], although this statement is a very simplistic description of Eq. 2.15.

Given the cosmological principle, which states that the Universe is isotropic (the same in all directions) and homogeneous (uniform in composition) on large scales [98], the Universe can be modelled as filled with an isotropic and homogeneous perfect fluid. A perfect fluid is characterised solely by its density and pressure, with no viscosity or heat conduction. Under these conditions, the stress-energy tensor, which describes the distribution of matter and energy in spacetime, is given by

$$\mathcal{T}_{\mu\nu} = (\rho + p)u_\mu u_\nu - p g_{\mu\nu}\,, \tag{2.16}$$

where, $\rho$ represents the energy density, and $p$ denotes the pressure of the fluid. The four-velocity $u_\alpha$ represents the macroscopic velocity of the fluid elements. In a Universe modelled as a perfect fluid, $u_\alpha$ cannot have a preferred spatial direction due to isotropy. Therefore, it must be aligned with the temporal component only, meaning $u^\alpha = (1, 0, 0, 0)$ [99, 19]

Having established the framework of GR where the geometry of spacetime is described by the curvature encoded in the Ricci scalar $\mathring{R}$, an alternative but equivalent formulation of gravity that focuses on torsion rather than curvature can be explored. This alternative approach, known as the Teleparallel Equivalent of General Relativity (TEGR), shifts the emphasis from the curvature of spacetime to the torsion that arises from a different choice of connection.

In TEGR, instead of the Levi-Civita connection used in GR, a connection that is curvatureless but possesses torsion is employed, as seen in Eq. 2.11. In this case, the curvature scalar, as calculated by the teleparallel connection vanishes. Instead a torsion scalar which is entirely dependant torsion tensor calculated by the teleparallel connection is defined by [72, 73]

$$T \equiv S_\rho{}^{\mu\nu} T^\rho{}_{\mu\nu} = \frac{1}{4} T^{\rho\mu\nu} T_{\rho\mu\nu} + \frac{1}{2} T^{\rho\mu\nu} T_{\nu\mu\rho} - T_{\rho\mu}{}^\rho T^{\nu\mu}{}_\nu\,. \tag{2.17}$$

where $S_\rho{}^{\mu\nu}$ is the superpotential previously defined. The torsion scalar $T$ plays a central role in this formulation, analogous to the Ricci scalar in GR. Remarkably, the torsion scalar $T$ and the Ricci scalar $\mathring{R}$ are related through a total divergence term, [99]

$$R = \mathring{R} + T - \frac{2}{e}\partial_\mu \left(e T^\sigma{}_\sigma{}^\mu\right) = 0\,, \tag{2.18}$$

where $e = \det\left(e^a{}_\mu\right) = \sqrt{-g}$ is the tetrad determinant. This implies that the Ricci and torsion scalar are equal to up to a boundary term, $B$ such that [66]

$$\mathring{R} = -T + \frac{2}{e}\partial_\mu \left(e T^\sigma{}_\sigma{}^\mu\right) := -T + B\,. \tag{2.19}$$

This forms the fundamental starting point for TG, highlighting that the same gravitational phenomena can be described from two different geometric perspectives; curvature in GR and torsion in TG. This equivalence is the essence of what is known as the TEGR.

In TEGR, much like the Einstein-Hilbert action in GR, the action is constructed by integrating the torsion scalar $T$ over spacetime. The TEGR action is expressed as [72, 66]

$$\mathcal{S}_{\text{TEGR}} = -\frac{1}{2\kappa^2}\int \mathrm{d}^4x\, eT + \int \mathrm{d}^4x\, e\mathcal{L}_{\text{m}}\,. \tag{2.20}$$

where $e$ (the determinant of the vierbein (tetrad field), which replaces the metric tensor as the fundamental dynamical variable in TEGR and $\mathcal{L}_{\text{m}}$ represents the matter Lagrangian, which remains the same as in GR.

The field equations derived from varying the tetrad field in TEGR are given as [72]

$$e^{-1}\partial_\nu(eS_A{}^{\mu\nu}) + \frac{1}{2}E_A{}^u T - T^\sigma{}_{\nu A}S_\sigma{}^{\nu\mu} + w^B{}_{A\nu}S_B{}^{\nu\mu} = \kappa^2\mathcal{T}_A{}^\mu\,, \tag{2.21}$$

where $S_A{}^{\mu\nu}$ is the superpotential tensor, $T^b{}_{\nu A}$ is the torsion tensor, and $w^b{}_{A\nu}$ denotes the spin connection.

The connection between these two frameworks is made explicit through the contorsion tensor. Specifically, the Riemann tensor can be expressed in terms of the torsion tensor and contorsion tensor. This relationship allows one to transform between the curvature-based equations of GR and the torsion-based equations of TEGR. By combining the definitions of the Riemann tensor and the contorsion tensor, the field equations of TEGR can be shown to reduce to those of GR [72, 100]. This reduction illustrates that TEGR and GR are equivalent at level of the field equations, despite being formulated in different geometric languages.

The transition from curvature to torsion provides a new perspective on gravity, ultimately leading to the same field equations as in GR, hence the name TEGR. In other words, this equivalence arises from the relationship between the Ricci scalar and the torsion scalar, as described in Eq. 2.19. In this equation, the boundary term $B$ vanishes because it is a total derivative, such that the action of TEGR becomes totally equivalent to the Einstein-Hilbert action [72, 101, 102].

## 2.3 | FLRW Framework: From Friedmann Equations to Cosmic Fluctuations

With the framework of GR and TEGR established and their equivalence demonstrated, attention is now shifted toward their applications in cosmology. The Friedmann-Leîmaitre-Roberston-Walker (FLRW) metric serves as the foundation for describing the Universe's

large-scale structure, while the Friedmann equations derived from this metric outline the dynamics of cosmic expansion. To gain a comprehensive understanding of the Universe's evolution, it is crucial to explore both the density variations that shape the cosmic structure and the primordial GW, which provide insights into the early Universe's conditions. These elements collectively enhance our knowledge of the Universe's past, present, and future and and will be explored in the following sections.

### 2.3.1 | FRLW and the Friedmann Equations

In modern cosmology, the foundational premise is the cosmological principle, which posits that on large scales, the Universe is both isotropic and homogeneous. To describe such a Universe, the FLRW metric is employed. This metric, named after Alexander Friedmann, Georges Lemaître, Howard Robertson, and Arthur Walker, is a solution to Einstein's field equations under the assumptions of the cosmological principle [29, 27, 28, 30]. It was first derived by Friedmann in 1922 [27], who showed that the equations of GR allowed for an expanding Universe, a concept that was revolutionary at the time. Lemaître independently arrived at similar conclusions, further developing the model, and Robertson and Walker later provided a more general formulation.

The flat FLRW metric is defined as [103, 98, 19, 90]

$$ds^2 = dt^2 - a^2(t)\left(dx^2 + dy^2 + dz^2\right), \tag{2.22}$$

where the metric tensor $g_{\mu\nu}$ is given by $\left(1, -a^2(t), -a^2(t), -a^2(t)\right)$.

The scale factor, $a(t)$, is a fundamental concept in cosmology that encapsulates how the distances between objects in the Universe evolve over time. The scale factor is a function of cosmic time $t$ and represents the relative expansion of the Universe, in a dimensionless fashion. When $a(t)$ increases, it signifies that the Universe is expanding [104]. At present times, the scale factor is normalised to 1, meaning that all distances are measured relative to their current values. The evolution of the scale factor over time is related to the redshift $z$ by the relation $a(t) = \frac{1}{1+z}$, where $z$ is a measure of the fractional change in wavelength due to the expansion of the Universe [43].

The FLRW metric, when applied to Einstein's field equations, leads to a set of equations that govern the dynamics of the Universe. By plugging the FLRW metric into Einstein's field equations, only the (00) and (ii) components yield non-trivial results. These resulting equations are known as the Friedmann equations, which are fundamental in cosmological models and describe how the Universe evolves over time [20, 104, 105].

The first Friedmann equation is given by

$$H^2 = \left(\frac{\dot{a}}{a}\right)^2 = \frac{8\pi G_N}{3}\rho \tag{2.23}$$

where $H$ is the Hubble parameter, defined as $H = \frac{\dot{a}}{a}$, which describes the expansion rate of the Universe and the quantity $\rho$ represents the energy density of the Universe, as referenced in Eq. 2.16. This equation encapsulates the relationship between the expansion rate of the Universe and the total energy density, providing insight into how the Universe's expansion is influenced by its matter and energy content.

The second Friedmann equation is

$$\frac{\ddot{a}}{a} = -\frac{4\pi G_N}{3}(\rho + 3p) \tag{2.24}$$

where $\ddot{a}$ is the second time derivative of the scale factor $a(t)$, and $p$ represents the pressure of the cosmic fluid (as referenced in Eq. 2.16). This equation governs the acceleration or deceleration of the Universe's expansion. The overdot in these equations refers to the derivative with respect to cosmic time $t$, so $\dot{a} = \frac{da}{dt}$ and $\ddot{a} = \frac{d^2a}{dt^2}$.

The matter content of the Universe, described by $\rho$ and $p$, are typically modelled as a combination of pressure-less matter (often referred to as dust) and radiation. This means the total energy density, $\rho$, is composed of contributions from both matter and radiation, expressed as $\rho = \rho_m + \rho_r$, where $\rho_m$ is the energy density of matter and $\rho_r$ is the energy density of radiation. Correspondingly, the pressure $p$ is given by $p = p_m + p_r$, with the pressure of matter $p_m = 0$, as pressure-less matter (dust) is assumed to have no pressure.

From the Friedmann equations Eqs. 2.23,2.24, a continuity equation can be derived, which describes the conservation of energy in the expanding Universe. This continuity equation is given by [103]

$$\dot{\rho} + 3H(\rho + p) = 0\,, \tag{2.25}$$

where $\dot{\rho}$ represents the time derivative of the energy density $\rho$. In cosmology, the relationship between the energy density $\rho$ and the pressure $p$ of a fluid is often characterised by the equation of state (EoS) parameter $w$, defined as [19]

$$p = w\rho\,, \tag{2.26}$$

where the parameter $w$ determines the nature of the fluid.

Substituting the equation of state into the continuity equation and rearranging terms, the energy density $\rho$ as a function of redshift $z$ can be obtained. Integrating the resulting equation gives $\rho = \rho_0 \exp\left[3\int \frac{1+w}{1+z}dz\right]$ where $\rho_0$ is the energy density at the present time (i.e., $z = 0$). In turn, specific values of $w$, corresponding to different components of the Universe such that

1. dust; $w = 0 \implies \rho_m = \rho_0(1+z)^3$

2. radiation; $w = \frac{1}{3} \implies \rho_r = \rho_0(1+z)^4$

It is standard to define the present-day density parameters for various components in the dimensionless ratio

$$\Omega_{i,0} = \frac{\rho_0}{\rho_{\rm cr}} = \frac{8\pi G_N \rho_0}{3H_0^2}\,, \tag{2.27}$$

where $\rho_{\rm cr} = \frac{3H_0^2}{8\pi G_N}$ and $H_0$ is the current rate of expansion.

Therefore, the first Friedmann equation Eq, 2.23 can be re-written in a more familiar format such that for flat spacetime

$$H^2(z) = H_0^2 \sum_i \Omega_{i,0}(1+z)^{3(1+w_i)} \tag{2.28}$$

$$= H_0^2 \left[\Omega_{m,0}(1+z)^3 + \Omega_{r,0}(1+z)^4\right]\,, \tag{2.29}$$

where $\Omega_{m,0}$ represents the density parameter for matter (including baryonic and dark matter) and $\Omega_{r,0}$ represents the density parameter for radiation.

Having derived the Friedmann equations, which describe the expansion dynamics of the Universe, the next step involves analysing how the expansion rate itself is evolving. This is quantified by the deceleration parameter, $q$, a key metric in cosmology that provides insights into the rate of change of cosmic expansion. The deceleration parameter is given by

$$q = -\frac{a\ddot{a}}{\dot{a}^2} = -1 - \frac{\dot{H}}{H^2}\,, \tag{2.30}$$

The deceleration parameter is used to gauge the nature of cosmic expansion. If

- If $\ddot{a} > 0$: The Universe's expansion rate is accelerating, indicating a period of accelerating expansion, and hence $q$ is negative ($q < 0$).

- If $\ddot{a} < 0$: The expansion rate is slowing down, corresponding to a decelerating phase, with $q$ being positive ($q > 0$).

- If $\ddot{a} = 0$: The expansion rate remains constant, and $q = 0$, signifying a static Universe or a transitional phase.

Thus, the deceleration parameter offers crucial information about how the expansion rate of the Universe is evolving over time, distinguishing between periods of acceleration, deceleration, and steady expansion.

### 2.3.2 | Density Fluctuations and Large-scale structure

The flat FLRW metric describes a homogeneous and isotropic Universe on large scales. However, on smaller scales, the Universe is not perfectly uniform; it is filled with structures such as galaxies and clusters. These structure arise from small density fluctuations that evolve over time due to gravitational interactions.

To mathematically model these structures, linear perturbations to Einsteins field equations within an FLRW background are applied. The key idea is to consider a slightly inhomogeneous Universe by introducing small perturbations to both the the metric tensor ($g_{\mu\nu} = \overline{g}_{\mu\nu} + \delta g_{\mu\nu}$, where $\overline{g}_{\mu\nu}$ is the background metric and $\delta g_{\mu\nu}$ is the perturbed metric) and the energy-momentum tensor such that the Einstein equations are given by [35]

$$\delta G^{\mu}{}_{\nu} = 8\pi G_N \delta \mathcal{T}_{\nu}{}^{\mu} \,. \tag{2.31}$$

The perturbed form of the FLRW metric relevant for these growth of structures becomes

$$ds^2 = (1-2\phi)dt^2 - a^2(t)(1-2\psi)\delta_{ij}dx^i dx^j \,, \tag{2.32}$$

where $\phi$ and $\psi$ are gravitational potentials under the Newtonian gauge and $\delta_{ij}$ is the Kronecker's delta. These equations yield the usual Friedmann equations that govern the large scale evolution of the Universe, along with additional equations that describe the evolution of the perturbations themselves [106, 35, 19].

In practice, the matter density $\rho(\mathbf{x})$ varies from point to point and can be expressed as [35, 87]

$$\rho(\mathbf{x}) = \rho(t)\left[1 + \delta(\mathbf{x})\right] \,, \tag{2.33}$$

where $\rho(t)$ is the average density at time $t$, and $\delta(\mathbf{x})$ represents the small perturbations or deviations from this average density. In most practical cases, these perturbations are small $\delta \ll 1$. Over time, these small density fluctuations grow due to gravitational attraction; regions with slightly higher density will attract more matter, becoming denser and eventually leading to the formation of galaxies, clusters, and other large structures. For convenience in analysis, it is often beneficial to work in Fourier space, with the sub-index wave vector $\mathbf{k}$ dropped for simplicity. This approach simplifies the mathematical treatment of perturbations.

For pressureless matter (cold dark matter), the Fourier transform of the density contrast $\delta = \frac{\delta\rho_m}{\rho_m}$, satisfies the following differential equation at the linear level and for sub-horizon scales [106, 107, 108]

$$\ddot{\delta} + 2H\dot{\delta} = 4\pi G_{\rm N}\rho\delta \,, \tag{2.34}$$

where $\delta$ is the matter perturbation. This equation is valid for linear perturbations and sub-horizon scales, where $k \gg aH$, with $a$ being the scale factor.

By changing the independent variable from cosmic time $t$ to redshift $z$, and using the relation for the matter density parameter $\Omega_m$ as defined in Eq. 2.27, Eq. 2.34 can be rewritten in terms of redshift $z$ as [109]

$$\delta''(z) + \left(\frac{H'(z)}{H(z)} - \frac{1}{1+z}\right)\delta'(z) = \frac{3}{2}\left(\frac{H_0}{H(z)}\right)^2 \Omega_{m,0}(1+z)\,\delta(z)\,, \tag{2.35}$$

where $\delta(z)$ is now the growth of the density contrast as a function of redshift [110].

One important property in probing the growth of large scale structure is the growth rate $f$, is defined as the logarithmic derivative of the matter perturbations $\delta(z)$ with respect to the logarithm of the cosmic scale factor [106, 35, 111]

$$f(z) = \frac{\mathrm{d}\ln\delta(z)}{\mathrm{d}\ln a} = -(1+z)\frac{\mathrm{d}\ln\delta(z)}{\mathrm{d}z} = -(1+z)\frac{\delta'(z)}{\delta(z)}\,. \tag{2.36}$$

However, to make contact with observations, the typical value reported is a combination of

$$f\sigma_8(z) = f(z) \times \sigma_8(z)\,, \tag{2.37}$$

where $f(z)$ is the growth data reported above , while $\sigma_8$ is defined as the root-mean-square density fluctuations within a sphere of radius $8h^{-1}$Mpc. This parameter evolves as

$$\sigma_8(z) = \sigma_{8,0}\frac{\delta(z)}{\delta_0}\,, \tag{2.38}$$

where the 0-subscript refers to the value at $z = 0$. Therefore, a bias-independent growth rate can be provided such that [112, 109]

$$f\sigma_8(z) = -(1+z)\frac{\sigma_{8,0}}{\delta_0}\delta'(z)\,. \tag{2.39}$$

The growth rate can now be easily obtained in terms of redshift by rearranging Eq. 2.36 such that

$$\delta'(z) = -\frac{f(z)}{1+z}\delta(z)\,, \tag{2.40}$$

and therefore

$$\delta''(z) = \left[\frac{f^2(z)}{(1+z)^2} + \frac{f'(z)}{1+z}\right]\delta(z)\,. \tag{2.41}$$

Substituting $\delta'$ and $\delta''$ into the transformed linear matter perturbation Eq. 2.35, the growth rate $f$ becomes [110, 111, 109]

$$f^2(z) + \left[2 - (1+z)\frac{H'(z)}{H(z)}\right]f(z) - (1+z)f'(z) = \frac{3}{2}\left(\frac{H_0}{H(z)}\right)^2 \Omega_{m,0}(1+z)^3\,. \tag{2.42}$$

The derived equations illustrate how the growth rate $f(z)$ and the matter overdensity $\delta(z)$ are interconnected, providing a framework to analyse the evolution of cosmic structures in a perturbed FLRW Universe. These expressions bridge theoretical models with observational data, such as RSD data and the evolution of $\sigma_8(z)$, to probe into the dynamics of large-scale structure formation. The equations derived here are thus essential for interpreting observational data, and play a crucial role in cosmological research.

### 2.3.3 | Primordial Gravitational Waves

An insightful approach to these linear perturbations in cosmology is to decompose the components of the metric perturbation tensor based on their behaviour. The perturbations can be categorised into three distinct types: scalar, vector, and tensor components. The scalar component, corresponding to the ii-component of the perturbation tensor, and are related to variations in the matter density and plays a crucial role in understanding large-scale structures in the Universe as seen in the previous section. The vector components, derived from the $0i$ or $i0$ parts, describe rotational effects but often decay in an expanding Universe. The remaining $ij$ components, forming a symmetric rank-two tensor, are linked to Gravitational Waves (GW), which provide insights into the Universe's early conditions [106].

Specifically, the focus of this section, will be on primordial GW–ripples in spacetime generated in the early Universe during the period of cosmic inflation. Primordial GW are tensor perturbations in the early Universe that originate from quantum fluctuations during the inflationary era [113]. These waves are essentially small distortions in the fabric of spacetime that were stretched to macroscopic scales due to the rapid expansion of the Universe during inflation [114]. Unlike, scalar perturbations, which are associated with density fluctuations and lead to the formation of large-scale structure, tensor perturbations correspond to GW and provide a unique probe into the the very early Universe [115].

The corresponding perturbed FLRW metric for these tensor perturbations is generally expressed as [116]

$$ds^2 = dt^2 - a^2(t)(\delta_{ij} + h_{ij})dx^i dx^j\,, \tag{2.43}$$

where $h_{ij}$ represents the gravitational wave perturbation.

One of the key signatures of primordial GW is their imprint in the CMB in the form of polarisation patters [114]. The polarisation of this after glow of the Big Bang (i.e the CMB) can be decomposed into E-modes and B-modes. While E-modes are primarily generated by scalar perturbations, B-modes are specifically linked to tensor perturbations. Therefore, the current best method to detect these GW is to look for the imprint they would have left in the CMB, in the form of B-modes. The polarisation signature that CMB experiments seek are shown in Fig. 2.3 [89]. The observed pattern of linear polarisation's can be decomposed

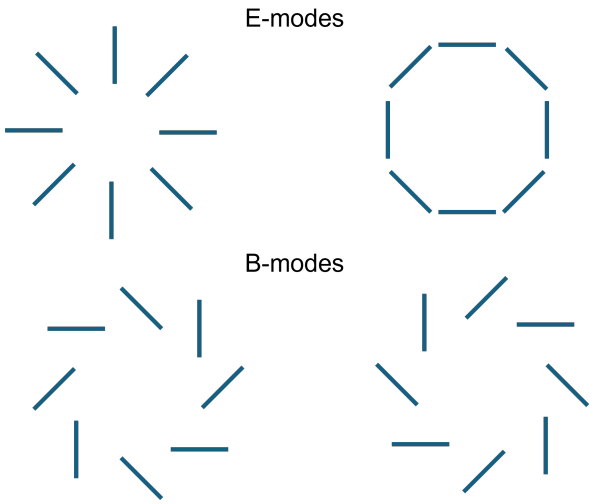


Figure 2.3: CMB polarisation patterns: E-modes exhibit radial or tangential alignments (top configurations), while B-modes are characterised by polarisation aligned at 45° angles to these directions (bottom configurations).

into curl-free (E-modes, upper part of Fig, 2.3) and curl components (B-modes, lower part of Fig. 2.3), named in analogy to the electric and magnetic field. Density fluctuations can only produce E-modes, while GW can produce both E-modes and B-modes. Therefore, B-modes are sourced by tensor perturbations but not by scalars [117, 118, 119].

Detecting these polarisation patterns in the CMB, has been central to understanding both scalar and tensor perturbations in the early Universe. E-modes, have been measured with high precision by experiments like Planck [14, 120] and WMAP [11, 12], providing valuable insights into the structure of the Universe. On the other hand, there are numerous observational efforts, such as BICEP/Keck [49, 51], POLARBEAR [121], and the Simons Observatory [122, 123], which have focused on detecting these elusive B-modes. While E-modes have been conclusively observed, B-modes remain more challenging to detect due to their weaker signal and interference from foreground effects. As observational techniques improve and sensitivities increase, detecting B-modes remains one of the most anticipated breakthroughs in cosmology.

Tensor perturbations evolve according to specific dynamical equations derived from the linearised Einstein field equations. In the context of an expanding Universe, the evolution of these tensor perturbations can be described by the following equation [116]

$$\ddot{h}_{ij} + 3H\dot{h}_{ij} - \frac{k^2}{a^2}h_{ij} = 0\,, \tag{2.44}$$

where $h_{ij}$ represents the tensor perturbations.

This equation captures the dynamics of GW and how they propagate, indicating how they evolve over time in an expanding Universe. These equations are essential for understanding how GW propagate through the cosmic medium and therefore, how they can be used to probe the conditions of the early Universe.

## 2.4 | Challenges of the Standard Model of Cosmology and Pathways to Modified Gravity

The above sections have established the foundational concepts of GR, TEGR, and key cosmological perturbations, such that the discussion now proceeds to the exploration of the Standard Model of Cosmology. While this model has been instrumental in explaining the Universe's evolution, it faces certain limitations, as previously discussed. These limitations prompt the consideration of modified gravity theories, such as $f(T)$ and $f(T, B)$ gravity, which offer potential avenues for a more comprehensive understanding of the Universe's structure and dynamics.

### 2.4.1 | The Standard Model of Cosmology

Recent observations have revealed that the deceleration parameter $q$, as defined in Eq. 2.30, is negative, signifying that the expansion of the Universe is accelerating [85, 19]. This discovery was pivotal in the formulation of the ΛCDM model, necessitating the introduction of an additional term in the Einstein field equations to account for the accelerated expansion. The cosmological constant, Λ, was proposed as this additional term [124].

Indeed, the Einstein field equations originally published in 1916 [125] did not include a cosmological constant. However, to reconcile the theory with the observed accelerated expansion rate [34, 33], the cosmological constant was introduced. By incorporating this term, the action for GR was modified to [20]

$$\mathcal{S}_{\Lambda\mathrm{CDM}} = \frac{1}{2\kappa^2}\int \mathrm{d}^4x\,\sqrt{-g}\left(\mathring{R} - 2\Lambda\right) + \int \mathrm{d}^4x\,\sqrt{-g}\mathcal{L}_{\mathrm{m}}\,, \tag{2.45}$$

where the energy-momentum tensor can be defined as $\mathcal{T}_{\mu\nu} := \frac{-2}{\sqrt{-g}}\frac{\delta\mathcal{L}_m}{\delta g^{\mu\nu}}$

The resulting field equations, which form the basis of the ΛCDM model, are then given by [92, 90, 35]

$$\mathring{R}_{\mu\nu} - \frac{1}{2}\mathring{R}g_{\mu\nu} + \Lambda g_{\mu\nu} = \kappa^2\mathcal{T}_{\mu\nu}\,. \tag{2.46}$$

This equation introduces the cosmological constant $\Lambda$ as a uniform energy density that drives the accelerated expansion, thereby extending the original formulation of GR to account for the observed dynamics of the Universe.

Together, the Friedmann equations, the FLRW metric, and the action principle form the foundation of the $\Lambda$CDM model, which includes dark energy and CDM. These equations encapsulate the evolution of the Universe, from the Big Bang to its present state and beyond, predicting key cosmological phenomena such as the expansion history, the age of the Universe, and the properties of the CMB radiation.

The introduction of the cosmological constant, $\Lambda$, modifies the original Friedmann equations by adding a term that accounts for the accelerated expansion of the Universe, now understood as the influence of dark energy. While the original equations, Eqs. 2.23 and 2.24, describe the expansion rate in terms of the Universe's energy content and curvature, the inclusion of $\Lambda$ expands this framework to encompass not only matter and radiation but also the mysterious dark energy driving the observed acceleration [35] such that

$$H^2 = \left(\frac{\dot{a}}{a}\right)^2 = \frac{\kappa^2}{3}\rho + \frac{\Lambda}{3}\,, \tag{2.47}$$

$$\left(\frac{\ddot{a}}{a}\right) = \frac{-\kappa^2}{6}\left(\rho + 3p\right) + \frac{\Lambda}{3}\,. \tag{2.48}$$

The negative pressure exerted by dark energy is reflected in the equation of state, Eq. 2.26 of the cosmological constant where $w = -1$, such that $p_\Lambda = -\rho_\Lambda$ [35, 16]. Therefore the using the same notation as Eq. 2.28, the first Friedmann equation becomes

$$\frac{H^2}{H_0^2} = \Omega_{m,0}(1+z)^3 + \Omega_{r,0}(1+z)^4 + \Omega_\Lambda\,, \tag{2.49}$$

where the additional term $\Omega_\Lambda$ represents the density parameter for dark energy. For a flat Universe, the sum of all the $\Omega$ terms equals to 1 such that, $\Omega_{m,0} + \Omega_{r,0} + \Omega_\Lambda = 1$ [85].

The $\Lambda$CDM model has been notably successful in explaining a wide range of cosmological phenomena. One of its most significant achievements is its accurate prediction of the Large Scale Structure (LSS) of the Universe [126, 127]. Observations of the CMB radiation, particularly from the Planck satellite, have confirmed the model's predictions regarding the distribution of temperature fluctuations [15]. The model has also accurately predicted the Baryon Acoustic Oscillations (BAO) feature-regular, periodic fluctuations in the density of baryonic matter in the Universe, resulting from sound waves in the early hot plasma, which provide a scale for measuring cosmic distances-which was confirmed in 2005 [128, 129]. This success underscores the model's robustness in describing the distribution of galaxies and galaxy clusters, as well as their formation and evolution. Furthermore, the $\Lambda$CDM

model has also effectively accounted for the accelerating expansion of the Universe. The model's ability to predict and explain these various phenomena highlights its effectiveness in capturing the complexities of the Universe's past and present dynamics.

Despite its remarkable success and the elegance of the ΛCDM model, its validity has faced scrutiny and debate [22, 130, 56, 18]. This scrutiny has been driven by several profound theoretical and observational challenges. One major theoretical issue is the fine-tuning problem, which arises from the significant discrepancy between the observed value of the cosmological constant and theoretical predictions [124, 131, 132]. Additionally, the coincidence problem poses a challenge by highlighting the striking alignment between the observed vacuum energy density and matter density, despite their vastly different evolutionary behaviours [133].

Beyond the theoretical challenges, several pressing issues and challenges have garnered significant attention within the scientific community as has been briefly discussed in Chapter 1. Among these, the most pertinent are the unresolved nature of dark energy and dark matter [52, 53, 54, 55]. Further compounding these theoretical uncertainties are two compelling observational challenges: the Hubble tension and the growth tension. The Hubble tension refers to the discrepancy between the local measurements of the Hubble constant $H_0$ and its value inferred from observations of the early Universe, particularly the CMB [4, 16]. The local measurement of $H_0$, primarily obtained using the cosmic distance ladder method, is in significant tension with the value inferred from the angular scale of CMB fluctuations under the ΛCDM model [22, 134]. Specifically, the distance ladder approach, which calibrates distances step by step through various methods, yields a value of $H_0$ that is approximately $5\sigma$ higher than the CMB-inferred value [57].

To illustrate, the Planck Collaboration, which analyses CMB data, reports an $H_0$ value of $H_0^{\mathrm{P18}} = 67.4 \pm 0.5\,\mathrm{km/s/Mpc}$ at 68% confidence level [16]. In contrast, the Supernovae $H_0$ for the Equation of State (SH0ES) Collaboration, using late-time measurements such as Type Ia supernovae as part of the distance ladder, reports a value of $H_0^{\mathrm{R22}} = 73.04 \pm 1.04\,\mathrm{km/s/Mpc}$ at 68% confidence level [4]. Additionally, alternative methods, such as those involving Tip of the Red Giant Branch (TRGB) stars, have produced an $H_0$ value of $H_0^{\mathrm{F21}} = 69.6 \pm 1.9\,\mathrm{km/s/Mpc}$ at 68% confidence level, which sits between the Planck and SH0ES results [135, 59, 60]. However, even within TRGB calibrations, there are studies whose results align more closely with either the early-time or late-time observations, fuelling an ongoing debate.

As it currently stands, the $5\sigma$ tension between the SH0ES and Planck measurements is one of the most prominent discrepancies in modern cosmology, as these measurements theoretically should converge to the same value of $H_0$ [39]. This tension extends beyond these two key collaborations and is observed across various late- and early-time observational

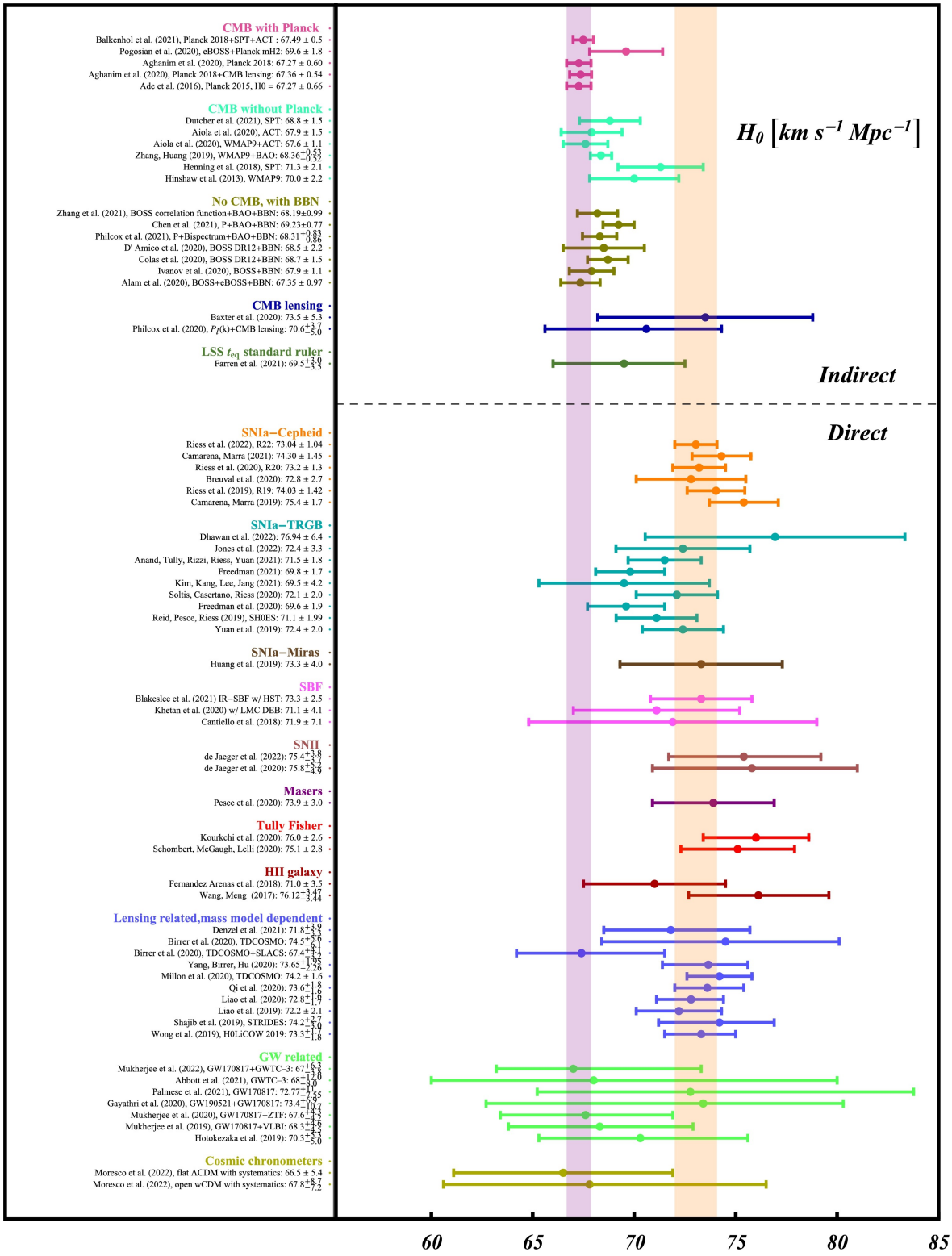


Figure 2.4: A comprehensive overview of the values of $H_0$ measurements coming form both early and late-times, taken from Ref. [22].

techniques. The disagreement is particularly evident when comparing direct, late-time, model-independent measurements—such as those from distance ladders and gravitational lensing—with early-time, model-dependent estimates, such as those derived from CMB and BAO data [22].

The Hubble tension has sparked the development and refinement of numerous methodologies aimed at independently measuring $H_0$. Beyond the well-known Planck (CMB) and SH0ES (distance ladder) results, a variety of approaches have been explored, each offering unique insights into the tension. Gravitational lensing time delays, for instance, leverage the deflection of light by massive foreground objects to estimate $H_0$. By measuring the time delay between multiple images of lensed quasars, this technique provides a direct, model-independent measurement of the Hubble constant. While current results from lensing generally favour intermediate values of $H_0$, further advancements in lensing models and improved data quality could help reduce uncertainties and refine the results [136, 137].

Another promising avenue is the use of gravitational wave standard sirens, which rely on the direct observation of the waveform emitted by inspiraling binary systems. These events provide an absolute distance scale, and when combined with redshift measurements, they yield independent estimates of $H_0$. Although current GW-based measurements have relatively large error bars, the anticipated increase in the number of detected events from next-generation observatories is expected to significantly enhance their precision [48].

As has already been discussed, cosmic chronometers offer yet another independent method for $H_0$ estimation, utilizing the age difference between passively evolving galaxies to directly measure the Hubble parameter at various redshifts. This technique is independent of any cosmological model and provides constraints on $H_0$ that are generally consistent with early-time measurements, though with larger uncertainties [138, 139]. In addition, BAO, also offer an indirect way to constrain $H_0$. While BAO measurements are tied to a fiducial cosmological model (often $\Lambda$CDM), they play a vital role in cross-validating results from other methods. Galaxy clustering and redshift-space distortions also provide valuable information, offering constraints on the expansion history of the Universe that indirectly inform $H_0$ estimates.

Quasars provide another intriguing avenue for measuring the Hubble constant, leveraging their unique characteristics as bright, distant sources. A key methodology involves reverberation mapping of quasars, where time delays between variations in the continuum emission and the response of the broad-line region are used to estimate the size of the emitting region. Combined with redshift measurements, this technique provides an independent estimate of the distance to quasars, and consequently, $H_0$ [140, 141]. Indeed, advancements in understanding quasar physics and the accumulation of high-quality data hold promise for reducing uncertainties.

Lastly, lensing-relations-based methods and Tully-Fisher-based techniques, which utilize the relationship between a galaxy's luminosity and rotational velocity, add further diversity to the landscape of $H_0$ determinations. These methods contribute to a more comprehensive understanding of the tension by probing different astrophysical phenomena and data sets.

A visual summary of this tension is provided in Fig. 2.4, taken from Ref. [22]. This whisker plot illustrates the Hubble tension by comparing direct and indirect measurements of the Hubble constant ($H_0$). The $x$-axis shows $H_0$ values in km/s/Mpc, while the $y$-axis lists various studies. The plot is divided into two sections: indirect methods (upper half), derived from early-Universe observations like the CMB (in pink), and direct methods (lower half), based on late-Universe measurements such as Cepheids (in orange). Each horizontal line represents a measurement with its error bars, highlighting uncertainty. The purple shaded region shows the confidence range for the P18 value, while the orange band represents the latest SH0ES value. The clear separation between these ranges visually emphasises the Hubble tension, as the two methods yield conflicting results, now exceeding $5\sigma$ significance.

A similar issue arises with the growth tension, which relates to discrepancies in the observed clustering of matter in the Universe. Recent observations of the LSS have provided direct measurements of the strength of matter clustering, which differ from those inferred from early Universe observations. Specifically, the anisotropies in the CMB measured by the Planck satellite suggest a different degree of matter clustering compared to what is observed at lower redshifts through probes like weak gravitational lensing and galaxy clustering [142, 64, 143, 144, 109, 145, 61, 16]. This discrepancy manifests as a tension of about $2-3\sigma$ when comparing the growth rate inferred from Planck's CMB data to that measured directly at lower redshifts [22, 18].

In the framework of GR, a slower growth rate implies either a lower matter density or a smaller amplitude of the primordial fluctuation spectrum than what is predicted by the Planck/ $\Lambda$CDM model. This tension is often quantified using the parameter $S_{8,0}$, defined as

$$S_{8,0} \equiv \sigma_{8,0}\sqrt{\Omega_{m,0}/0.3}\,, \tag{2.50}$$

which is closely related to the growth rate parameter $f\sigma_{8,0}$ measured by RSD, as will be discussed in more detail later.

Generally, lower-redshift observations favour a smaller value of $S_{8,0}$ compared to the higher value inferred from the CMB data. For instance, as shown in Fig. 2.5, the Planck CMB estimate of $S_{8,0}^{\rm P18} = 0.834 \pm 0.016$ [16] is in tension with late-Universe measurements, such as the value obtained from the Kilo-Degree Survey (KiDS-1000) (KiDS), which reported $S_{8,0}^{\rm KiDS} = 0.766^{+0.020}_{-0.014}$. Although the tension is less pronounced than the Hubble tension, it still

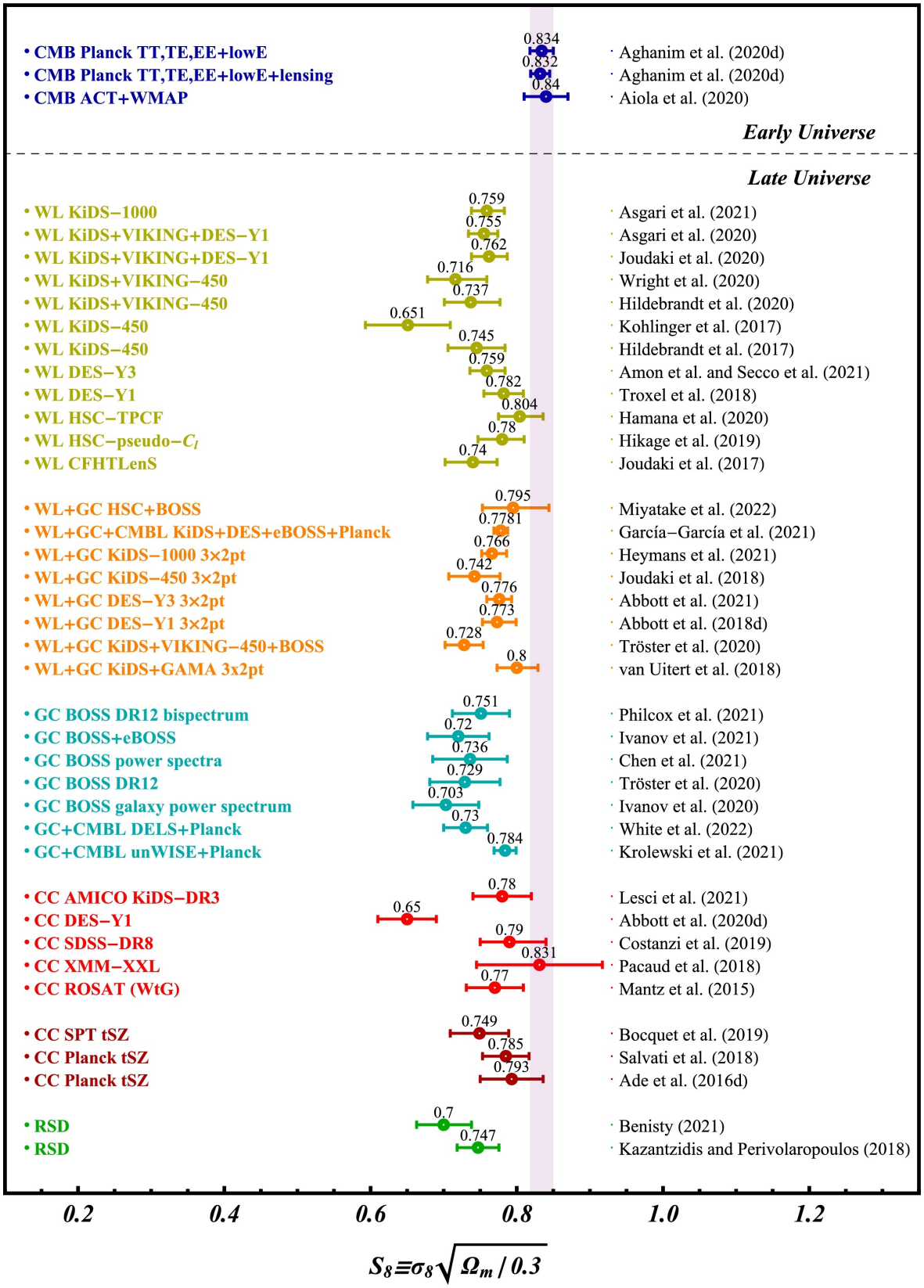


Figure 2.5: Constraints on $S_{8,0}$ and their corresponding 68% confidence levels derived from recent measurements. Taken from Ref. [22].

represents a significant challenge to the ΛCDM model. The $x$-axis in Fig. 2.5 shows $S_{8,0}$ values, while the $y$-axis lists different studies. Similar to the previous figure, the plot is divided into two sections: Early Universe (top), based on CMB measurements (in blue), and Late Universe (bottom), using weak lensing (WL), galaxy clustering (GC), and RSD (in green, orange, yellow, and red).

Each horizontal line represents an $S_{8,0}$ measurement, with error bars indicating uncertainties. The vertical shaded purple region highlights the early-Universe $S_{8,0}$ value from Planck values. On the other hand late-Universe measurements generally fall below this range, between $0.75 - 0.80$. This tension in $S_{8,0}$ values, although less pronounced than the Hubble tension, represents a growing challenge in cosmology, hinting at potential inconsistencies in our understanding of the Universe's structure formation or underlying physics.

As one can observe, the late-time measurements, despite involving different probes and methods, generally provide consistent results for both the $H_0$ tension and, to a lesser extent, the $S_{8,0}$ tension. This consistency strongly suggests that these tensions are unlikely to arise from systematic or statistical errors within the data itself, but rather point to an intrinsic issue within the current cosmological framework [18, 39, 56, 22].

The persistence and significance of these tensions across various observations may indicate the need for new physics beyond the standard ΛCDM model. The literature presents a wide range of innovative approaches to address these growing cosmic tensions. Some proposals involve reexamining the cosmological principle [146, 147], exploring the potential impacts of early Universe dark energy [148, 149], or considering the introduction of extra degrees of freedom, such as additional neutrino species in the early Universe [150, 151]. Among these approaches, modified gravity stands out as it offers a way to implement smaller, yet pervasive, changes that can affect the Universe's evolution across a broad range of redshifts. Modifications to GR can impact both the background and perturbative levels of the cosmological model. A particularly promising and natural avenue is TG [21, 152] (as discussed in more detail Sec. 2.2), where in turn, a natural extension of this approach is to generalise the TEGR Lagrangian to a more general function $\tilde{f}(T)$, which will be discussed in more detail in the next subsection.

### 2.4.2 | $f(T)$ Gravity

One promising avenue to address the aforementioned cosmological tensions is through a natural extension of TEGR, known as $\tilde{f}(T)$ gravity. This approach is inspired by the $f(\mathring{R})$ class of theories, where the gravitational Lagrangian is generalised to a function of the torsion scalar $T$, rather than the Ricci scalar $\mathring{R}$ [70, 153, 154]. By doing so, it introduces additional degrees of freedom, which can be used to modify the cosmological dynamics [65].

Furthermore, the significance of the boundary term $B$ in the relationship between $\mathring{R}$ and $T$ suggests a further natural extension to a more generalised framework, such as $\tilde{f}(T, B)$ gravity [80, 155]. However, this extension, will be explored further in the next subsection.

The flexibility in $\tilde{f}(T)$ gravity is particularly appealing for addressing the challenges posed by ΛCDM. Firstly, it preserves the fundamental principles of gravity while only changing the approach to the geometry of spacetime. Secondly, by adjusting the functional form of $\tilde{f}(T)$, it becomes possible to account for the observed accelerated expansion of the Universe without the need to introduce a cosmological constant.

Moreover, $\tilde{f}(T)$ gravity holds the potential to reconcile early- and late-time cosmological observations by introducing modifications that are relevant at different epochs in the Universe's history. This could provide a unified framework that addresses both the $H_0$ and $S_8$ tensions, offering a more complete understanding of the Universe's evolution.

Indeed, this $\tilde{f}(T)$ framework has been verified in solar system and white dwarfs tests, as shown in the works of Farrugia et al. [156] and Bahamonde et al. [66]. These models have also been confirmed in several other contexts, including studies involving white dwarfs, further supporting the consistency of the framework with both local observations and solar system constraints. These results suggest that, even without a screening mechanism, the deviations from General Relativity predicted by f(T) remain within the bounds established by stringent tests in these regimes.

The $\tilde{f}(T)$ gravity theory, which was introduced nearly a decade ago [157, 158], can be understood as a straightforward extension of TG. It introduces modifications to TEGR by focusing solely on the torsion scalar $T$. In this context, the theory is expressed as $\tilde{f}(T) = -T + f(T)$, and the corresponding action is given by [99, 66]:

$$\mathcal{S}_{f(T)} = \frac{1}{2\kappa^2}\int \mathrm{d}^4x\, e\,(-T + f(T)) + \int \mathrm{d}^4x\, e\mathcal{L}_{\mathrm{m}}\,. \tag{2.51}$$

It is important to highlight that, while GR and TEGR are equivalent at the level of their field equations, this equivalence breaks down when considering their extensions $\tilde{f}(\mathring{R})$ and $\tilde{f}(T)$. As discussed earlier in Eq. 2.19, the relationship $\mathring{R} = -T + B$ shows that $B$ is a boundary term that does not contribute to the Lagrangian in TEGR. However, in $\tilde{f}(T)$ gravity, which can involve a non-linear function and therefore, the equivalence between the two theories is no longer equivalent [65].

Studying the action in Eq. 2.51, the TEGR limit can be achieved by setting $f(T) \to 0$. On the other the ΛCDM limit is recovered in the limits in which $f(T)$ takes a constant value, such that $f(T) \to -2\Lambda$.

Varying the action with respect to the tetrad $e^A{}_\mu$, the field equations in a flat, homoge-

neous and isotropic Universe, the field equations for $f(T)$ read [65]

$$e^{-1}\partial_\nu \left(eS_A{}^{\mu\nu}\right)(-1+f_T) + T^B{}_{\nu A}S_B{}^{\nu\mu}(-1+f_T) - \frac{1}{2}E_A{}^\mu(-T+f(T)) + S_A{}^{\mu\nu}\partial_\nu(-1+f_T) + \omega^B{}_{A\nu}S_B{}^{\nu\mu}(-1+f_T) = \kappa^2 \mathcal{T}_A{}^\mu , \tag{2.52}$$

where subscripts refer to derivatives, such that $f_T$ refers to the first derivative of $f$ with respect to $T$ and $f_{TT}$ is the second derivative of the function.

This study investigates cosmology within the framework of the FLRW metric as described in Eq. 2.22, employing the tetrad choice [159, 160]

$$e^A{}_\mu = \mathrm{diag}\,(1,\, a(t),\, a(t),\, a(t))\ . \tag{2.53}$$

For this particular tetrad, the spin connection vanishes [66]. In this configuration, the torsion scalar $T$ is derived as [66, 65] [3]

$$T = -6H^2\,, \tag{2.54}$$

while the corresponding boundary term $B$ is given by

$$B = -6(3H^2 + \dot{H})\,. \tag{2.55}$$

From these expressions, the standard Ricci scalar can be directly related to the torsion scalar and boundary term, leading to a deeper understanding of the dynamics governed by the TEGR.

Using the diagonal tetrad in the field equations, the modified Friedmann equations for $f(T)$ gravity can be written as [65, 66]

$$H^2 + \frac{T}{3}f_T - \frac{f}{6} = \frac{\kappa^2}{3}\rho\,, \tag{2.56}$$

$$\dot{H}\,(1 - f_T - 2Tf_{TT}) = -\frac{\kappa^2}{2}\,(\rho + p)\ . \tag{2.57}$$

Evidently, $f(T)$ gravity can be interpreted such that the "extra terms" in the above equations can be explained as an effective dark energy and the modified Friedmann equation take the following shape [65, 66]

$$3H^2 = \kappa^2(\rho + \rho_{\mathrm{eff}})\,, \tag{2.58}$$

$$2\dot{H} + 3H^2 = -\kappa^2(p + p_{\mathrm{eff}})\,, \tag{2.59}$$

[3] It is important to note that in Chapter. 4, the signs of $T$ and $B$ are reversed, with $T = 6H^2$ and $B = 6(3H^2 + \dot{H})$. This difference rises from a choice of convention, which depends on the signature of the metric. In Chapter 4, the metric is taken to be $g_{\mu\nu} = \left(-1, a^2(t), a^2(t), a^2(t)\right)$. However, it is crucial to recognise that at the level of the Hubble parameter within the Friedman equations, both conventions yield equivalent results.

such that

$$\rho_{\text{eff}} := \frac{1}{2\kappa^2}\left(f - 2Tf_T\right), \tag{2.60}$$

$$p_{\text{eff}} := -\frac{1}{\kappa^2}\left[-2\dot{H}\left(f_T + 2Tf_{TT}\right)\right] - \rho_{\text{eff}}\,. \tag{2.61}$$

The effective fluid also satisfies the standard conservation equation [161, 66]

$$\dot{\rho}_{\text{eff}} + 3H\left(\rho_{\text{eff}} + p_{\text{eff}}\right) = 0\,, \tag{2.62}$$

and can be used to define an effective equation of state giving [65]

$$\omega_{\text{eff}} := \frac{p_{\text{eff}}}{\rho_{\text{eff}}} = -1 + \frac{(f - T - 2Tf_T)(f_T + 2Tf_{TT})}{(1 + f_T + 2Tf_{TT})(f - 2Tf_T)}\,. \tag{2.63}$$

In the upcoming chapters, particularly Chapter 8, a detailed analysis of the $H_0$ and $S_{8,0}$ tensions is conducted within the context of $f(T)$ gravity. Alongside the Friedmann equations (Eqs. 2.56, 2.57), the equation governing the evolution of matter perturbations in the linear regime (Eq. 2.34) is also explored. In $f(T)$ gravity, as in many other modified gravity theories, the gravitational constant $G_{\text{eff}}$ becomes an effective, dynamic parameter rather than a fixed constant [162]. This arises because the function $f(T)$ modifies the field equations, causing $G_{\text{eff}}$ to vary with the torsion scalar $T$, thereby reflecting the changing nature of gravitational interactions across different cosmological contexts. This relationship is captured by the equation [65, 22, 66]

$$\ddot{\delta} + 2H\dot{\delta} = 4\pi G_{\text{eff}}\,\rho\,\delta\,, \tag{2.64}$$

where $G_{\text{eff}}$ generally depends on redshift $z$ and the cosmic wave vector $\mathbf{k}$ [35, 163]. However, for the specific limits and data sets under consideration, $G_{\text{eff}}$ can be considered independent of $\mathbf{k}$. In GR $G_{\text{eff}}$ is equal to $G_N$. In the context of $f(T)$ gravity, the evolution of linear matter perturbations is expressed as [162, 164]

$$G_{\text{eff}}(z) = \frac{G_N}{1 + f_T(z)}\,. \tag{2.65}$$

Thus, the sensitivity of the linear matter perturbation equation to $f(T)$ gravity highlights the potential of large-scale structure data to place observational constraints on viable models. In this setting, Eq. 2.35 takes the form,

$$\delta''(z) + \left(\frac{H'(z)}{H(z)} - \frac{1}{1+z}\right)\delta'(z) = \frac{3}{2}\frac{G_{\text{eff}}(z)}{G_N}\left(\frac{H_0}{H(z)}\right)^2 \Omega_{m,0}\,(1+z)\,\delta(z)\,. \tag{2.66}$$

In addition to the analysis of density fluctuations, the propagation of GW within $f(T)$ gravity (specifically in Chapter 9). The generalised form of the tensor perturbation equation, extending Eq. 2.44 to this context, is given by [165, 166]

$$\ddot{h}_{ij} + (3 + \alpha_m)\dot{h}_{ij} - (1 + \alpha_T)\frac{k^2}{a^2}h_{ij} = 0\,, \tag{2.67}$$

where $\alpha_T$ represents the *tensor excess speed* and $\alpha_m$ denotes the *Planck mass rate*. The tensor excess speed $\alpha_T$ quantifies the deviation of the propagation speed of GW from the speed of light, characterised by the relation $c_T^2 = 1 + \alpha_T$, where $c_T$ is the speed of gravitational waves. In $f(T)$ gravity, as in GR, gravitational waves propagate at the speed of light, implying that $c_T^2 = 1$ [167, 168], and consequently,

$$\alpha_T = 0\,. \tag{2.68}$$

The Planck mass rate $\alpha_m$ introduces a friction-like term in the tensor perturbation equation. This term corresponds to a redefinition of the Planck mass and is related to the cosmological strength of gravity, denoted by $M_*^2$ (the kinetic term of the tensor perturbations) [165, 169]. In the context of $f(T)$ gravity, $\alpha_m$ is given by [66]

$$\alpha_m = \frac{1}{H}\frac{\dot{f}_T}{f_T}\,. \tag{2.69}$$

When expressed in terms of redshift, the tensor perturbation equation can be rewritten as

$$h_{ij}'' + (2 + \alpha_m)aHh_{ij}' + (1 + \alpha_T)k^2 h_{ij} = 0\,, \tag{2.70}$$

with $\alpha_m = -12\frac{H'}{a}\frac{f_{TT}}{f_T}$. This formulation emphasises the dependence of the propagation dynamics on the modified gravity model parameters and provides insight into the effects of $f(T)$ gravity on GW propagation across different cosmological epochs.

### 2.4.3 | $f(T, B)$ gravity

A rather more generalised extension of TEGR can be achieved by taking the arbitrary function $\tilde{f}(T, B)$ which encapsulates both the torsion scalar and the boundary term. In this case, one can deviate from TEGR by considering the arbitrary function $\tilde{f}(T, B)$ such that $\tilde{f}(T, B) = -T + F(B)$. This arises naturally when aiming to isolate purely fourth-order modifications of gravity, as the boundary term $B$ encapsulates the divergence between the Ricci scalar and the torsion scalar. By choosing $F(B)$ as the modification term, the distinction between first- and fourth-order effects is maintained, avoiding the additional complexity introduced by mixed $T - B$ terms.

Excluding mixed $T - B$ terms simplifies the theoretical landscape and ensures that deviations from GR are sourced exclusively by $B$. This has implications for the structure of

the field equations, which remain manageable and analytically tractable, making it easier to connect the models with observational data.

While the absence of such terms simplifies the framework and retains a clear distinction between $T$ and $B$ contributions, mixed terms have been explored in the literature, such as Ref. [80] and shown to yield interesting dynamical behaviours.

Therefore, the action becomes [155, 66]

$$\mathcal{S}_{f(T,B)} = \frac{1}{2\kappa^2}\int \mathrm{d}^4x\, e\,(-T + F(B)) + \int \mathrm{d}^4x\, e\mathcal{L}_\mathrm{m}\,. \tag{2.71}$$

The TEGR limit is achieved when $\tilde{f}(T,B) \to -T$, implying there will be no contribution from the boundary term $B$ and $F(B) = 0$. The $\Lambda$CDM limit, on the other hand, is obtained for a constant $F(B)$, where $F(B) \to 2\Lambda$, such that $\tilde{f}(T,B) \to -T + 2\Lambda$.

Thus, the field equations for such action can be obtained by taking the variation with respect to the tetrad [155]

$$\begin{aligned} E_A{}^\mu \mathring{\Box} F_B - E_A{}^\nu \mathring{\nabla}^\mu \mathring{\nabla}_\nu F_B + \frac{1}{2}BF_B E_A{}^\mu - (\partial_\nu F_B - 1)S_A{}^{\mu\nu} + \frac{1}{e}\partial_\nu(eS_A{}^{\mu\nu}) - T^B{}_{\nu A}S_B{}^{\nu\mu} \\ -\omega^B{}_{A\nu}S_B{}^{\nu\mu} - \frac{1}{2}(-T + F(B))E_A{}^\mu = \kappa^2 \mathcal{T}_A{}^\mu \end{aligned} \tag{2.72}$$

where $\Box = \nabla^\mu\nabla_\mu$ is the d'Alembert operator and $F_B$ is the derivative of $F$ with respect to $B$.

Following the $f(T)$ FLRW cosmology, Eqs. 2.53 – 2.55 remain exactly the same. The modified Friedmann equation for $f(T,B)$ thus become

$$3H\dot{F}_B - 3H^2(-2 + F_B) - 3F_B\dot{H} - \frac{1}{2}F(B) = \kappa^2\rho\,, \tag{2.73}$$

$$-(3H^2 + \dot{H})(-2 + 3F_B) + \ddot{F}_B - \frac{1}{2}F(B) = -\kappa^2 p\,, \tag{2.74}$$

where $\dot{F}_B$ is the time derivative of $F_B = \frac{\mathrm{d}F(B)}{\mathrm{d}B}$ whilst $\ddot{F}_B$ is the second derivative with respect to time of said term.

Similarly to $f(T)$, $f(T,B)$ can be interpreted as a gravitational fluid with associated energy density $\rho_\mathrm{eff}$ and $p_\mathrm{eff}$, such that the above equations can be rewritten in the form

$$3H^2 = \kappa^2(p + \rho_\mathrm{eff}) \tag{2.75}$$

$$3H^2 + 2\dot{H} = -\kappa^2(p + p_\mathrm{eff}\,, \tag{2.76}$$

with the gravitational fluid defined as

$$\kappa^2\rho_{\text{eff}} := 3H^2(3F_B) - 3H\dot{F}_B + 3H\dot{F}_B + 3\dot{H}F_B + \frac{F(B)}{2} \tag{2.77}$$

$$\kappa^2 p_{\text{eff}} := \frac{F(B)}{2} - 3F_B(3H^2 + \dot{H}) + \ddot{F}_B\,. \tag{2.78}$$

Consequently the effective, EoS becomes [82, 80]

$$w_{\text{eff}} := \frac{p_{\text{eff}}}{\rho_{\text{eff}}} = -1 + \frac{\ddot{F}_B - 3H\dot{F}_B}{3H^2(3F_B) - 3H\dot{F}_B + 3\dot{H}F_B + \frac{1}{2}F}\,. \tag{2.79}$$

## 2.5 | Conclusion

In this chapter, the foundational concepts of modern cosmology, centring on the interplay between curvature and torsion, as well as the frameworks of GR and TEGR were explored. These discussions provide a comprehensive backdrop for understanding the evolution of our Universe and the fundamental forces that govern it.

At the heart of classical gravitational theories lies the distinction between curvature and torsion as geometric properties of spacetime. In GR, gravity is understood as the manifestation of spacetime curvature, encoded in the Ricci scalar $\mathring{R}$, which is derived from the Levi-Civita connection. The Levi-Civita connection, in turn, is torsion-free, implying that torsion does not play a direct role in the formulation of GR. This geometric interpretation of gravity has been extraordinarily successful in explaining a wide array of physical phenomena, from the perihelion precession of Mercury to the deflection of light by massive objects and the expansion of the Universe.

Indeed, the successes of GR has laid the foundation for ΛCDM model, which has become the standard model of cosmology. It elegantly combines GR with the cosmological constant $\Lambda$ and a dark matter component, explaining the accelerated expansion of the Universe, the formation of large-scale structures, and the anisotropies in the CMB. Yet, despite its successes, ΛCDM is not without its challenges. Two of the most prominent issues are the so-called $H_0$ tension and $S_{8,0}$ tension. The $H_0$ tension refers to the discrepancy between the value of the Hubble constant $H_0$ as inferred from early Universe observations (such as CMB) and its value as measured in the late Universe (using local distance indicators like Cepheid variables and supernovae). The $S_{8,0}$ tension, on the other hand, arises from differences in the inferred amplitude of matter fluctuations on a scale of 8 Mpc, again between early Universe measurements and those from large-scale structure surveys.

These tensions suggest that there might be more to our Universe than what is encapsulated within the ΛCDM paradigm. They may hint at new physics beyond the standard

model of cosmology, possibly requiring modifications to GR or the introduction of new components beyond dark matter and dark energy.

Admittedly, the perspective of perceiving gravity through curvature is not the only way to describe gravity. An alternative approach is offered by TG, wherein gravity is attributed not to curvature, but to torsion. In this framework, the Teleparallel connection, which is curvature-free but possesses torsion, replaces the Levi-Civita connection. The TEGR is a particular formulation of this theory, where the torsion scalar $T$ plays a role analogous to the Ricci scalar in GR (up to a boundary term $B$). Remarkably, TEGR is dynamically equivalent to GR, meaning it reproduces the same field equations and thus the same phenomenology, despite its distinct geometric foundation.

Given the challenges faced by $\Lambda$CDM, particularly the $H_0$ and $S_{8,0}$ tensions, the exploration of extended modified gravity theories becomes a compelling avenue for addressing these cosmological issues. One such extension is $f(T)$ gravity, a generalisation of TEGR where the Lagrangian is a function of the torsion scalar $T$. This natural modification, allows for further exploration in the subsequent chapters and its implications for cosmic evolution, structure formation, and the propagation of gravitational waves will also be investigated.

Furthermore, the $f(T, B)$ theory represents an even more generalised approach by incorporating the boundary term $B$ into the gravitational action. In $f(T, B)$ gravity, the boundary term $B$ serves as a bridge between curvature-based and torsion-based descriptions of gravity, making it a natural extension for addressing the inconsistencies within $\Lambda$CDM and to also study its implications.

The aim of exploring these alternatives to $\Lambda$CDM, is to investigate whether these models can provide a better fit to observational data. These alternatives might offer solutions that resolve the existing discrepancies without conflicting with the successful predictions of $\Lambda$CDM in other areas. Furthermore, these explorations have the potential to reveal new insights into the fundamental nature of gravity, and the behaviour of dark energy, and the overall dynamics of the cosmos. In essence, the goal is to push the boundaries of our knowledge, and see if these approaches can provide a clearer picture of the Universe and deepen our understanding of its fundamental workings

# 3

# Methods, Observations and the Road to Cosmological Models

In the evolving field of cosmology, understanding the dynamics of the Universe's expansion remains a central pursuit. Over recent decades, the standard cosmological model, ΛCDM, has provided a foundational framework for interpreting observations of cosmic structure and evolution. However, the quest to explore alternative theories has driven significant research into modifications of general relativity and extensions to the standard model. Among these alternatives, $f(T)$ gravity stands out as a compelling framework that modifies the TEGR to address phenomena such as cosmic acceleration.

In cosmology, traditional computational methodologies often revolved around analytical approximations and direct numerical integration techniques. While these approaches were effective in simple cases, their limitations became evident with increasingly complex datasets and models. The advent of MCMC methods represented a significant advancement, offering robust tools for model selection and parameter estimation by sampling from high-dimensional probability distributions. MCMC methods, and its algorithms such as the Metropolis-Hastings, remain widely used for their reliability and ability to explore posterior distributions comprehensively.

More recently, GPs have gained prominence as a versatile non-parametric method. Unlike MCMC, which relies on explicit assumptions about the model's functional form, GPs provide a data-driven approach to reconstruct functions and quantify uncertainties. This has proven particularly valuable in cosmological reconstructions, where flexibility and adaptability are crucial.

Additionally, the rise of machine learning has introduced neural networks and other Artificial Intelligence-based methods as computational tools. These techniques have demonstrated potential in areas such as classification and clustering of cosmological data. How-

ever, their application to parameter estimation and model selection is still in its infancy, with challenges surrounding interpretability and the need for extensive training datasets.

In this context, MCMC and GPs stand out as a mature and well-established methodology, providing an ideal balance between interpretability, flexibility, and computational efficiency. Therefore, this chapter delves into a comprehensive analysis of several $f(T)$ cosmological models, utilising advanced statistical techniques to assess their viability. Specifically, key methodologies employed include GPs and MCMC simulations, which offer powerful tools for extracting meaningful insights from observational data. The observational datasets used, while current at the time of analysis, will undoubtedly evolve as new data becomes available. This ongoing development underscores the importance of continually refining models and datasets to stay up-to-date of the latest cosmic measurements.

The chapter begins with a detailed introduction of the methods employed in the analysis: GP and MCMC. These methods are crucial in analysing the $f(T)$ (ans later on $f(T, B)$ framework and extract insights from observational data. MCMC provides a framework for exploring the parameter space of these models, while GP offers a flexible approach for reconstructing the Hubble parameter and the $f(T)$ function.

Following the discussion of methodologies, the chapter transitions to a review of the observational data used in the analysis. Then, five distinct $f(T)$ models, each offering unique perspectives on the dynamics of cosmic expansion are presented and explored. These models will be later on compared against the observational data, with a particular emphasis on their comparative performance relative to the $\Lambda$CDM model. To facilitate this comparison, statistical criteria such as the Akaike Information Criteria (AIC) and Bayesian Information Criteria (BIC) are employed, with results interpreted through the lens of the Jeffreys' Scale (which will be explained in detail further on) to gauge the strength of evidence supporting each model and help identify which models offer the best balance between fit and complexity.

In the course of this analysis, future work will extend this investigation to include more complex models, such as $f(T, B)$ gravity, which incorporates additional parameters to further refine our understanding of cosmic dynamics. This forthcoming analysis will build upon the insights gained from the current models, offering a broader and more detailed perspective on cosmological evolution.

Through this exploration, the chapter aims to contribute to the broader dialogue on cosmological models, providing a better evaluation of $f(T)$ gravity and its potential to offer new perspectives on the Universe's expansion. The subsequent section will start off with the first method used: Gaussian Process (GP).

## 3.1 | Gaussian Processes

Least squares regression is a fundamental statistical technique used to estimate parameters by minimising the sum of squared differences between observed and predicted values [170]. This method assumes a specific form for the underlying function and provides point estimates for the parameters. However, it may not effectively capture the uncertainty in predictions or handle complex, non-linear relationships.

As data complexity increases, Gaussian Processs (GPs) present a robust alternative. Unlike least squares regression, which relies on predefined parametric forms, GPs offer a non-parametric approach that does not require an explicit functional form for the data. This flexibility is crucial for modelling intricate relationships and for scenarios where the underlying data structure is unknown.

GPs are a powerful tool within the machine learning toolbox [171], providing a sophisticated method for making predictions by incorporating prior knowledge. Given a set of data points, there are potentially infinite functions that could fit the data. However, GPs address this by assigning a probability distribution to each possible function, rather than selecting a single model. The mean of this distribution represents the most probable characterisation of the data, while the probabilistic framework allows for the incorporation of confidence intervals in the predictions [171].

In the following subsections, the fundamental principles and core concepts of GPs will be explored. A detailed discussion of the most commonly used covariance matrices will follow, providing insight into their roles and applications. This will be followed by a comprehensive overview of how to effectively implement GPs. Finally, the discussion will extend beyond predicting the underlying function to include the modelling of its derivatives.

### 3.1.1 | Fundamentals of Gaussian Processes

The fundamental building block of GPs is the Gaussian (or normal) distribution, which describes the distribution of a random variable. GP generalises this concept to model functions within a stochastic statistical process. Formally, a GP is defined as a collection of random variables, any finite number of which have a joint Gaussian distribution [171]. This enables GPs to reconstruct the most plausible continuous function that describes the data and its derivatives, while also providing confidence intervals without requiring a predefined functional form [172].

By using GPs, predictions can be made for function values at new points based on observed data, without assuming a specific functional form. This non-parametric approach offers a significant advantage over traditional parametric models by providing a distribu-

tion as a prediction, which reflects the uncertainty inherent in the model. Therefore, GPs are particularly valuable for handling complex, non-linear relationships and for scenarios requiring model independence.

The process of reconstructing a function using GPs is outlined as follows. Given a dataset $\mathcal{D}$ comprising of $n$ observations

$$\mathcal{D} = \{(\tilde{z}_i, y_i) \mid i = 1, \ldots, n\}\,, \tag{3.1}$$

in which GP aims to reconstruct the function $g(z)$ that best represents this data. Similar to a multivariate normal distribution, a GP is characterised by two fundamental components: a mean function $\mu(z)$ and a covariance function $\mathcal{C}(z, z')$ [173]. The GP ($\mathcal{GP}$) can be formally expressed as

$$g(z) \sim \mathcal{GP}(\mu(z), \mathcal{C}(z, z'))\,. \tag{3.2}$$

In many cases, the mean function $\mu(z)$ can be assumed to be zero across all points, as each point is insensitive to this. The covariance function, $\mathcal{C}(z, z')$ captures the dependencies between function values at different points $z$ and $z'$, indicating how they are correlated.

In GPs, the mean function is often set to zero as a simplifying assumption, especially when no prior knowledge about the data is available. The choice of mean function typically doesn't affect the results significantly as long as the covariance structure (the kernel) is well-defined and captures the data's underlying structure. Mathematically, setting $\mu = 0$ implies that the GP prior assumes no initial bias or trend, which allows the covariance function to dictate the correlations between the function values at different input points. Thus, by relying solely on the covariance structure, we ensure that the GP model remains flexible and can adapt to the data without imposing unnecessary assumptions on its baseline.

When the mean function is not set to zero, it introduces an assumption about the baseline of the data. For instance, using a constant mean assumes a fixed baseline, which may influence predictions if the true mean deviates from this assumption. However, without prior knowledge of the mean, this choice could lead to bias in the model's predictions if the assumed mean does not align with the true underlying behaviour of the data.

For redshift points $z^*$ where no direct data is available but where function values need to be reconstructed, the covariance function is defined as $\mathcal{C}(z^*, z^{*'}) \equiv \mathcal{K}(z^*, z^{*'})$. Here, $\mathcal{K}(z^*, z^{*'})$ denotes the kernel function, which describes the correlation between the function values at $z^*$ and $z^{*'}$. This kernel is thus far unknown, but the function must be symmetric and encapsulates information about the correlation structure and the scale of deviations from the mean.

Therefore, the GP generates a Gaussian vector $\boldsymbol{g}^*$ of function values at the redshift points $z^*$, where $g_i^* = g(z_i^*)$. The distribution of $\boldsymbol{g}^*$ follows a multivariate normal distribution

$$\boldsymbol{g}^* \sim \mathcal{N}(\mathbf{0}, \mathcal{C}(\boldsymbol{Z}^*, \boldsymbol{Z}^*)) \,, \tag{3.3}$$

where $\boldsymbol{\mu}^* = \mathbf{0}$, $\boldsymbol{Z}^* = \{z_i^*\}$, and $\mathcal{C}(\boldsymbol{Z}^*, \boldsymbol{Z}^*)$ is the covariance matrix with entries $\mathcal{C}(\boldsymbol{Z}^*, \boldsymbol{Z}^*)_{|_{ij}} = \mathcal{C}(z_i^*, z_j^*)$. This matrix encapsulates the covariances between all pairs of points in the set $\boldsymbol{Z}^*$, facilitating the reconstruction of the function at unobserved locations based on the observed data. This

It is also important to note that the notation $\mathcal{N}$ signifies that the GP ($\mathcal{GP}$) is evaluated at specific points $z^*$, where $g(z^*)$ is a random variable drawn from a normal distribution. As the function itself is not constrained by prior observations, it initially appears arbitrary. However, the covariance function imposes correlations between function values at different locations $z^*$. This covariance function acts as a prior that influences the selection of potential output functions. The introduction of additional observational data points $\tilde{z}_i$ subsequently refines and constrains the function further, ensuring that the predictions are consistent with the observed data.

In the case of observational data points, $\tilde{z}$, the correlations and uncertainties are accessible and thus, the covariance matrix, $\mathcal{G}(\tilde{z}, \tilde{z}')$, between these points is known. This can be used as the first step to finding a relation between the data and the underlying function as the covariance function for observational data points can be defined as $\mathcal{C}(\tilde{z}, \tilde{z}') \equiv \mathcal{K}(\tilde{z}, \tilde{z}') + \mathcal{G}(\tilde{z}, \tilde{z}')$. This leads to to the following multivariate normal distribution

$$\boldsymbol{y} \sim \mathcal{N}(\mathbf{0},\, \mathcal{C}(\tilde{\boldsymbol{Z}}, \tilde{\boldsymbol{Z}})) \,, \tag{3.4}$$

where $\boldsymbol{\mu} = \mathbf{0}$, $\tilde{\boldsymbol{Z}} = \{\tilde{z}_i\}$ and thus, $\mathcal{C}(\tilde{\boldsymbol{Z}}, \tilde{\boldsymbol{Z}})$ is the covariance matrix defined by $\mathcal{C}(\tilde{\boldsymbol{Z}}, \tilde{\boldsymbol{Z}})_{|_{ij}} = \mathcal{C}(\tilde{z}_i, \tilde{z}_j)$.

However, there remains an unknown correlation between observational data points $\tilde{z}$ and the general points $z^*$ for which the covariance function can be defined as $\mathcal{C}(\tilde{z}, z^*) \equiv \mathcal{K}(\tilde{z}, z^*)$, where $\mathcal{K}(\tilde{z}, z^*)$ is yet to be defined.

The above two GP can be incorporated together in the below joint probability distribution

$$\begin{bmatrix} \boldsymbol{y} \\ \boldsymbol{g}^* \end{bmatrix} \sim \mathcal{N}\left( \mathbf{0}\,, \begin{bmatrix} \mathcal{C}(\tilde{\boldsymbol{Z}}, \tilde{\boldsymbol{Z}}) & \mathcal{C}(\tilde{\boldsymbol{Z}}, \boldsymbol{Z}^*) \\ \mathcal{C}(\boldsymbol{Z}^*, \tilde{\boldsymbol{Z}}) & \mathcal{C}(\boldsymbol{Z}^*, \boldsymbol{Z}^*) \end{bmatrix} \right) . \tag{3.5}$$

From the above equation, $\boldsymbol{y}$ can be obtained from observations, however, $\boldsymbol{g}^*$ needs to be reconstructed by using a following conditional distribution [173]

$$\boldsymbol{g}^* | \boldsymbol{Z}^*, \boldsymbol{Z}, \boldsymbol{y} \sim \mathcal{N}(\overline{\boldsymbol{g}^*}, \mathrm{cov}(\boldsymbol{g}^*)) \,. \tag{3.6}$$

Thus, the mean value ($\overline{g^*}$) and the covariance $\mathrm{cov}(f^*)$ of the reconstructed function $g^*$ at point $z^*$ can be shown to be

$$\overline{g^*} = \overline{g}(z^*) = \sum_{i,j=1}^{n} \mathcal{C}(z^*, \tilde{z}_j)[\mathcal{C}(\tilde{z}_i, \tilde{z}_j)]^{-1}(y)\,, \tag{3.7}$$

$$\mathrm{cov}(g^*) = \mathcal{C}(z^*, z^*) - \sum_{i,j=1}^{n} \mathcal{C}(z^*, \tilde{z}_i)[\mathcal{C}(\tilde{z}_i, \tilde{z}_j)]^{-1}\mathcal{C}(\tilde{z}_j, z^*) \tag{3.8}$$

### 3.1.2 | Overview of Kernel Functions

A diverse range of kernel functions, $\mathcal{K}(z, z')$, mentioned earlier, are available for use in Gaussian processes [171], each offering distinct advantages and limitations depending on the specific application or problem at hand. The effectiveness of these kernels is an area of ongoing research and debate [172, 174]. Central to these kernel functions are two crucial parameters known as hyperparameters, which impact the performance and flexibility of the GP. These hyperparameters control the kernel's ability to accurately model and fit the underlying data. An understanding of these hyperparameters is essential for tailoring the kernel to the specific characteristics of the data. The following points will first describe these hyperparameters in detail, followed by an overview of the specific kernels employed in this study.

- *Vertical Scale Parameter* ($\sigma_g$): This parameter governs the magnitude of the function's variations and the strength of correlations between uncertainties. By adjusting $\sigma_g$, one can control the vertical scaling of the function, which directly influences the amplitude of the fluctuations in the predicted values. A larger $\sigma_g$ results in a broader range of values for the function, reflecting greater uncertainty in the predictions [175].

- *Length Scale Parameter* ($l_g$): The length scale, denoted as $l_g$, determines how the correlation between data points diminishes with distance. Specifically, $l_g$ defines the spatial range over which the function values remain correlated. When the distance between two points $|z - z'|$ is much smaller than $l_g$, the function values are strongly correlated. Conversely, as the distance increases beyond $l_g$, the correlation rapidly decreases. Thus, $l_g$ sets the scale for how quickly the influence of one data point fades with distance [176]. This parameter is crucial for capturing the smoothness and variability of the function over the input space [175].

For the purposes of this project, several kernel functions were evaluated to assess their impact on the reconstruction of the function. The following equations present four of the most widely used kernels, which were employed in this study.

- **Squared-Exponential kernel**

$$\mathcal{K}\left(z, z'\right) = \sigma_g^2 \exp\left[-\frac{\left(z - z'\right)^2}{2l_g^2}\right], \tag{3.9}$$

where $\sigma_g$ and $l_g$ are hyperparameters of the kernel functions. This kernel is considered to be a general purpose kernel and thus, it is one of the most actively used kernel [172]. This kernel function is also infinitely differentiable and is therefore, very smooth. This is a useful property for constructing higher-order derivatives as well [171, 177]. If $z \approx z'$, then $\mathcal{K}(z, z')$ approaches a maximum, which in turn means that $g(z)$ and $g(z')$ are almost perfectly correlated with each other. This continues to substantiate the point that for neighbouring points the functions must have have similar values and thus, it will be a smooth function. If on the other hand, $z$ and $z'$ are distant from each other, then $\mathcal{K}(z, z') \approx 0$ and the function at these points will have no correlation with each other [178]. The length scale $l_g$ determines how quickly this correlation decays, influencing the function's smoothness, while $\sigma_g^2$ scales the overall variability of the function. This kernel's properties make it particularly effective for modelling continuous trends and smooth variations in data, making it a popular choice in Gaussian process regression for its flexibility and capability to handle a wide range of smooth functions.

- **Cauchy Kernel**

$$\mathcal{K}\left(z, z'\right) = \sigma_g^2 \left[\frac{l_g}{\left(z - z'\right)^2 + l_g^2}\right], \tag{3.10}$$

which is also dependant on the hyperparameters $\sigma_g$ and $l_g$. Unlike the squared exponential kernel, which features an exponential decay in covariance, the Cauchy kernel decreases polynomially with distance. This behaviour is governed by the term $(z - z')^2 + l_g^2$ in the denominator. This decay allows the Cauchy kernel to accommodate data with abrupt changes and outliers, as it does not penalise large deviations as severely as kernels with exponential decay.

The Cauchy kernel's ability to handle such heavy-tailed behaviour makes it particularly valuable for modelling functions where data may exhibit irregularities over large distances. Its sharp variations makes it a suitable choice for scenarios where traditional smooth kernels might fail to capture essential features of the data [174].

- **Matérn Kernel**

$$\mathcal{K}\left(z, z'\right) = \sigma_g^2 \left(1 + \frac{\sqrt{3}|z - z'|}{l_g}\right) \exp\left[-\frac{\sqrt{3}|z - z'|}{l_g}\right], \tag{3.11}$$

.

The Matérn kernel incorporates both a polynomial term and an exponential term to control the smoothness of the resulting function. The term $\frac{\sqrt{3}|z-z'|}{l_g}$ introduces a lengthscale-dependent decay, while the exponential function $\exp\left[-\frac{\sqrt{3}|z-z'|}{l_g}\right]$ modulates the rate of decay. This combination allows the Matérn kernel to interpolate between different degrees of smoothness.

The Matérn kernel is known for its ability to produce functions that exhibit less smoothness compared to the squared exponential kernel, making it suitable for modelling functions with rougher features or varying smoothness [179].

- **Rational quadratic kernel**

$$\mathcal{K}\left(z, z'\right) = \sigma_g^2 \left[1 + \frac{(z-z')^2}{2\alpha l_g^2}\right]^{-\alpha}, \tag{3.12}$$

In this case, an additional hyperparameter is included, the $\alpha$ parameter, which governs the flexibility of the kernel. The parameter $\alpha$ controls the relative weighting of these varying length scales. Essentially, $\alpha$ adjusts the average distance over which the function exhibits vertical variations. The Rational Quadratic kernel can be seen as a scale mixture of squared exponential kernels, allowing it to effectively capture both short-range and long-range dependencies in the data. This makes it particularly useful for handling data with different scales of variation and complex patterns [171].

To reconstruct the function using GPs the choice of kernel function and its associated hyperparameters, such as $\sigma_g$ and $l_g$, play a crucial role. The kernel function determines the covariance structure of the data, while the hyperparameters tune the kernel to best fit the observed data. The reconstruction process depends on these choices, as described by the kernel equations. This process ensures that the model captures the underlying patterns of the data by adjusting the hyperparameters to minimize the discrepancy between the model's predictions and the observed data.

Therefore, the hyperparameters need to be optimised by maximising the marginal likelihood, which involves integrating over the possible functions $\boldsymbol{g}$ evaluated at the data points $\tilde{\boldsymbol{Z}}$. This is represented mathematically as

$$p(\boldsymbol{y}|\tilde{\boldsymbol{Z}}, \sigma_g, l_g) = \int p(\boldsymbol{y}|\boldsymbol{g}, \tilde{\boldsymbol{Z}}) p(\boldsymbol{g}|\tilde{\boldsymbol{Z}}, \sigma_g, l_g)\, d\boldsymbol{g}\,, \tag{3.13}$$

where $p(\boldsymbol{y}|\boldsymbol{g}, \tilde{\boldsymbol{Z}})$ is the likelihood of the observed data given the function values, and $p(\boldsymbol{g}|\tilde{\boldsymbol{Z}}, \sigma_g, l_g)$ is the prior distribution over the functions. This integration marginalises over the function values, focusing only on the observed data locations $\tilde{\boldsymbol{Z}}$ and not on the new reconstruction points $\boldsymbol{Z}^*$.

Assuming a Gaussian prior for the function values, $\boldsymbol{g}|\tilde{\boldsymbol{Z}}, \sigma_g, l_g \sim \mathcal{N}(\boldsymbol{\mu}, \mathcal{K}(\tilde{\boldsymbol{Z}}, \tilde{\boldsymbol{Z}}))$, and that the observations are also Gaussian, $\boldsymbol{y}|\boldsymbol{g} \sim \mathcal{N}(\boldsymbol{g}, \mathcal{G})$, the marginal likelihood simplifies to

$$\ln \mathcal{L} = \ln p(\boldsymbol{y}|\tilde{\boldsymbol{Z}}, \sigma_g, l_g) \tag{3.14}$$

$$= -\frac{1}{2}\sum_{i,j=1}^{n}(y_i - \mu_i)^T[\mathcal{C}(\tilde{\boldsymbol{Z}}, \tilde{\boldsymbol{Z}})]^{-1}(y_j - \mu_j) - \frac{1}{2}\ln|\mathcal{C}(\tilde{\boldsymbol{Z}}, \tilde{\boldsymbol{Z}})| - \frac{n}{2}\ln 2\pi\,, \tag{3.15}$$

where $\mathcal{C}(\tilde{\boldsymbol{Z}}, \tilde{\boldsymbol{Z}})$ denotes the covariance matrix with entries $\mathcal{C}(\tilde{z}_i, \tilde{z}_j)$, and $\mathcal{L}$ represents the marginal likelihood. The hyperparameters $\sigma_g$ and $l_g$ are selected to maximise this likelihood, ensuring that the Gaussian Process best fits the given dataset. Notably, the marginal likelihood depends only on the observed data points $\tilde{z}_i$, and thus, the optimisation of hyperparameters effectively tunes the model to the observed data.

### 3.1.3 | Applying Gaussian Processes

Therefore, as has been mentioned, the process involves first defining the kernel function, then tuning its hyperparameters by maximising the marginal likelihood, thereby fitting the GP model to the data and providing a robust reconstruction of the underlying function.

In summary, the application of GPs follows the summarised steps, which are illustrated in Fig. 3.1.

1. **Select a Dataset**: Initiate the process by selecting a dataset that includes observational input locations $\tilde{z}_i$, their corresponding output values $y_i$, and associated variances. This step is depicted in Fig. 3.1(a).

2. **Define Reconstruction Points**: Identify the points $z^*$ where no observational data is available but where predictions are desired as shown in Fig. 3.1(b).

3. **Choose a Kernel Function**: Select an appropriate kernel function to model the covariance structure of the data. This step is illustrated in Fig. 3.1(c) In this study, the following kernels are considered: the Squared Exponential kernel, the Cauchy kernel, the Matérn kernel, and the Rational Quadratic kernel.

4. **Optimise Hyperparameters**: Each chosen kernel function has associated hyperparameters, such as $\sigma_g$ (vertical scale) and $l_g$ (lengthscale), shown in Fig. 3.1(d). These hyperparameters are optimised by maximising the log marginal likelihood, as defined in Eq. 3.14.

5. **Compute the Covariance Matrix**: With the optimised hyperparameters, compute the final covariance matrix, (Fig. 3.1(e)) required in Eq. 3.5.

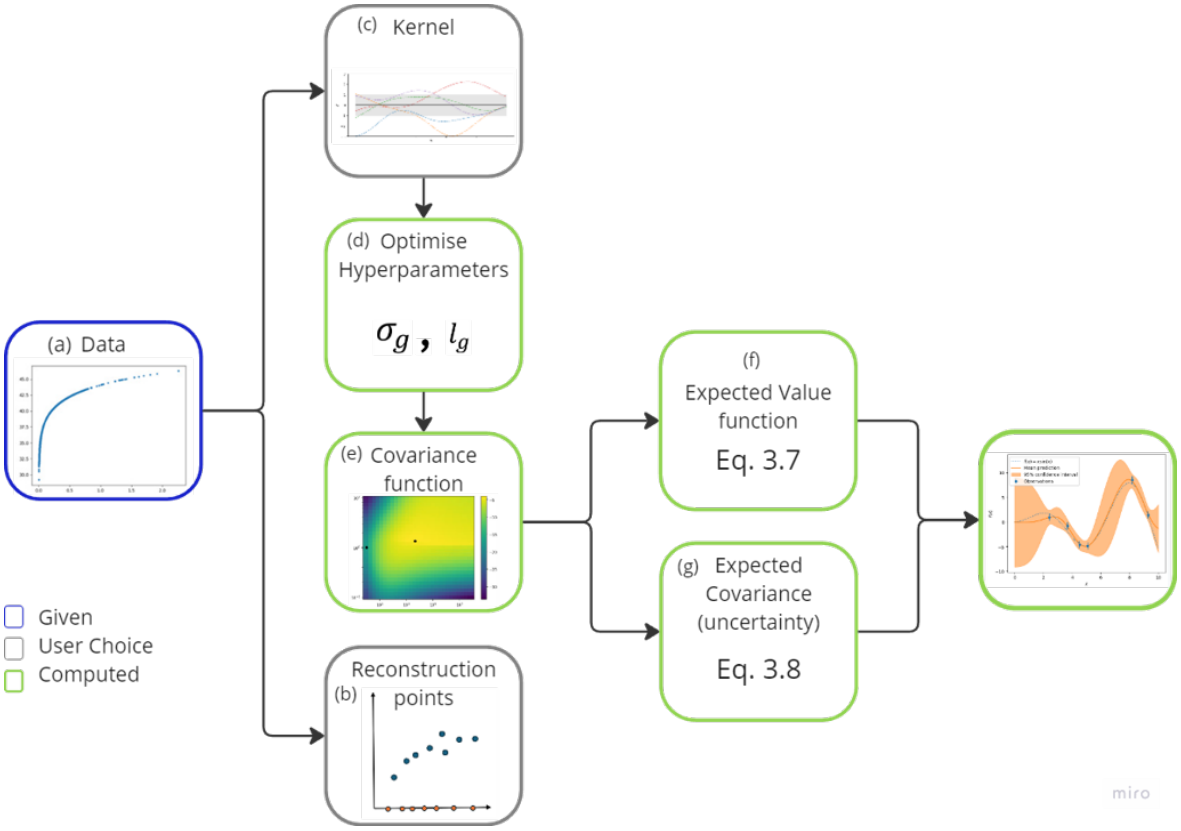


Figure 3.1: This diagram illustrates the workflow of Gaussian Processes. The blue box represents the initial inputs, including the dataset. Modelling choices, such as the selection of kernel functions and reconstruction points, are depicted by the grey boxes. The green boxes indicate the essential computations, including the determination of final covariances, optimisation of hyperparameters, and the prediction of the mean and uncertainties for the reconstructed function, which is shown in the final box.

6. **Make Predictions**: Utilise the covariance matrix and optimised parameters to predict the mean using Eq. 3.7 and uncertainty of the function at the reconstruction points, using Eq. 3.8 as shown in Fig. 3.1(f), (g).

### 3.1.4 | Reconstructing the derivative of a function

GPs extend beyond the prediction of functions to also model the derivatives of these functions. Notably, the derivative of a GP itself adheres to the framework of a GP [171].

In the GP framework, a function $g(z)$ is represented as a sample from a GP. If $g(z)$ is smooth, its derivatives, including $g'(z)$ and higher-order derivatives, can also be modelled as samples from GPs. The covariance structure between observational data points remains consistent with the standard GP formulation. However, the covariance between the function

and its derivative, as well as between different derivatives, is derived from the original covariance function

$$\operatorname{cov}\left(g_i, \frac{\partial g_i}{\partial z_j}\right) = \frac{\partial \mathcal{K}(z_i, z_j)}{\partial z_j}, \tag{3.16}$$

$$\operatorname{cov}\left(\frac{\partial g_i}{\partial z_i}, \frac{\partial g_j}{\partial z_j}\right) = \frac{\partial^2 \mathcal{K}(z_i, z_j)}{\partial z_i \partial z_j}. \tag{3.17}$$

Analogously, the covariances for higher derivatives can be determined in the same manner.

The GP for the first and second derivative are given by the following equations, provided that the GP for $g(z)$ has already been computed

$$g(z) \sim \mathcal{GP}\left(\mu(z), \mathcal{C}(z, z')\right), \tag{3.18}$$

$$g'(z) \sim \mathcal{GP}\left(\mu'(z), \frac{\partial^2 \mathcal{C}(z, z')}{\partial z \partial z'}\right), \tag{3.19}$$

$$g''(z) \sim \mathcal{GP}\left(\mu''(z), \frac{\partial^4 \mathcal{C}(z, z')}{\partial x \partial z'}\right). \tag{3.20}$$

In the subsequent part, the reconstruction of the first derivative of $g$ is shown, however it is noteworthy to say that the reconstruction of higher derivatives are done likewise. Similar to the previous case, the joint distribution of $y$ and $g^{*'}$ is defined as

$$\begin{bmatrix} \boldsymbol{y} \\ \boldsymbol{g}^{*'} \end{bmatrix} \sim \mathcal{N}\left(\mathbf{0}, \begin{bmatrix} \mathcal{C}(\tilde{\boldsymbol{Z}}, \tilde{\boldsymbol{Z}}') & \mathcal{C}'(\tilde{\boldsymbol{Z}}, \boldsymbol{Z}^*) \\ \mathcal{C}'(\boldsymbol{Z}^*, \tilde{\boldsymbol{Z}}) & \mathcal{C}''(\boldsymbol{Z}^*, \boldsymbol{Z}^{*'}) \end{bmatrix}\right), \tag{3.21}$$

where

$$\mathcal{C}'(\tilde{\boldsymbol{Z}}, \boldsymbol{Z}^*)_{|ij} = \frac{\partial \mathcal{C}(\tilde{z}_i, z_j^*)}{\partial z_j^*},$$

and

$$\mathcal{C}''(\boldsymbol{Z}^*, \boldsymbol{Z}^{*'})_{|ij} = \frac{\partial^2 \mathcal{C}(z_i^*, z_j^*)}{\partial z_i^* \partial z_j^*}.$$

In turn, the conditional distribution can be defined as [173]

$$\boldsymbol{g}^{*'} | \boldsymbol{Z}^*, \boldsymbol{Z}, \boldsymbol{y} \sim \mathcal{N}\left(\overline{\boldsymbol{g}^{*'}}, \operatorname{cov}(\boldsymbol{g}^{*'})\right). \tag{3.22}$$

The reconstructed mean value and the covariance of $g^{*'}$ at point $z^*$ can then be written as follows

$$\overline{g^{*'}} = \sum_{i,j=1}^{n} \mathcal{C}'(z^*, \tilde{z}_i)[\mathcal{C}(\tilde{z}_i, \tilde{z}_j)]^{-1} y(\tilde{z}_j), \tag{3.23}$$

$$\operatorname{cov}(g^{*'}) = \mathcal{C}''(z^*, z^*) - \sum_{i,j=1}^{n} \mathcal{C}'(z^*, \tilde{z}_i)[\mathcal{C}(\tilde{z}_i, \tilde{z}_j)]^{-1} \mathcal{C}'(\tilde{z}_j, z^*). \tag{3.24}$$

In addition, the maximum marginal likelihood, Eq. 3.14, depends only on the input observational data points and thus, the hyperparameters in this case are trained in the same manner as before since the equation itself is independent of the function needed to be reconstructed.

Finally, GPs are extensively utilised by cosmologists for the reconstruction and analysis of cosmological data, facilitating the prediction and refinement of cosmological parameters across various redshifts [180]. Their non-parametric nature proves invaluable in addressing issues such as the Hubble tension [181], constraining cosmological parameters with flexibility [182], and exploring phenomena related to dark energy [173]. This capacity to model data without predefined functional forms enhances their effectiveness in studying intricate cosmological phenomena. In this context, the methodology of GPs is applied to impose constraints on TG models, specifically $f(T)$ gravity. The subsequent chapters will detail how this approach is used to investigate and constrain these gravity models, illustrating the practical application of GPs in modern cosmological research.

## 3.2 | Markov Chain Monte Carlo

The GP approach has been primarily described for its capacity to model and predict complex relationships within data. While GP provides a strong framework for understanding and predicting functions, it operates primarily in the realm of predictive modelling and does not extend to parameter estimation. For this purpose, Markov Chain Monte Carlo (MCMC) methods offer a valuable alternative. MCMC methods are employed for sampling from intricate probability distributions and are particularly advantageous in Bayesian inference for estimating posterior distributions of model parameters. Understanding the complementary nature of MCMC's parameter estimation and GP's predictive capabilities offers a broader perspective on how these methods can be applied to various research problems.

MCMC methods were first introduced in the 1950s by Metropolis et al. [183] as a means to efficiently sample from unknown probability distributions [184, 185]. Since their inception, MCMC techniques have become widely used in cosmology for parameter estimation [10, 186, 187, 188, 189, 190]. Through these methods, chains are generated to sample the posterior probability distribution, following the Bayesian approach.

At the core of MCMC methods are two key concepts: *Markov Chains* and *Monte Carlo* methods. The term *Monte Carlo* refers to a class of computational algorithms that rely on random sampling to obtain numerical results, a concept named after the Monte Carlo district in Monaco, famous for its association with gambling and, consequently, randomness [191]. The second fundamental concept is that of a *Markov Chain*—a sequence of random

variables where each variable depends only on its immediate predecessor. This implies that the probability of a particular state in the chain depends solely on the previous state, independent of the chain's history [192, 193]. MCMC algorithms combine these two concepts, allowing for random sampling in high-dimensional spaces, which is essential for complex probabilistic modelling [184].

With the foundational concepts of Markov Chains and Monte Carlo methods established, attention can now be turned to the formal structure and mechanics of the MCMC algorithm. MCMC is particularly significant in statistical modelling, especially in Bayesian inference, where it is utilised to approximate posterior distributions.

In the discussion that follows, the principles underlying MCMC will be explored, beginning with an overview of the algorithm's key components and the theoretical basis that supports its operation. The most commonly used MCMC algorithms, such as the Metropolis-Hastings algorithm, will then be examined, with their respective advantages and practical applications highlighted. Finally, the computational techniques of using MCMC will be discussed.

### 3.2.1 | Fundamental Concepts of MCMC

In Bayesian inference, the objective is to update beliefs about a set of parameters $\Theta$, given observational data $\mathcal{D}$ and an underlying model $\mathcal{M}$ [194]. These elements are combined using Bayes' Theorem, allowing the probability of the parameters $\Theta$, given $\mathcal{D}$ and $\mathcal{M}$, to be determined [191]

$$P(\Theta|\mathcal{D},\mathcal{M}) = \frac{P(\mathcal{D}|\Theta,\mathcal{M})P(\Theta|\mathcal{M})}{P(D|\mathcal{M}\mathcal{D})}, \tag{3.25}$$

where

- $P(\Theta|\mathcal{D},\mathcal{M})$ is the (joint) posterior distribution of some parameters $\Theta$, conditioned upon some data $\mathcal{D}$ of the model
- $P(\mathcal{D}|\Theta,\mathcal{M})$ is the likelihood, quantifying how well the parameters $\Theta$ explain the observed data
- $P(\Theta|\mathcal{M})$ is the prior distribution, representing our belief before observing the data.
- $P(\mathcal{D}|\mathcal{M})$ is the evidence term or marginal likelihood, acting as a normalising constant across all possible parameter values.

The aim is to transition from a prior belief to a posterior belief by incorporating observational data. The likelihood function, $P(\mathcal{D}|\Theta,\mathcal{M})$, denoted by $\mathcal{L}$, represents the conditional probability of the data given a particular choice of $\Theta$ within the model $\mathcal{M}$ [195]. The prior,

$P(\Theta|\mathcal{M})$, denoted by $\pi$, describes the probability of specific values of $\Theta$ for the given model $\mathcal{M}$ before the data is considered, and can be computed in advance [194]. In other words, the prior reflects the initial belief about the model before the data is introduced [192]. The evidence term in the denominator of Eq. 3.25 indicates how well the model $\mathcal{M}$ explains the data. Since it does not depend on $\Theta$, it serves as a normalising factor [184]. The left-hand side of Eq. 3.25 represents the posterior, denoted as $\mathcal{P}$, which provides a description of the parameters $\Theta$ given the data $\mathcal{D}$ and the model $\mathcal{M}$. This posterior is derived by combining the prior $\pi$ with the likelihood $\mathcal{L}$, and normalising by the evidence, thereby yielding the most probable parameters $\Theta$ [194].

Building upon the aforementioned equation, the MCMC process utilises the observational data, denoted as $\mathcal{D}$, as its input to ultimately produce a posterior distribution of the parameters $\Theta$, conditioned on the data $\mathcal{D}$ and a pre-selected model $\mathcal{M}$ [196]. The fundamental objective of an MCMC algorithm is to construct a chain, or a sequence of points, within the parameter space and to evaluate the posterior distribution as derived from Bayes' theorem, as shown in Eq. 3.25. This process, in its simplified form, is depicted in Fig. 3.2.

As has been mentioned, the denominator in Bayes' theorem serves as a normalising factor, ensuring that the total probability integrates to one. However, since this normalising factor is independent of the parameters $\Theta$, it does not influence the shape of the posterior distribution. Consequently, Eq. 3.25 can be simplified for the purposes of MCMC calculations, reducing to the following proportionality [192]

$$P(\Theta|\mathcal{D},\mathcal{M}) \propto P(\mathcal{D}|\Theta,\mathcal{M})\, P(\Theta|\mathcal{M}) \quad \text{or}$$
$$\mathcal{P} \propto \mathcal{L}\ \pi\,. \tag{3.26}$$

This simplification highlights that the posterior distribution $\mathcal{P}$ is directly proportional to the product of the likelihood $\mathcal{L}$ and the prior $\pi$. As such, MCMC methods focus on this proportional relationship, allowing the posterior to be effectively sampled without needing to explicitly compute the normalising constant, which can often be intractable in complex models.

In general, the prior distribution serves to adjust the likelihood function based on existing knowledge or beliefs about the parameters before observing the data. As a probability distribution, the prior is constrained to lie within the range of 0 to 1. One common approach is to use an uninformative prior, which provides a way to specify the acceptable range for the parameters, effectively defining the parameter space over which the search for the optimal model is conducted.

For instance, if the goal is to estimate a parameter $b$ within the range $0 < b < 10$, an uninformative prior can be defined such that the prior probability is 1 within this range and

0 outside of it. Explicitly, the prior function $\pi(b)$ could be defined as

$$\pi(b) = \begin{cases} 1 & \text{for } 0 < b < 10, \\ 0 & \text{otherwise.} \end{cases} \tag{3.27}$$

This choice of prior reflects the belief that values of $b$ outside the specified range are not considered plausible or relevant for the model. By setting the prior in this manner, the search for the optimal model is confined to the parameter space of interest, aligning the prior with the constraints and expectations of the problem at hand.

Therefore, with the prior distribution already computed ( and the posterior distribution being the ultimate goal), the primary task is to evaluate the likelihood. The likelihood, denoted as $\mathcal{L} = P(\mathcal{D}|\Theta, \mathcal{M})$, represents the probability (through a function, such as the normal distribution) of observing the given data under a specific set of parameters within the model $\mathcal{M}$ [193].

For a dataset $\mathcal{D} = \{y_1, y_2, \ldots, y_n\}$ and given parameters, the likelihood is expressed as the product of individual probabilities [191], such that

$$\mathcal{L} = P(\mathcal{D}|\Theta, \mathcal{M}) = \prod_{i=1}^{n} P(y_i|\Theta, \mathcal{M})\,. \tag{3.28}$$

Here, $P(y_i|\Theta, \mathcal{M})$ is defined as follows, assuming the data follows a normal distribution [193]

$$P(y_i|\Theta, \mathcal{M}) = \frac{1}{\sqrt{2\pi\sigma_{y_i}^2}} \exp\left(-\frac{r_i^2}{2\sigma_{y_i}^2}\right), \tag{3.29}$$

where $r_i$ represents the residuals between the observed data $y_i$ and the model prediction with the chosen parameters, and $\sigma_{y_i}$ denotes the uncertainty associated with $y_i$.

Therefore the likelihood function provides a measure of how well the model with given parameters explains the observed data. Consequently, the parameters that maximise the likelihood function, as given by Eq. 3.28, are considered the most probable. However, directly maximising $\mathcal{L}$ can be challenging due to the product of probabilities, particularly when dealing with large datasets. To simplify this process, it is common practice to work with the logarithm of the likelihood function [184]. Taking the natural logarithm of $\mathcal{L}$, Eq. 3.28

$$\begin{aligned} \ln \mathcal{L} &= \sum_{i=1}^{n} \ln P(y_i|\Theta, \mathcal{M}) \\ &= K - \sum_{i=1}^{n} \frac{r_i^2}{2\sigma_{y_i}^2} = K - \frac{1}{2}\chi^2\,, \end{aligned} \tag{3.30}$$

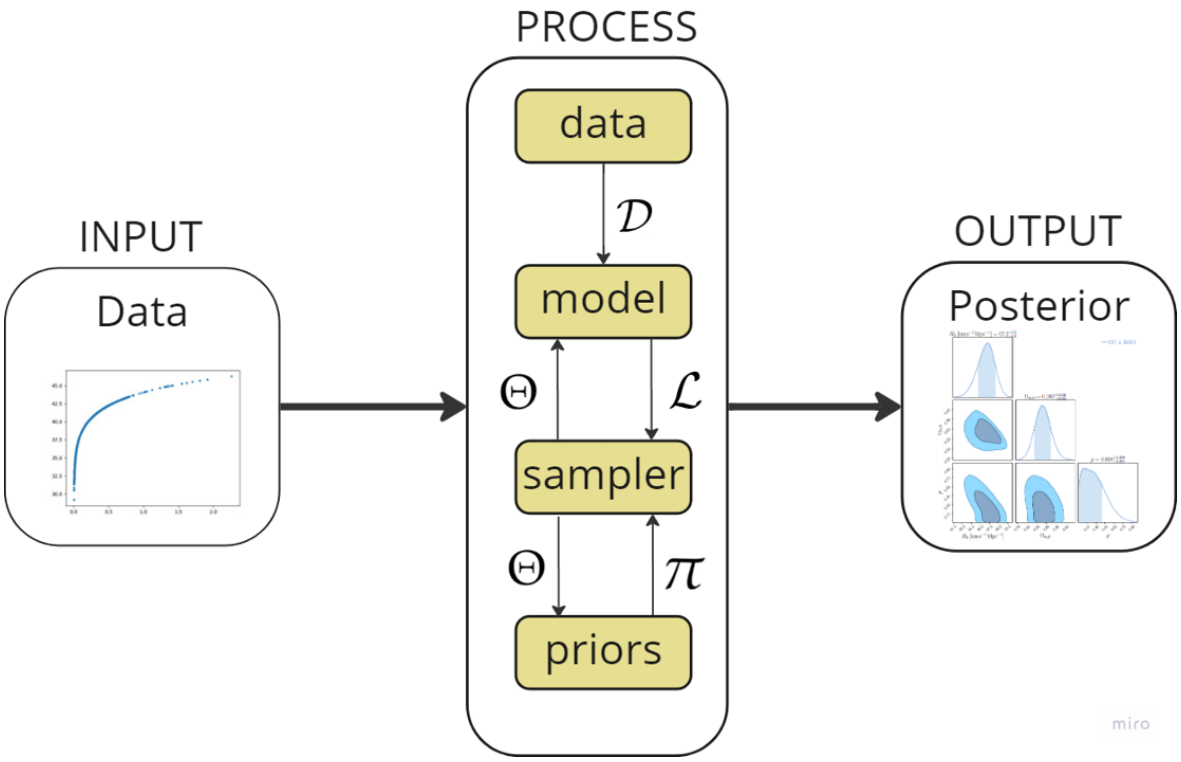


Figure 3.2: Illustration of the MCMC process. On the left-hand side, observational data $\mathcal{D}$ is input into the system. The sampler explores the parameter space by generating random samples of $\Theta$. These samples are evaluated within the model, where they, along with the data, contribute to calculating the likelihood $\mathcal{L}$. The prior distribution is also assessed based on the generated $\Theta$ values such that in turn, the posterior distribution is computed. The sampler iteratively refines its guesses to maximise the posterior probabilities, ultimately producing corner plots that represent the distribution of parameter values.

where $K$ is a constant that does not depend on the parameters $\Theta$, and $\chi^2 = \sum_{i=1}^{n} \frac{r_i^2}{\sigma_{y_i}^2}$ is the chi-squared statistic, which measures the goodness-of-fit between the observed data and the model predictions.

By maximising $\ln \mathcal{L}$, which is equivalent to minimising $\chi^2$, one effectively identifies the parameter values $\Theta$ that provide the best fit to the data. This approach is computationally advantageous, as it transforms the problem from handling products of probabilities to summing log-probabilities, which is numerically more stable and manageable. Therefore, the optimisation process for parameter estimation often focuses on obtaining the chi-squared value, aligning the fit of the model to the observed data.

The general process of MCMC is illustrated in Fig. 3.2. In this process, the observational data is first introduced as the input. The core of the MCMC method involves the insertion of this data into a predefined model to evaluate various parameter sets. Initially, the

sampler generates random proposals for the parameter vectors, denoted as $\Theta$. These proposed values are then used to assess their validity based on the prior distribution. If the proposed parameters fall within the acceptable range defined by the prior, the likelihood for the given parameter set is calculated using Eq. 3.30. This calculation incorporates both the data and the model to determine the fit of the parameters. Following this, the sampler makes more refined or "intelligent" proposals for $\Theta$ based on the posterior probabilities derived from the likelihood and prior. The goal is to explore the parameter space effectively to maximise the posterior probability. This iterative process allows the sampler to focus on regions of higher posterior probability, refining the search for the most probable parameter values. Ultimately, the output of the MCMC process is a collection of samples representing the posterior distribution of the parameters. These samples can be visualised in a corner plot, which displays the posterior distributions for each parameter and their correlations, providing a comprehensive view of the inferred parameter values.

### 3.2.2 | The Metropolis-Hastings algorithm

While the general MCMC process involves iteratively exploring the parameter space to obtain a posterior distribution, this exploration is typically conducted using a specific sampling algorithm. In this work, the Metropolis-Hastings algorithm will be employed to facilitate this exploration.

The algorithm derives its name partly from Nicholas Metropolis, who, along with his colleagues, introduced the original version in 1953 for cases involving symmetric proposal distributions [183]. Later, in 1970, W.K. Hastings generalised the algorithm to accommodate asymmetric proposal distributions, thus extending its applicability to a broader range of problems [197]. This generalised approach became widely recognised as the Metropolis-Hastings algorithm, reflecting the contributions of both Metropolis and Hastings.

The Metropolis-Hastings algorithm is used to sample from the posterior distribution to make more refined or “intelligent ” proposals for $\Theta$ and thus explore the parameter space. This sampling procedure can be thought of as a random walk through the parameter space each time proposing new steps which are accepted or rejected, depending on whether it fits the data better for the model or not. If the new step is worse then the previous one, it may still be accepted with a certain probability since it could be the that, if the accepted steps are only those with better probability, the chain could be converging to a local maximum in the parameter space and therefore not completely mapping all of the points.

To initiate the parameter exploration process, often referred to as the "walk" through the parameter space, an initial guess for the parameter, denoted as $\Theta_0$, must be specified. Using this initial parameter set, the likelihood and prior are computed based on the previously

outlined information. Consequently, the initial posterior $\mathcal{P}_0$ is inferred.

The Metropolis-Hastings algorithm then proposes a new set of parameters, $\Theta_{\text{trial}}$. The likelihood $\mathcal{L}_{\text{trial}}$ and prior $\pi_{\text{trial}}$ associated with the proposed parameters are computed, yielding a new trial posterior $\mathcal{P}_{\text{trial}} = P(\Theta_{\text{trial}}|\mathcal{D}, \mathcal{M})$.

The acceptance of the proposed parameters, $\Theta_{\text{trial}}$, is determined based on the acceptance ratio, which is given by [184, 193]

$$s = \min\left(1, \frac{P(\Theta_{\text{trial}}|\mathcal{D}, \mathcal{M}) \cdot q(\Theta_{\text{current}}|\Theta_{\text{trial}})}{P(\Theta_{\text{current}}|\mathcal{D}, \mathcal{M}) \cdot q(\Theta_{\text{trial}}|\Theta_{\text{current}})}\right) \tag{3.31}$$

where, $P(\Theta_{\text{trial}}|\mathcal{D}, \mathcal{M})$ and $P(\Theta_{\text{current}}|\mathcal{D}, \mathcal{M})$ represent the posterior probabilities of the trial and current parameters, respectively. The terms $q(\Theta_{\text{current}}|\Theta_{\text{trial}})$ and $q(\Theta_{\text{trial}}|\Theta_{\text{current}})$ are the proposal probabilities for the moves between the current and trial parameters. In general, the proposal distribution $q(\Theta'|\Theta)$ in the Metropolis-Hastings algorithm is used to generate candidate parameters $\Theta'$ based on the current parameters $\Theta_{\text{current}}$, guiding the exploration of the parameter space and facilitating the sampling of the posterior distribution.

If the proposal distribution $q(\Theta_{\text{trial}}|\Theta_{\text{current}}) = q(\Theta_{\text{current}}|\Theta_{\text{trial}})$, then the accepatnce rate simplifies to

$$s = \min\left(1, \frac{P(\Theta_{\text{trial}}|\mathcal{D}, \mathcal{M})}{P(\Theta_{\text{current}}|\mathcal{D}, \mathcal{M})}\right) \tag{3.32}$$

It also noteworthy to see that the normalisation factor (the evidence) is the same for both the numerator and the denominator, therefore it cancels out, meaning that the algorithm can function without needing to compute the marginal likelihood.

The proposed parameters are accepted with probability $s$. However, to be able to accept or reject the trial parameters, a random number $u$ is generated from a uniformly distribution between 0 and 1. If

- $u \leq s$, accept the new parameters $\Theta_{\text{new}}$, where $\Theta_{\text{new}} = \Theta_{\text{trial}} = \Theta_{\text{current}}$.
- $u > s$, reject $\Theta_{\text{trial}}$ and retain $\Theta_{\text{current}}$.

The key idea is that even if $\Theta_{\text{trial}}$ has a lower posterior probability then $\Theta_{\text{current}}$, there is still a chance of accepting it, which helps the algorithm from getting stuck in local maxima.

This iterative process continues, allowing the algorithm to explore the parameter space and converge towards the posterior distribution. The algorithm will keep on jumping from one step to another until it converges in a high posterior probability region where it has a high likelihood [196] as shown in Fig. 3.3.

The successful jumps from one step to another are part of the Markov chain and as a whole can be referred to as a random walk. It also noteworthy, that the initial steps which are far away from the high posterior probability region are identified as the *burn-in* chain and

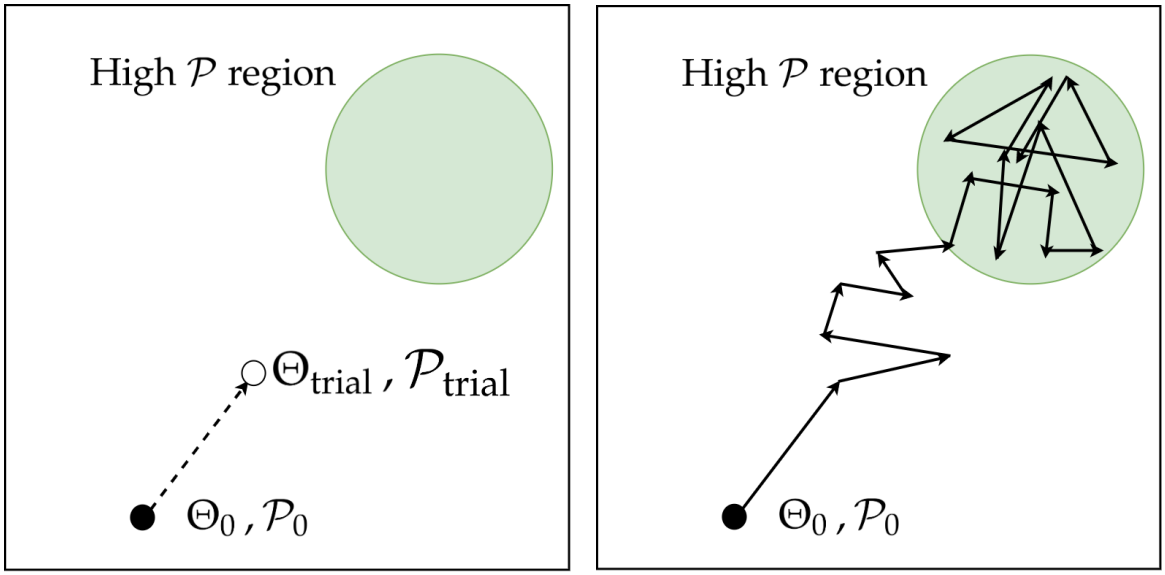


Figure 3.3: **The MCMC Process.** *Left:* Initial conditions for the Metropolis-Hastings algorithm are set. The algorithm proposes a new set of parameters, $\Theta$, with an associated posterior probability, $\mathcal{P}_{\text{trial}}$. These proposed parameters are evaluated and accepted based on the acceptance rate $r$ and the proposal distribution. *Right:* The random walk illustrates the algorithm's progression through the parameter space. Initially, the chain explores various parameter values, represented as the burn-in period, which are outside the high posterior probability region (depicted in green). After this burn-in phase, the chain continues to sample within the high posterior region, converging towards a set of parameters that maximise the likelihood.

are removed as they are not relevant or close to the converging region [195]. This avoids any initialisation effect in the final posterior distribution [198]. In Fig. 3.3 the burn-in chain are those steps which are outside the high likelihood region (the green region). The remaining samples are then used to represent the posterior distribution the parameters and can be visualised in corner plots, which show the posterior distributions of individual parameters and their pairwise correlations.

Therefore, in summary, the full algorithm can therefore be detailed as follows

1. **Choose initial Parameters**: Select an initial set of parameters $\Theta_0$.

2. **Compute initial Likelihood and Prior**: Calculate the likelihood $\mathcal{L}_0$ and $\pi_0$, based on your model and data.

3. **Compute initial posterior**: Compute the initial posterior using Bayes Theorem, Eq. 3.26.

4. **Propose New Set of Parameters**: Generate new candidate parameters $\Theta_{\text{trial}}$, and compute the likelihood $\mathcal{L}_{\text{trial}}$ and prior $\pi_{\text{trial}}$.

5. **Calculate the New Posterior**: Compute the new posterior for the new parameters $\mathcal{P}(\Theta_{\text{trial}})$.

6. **Compute the Acceptance Rate**: Calculate the acceptance rate, $s$ using Eq. 3.31.

7. **Accept or Reject the New parameters**: From the uniformly distributed $u$, accept or reject the new parameters. If accepted the trial parameters become the current parameters, otherwise propose new parameters.

8. **Repeat Process**: Repeat the process until one has a large enough chain.

The MCMC algorithm, described above, was implemented using the well-established Python package *emcee*, developed by Foreman-Mackey et al. [199] [4]. One of the key advantages of *emcee* is its use of an ensemble of multiple walkers, which allows for parallel exploration of the parameter space rather than relying on a single random walk. This multi-walker approach enhances the efficiency and robustness of the sampling process.

Following convergence, the outputs from these walkers are aggregated to sample the posterior distribution. To analyse the results, the *ChainConsumer* package was utilised [200] [5]. This specialised Python tool is designed to handle and interpret the output from MCMC processes. *ChainConsumer* facilitates the visualisation of the posterior distribution by generating plots of the posterior surface, evaluating the convergence and mixing of chains through walk plots, and producing corner plots to illustrate parameter correlations and distributions.

## 3.3 | Distances and Observational Data

To apply the GP and MCMC algorithms effectively, it is crucial to have a strong set of observational data. This data serves as the foundation for both methodologies, enabling the the development of predictive models and exploration of parameter spaces. For GPs, the data is essential as a baseline to make accurate predictions and understand underlying trends. In the context of MCMC, the observational data is used to calculate the likelihood (and hence the $\chi^2$), which in turn drives the exploration of the parameter space towards the posterior distribution. Therefore, acquiring high-quality, relevant observational data is a critical first

[4] https://emcee.readthedocs.io
[5] https://pypi.org/project/ChainConsumer

step, ensuring that the subsequent analysis through GP and MCMC methods yields meaningful and reliable results.

## 3.3.1 | Distances in Cosmology

To begin, the first subsection will focus on the concepts of distances and geometry, which are fundamental to understanding the observational data required for the analysis. Distances and geometric relationships play a crucial role in interpreting the data, as they provide the necessary framework for understanding the observed phenomena. Understanding these concepts is essential for accurately processing and applying the observational data within both the GP and MCMC algorithm. This subsection will delve into the key principles of distances and geometry, setting the stage for their application in the data analysis that follows.

Distances to cosmological objects constitute the most common way to probe the cosmic metric and the expansion history of the Universe. Astronomical observations, including those that provide clues about nature of dark energy, fundamentally rely on two basic techniques; measuring fluxes from objects and measuring angles on the sky. It is therefore useful to define these types of distances [201, 18].

### 3.3.1.1 | Luminosity distance

**Luminosity Distance** is a fundamental concept in both astrophysics and cosmology, crucial for determining the distance to astronomical objects based on their observed brightness. Consider a luminous cosmological source with an absolute luminosity $L$, which represents the total power emitted by the source. If an observer is located at a distance $d_L$ from this source, in a static Universe, the emitted power is assumed to be conserved as it spreads uniformly across a spherical surface area of $4\pi d_L^2$. Consequently, the luminosity distance $d_L$ can be defined by the following relationship [35]

$$d_L^2 = \frac{L}{4\pi\mathcal{F}}\,, \tag{3.33}$$

where $\mathcal{F}$ represents the apparent luminosity, or the observed flux. Here, flux is understood as the amount of energy per unit area received by an observer from a luminous object [31]. This concept is visually illustrated in Fig. 3.4.

However, in an expanding Universe, the relationship between luminosity distance and the observed flux becomes more complex due to the effects of cosmic expansion. The luminosity distance must be adjusted to account for the redshift $z$ of the source, which is a result of the Universe's expansion. In this context, the luminosity distance $d_L(z)$ is expressed as

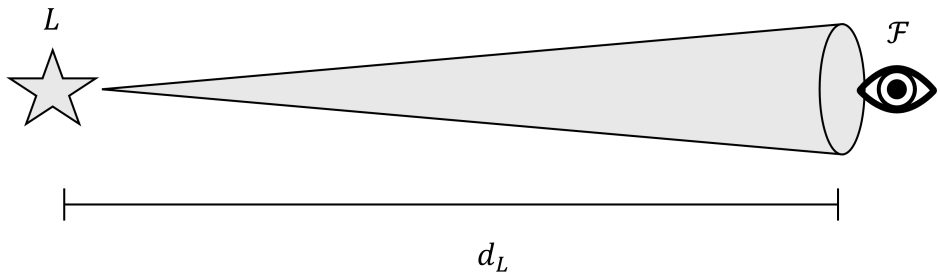


Figure 3.4: Definition of the luminosity distance as an analogy to $1/r^2$ dimming in flat Euclidean space. A source with luminosity $L$ is observed with flux $\mathcal{F} \propto 1/d_L^2$ .

an integral over the redshift, incorporating the cosmological parameters that govern the expansion [86, 202]. The equation is given by

$$d_L(z) = (1+z) \int_0^z \frac{c\, dz'}{H(z')} \tag{3.34}$$

where $c$ is the speed of light, and $H(z')$ is the Hubble parameter as a function of redshift $z'$. This integral reflects how the expansion of the Universe stretches the wavelengths of light, affecting the observed luminosity and thus the perceived distance to the source.

#### 3.3.1.2 | Comoving distance

The **Comoving Distance** is a fundamental concept in cosmology used to measure the distance between objects in the Universe while accounting for its expansion. Imagine two galaxies that are moving apart due to the expansion of the Universe. The comoving distance is the measure of their separation that remains constant over time if both galaxies are following the general expansion of space (Hubble flow).

Mathematically, the comoving distance $d_C(z)$ to an object at redshift $z$ is given by

$$d_C(z) = c \int_0^z \frac{dz'}{H(z')} \tag{3.35}$$

The comoving distance is crucial because it provides a baseline for defining other types of cosmological distances.

#### 3.3.1.3 | Transverse Comoving Distance

The **Transverse Comoving Distance** $d_M(z)$ is an extension of the comoving distance that is especially important for cosmological models where the Universe has curvature, whether it is open or closed. It helps in understanding how distances are affected by the overall shape of the Universe.

In a flat Universe, where space is not curved, the transverse comoving distance is simply the same as the comoving distance

$$d_M(z) = d_C(z) \tag{3.36}$$

However, in Universes with curvature—where the geometry of space is either open (negatively curved) or closed (positively curved)—the transverse comoving distance accounts for this curvature. It adjusts the distance calculation based on whether the Universe is curved and by how much. The formula for the transverse comoving distance depends on the curvature parameter $\Omega_k$ and is given by [203]

$$d_M(z) = \begin{cases} \frac{c}{H_0} \sinh\left(\frac{H_0\sqrt{\Omega_k} d_C(z)}{c}\right), & \text{for a closed Universe } (\Omega_k > 0) \\ d_C(z), & \text{for a flat Universe } (\Omega_k = 0) \\ \frac{c}{H_0} \sin\left(\frac{H_0\sqrt{|\Omega_k|} d_C(z)}{c}\right), & \text{for an open Universe } (\Omega_k < 0) \end{cases} \tag{3.37}$$

In simple terms, the transverse comoving distance provides a way to measure how far apart objects are in a curved Universe, correcting for the way the Universe's shape affects our distance calculations. For a flat Universe, this distance is straightforwardly the same as the comoving distance, but for curved Universes, it adjusts the distance accordingly to account for the curvature.

#### 3.3.1.4 | Angular Diameter distance

Consider an astronomical source with a known physical scale $D$, often referred to as a 'standard ruler', which subtends a small angle $\theta$ in the sky, as illustrated in Fig. 3.5. In an Euclidean space, where geometry is flat, the physical **angular diameter distance** $d_A$ is defined as

$$d_A(z) = \frac{D}{\theta}\,. \tag{3.38}$$

For an expanding Universe, the physical angular diameter distance needs to be amended and is given by [86]

$$d_A(z) = \frac{c}{(1+z)} \int_0^z \frac{dz'}{H(z')} = \frac{d_M(z)}{(1+z)} = \frac{d_L(z)}{(1+z)^2}\,. \tag{3.39}$$

The angular diameter distance $d_A$ is reduced by a factor of $1+z$ compared to the transverse comoving distance $d_M$. This reduction accounts for the stretching of space during the light's journey from the source to the observer.

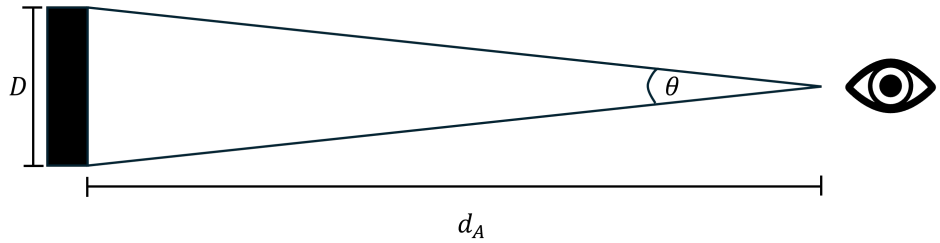


Figure 3.5: Diagram of the definition of the angular diameter distance, which is obtained from the angular and physical scales.

In essence, the angular diameter distance $d_A$, is also related to the luminosity distance, $d_L$, as $d_A$ measures the distance between the observer and the object when the light was emitted as shown in Eq. 3.39 [89].

#### 3.3.1.5 | Comoving Volume Distance

The **comoving volume distance,** $d_V$, measure is used to describe the effective distance that accounts for the volume of space within a certain redshift. It incorporates the transverse comoving distance and the rate of the expansion of the Universe. This distance helps in the understanding of how the volume of the Universe evolves with redshift, providing insights into the distribution and density of cosmic structures.

[204]

$$d_V(z) = \left[ d_M^2(z) \frac{cz}{H(z)} \right]^{1/3} \tag{3.40}$$

#### 3.3.1.6 | Hubble Distance

Apart from the above distances, some surveys also report the value of the **Hubble distance,** $d_H$. It is defined as the distance of an object based in the Hubble flow, such that [35]

$$d_H = \frac{c}{H_0} \tag{3.41}$$

tells us how far light travels in one Hubble time (the inverse of the Hubble constant). This gives the distance from the observer at which the recession velocity of a galaxy would equal the speed of light. Roughly speaking, the Hubble radius is the radius of the observable Universe.

### 3.3.2 | Expansion Data Sets

Over the years, several cosmological probes have been developed to explore the fundamental questions surrounding the expansion of the Universe, as well as the nature of dark energy and dark matter. These probes work by measuring how the Universe is expanding and modelling it through various cosmological parameters. Thanks to significant advancements in methodology, technology, and theory, some of these probes have now reached a level of maturity that allows them to be considered 'standard' in cosmological studies. Among these are the SNe Ia and BAO [201]. Ongoing and completed cosmological missions have continuously refined the accuracy and precision of these measurements, pushing the capabilities of these probes to their limits. Notable examples include SNe Ia for SNe Ia, and the BOSS and eBOSS surveys [205] for BAO.

This discussion on various cosmological distances, such as luminosity distance, angular diameter distance, and comoving distance, forms the basis for understanding the observational data utilised in this work. Specifically, datasets like PN (Type Ia Supernovae), BAO, and Cosmic Chronometers (CC) play a crucial role in constraining cosmological parameters and providing insights into the expansion history of the Universe. These datasets offer complementary perspectives, helping to piece together a comprehensive picture of the cosmos and refine our teleparallel models

#### 3.3.2.1 | Cosmic Chronometers

Cosmic Chronometerss (CCs) refer to astrophysical objects whose evolutionary history is well understood. A prime example of such objects includes certain types of galaxies, particularly massive and passively evolving. By observing these galaxies at different redshifts and comparing their evolutionary stages, researchers can directly estimate the value of the Hubble parameter, $H(z)$, at each redshift $z$ .

The CC method is conceptually straightforward and involves determining the Hubble parameter as a function of redshift $z$ without relying on any specific cosmological model. This technique, first proposed by Jimenez and Loeb over 20 years ago [138] , is based on the relationship between time and redshift. In the context of a flat FLRW metric, this relationship can be expressed as

$$H(z) = -\frac{1}{1+z}\frac{dz}{dt} \approx -\frac{1}{1+z}\frac{\Delta z}{\Delta t}\,. \tag{3.42}$$

One method of obtaining $H(z)$ is by calculating the differential age of two passively evolving galaxies at different redshifts [138]. This spectroscopic dating of galaxies is referred to as the CC method and has proven to be a useful tool for acquiring observational $H(z)$

values at redshifts $z \lesssim 2$ [176]. In this context, $\Delta z$ in Eq. 3.42 represents the redshift difference between the galaxies, which can be accurately measured using spectroscopic observations. However, obtaining the age difference $\Delta t$ is more challenging, as it requires a reliable 'cosmic clock' [206].

Empirical evidence suggests that the best CCs are galaxies that have been evolving passively, with star formation ceasing at redshifts $z \sim 3$ or earlier. These galaxies, particularly those that have not formed new stars since $z \sim 2$, provide a reliable cosmic clock for measuring $\Delta t$ [207, 208]. A particularly useful feature for determining the age of these galaxies is the 4000Å break in their spectra. This break, caused by the accumulation of metal absorption lines (mainly from elements like calcium and iron), appears as a discontinuity in the spectrum, with the flux just appears as a noticeable drop in the spectrum at 4000 Å The strength of this break increases with the age of the stellar population, making it a valuable tool for estimating $\Delta t$ when combined with known metallicity [209, 210] [209, 210].

Thus, the CC method provides a direct way to measure $H(z)$ from observations, offering an advantage over other cosmological probes that rely on integrated quantities like luminosity distance. In this work, 31 CC data points were used. The data points were adopted from Refs. [211, 212, 139, 213, 214, 215, 216] and have been compiled in Table [180].

As discussed in Sec. 3.2 and Eq. 3.14, the MCMC technique involves the critical step of maximising the likelihood, or equivalently, minimising the $\chi^2$ statistic. For the CC dataset, this is expressed as [217]

$$\chi^2_H(\Theta) = \sum_{i=1}^{31} \frac{\left(H(z_i, \Theta) - H_{\rm obs}(z_i)\right)^2}{\sigma^2_H(z_i)}\,, \tag{3.43}$$

where $H(z_i, \Theta)$ represents the theoretical values of the Hubble parameter at redshift $z_i$ based on the model parameters $\Theta$, $H_{\rm obs}(z_i)$ denotes the corresponding observational data points obtained through the CC method, and $\sigma_H(z_i)$ are the associated observational uncertainties. It is important to highlight that the numerator in Eq. 3.43 corresponds to the residuals term in Eq. 3.30, representing the difference between the observed and theoretical values of the Hubble parameter.

#### 3.3.2.2 | Supernovae of Type Ia

One of the most effective methods for studying the expansion of the Universe is through the observation of supernovae, particularly Supernovae of Type Ia (SNe Ia), which are the explosive deaths of certain types of stars [218]. These events, which often occur at the end of a star's life cycle, are characterised by exceptionally bright explosions. The consistent peak brightness of SNe Ia allows them to serve as standard candles, enabling for the the accurate

measurement of extragalactic distance and to probe the history of cosmic expansion. [35]. Indeed, observations of these supernovae provided the first direct evidence of the accelerating expansion of the Universe, as revealed by the groundbreaking work projects led by Riess et al. [34] and Perlmutter et al. [33].

Supernovae are generally classified into two broad categories: Type I and Type II, distinguished by the presence or absence of hydrogen lines in their spectra [95]. Type I supernovae, which lack hydrogen lines, are further subdivided, with Type Ia supernovae being identified by a strong absorption line of singly ionized silicon (Si II) [219]. These Type Ia supernovae are of particular interest in cosmology due to their consistent peak luminosity, which makes them reliable standard candles for measuring cosmic distances [35].

The SNe Ia typically occur in a binary system where a white dwarf accretes matter from its companion star. When the white dwarf's mass approaches the Chandrasekhar limit—approximately 1.4 times the mass of the Sun—it undergoes a runaway thermonuclear explosion [96].[6] Due to the nearly uniform mass at which this explosion occurs, the resulting luminosity is also nearly uniform, making these supernovae powerful tools for measuring distances across the Universe [220].

In cosmology, the brightness of a supernova is measured using its apparent magnitude, denoted by $m$, which relates to the observed flux $\mathcal{F}$ through the relation $m = -2.5\log_{10}(\mathcal{F})$. However, to understand the intrinsic brightness, the absolute magnitude $M$ is used. Absolute magnitude is defined as the apparent magnitude an astrophysical source would have if it were placed at a standard distance of 10 parsecs from the observer. The relationship between apparent magnitude, absolute magnitude, and distance is encapsulated in the distance modulus $\mu$ [18]

$$\mu \equiv m - M = 5\log_{10}\left(\frac{d_L}{\text{Mpc}}\right) + 25\,, \tag{3.44}$$

where $\mu$ is the distance modulus, and $d_L$ is the luminosity distance to the supernova, expressed in megaparsecs (Mpc) as given in Eq. 3.34.

To facilitate analysis, a dimensionless form of the luminosity distance denoted $D_L$ is often used, which is defined as

$$D_L = \frac{H_0 d_L(z)}{c}\,, \tag{3.45}$$

such that the apparent magnitude can be expressed as

$$m = M + 5\log_{10}(D_L) + 5\log_{10}\left(\frac{c/H_0}{\text{Mpc}}\right) + 25\,. \tag{3.46}$$

[6]The Chandrasekhar limit represents the maximum mass a stable white dwarf can have before collapsing under its own gravity.

A critical aspect of using SNe Ia as standard candles is the calibration of their absolute magnitude $M$, which is an essential part of the cosmic distance ladder. The first rung of this ladder involves measuring the distances to nearby stars through parallax, a method that relies on observing the apparent shift in a star's position as the Earth orbits the Sun. With parallax providing precise distances to nearby stars, the next step involves Cepheid variable stars, which serve as primary distance indicators. Cepheids have a well-established relationship between their luminosity and pulsation period, allowing their absolute magnitude to be determined accurately. By measuring distances to galaxies that contain both Cepheids and Type Ia supernovae, astronomers can calibrate the absolute magnitude of the supernovae. This calibration is crucial for converting observed apparent magnitudes into reliable measurements of cosmic distances, thereby enabling a deeper understanding of the Universe's expansion [221].

The redshift $z$ of the supernova, which provides insight into the cosmic expansion, is determined by analysing the absorption lines in its spectrum. The redshift $z$ is calculated as

$$z \equiv \frac{\lambda_{\rm obs}}{\lambda_{\rm rest}} - 1\,, \tag{3.47}$$

where $\lambda_{\rm obs}$ is the observed wavelength, and $\lambda_{\rm rest}$ is the known rest-frame wavelength. With the redshift $z$ measured from spectroscopy and the ratio of apparent magnitude to their intrinsic brightness known, the luminosity distance can be found.

The dataset used in this analysis is the Pantheon Type Ia Supernova Compilation [222] (PN), which includes 1048 apparent magnitude measurements over a redshift range of $0.01 < z < 2.26$. This dataset is crucial for estimating the Hubble constant ($H_0$) and other cosmological parameters within the framework of MCMC analysis. The absolute magnitude $M$, calibrated as described, is treated as a nuisance parameter in these analyses, meaning it is essential for accurate data modelling but does not provide direct insights into the underlying cosmological model [199].

In this context, the associated $\chi^2_{\rm SN}$ is expressed as [223]:

$$\chi^2_{\rm SN}(\Theta) = \left(\Delta\mu(z_i, \Theta)\right)^T C^{-1}_{\rm SN}\, \Delta\mu(z_i, \Theta) \tag{3.48}$$

where $C_{\rm SN}$ is the total covariance matrix, and $\Delta\mu(z_i, \Theta) = \mu(z_i, \Theta) - \mu_{\rm obs}(z_i)$, with $\mu(z_i, \Theta)$ being the theoretical value of the distance modulus and $\mu_{\rm obs}(z_i)$ obtained from the Pantheon dataset.

It is also noteworthy that, as shown in Eq. 3.46, $H_0$ and $M$ are degenerate parameters, meaning different combinations of $\{H_0, M\}$ can yield the same observed apparent magnitude $m$. This degeneracy necessitates a joint analysis to obtain the most accurate estimates for both parameters [224, 225].

#### 3.3.2.3 | Baryon Acoustic Oscillations

Before the era of recombination (at redshift $z > 1100$), the early Universe was a hot, dense plasma composed of baryons and photons. This plasma underwent pressure-driven oscillations, known as sound waves, due to density fluctuations. In regions of overdense primordial plasma, gravitational attraction drew in matter, particularly dark matter. The trapped photons within these density peaks exerted an outward pressure due to the intense heat generated by photon-matter interactions. The competing forces of gravitational attraction and photon pressure generated oscillations, forming sound waves of baryons and photons. As the Universe expanded and cooled, it eventually reached a critical temperature where protons and electrons could combine to form neutral hydrogen—the event known as recombination. This decoupling of photons from baryons allowed photons to travel freely, while the baryonic matter was left behind, marking a pivotal moment in cosmic evolution [226]..

At decoupling, the sound waves stopped, leaving behind a shell of baryonic matter around each initial density peak. These shells, "frozen" in place, are relics of the early Universe, now observed at lower redshifts in the distribution of galaxies and galaxy clusters. The distance these sound waves travelled before decoupling is known as the sound horizon, a fundamental scale in the Universe.

This process imprinted a characteristic pattern in the distribution of matter, observed today as Baryon Acoustic Oscillations (BAO). These oscillations act as a standard cosmological ruler, offering a powerful tool to study the large-scale structure of the Universe [227, 228, 229, 230].

The angular scale of the sound horizon, $\theta_s$, measured at the drag epoch (when photons decoupled from baryons) provides valuable insights into the Hubble expansion rate through the standard ruler relation [35]

$$\theta_s = \frac{r_d}{(1+z)d_A}\,, \tag{3.49}$$

where $\theta_s$ represents the subtended angle of the sound horizon, $r_d$ denotes the comoving radius of the sound horizon at the last scattering surface and $d_A$ is the comoving angular distance defined by Eq. 3.39. By measuring this radius, cosmologists can infer the expansion rate of the Universe, since the sound waves participate in cosmic expansion [231].

The sound horizon, which acts as a standard ruler, remains constant in comoving distance, a scale that accounts for the expansion of the Universe. This distance can be calculated from the Big Bang to the recombination era at $z = z_d$ using the formula [35]

$$r_d(z_d) = \int_0^{t_d} \frac{c_s(t)}{a(t)}\, dt = \int_{z_d}^{\infty} \frac{c_s(z)}{H(z)}\, dz\,, \tag{3.50}$$

where $c_s$ is the sound speed, defined as $c_s = \frac{c}{\sqrt{3(1+R)}}$, and $R$ represents the ratio of baryon to radiation energy densities, given by $R = \frac{3\rho_b}{4\rho_\gamma}$.

Eq. 3.50 demonstrates that the sound horizon $r_d$ is influenced by factors such as the recombination era, the Universe's expansion rate, and the baryon-to-photon ratio. Therefore, this calculation is based on a cosmological model, and use physical parameters well-constrained by CMB observations, including the baryon-to-photon ratio and the sound horizon itself [204]. This indicates that BAO measurements are not entirely model-independent. However, they provide valuable complementary data, to for example, PN supernova measurements, which provide more detailed, fine-grained information about the Universe's expansion history [95]. Together, these measurements enhance our understanding of cosmic expansion.

As mentioned earlier, BAO can serve as cosmological probes, particularly through measurements of the angular-diameter distance. However, unlike SNe Ia, BAO measurements can differ depending on how they are defined. For the GP method, the BAO data utilised include $H(z)$ measurements from the Sloan Digital SKy Survey (SDSS)-IV Extended Baryon Oscillation Spectroscopic Survey (eBOSS) DR14 quasar survey at redshifts $z_{\text{eff}} = \{0.98, 1.23, 1.52, 1.94\}$ [232] and from the SDSS-III Baryon Oscillation Spectroscopic Survey (BOSS) DR12 consensus at redshifts $z_{\text{eff}} = \{0.38, 0.51, 0.61\}$[204]. These datasets are supplemented with their respective correlation matrices.

For the MCMC analysis, a more comprehensive dataset is used since MCMC can handle more than one type of observation. Therefore, to complement these $H(z)$ measurements, the third generation of the SDSS mission (SDSS BOSS DR12, [204]) was used to add the corresponding comoving angular diameter $d_M$ at $z_{\text{eff}} = \{0.38, 0.51, 0.61\}$. The fourth generation of the SDSS mission (SDSS IV eBOSS DR 14 [232]) also include angular diameter distance $d_A$ at $z_{\text{eff}} = \{0.98, 1.23,\ 1.52, 1.94\ \}$.

Further to these measurements, comoving volume distance, $d_V$ data points from the 6df Galaxy Survey (6dFGS) at $z_{\text{eff}} = 0.106$ [233] and SDSS Main Galaxy Sample measurement at $z_{\text{eff}} = 0.15$ [234] were also included. In addition, the Hubble distance, $d_H$ (as defined in Eq. 3.41, measurement at $z_{\text{eff}} = 2.4$ from the BOSS DR11 quasar Lymann-$\alpha$, [235] was also considered.

Measurements from these studies are quoted with a scaling factor, $H(z) \times (r_d/r_{d,\text{fid}})$, where $r_{d,\text{fid}}$ is the sound horizon for the fiducial model. This scaling ensures that the measurements are independent of the fiducial model. Therefore, the following corresponding

combination of results $\mathcal{G}(z_i) = D_V(z_i)/r_s(z_d)$, $r_s(z_d)/D_V(z_i)$, $D_H(z_i)$, $D_M(z_i)(r_{s,\mathrm{fid}}(z_d)/r_s(z_d))$, $H(z_i)(r_s(z_d)/r_{s,\mathrm{fid}}(z_d))$, $D_A(z_i)(r_{s,\mathrm{fid}}(z_d)/r_s(z_d))$. had to be calculated.

In this context, the fiducial cosmological model used is a flat ΛCDM model. Measurements from these studies are quoted with a scaling factor, $H(z) \times (r_d/r_{d,\mathrm{fid}})$, where $r_{d,\mathrm{fid}}$ is the sound horizon for the fiducial model. This scaling ensures that the measurements are independent of the fiducial model.

Alam et al. [204] report a value for $r_d$ of 147.78 Mpc, while the baryon density parameter is given as $\Omega_{b,0} = 0.02242/h^2$ and the radiation density parameter as $\Omega_{r,0} = 2.4697 \times 10^{-5}/h^2$ [16] with $h = H_0/100$. The comoving sound horizon $r_d(z)$ was computed using Equation 3.50 at redshift $z_d \approx 1059.94$ [16].

For the MCMC analysis, the corresponding chi-squared statistic $\chi^2_{\mathrm{bao}}$ for the BAO dataset is defined as

$$\chi^2_{\mathrm{BAO}}(\Theta) = (\Delta\mathcal{G}(z_i,\Theta))^T\, C^{-1}_{\mathrm{BAO}}\, \Delta\mathcal{G}(z_i,\Theta)\,, \tag{3.51}$$

where $\Delta G(z_i,\Theta) = G(z_i,\Theta) - G_{\mathrm{obs}}(z_i)$and $C_{\mathrm{BAO}}$ is the corresponding covariance matrix for the BAO observations. The total $\chi^2_{\mathrm{BAO}}$ is therefore the sum of all the individual $\chi^2$ corresponding to each dataset.

#### 3.3.2.4 | Hubble Constant priors

The growing tension between the locally measured values of the Hubble constant, $H_0$, and those predicted by the ΛCDM model based on early Universe observations has been widely discussed in the literature. To provide a comprehensive analysis, different $H_0$ priors were selected from recent studies.

The lowest of these values is derived from the TRGB, where $H_0^{\mathrm{TRGB}} = 69.8 \pm 1.9\,\mathrm{km\,s^{-1}Mpc^{-1}}$ [135]. The TRGB method employs the luminosity of the brightest red-giant branch stars in a galaxy as a standard candle to estimate the galaxy's distance [105]. Specifically, in Ref. [135], this $H_0$ prior was calibrated using TRGB observations and then applied to host galaxies of SNe Ia.

At the other end of the spectrum is the $H_0$ value obtained by the SH0ES Collaboration in 2019, where $H_0^{\mathrm{R19}} = 74.22 \pm 1.82\,\mathrm{km\,s^{-1}Mpc^{-1}}$ [2]. This estimate, referred to as the Riess prior (R19), is based on long-term observations of Cepheid variable stars in the Large Magellanic Cloud (LMC) using the Hubble Space Telescope (HST). Cepheid variables are pulsating stars whose periodic brightness variations make them reliable distance indicators [105]. Their high luminosity and well-defined periodicity enable precise distance measurements across cosmological scales [4].

The third $H_0$ prior, falling between the TRGB and R19 values, is provided by the H0LiCOW Collaboration, where $H_0^{\mathrm{HW}} = 73.3^{+1.7}_{-1.8}\,\mathrm{km\,s^{-1}Mpc^{-1}}$ [136]. This value is derived from obser-

vations of six strongly lensed quasars. Quasars, extremely luminous objects powered by supermassive black holes, are among the most distant and bright objects in the Universe, making them useful probes for gravitational lensing studies [105]. The gravitational lensing method relies on the bending of quasar light as it passes through the curved spacetime near massive objects, allowing for precise $H_0$ measurements based on the time delays between multiple lensed images [136].

The above selected $H_0$ priors are summarised in the upper part of Table 3.1, along with their corresponding references and the labels used throughout this work.

| $H_0$ Prior Program | Label | $H_0$ Value ($\mathrm{km\,s^{-1}Mpc^{-1}}$) | Ref. |
|---|---|---|---|
| SH0ES Collaboration | R19 | $74.22 \pm 1.82$ | [2] |
| H0LiCOW Collaboration | HW | $73.3^{+1.7}_{-1.8}$ | [136] |
| Carnegie-Chicago Hubble Program | TRGB | $69.8 \pm 1.9$ | [135] |
| SH0ES Collaboration | R21 | $73.30 \pm 1.04$ | [4] |
| TRGB | F21 | $69.8 \pm 1.7$ | [60] |

Table 3.1: Summary of the $H_0$ priors used in this analysis. The first column lists the research program from which each prior was obtained, the second column provides the label used in this work, and the third column shows the corresponding $H_0$ value. The final column contains the relevant references. In the top section, lists the values used in Chapters 4 and 5, whilst in the bottom section presents updated values used in the subsequent of the Chapters.

Over time, these values have undergone further refinement as new data and techniques became available as shown in the lower part of Table 3.1. The SH0ES Collaboration updated their measurement, leading to the R21 value, $H_0^{\mathrm{R21}} = 73.3 \pm 1.04\,\mathrm{km\,s^{-1}Mpc^{-1}}$, as reported in [4]. This revision incorporated additional observations of Cepheid variables, further tightening the uncertainty and strengthening the tension between local measurements and those inferred from the early Universe. Similarly, Freedman et al. [60] provided an updated value in 2021 using TRGB as a standard candle, known as F21, with $H_0\mathrm{F21} = 69.8 \pm 1.7\,\mathrm{km\,s^{-1}Mpc^{-1}}$ . This updated TRGB result reduced the uncertainty compared to earlier measurements, continuing to support a lower value of $H_0$. These revisions reflect the ongoing effort within the scientific community to resolve the Hubble tension, offering increasingly precise measurements but also deepening the disparity between early- and late-Universe estimates.

## 3.4 | $f(T)$ Cosmological Models for Parameter Inference

With the key observational datasets and $H_0$ priors established, attention is now directed towards the cosmological models that are fundamental to the MCMC analysis, with a primary focus on $f(T)$ gravity models [7]. The accuracy of cosmological inferences depends significantly on the models applied to interpret observational data. These models encapsulate the current understanding of the Universe's expansion history and are essential for making predictions and inferring parameters with high confidence. Within the MCMC framework, these models serve as the basis for generating theoretical predictions that are compared against observed data, enabling the determination of cosmological parameters such as the Hubble constant, matter density, and other properties, through the use of the associated $\chi^2$ equations. The following sections introduce the specific models employed in this study, detailing their theoretical foundations and their role in the MCMC analysis.

### 3.4.1 | Power Law Model

The first cosmological model considered in this analysis is the Power Law Model, denoted as $f_1$CDM. This model, inspired by the work of Bengochea and Ferraro [157] and further explored by Linder [78], modifies the standard GR framework by introducing a specific function of the torsion scalar $T$ into the gravitational action. In this model, the function $f(T)$ follows a power-law dependence on $T$, expressed as

$$f_1(T) = \alpha_1(-T)^{p_1}\,, \tag{3.52}$$

where $\alpha_1$ is a constant, and $p_1$ is a dimensionless model parameter that governs the deviation from the standard $\Lambda$CDM model.

This model is of particular interest because it allows for an alternative explanation of the accelerated expansion of the Universe, through the power-law dependence of the torsion scalar $T$, which is traditionally attributed to the cosmological constant $\Lambda$. The parameter $p_1$ introduces a new dynamical degree of freedom, and varying $p_1$ can lead to different cosmological behaviours. Specifically, the model reduces to the $\Lambda$CDM scenario when $p_1 = 0$, and it approaches the GR/TEGR limit with a redefined gravitational constant when $p_1 = 1$.

To ensure the parameters in the MCMC technique are left to a minimum, the parameter $\alpha_1$ is determined by evaluating the modified Friedmann equation at the present time. By substituting the expression for $f_1(T)$ from Eq. 3.52 and its derivative $f_{1_T} = -\alpha_1 p_1(-T)^{p_1-1}$

[7] While $f(T, B)$ models are also derived from the following models, they are discussed in detail in the relevant chapter.

into the Friedmann equation, Eq. 2.56, the constant $\alpha_1$ can be written as

$$\alpha_1 = (6H_0^2)^{1-p_1} \frac{1 - \Omega_{m,0} - \Omega_{r,0}}{1 - 2p_1}, \tag{3.53}$$

where as a reminder $H_0$ represents the current value of the Hubble constant, $\Omega_{m,0}$ denotes the current matter density parameter, and $\Omega_{r,0}$ is the current radiation density parameter, taken to be as $\Omega_{r,0} = 4.1534 \times 10^{-5}/h^2$, where $h = H_0/(100\,\mathrm{km\,s^{-1}Mpc^{-1}})$ [16]. This expression is crucial as it ensures that the model aligns with the observed expansion rate of the Universe today.

The modified Friedmann equation for the $f_1$CDM model, incorporating the power-law function $f_1(T)$, can then be expressed as

$$E^2(z) = \Omega_{m,0}\,(1+z)^3 + \Omega_{r,0}\,(1+z)^4 + (1 - \Omega_{m,0} - \Omega_{r,0})\,E^{2p_1}(z), \tag{3.54}$$

where $E(z) = H(z)/H_0$ is the normalised Hubble parameter. This equation describes the evolution of the Hubble parameter as a function of redshift $z$, reflecting the influence of the parameter $p_1$ on the cosmic expansion history. It is worth noting that this equation cannot be solved analytically. Therefore, numerical methods were employed to calculate $E(z)$at each redshift point. Consequently, using MCMC analysis, parameter values were obtained by solving for each redshift point where observational data exists

To visualise the implications of the $f_1$CDM model and the imapct of the parameter $p_1$ on cosmic evolution, a Hubble diagram has been illustrated in Fig. 3.6. This diagram plots the Hubble parameter $H(z)$ against redshift $z$ for various values of the parameter $p_1$. The Hubble diagram is a key diagnostic tool in cosmology, as it directly illustrates the rate of expansion of the Universe at different epochs.

In this analysis, the Hubble diagram includes curves corresponding to several values of $p_1$. The colours on the diagram represent different values of $p_1$, illustrating how this parameter influences the expansion rate. As $p_1$ increases, the model predicts a higher expansion rate at late times, which corresponds to a steeper slope in the Hubble diagram. This behaviour indicates that the $f_1$CDM model can drive accelerated expansion without the need for a cosmological constant. The ability of the model to match the observed accelerated expansion of the Universe at late times is a critical test of its viability.

Furthermore, the Hubble diagram serves as a comparison between the theoretical predictions of the $f_1$CDM model and observational data, in particular the CC data. The consistency of the model's predictions with the observed $H(z)$ values across a range of redshifts is crucial for validating the model. The analysis shows that the $f_1$CDM model can reproduce the key features of the observed cosmic acceleration, making it a compelling alternative to the $\Lambda$CDM model.

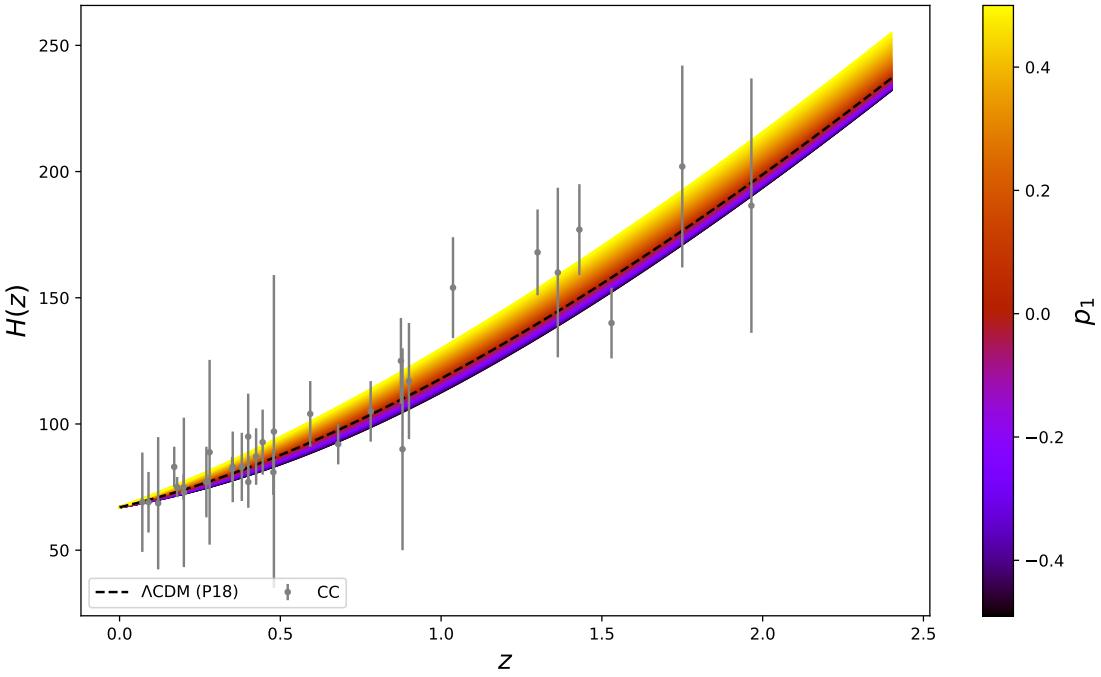


Figure 3.6: Hubble diagram of $H(z)$ versus $z$ for Power Law Model as defined in Eq. 3.54. The $H(z)$ data points from the CC datasets are also depicted.

This Hubble diagram analysis also highlights how the parameter $p_1$ influences the model's predictions. For instance, at $p_1 = 0$, the $f_1$CDM model reduces to the ΛCDM model, which serves as a baseline for comparison and is represented by the dashed black line. The Hubble diagram also gives an indication to the prior range that needs to be inserted in the MCMC analysis for the $p_1$ parameter.

In summary, the Power Law Model ($f_1$CDM) offers a versatile framework for explaining the accelerated expansion of the Universe. The detailed analysis of the Hubble diagram, including its dependence on the parameter $p_1$, provides strong evidence that this model is capable of reproducing key cosmological observations. As such, it stands as a significant alternative to the ΛCDM model, with the potential to offer new insights into the nature of cosmic acceleration.

### 3.4.2 | Square-root Exponential Model

The second cosmological model under consideration is the Linder model or the Square-root Exponential Model, hereafter referred to as $f_2$CDM. Unlike the Power Law model discussed earlier, which generalises the cosmic expansion behaviour through a power-law dependence on the torsion scalar, the Linder model is specifically designed to naturally incorporate late-

time accelerated expansion. This model, proposed by Linder [78], offers a different functional form of $f(T)$ that achieves accelerated expansion through an exponential modification of the torsion scalar

$$f_2(T) = \alpha_2 T_0 \left(1 - \mathrm{Exp}\left[-p_2\sqrt{T/T_0}\right]\right) , \tag{3.55}$$

where $\alpha_2$ and $p_2$ are the model parameters, and $T_0 = T|_{t=t_0} = -6H_0^2$ corresponds to the present-day value of the torsion scalar.

In the same light as $f_1$CDM, $\alpha_2$ can be defined by evaluating the Friedmann equation at current times

$$\alpha_2 = \frac{1 - \Omega_{m,0} - \Omega_{r,0}}{(1+p_2)\, e^{-p_2} - 1} . \tag{3.56}$$

This makes $p_2$ the new parameter for the $f_2$CDM model, apart from the current density matter $\Omega_{m,0}$ and the functional form in the exponential term $H/H_0$.

The corresponding Friedmann equation for the Linder model, which describes the evolution of the Hubble parameter $H(z)$ with redshift, is given by:

$$E^2(z) = \Omega_{m,0}(1+z)^3 + \Omega_{r,0}(1+z)^4 + \frac{1 - \Omega_{m,0} - \Omega_{r,0}}{(p_2+1)e^{-p_2} - 1}\left[(1 + p_2 E(z))\,\mathrm{Exp}\left[-p_2 E(z)\right] - 1\right] , \tag{3.57}$$

where $E(z) = H(z)/H_0$ is the normalised Hubble parameter. The $p_2$ parameter in this equation provides a different interpretation compared to $p_1$ from the Power Law model, reflecting the exponential nature of the functional form.

By construction, the Linder model is tailored to ensure accelerated expansion at late times, a feature that aligns with current cosmological observations [236, 78]. This intrinsic characteristic distinguishes it from the Power Law model, where the nature of expansion depends more heavily on the specific value of $p_1$. Indeed, Eq. 3.55 for $p_2 \to +\infty$ the $f_2$CDM reduces to $\Lambda$CDM, since

$$\lim_{p_2 \to +\infty} \left[-T + f(T)\right] = -T + 2\Lambda . \tag{3.58}$$

To enhance numerical stability, the $f_2$CDM parameter can be redefined as $1/p_2$, where the $\Lambda$CDM limit is approached as $1/p_2 \to 0^+$. This reparameterisation to $1/p_2$ is crucial for ensuring numerical stability, particularly in MCMC analyses where precise parameter estimation is required. The parameter $p_2$ controls the deviation from the standard model of cosmology. However, directly working with $p_2$ in numerical simulations can lead to instability due to the exponential nature of the function $f_2(T)$. When $p_2$ is large, small changes in $p_2$ can cause significant variations in the model's predictions, making it difficult to achieve convergence in MCMC chains. By reparameterising to $1/p_2$, the model becomes more tractable,

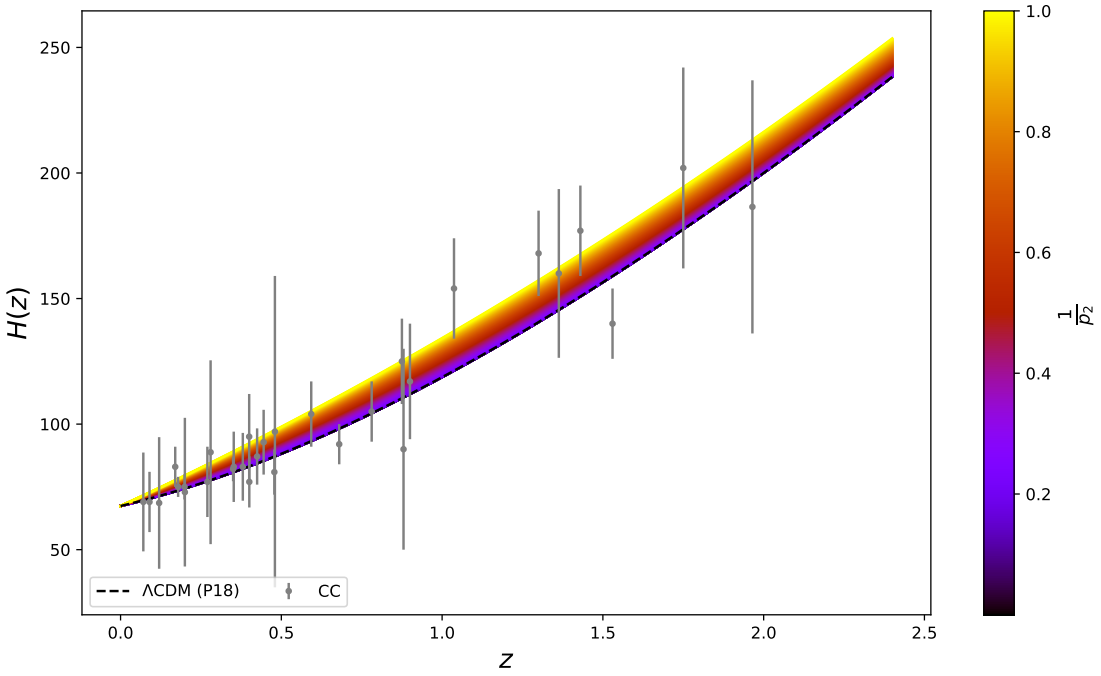


Figure 3.7: Hubble diagram of $H(z)$ versus $z$ for Linder Model as defined in Eq. 3.57. The $H(z)$ data points from the CC datasets are also depicted, together with the ΛCDM curve

allowing for smoother convergence. This approach mitigates issues of numerical instability and enhances the strength of the analysis, especially when exploring the parameter space close to the ΛCDM limit.

In terms of observational consequences, a Hubble diagram plotting $H(z)$ versus $z$ is presented for the Linder model in Fig. 3.7, showing how different values of $1/p_2$ influence the expansion rate across redshifts. The comparison with the Power Law model will illustrate how the exponential form in $f_2$CDM consistently leads to a more pronounced acceleration at late times, as expected by its design. The diagram also reveals the prior range for $1/p_2$ parameter, which spans from $0 < 1/p_2 < 1$.

In conclusion, while both $f_1$CDM and $f_2$CDM are capable of explaining late-time acceleration, the Linder model does so with an inherently different approach, leveraging the exponential form of its functional dependence on $T$. This difference not only impacts the theoretical framework but also the observational signatures predicted by each model, making the Linder model a compelling candidate for explaining dark energy within the modified gravity paradigm.

### 3.4.3 | Exponential Model

The third cosmological model under consideration is the Exponential Model, denoted as $f_3$CDM, which is inspired by extended gravity theories within the context of GRas proposed by Linder [236] and further developed by Nesseris et al. [237]. This model introduces a variant of the Linder model by modifying the functional form of $f(T)$ to incorporate an exponential dependency on the torsion scalar $T$. The model is described by the function

$$f_3(T) = \alpha_3 T_0 \left(1 - \mathrm{Exp}\left[-p_3 T/T_0\right]\right) , \tag{3.59}$$

where $\alpha_3$ and $p_3$ are the model's parameters, and $T_0$ represents the value of the torsion scalar at the current time ($T_0 = -6H_0^2$). Similar to the $f_2$CDM model, $\alpha_3$ is determined by evaluating the Friedmann equation at the present epoch, leading to

$$\alpha_3 = \frac{1 - \Omega_{m,0} - \Omega_{r,0}}{(1 + 2p_3)\, e^{-p_3} - 1} . \tag{3.60}$$

Substituting these expressions for $f_3(T)$ and $\alpha_3$ into the modified Friedmann equation, Eq. 2.56 the evolution equation for the normalised Hubble parameter $E(z) = H(z)/H_0$ becomes

$$E^2(z) = \Omega_{m,0}\,(1+z)^3 + \Omega_{r,0}\,(1+z)^4 + \frac{1 - \Omega_{m,0} - \Omega_{r,0}}{(1+2p_3)e^{-p_3} - 1}\left[\left(1 + 2p_3 E^2(z)\right)\mathrm{Exp}\left[-p_3 E^2(z)\right] - 1\right] . \tag{3.61}$$

The $f_3$CDM model bears similarities to the $f_2$CDM Linder model, particularly in its ability to reduce to the $\Lambda$CDM model in the appropriate limit. Specifically, as $p_3 \to +\infty$, the exponential term diminishes, leading the model to converge to the standard $\Lambda$CDM cosmology. This is analogous to the behaviour of the $f_2$CDM model where $p_2$ controls the deviation from $\Lambda$CDM. However, unlike the power-law model ($f_1$CDM), which introduces a simpler power-law dependency on the torsion scalar, the $f_3$CDM model incorporates a more complex exponential function, offering a distinct approach to modelling the late-time acceleration of the Universe.

In both the $f_2$CDM and $f_3$CDM models, reparameterisation is employed for numerical stability during analysis. Specifically, the reparameterisation to $1/p_3$ is introduced to ensure smooth convergence in MCMC simulations, particularly when exploring parameter spaces close to the $\Lambda$CDM limit. This technique is consistent with the approach used in the Linder model ($f_2$CDM) and highlights the necessity of such transformations for such cosmological analysis.

To further examine, the $f_3$ model's behaviour, a Hubble diagram is constructed, illustrated the relationship parameter $h(z)$ and redshift $z$ in Fig. 3.8. This diagram highlights the impact of the $p_3$ parameter on the expansion history of the Universe, in the range of

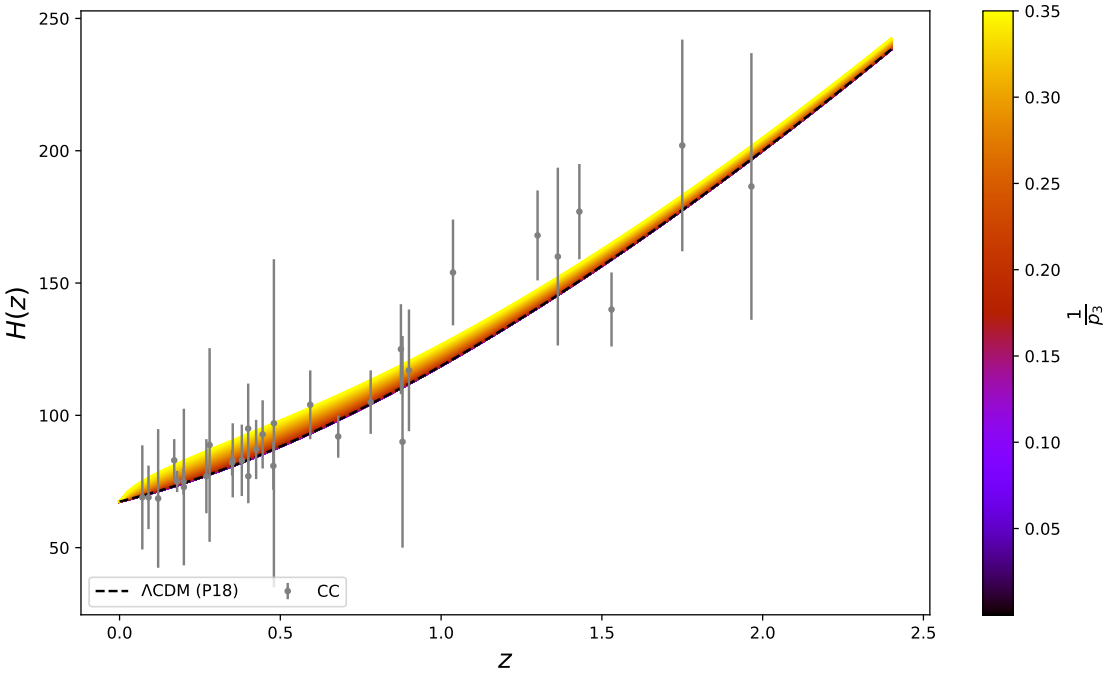


Figure 3.8: Hubble diagram of $H(z)$ versus $z$ for the Exponential Model as defined in Eq. 3.61. The $H(z)$ data points from the CC datasets are also depicted, together with the ΛCDM curve.

our dataset. This analysis is crucial for understanding the model's ability to replicate the observed accelerated expansion of the Universe. The diagram shows that for smaller values of $1/p_3$, the model closely follows ΛCDM, while for larger values, deviations become more pronounced, particularly at higher redshifts. This behaviour is consistent with the design of the model, which, like the Linder model, is intended to capture late-time acceleration.

Therefore, the $f_3$CDM model adds another dimension to our exploration of modified gravity theories, using an exponential form to capture the dynamics of cosmic expansion. By comparing it to the power-law and Linder models, the range of possible behaviours these models predict can be better understood, particularly in relation to the Universe's accelerated expansion.

### 3.4.4 | Logarithmic Model

The fourth cosmological model considered in this analysis is the logarithmic model proposed by Bamba et al. [238], which is denoted as $f_4$CDM. This model is characterised by the $f(T)$ function given by

$$f_4(T) = \alpha_4 T_0 \sqrt{\frac{T}{p_4 T_0}} \log\left[\frac{p_4 T_0}{T}\right], \tag{3.62}$$

where $\alpha_4$ and $p_4$ are the model parameters, and $T_0$ is previously defined. The parameter $\alpha_4$ is determined by evaluating the Friedmann equation at the current epoch, which leads to:

$$\alpha_4 = -\frac{(1 - \Omega_{m,0} - \Omega_{r,0})\sqrt{p_4}}{2}. \tag{3.63}$$

Substituting the function $f_4(T)$ and $\alpha_4$ into the modified Friedmann equation, the logarithmic Friedmann equation becomes

$$E^2(z) = \Omega_{m,0}(1+z)^3 + \Omega_{r,0}(1+z)^4 + (1 - \Omega_{m,0} - \Omega_{r,0})\, E(z)\,. \tag{3.64}$$

The logarithmic model stands out due to its distinct characteristics compared to the previously discussed models. Unlike the power-law model $f_1$CDM and the Linder model $f_2$CDM, which can approximate $\Lambda$CDM cosmology under certain conditions, the $f_4$CDM model does not reduce to $\Lambda$CDM for any value of $p_4$. This is because the Friedmann equation for the logarithmic model, as shown in Eq. 3.64, does not involve the parameters $\alpha_4$ or $p_4$ in a way that allows for a direct comparison with $\Lambda$CDM. Although $p_4$ is absent at the background level, these parameters could emerge at the perturbative level, which would make them semi-independent of background observations.

The fact that the logarithmic model is not capable of matching $\Lambda$CDM parameters highlights its distinctive behaviour. Specifically, this model does not exhibit the same parameter tuning flexibility as $f_1$CDM or $f_2$CDM. Consequently, it provides a more rigid framework for evaluating cosmological data, making it less prone to fitting biases that could arise from adjusting parameters to mimic $\Lambda$CDM.

In terms of the Hubble diagram. in Fig 3.9 the logarithmic model presents a more constrained scenario compared to $f_1 - f_3$CDM models. The Hubble diagram for the $f_4$CDM model produces a specific curve that reflects the unique relationship between $H(z)$ and $z$. This is because the model's functional form does not include adjustable $p_4$ parameter that would otherwise alter the shape of the curve.

However, while the $f_4$CDM model's Hubble diagram does not exhibit variability with $p_4$, it can still be influenced by changes in the cosmological parameters $H_0$ and $\Omega_{m,0}$. These parameters determine the overall shape and positioning of the Hubble curve relative to observational data and the $\Lambda$CDM model. This characteristic makes the logarithmic model valuable for comparative studies, as it provides a clear benchmark that contrasts with the more flexible behaviours of the power-law and Linder models, as will be shown in the MCMC analysis.

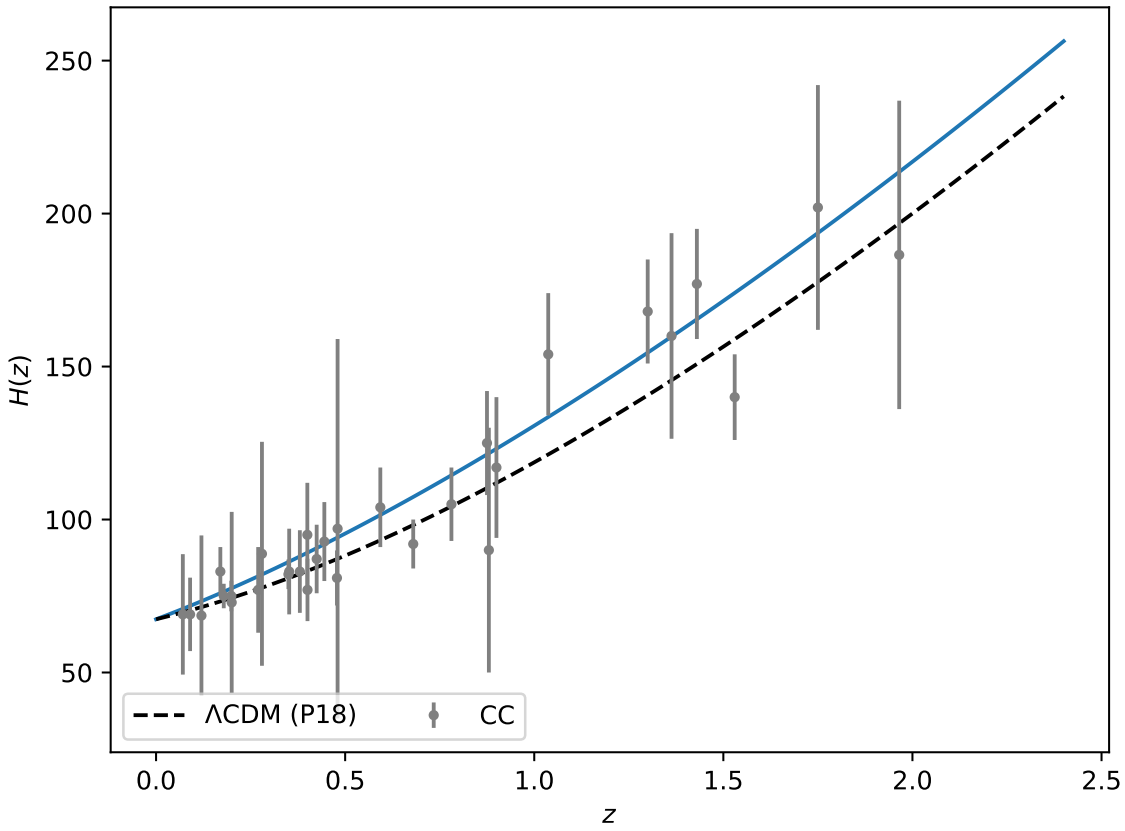


Figure 3.9: Hubble diagram if $H(z)$ versus $z$ for the Logarithmic Model as defined in Eq. 3.62. In this case only one instance of the Hubble diagram is taken, since the Friedmann Equation is independent of the $p$ parameter. The $H(z)$ data points from the CC dataset are also depicted, together with the ΛCDM curve illustrated by the black dashed line.

The absence of parameter-driven variation in the Hubble diagram for the logarithmic model underscores its unique place in cosmological analyses. This feature helps in understanding the fundamental differences between models that approximate ΛCDM and those that inherently exhibit different dynamical properties.

### 3.4.5 | Hyperbolic-tangent Model

The final cosmological model analysed is the hyperbolic-tangent model, denoted as $f_5$CDM, as proposed by Wu et al. [239]. This model introduces the $f(T)$ function given by

$$f_5(T) = \alpha_5(-T)^{p_5}\text{Tanh}\left(\frac{T_0}{T}\right), \tag{3.65}$$

where $\alpha_5$ and $p_5$ are the model parameters. The parameter $\alpha_5$ is determined by evaluating the Friedmann equation at the present epoch, resulting in

$$\alpha_5 = \frac{\left(6H_0^2\right)^{1-p_5}\left(1-\Omega_{m,0}-\Omega_{r,0}\right)}{(1-2p_5)\tanh(1)+2\mathrm{Sech}^2(1)}. \tag{3.66}$$

Substituting $f_5(T)$ and $\alpha_5$ into the modified Friedmann equation yields

$$E^2(z) = \Omega_{m,0}(1+z)^3 + \Omega_{r,0}(1+z)^4 + \frac{1-\Omega_{m,0}-\Omega_{r,0}}{(2p_5-1)\tanh(1)-2\mathrm{Sech}^2(1)} E^{2(p_5-1)}(z)\left[(2p_5-1)E^2(z)\mathrm{Tanh}(E^{-2}(z)) - 2\mathrm{Sech}^2(E^{-2}(z))\right]. \tag{3.67}$$

The hyperbolic-tangent model $f_5$CDM introduces a distinctive functional form that sets it apart from the previously discussed models. Unlike the power-law model ($f_1$CDM), Linder model ($f_2$CDM) and Variant of the Linder Model ($f_3$CDM), the $f_5$CDM model does not approximate $\Lambda$CDM cosmology for any value of $p_5$. This is because the hyperbolic-tangent function introduces a non-trivial dependence on the torsion scalar $T$, which affects the modified Friedmann equation in a manner that prevents it from reducing to $\Lambda$CDM.

In comparison, the power-law model exhibits a straightforward dependency on $T$ with the possibility of reducing to $\Lambda$CDM when $p_1 \to 0$. In addition, the Linder model is designed to achieve late-time acceleration, similar to $f_5$CDM. However, $f_2$CDM approaches $\Lambda$CDM in the limit of $p_2 \to \infty$, whereas $f_5$CDM retains its distinct behavior due to the hyperbolic-tangent function. The $f_5$CDM model, does not allow for such a reduction, reflecting a more complex interplay between the parameters.

The logarithmic model cannot replicate $\Lambda$CDM either, but the reasons are different. While $f_4$CDM does not include parameters that would allow it to mimic $\Lambda$CDM, $f_5$CDM's functional form inherently prevents such a reduction.

The Hubble diagram for the hyperbolic-tangent model $f_5$CDM , in Fig. 3.10 illustrates the dependence of $H(z)$ on the redshift parameter $z$ and the model parameter $p_5$. This diagram reveals how variations in $p_5$ influence the Hubble parameter, with the model exhibiting a striking similarity to the $\Lambda$CDM curve. Despite the absence of a formal $\Lambda$CDM limit within this model, it closely approximates $\Lambda$CDM, demonstrating a remarkable alignment with its predictions.

In summary, the hyperbolic-tangent model offers a distinct and intricate alternative to $\Lambda$CDM, providing a different perspective on cosmological dynamics compared to the power-law, Linder, and logarithmic models. This model's behaviour suggests it can replicate $\Lambda$CDM outcomes under certain conditions, thereby enriching our understanding of cosmological models.

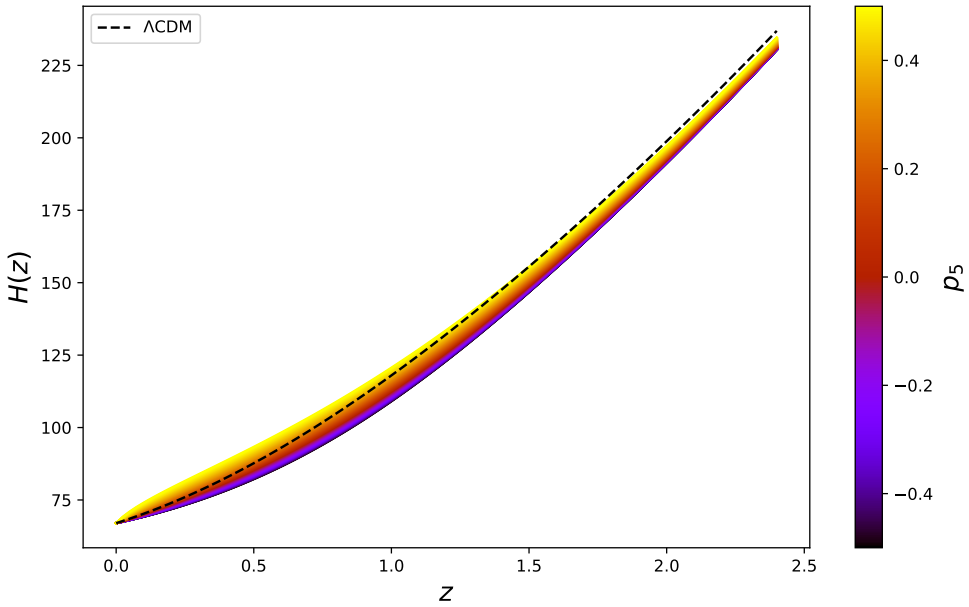


Figure 3.10: Hubble diagram of $H(z)$ versus $z$ for the Hyperbolic-tangent Model as defined in Eq. 3.67. The $H(z)$ data points from the CC datasets are also depicted, together with the $\Lambda$CDM curve.

## 3.5 | Statistical Indicators

In this section, the focus shifts to the statistical evaluation of the models just described. These models will be analysed and parameters will be extracted when using the MCMC algorithm with observational data to assess their viability in describing the Universe. These models selected for their previous application in alternative gravity theories will be examined to understand further their predictive power relative to recent cosmological parameters in particular $H_0$.

To evaluate the performance of each model, a comparative analysis needs to be conducted and also compared to the $\Lambda$CDM model. Two-widely used statistical indicators are; the AIC and BIC to quantify how well each model fits the observational data.

### 3.5.1 | Akaike Information Criterion

The Akaike Information Criteria (AIC), a widely used criterion for model selection that balances goodness of fit with model complexity was first introduced by Akaike in 1974 [240]. It provides a quantitative measure for comparing different models based on their fit to the

observational data and their complexity [241]. The AICis defined as

$$\mathrm{AIC} = -2\ln\mathcal{L}_{\max} + 2n\,, \tag{3.68}$$

where $\mathcal{L}_{\max}$ is the maximum likelihood of the model given the data, and $n$ represents the number of parameters in the model. The likelihood function, $\mathcal{L}_{\max}$, is related to the chi-square statistic ($\chi^2$) through the relationship

$$\chi^2 = -2\ln\mathcal{L}_{\max}\,. \tag{3.69}$$

The AIC evaluates model performance by incorporating both the fit of the model (via $\mathcal{L}_{\max}$) and a penalty for model complexity (via $2n$) [241]. A higher value of $\mathcal{L}_{\max}$ indicates a better fit to the data, while the penalty term $2n$ increases with the number of parameters, discouraging overly complex models. Typically, models with an insufficient number of parameters tend to provide a poor fit to the data, and therefore, have a low log-likelihood. Thus, a lower AIC value signifies a model that achieves a good trade-off between fit and simplicity [242]

In practice, the AIC is particularly useful when comparing models with different numbers of parameters. It helps identify models that provide a good fit to the data without unnecessary complexity, thereby aiding in selecting the most parsimonious model that adequately describes the observed phenomena.

### 3.5.2 | Bayesian Information Criterion

The Bayesian Information Criteria (BIC), proposed by Schwarz in 1978 [243], serves as another important model selection criterion. While similar to the AIC, the BIC imposes a stronger penalty for models with more parameters, making it a more stringent criterion for model complexity. The BIC is expressed as

$$\mathrm{BIC} = -2\ln\mathcal{L}_{\max} + n\ln m\,, \tag{3.70}$$

where $m$ denotes the sample size of the observational data. The term $n\ln m$ adds a penalty that increases with both the number of parameters and the size of the dataset [241]. This greater penalty for additional parameters makes the BIC a more conservative measure of model performance compared to the AIC.

The BIC is especially useful when comparing models with large sample sizes, as the penalty term $n\ln m$ becomes significant. A lower BIC value indicates a model that not only fits the data well but also does so with minimal complexity relative to the amount of data. Both AIC and BIC are used to identify models that provide a good balance between fit and

simplicity, but the BIC's stricter penalty makes it more suitable for evaluating model performance in scenarios with large datasets.

### 3.5.3 | Comparative Criteria

To compare the performance of each $f(T)$ cosmological model against the standard $\Lambda$CDM model, the differences in AIC and BIC values are calculated, denoted as $\Delta$AIC and $\Delta$BIC. These differences are computed as follows

$$\Delta\text{AIC} = \text{AIC}_{\text{model}} - \text{AIC}_{\Lambda\text{CDM}} = \Delta\chi^2_{\text{min}} + 2\Delta n\,, \tag{3.71}$$

$$\Delta\text{BIC} = \text{BIC}_{\text{model}} - \text{BIC}_{\Lambda\text{CDM}} = \Delta\chi^2_{\text{min}} + \Delta n \ln m\,. \tag{3.72}$$

In these equations, $\Delta$AIC and $\Delta$BIC represent the differences between the AIC and BIC values of each $f(T)$ model and those of the $\Lambda$CDM model, respectively. Smaller $\Delta$AIC and $\Delta$BIC values indicate that the particular $f(T)$ model performs more similarly to the $\Lambda$CDM model, suggesting that it better approximates the observational data while accounting for model complexity.

By evaluating these differences, an assessment of which $f(T)$ models offer a competitive fit compared to the $\Lambda$CDM model can be easily made. This approach facilitates a detailed comparison of the models based on their ability to describe the cosmological dynamics, providing insights into how well each model aligns with observational data and how it measures up against the well-established $\Lambda$CDM framework.

Overall, the AIC and BIC provide essential tools for model comparison, helping to identify the most suitable model based on a balance of fit and complexity. Their application to the $f(T)$ cosmological models allows for a rigorous evaluation of how these alternative theories perform in describing the late-time expansion history of the Universe in comparison to the standard $\Lambda$CDM model.

To assess how well these different models fit the data relative to one another, the Jeffreys' Scale can be applied. First introduced by Sir Harold Jeffreys' in 1939 [244, 245], this scale offers a qualitative interpretation of the numerical differences obtained from statistical measures like the AIC and BIC. The Jeffreys' Scale provides insights into how much more favourable one model is compared to another by translating these numerical differences into qualitative evidence. This approach is especially valuable in practical settings where decision-making relies not only on numerical outcomes but also on the interpretive strength of the results.

For instance, when comparing cosmological models or other statistical models, the Jeffreys' Scale helps determine whether the complexity and fit of a model justify its selection over competing models. It offers a clearer perspective on how well the models align with the observed data and aids in communicating the relative strengths of different models in a way that is both accessible and informative [246, 217].

Regarding AIC and BIC, the scale typically categorises the strength of evidence into several ranges: **0 to 2:** This range suggests weak evidence in favour of the preferred model, indicating that the model with the lower AIC or BIC value does not significantly outperform the alternative. **2 to 6:** This range represents positive evidence for the model with the lower criterion value, showing a notable improvement in fit or efficiency compared to the other, suggesting a clear but not overwhelming advantage. **6 to 10:** This range indicates strong evidence supporting the model with the lower criterion value, reflecting a substantial improvement in fit and providing a strong indication that the model is significantly better [247].

Therefore, the Jeffreys' Scale, rooted in Bayesian statistics, remains a vital tool as it enhances the interpretation of AIC and BIC results. It provides a structured way to interpret the strength of evidence in model comparisons, helping to bridge the gap between numerical analysis and practical decision-making.

## 3.6 | Conclusion

In conclusion, this chapter has undertaken a deep exploration of two methodological framework, including GP (Sec. 3.1) and MCMC (Sec. 3.2) techniques. These methodologies have proven instrumental in effectively reconstructing cosmological functions and constraining parameters with several $f(T)$ cosmological models.

The application of GP has allowed for a non-parametric approach to reconstruct cosmological functions directly from observational data, offering flexibility and precision. Its non-parametric nature can reveal subtle features in the data that might be missed by more rigid parametric models within the $f(T)$ gravity. By employing GP, insights into the underlying dynamics of the Universe can be gained, independent of specific model assumptions, which serves as a powerful complement to the traditional parametric models.

MCMC, on the other hand, has enabled the systematic exploration of parameter spaces with modified gravity theories such as $f(T)$ and $f(T, B)$, providing a probabilistic assessment of the model parameters that best fit the data. The stochastic nature of MCMC allows for a probabilistic assessment of the parameter distributions, helping us identify the most likely values that fit the observational data and hence, allow for meaningful constraints from

observational data.

The observational data employed in this study, encompassing a range of measurements from the CC, BAO, SNe Ia (PN) and recent model-independent measurements of the Hubble constant ($H_0$), form the backbone of our analysis. These datasets will be considered as the baseline datasets. It is important to note that while these datasets represent the most reliable and widely accepted observations available at the present time when the study was conducted, these datasets are subject to continuous revisions and refinements as new observations are made and analysis techniques improve. As such, the datasets discussed in this chapter are constantly revisited and reassessed in light of new datasets to ensure the most accurate and up-to-date cosmological interpretations as the observational landscape evolves.

The five $f(T)$ models (Power-Law Model - Sec. 3.4.1, Linder Model - Sec. 3.4.2, Variant of the Linder Model - Sec. 3.4.3, Logarithmic Model - Sec. 3.4.4 and Hyperbolic-Tangent model - Sec. 3.4.5) examined in this chapter were chosen for their potential to offer viable alternatives to the standard $\Lambda$CDM model. Some of these models have been well-studied in other contexts and have shown promise in capturing key aspects of the Universe's expansion history. The analysis revealed that while some models provide a close match to the $\Lambda$CDM predictions, others diverge in interesting ways, offering new perspectives on the late-time acceleration of the Universe. These differences highlight the importance of exploring a diverse range of models to fully understand the possible variations in cosmic evolution.

Finally, the use of model selection criteria, specifically the AIC and the BIC, provides a quantitative means of evaluating the relative performance of these models. By applying the Jeffreys' Scale to interpret the differences in AIC and BIC values, the statistical evidence supporting each model can be contextualised. This helps in identifying which models offer the most promising alternatives to $\Lambda$CDM in the context of $f(T)$ gravity (and later on $f(T, B)$ gravity as well).

Overall, this chapter has laid a foundation for further investigations into $f(T)$ gravity (and also the extension of $f(T, B)$ gravity, later on) as a potential alternative to $\Lambda$CDM. The methodologies employed here, combined with the latest observational data, will allow for rigorous testing of these models and hence, an assessment of their viability. As cosmological data continues to improve, the approaches developed in this chapter will remain crucial tools for advancing our understanding of the Universe's expansion history and the fundamental forces that govern it.

In the subsequent chapter, the focus will first shift to the application of GP within the context of $f(T)$ gravity. This method will be employed to reconstruct the Hubble parameter, $H(z)$, and the $f(T)$ function directly from observational data. By using GP, the underlying dynamics of $f(T)$ models will be investigated without the need to impose specific paramet-

ric forms, offering a more flexible and potentially revealing analysis of the cosmic expansion history. Through this approach, new aspects of $f(T)$ models may be uncovered, further contributing to the understanding of the mechanisms driving the accelerated expansion of the Universe.

# 4

# Gaussian Processes in $f(T)$ Gravity

Throughout the years, cosmologists have had to continuously revise their understanding of the Universe to accommodate new observations. This iterative process has led to the development of the standard model of cosmology, which has proven successful in explaining many phenomena. Nevertheless, a prominent issue that consistently arises is the $H_0$ tension, which challenges the $\Lambda$CDM model. In response to this, alternative theories have been proposed, one of which involves exploring extended modified gravity theories such as $f(T)$ gravity, which is based on torsional formalism. The literature presents several observational tests showing that $f(T)$ gravity holds significant promise [73, 237, 248, 249, 250, 251].

An effective tool in addressing these cosmological questions is the GP, a sophisticated class of statistical models that defines a probability distribution over random functions. Rather than specifying an explicit mathematical formula for the function from which observations are derived, GP models the covariance between pairs of samples. This approach leverages available data to guide the modelling process, allowing for a reconstruction of the function $f(z_i) \pm \sigma_i$ from data points using a point-to-point Gaussian distribution [252, 253, 254, 255, 161].

In this chapter, the GP method is employed for reconstructing functions related to $f(T)$ gravity using various cosmological datasets. The GP framework offers a Bayesian approach that allows for the direct reconstruction of functions from data without assuming a specific parametrisation. The only requirement for the GP analysis is the covariance function. Consequently, the model-independent GP has been extensively used to explore the expansion dynamics of the Universe [256, 257, 258], including tests of the $\Lambda$CDM model [259]. Therefore, GP is an effective, cosmology-independent tool, and has the ability to build reconstruction pipelines on which the $f(T)$ models can be built upon.

Therefore, the GP approach will be used to explore $f(T)$ gravity, with the aim of reconstructing the arbitrary function $f(T)$ in a manner that is independent of specific mod-

els. The analysis will begin with the reconstruction of the Hubble parameter $H(z)$ and its derivatives, derived from observational data. These reconstructions will then facilitate the examination of $f(T)$ by applying the cosmological dynamics discussed in Chapter 2. By analysing these reconstructions, any deviations from the ΛCDM model can be identified and hence, recognise tendencies that should be considered when developing $f(T)$ models. This chapter builds upon the work which has been presented and published in Briffa et. al [161].

## 4.1 | Reconstruction of Hubble data

The GP algorithm can be applied to a variety of $H(z)$ data sources, facilitating the reconstruction of the $H_0$ parameter. This implementation, through the publicly available Python code Gaussian Process in Python (GaPP) [8] [178], provides three core options: the choice of dataset combinations, the selection of priors (if any), and the choice of kernel (Squared-Exponential, Cauchy, Matérn, or Rational Quadratic kernels).

The analysis includes three principal data sources: CC, SNe Ia, and BAO. The CC data is highly efficient, as explained in Sec. 3.3.2.1. The second component of the dataset consists of observations from SNe Ia reported by the PN [222], combined with data from CANDELS and Multi-Cycle Treasury (MCT) [260]. As a reminder, the PN dataset primarily includes 1048 apparent magnitude measurements within the redshift range $0.01 < z < 2.3$ as has been explained in Sec 3.3.2.2. The MCT data focuses on higher redshifts, mainly $z > 1$. For this study, the combined data from SN and MCT are collectively referred to as SN.

Since the GP approach requires Hubble data measurements, the raw SN measurements are converted and compressed into six Hubble rate measurements $E(z) \equiv H(z)/H_0$ by Ref. [260], accompanied by their correlation matrix. However, following Ref. [176], only five data points are used in this work, excluding the sixth data point at $z = 1.5$ due to its non-Gaussian distribution.

The analysis also incorporates CC data along with SN data. Since the compressed SN data consists of Hubble rate data points $E(z)$, these must first be converted into Hubble function data $H(z)$ using the relation $H(z) = H_0 E(z)$. Here, $H_0$ is the linking parameter between $H(z)$ and $E(z)$. In the dataset combining CC and SN, an initial value for $H_0$ is not available. Therefore, an iterative numerical procedure [176], explained below, is employed to determine this value.

The GP approach is initially applied to the CC data alone to obtain an estimate for $H_0$. This determined $H_0$ is then used to convert the SN data using the equation $H(z) = H_0 E(z)$.

[8] https://github.com/carlosandrepaes/GaPP

Subsequently, a Monte Carlo error propagation is applied to estimate the mean values and uncertainties of $H(z_i)$. The Monte Carlo routine introduces randomness by drawing normal distributions for $H_0$ and $E(z)$ at various redshifts $z_i$, with mean standard deviations derived from the GP and SN datasets. Using the relation $H(z) = H_0 E(z)$, $n$ samples of $H(z)$ are obtained. A normal distribution is then fitted over these $n$ samples to determine the mean and standard deviation for $H(z)$. The GP approach is iteratively applied to the combined CC and SN datasets until the successive values of $H_0$ converge to within $10^{-4}$. This iterative process ensures that the resulting $H_0$ value and its uncertainty are precise.

The third component of the dataset is the BAO data, as explained in Sec. 3.3.2.3. Therefore, the GP approach was applied to these various sources of Hubble data,that include CC, CC+PN and CC+PN+BAO, along with the priors, R19, TRGB and HW, described in Sec. 3.3.2.4. In this way, the $H(z)$ function was reconstructed using various kernels and thus, $H_0$ values could be inferred. These $H_0$ values are presented in Tables 4.1, 4.2, 4.3, and 4.4, which display the outcomes for all kernel types and dataset combinations.

The last four columns of each table show the distance, in $\sigma$ units, between the GP-inferred values of $H_0$ and the literature priors. Generally, the distance between two values of the Hubble constant, $H_{0,i}$ and $H_{0,j}$ or the concordance (or discordance) between the values of $H_0$, can be defined as

$$T_{H_0} \equiv d(H_{0,i}, H_{0,j}) = \frac{H_{0,i} - H_{0,j}}{\sqrt{\sigma_i^2 + \sigma_j^2}}\,. \tag{4.1}$$

where, in this case, $\sigma_i$ and $\sigma_j$ are the respective $1\sigma$ uncertainties, and $H_{0,j}$ refers to $H_0^{\mathrm{R19}}$ (R19), $H_0^{\mathrm{TRGB}}$ (TRGB), $H_0^{\mathrm{HW}}$ (H0LiCOW (HW)), and $H_0^{\mathrm{P18}}$ (P18). The last column of Tables 4.1 through 4.4 displays the distance between the reconstructed $H_0$ and P18, which is $H_0^{\mathrm{P18}} = 67.04 \pm 0.5\,\mathrm{km\ s^{-1}Mpc^{-1}}$ (Planck Collaboration measurement).

To complement these tables, full plots of the results for the four kernels are presented in Figs. 4.1 through 4.4. These figures illustrate the GP reconstruction of $H(z)$ across the entire redshift range covered by the data. Each curve represents the GP reconstruction of $H(z)$ for different dataset combinations, while circle markers denote the observational data for $H(z)$ along with their $1\sigma$ uncertainties. The reconstructed GP curves are accompanied by their $1\sigma$ and $2\sigma$ regions. Additionally, each sub-figure displays the GP reconstruction with an $H_0$ prior included with the original datasets. The figures also feature the $\Lambda$CDM curve, which serves as a reference point for the analysis.

From Tables 4.1 through 4.4, it can be observed that the lower values of $H_0$ are generally produced by the Squared-Exponential kernel. Conversely, the CC data consistently yields the highest reconstructed values of the Hubble constant. This outcome is due to the fact that the CC data is situated at lower redshifts, which tends to push $H_0$ to higher values. It

| Data set(s) | $H_0$ | $d(H_0, H_0^{\rm R19})$ | $d(H_0, H_0^{\rm TRGB})$ | $d(H_0, H_0^{\rm HW})$ | $d(H_0, H_0^{\rm P18})$ |
|---|---|---|---|---|---|
| CC | $67.539 \pm 4.772$ | $-1.303$ | $-0.440$ | $-1.133$ | 0.0290 |
| CC+SN | $67.001 \pm 1.653$ | $-3.225$ | $-1.118$ | $-2.616$ | $-0.230$ |
| CC+SN+BAO | $66.197 \pm 1.463$ | $-3.847$ | $-1.512$ | $-3.113$ | $-0.777$ |
| CC+R19 | $73.782 \pm 1.374$ | $-0.1255$ | 1.710 | 0.216 | 4.364 |
| CC+SN+R19 | $72.022 \pm 1.075$ | $-1.127$ | 1.026 | $-0.622$ | 3.896 |
| CC+SN+BAO+R19 | $71.180 \pm 1.024$ | $-1.627$ | 0.644 | $-1.047$ | 3.315 |
| CC+TRGB | $69.604 \pm 1.755$ | $-1.959$ | $-0.076$ | $-1.490$ | 1.207 |
| CC+SN+TRGB | $68.468 \pm 1.221$ | $-2.965$ | $-0.594$ | $-2.264$ | 0.809 |
| CC+SN+BAO+TRGB | $67.811 \pm 1.147$ | $-3.407$ | $-0.903$ | $-2.623$ | 0.328 |
| CC+HW | $72.966 \pm 1.663$ | $-0.486$ | 1.261 | $-0.138$ | 3.204 |
| CC+SN+HW | $70.850 \pm 1.199$ | $-1.711$ | 0.471 | $-1.155$ | 2.655 |
| CC+SN+BAO+HW | $69.911 \pm 1.127$ | $-2.271$ | 0.050 | $-1.628$ | 2.035 |

Table 4.1: GP reconstructions of $H_0$ (in km/s/Mpc units) for the various datasets and prior combinations for the square exponential kernel function of Eq. 3.9. The last 4 columns show the distance (in units of $\sigma$) between $H_0$ and literature priors.

| Data set(s) | $H_0$ | $d(H_0, H_0^{\rm R19})$ | $d(H_0, H_0^{\rm TRGB})$ | $d(H_0, H_0^{\rm HW})$ | $d(H_0, H_0^{\rm P18})$ |
|---|---|---|---|---|---|
| CC | $69.396 \pm 5.186$ | $-0.861$ | $-0.073$ | $-0.713$ | 0.383 |
| CC+SN | $67.082 \pm 1.681$ | $-3.156$ | $-1.078$ | $-2.561$ | $-0.181$ |
| CC+SN+BAO | $66.179 \pm 1.471$ | $-3.839$ | $-1.517$ | $-3.114$ | $-0.785$ |
| CC+R19 | $73.802 \pm 1.375$ | $-0.115$ | 1.718 | 0.225 | 4.373 |
| CC+SN+R19 | $72.056 \pm 1.082$ | $-1.105$ | 1.040 | $-0.604$ | 3.904 |
| CC+SN+BAO+R19 | $71.166 \pm 1.027$ | $-1.634$ | 0.637 | $-1.0516$ | 3.294 |
| CC+TRGB | $69.695 \pm 1.760$ | $-1.916$ | $-0.040$ | $-1.452$ | 1.254 |
| CC+SN+TRGB | $68.508 \pm 1.232$ | $-2.936$ | $-0.574$ | $-2.238$ | 0.833 |
| CC+SN+BAO+TRGB | $67.796 \pm 1.151$ | $-3.410$ | $-0.909$ | $-2.627$ | 0.315 |
| CC+HW | $73.003 \pm 1.666$ | $-0.469$ | 1.275 | $-0.122$ | 3.220 |
| CC+SN+HW | $70.892 \pm 1.208$ | $-1.683$ | 0.488 | $-1.132$ | 2.669 |
| CC+SN+BAO+HW | $69.895 \pm 1.132$ | $-2.276$ | 0.043 | $-1.633$ | 2.016 |

Table 4.2: GP reconstructions of $H_0$ (in km/s/Mpc units) for the various datasets and prior combinations for the Cauchy kernel function of Eq. 3.10. The last 4 columns show the distance (in units of $\sigma$) between $H_0$ and literature priors.

| Data set(s) | $H_0$ | $d(H_0, H_0^{\rm R19})$ | $d(H_0, H_0^{\rm TRGB})$ | $d(H_0, H_0^{\rm HW})$ | $d(H_0, H_0^{\rm P18})$ |
|---|---|---|---|---|---|
| CC | $68.434 \pm 5.029$ | $-1.070$ | $-0.254$ | $-0.913$ | 0.204 |
| CC+SN | $66.981 \pm 1.679$ | $-3.204$ | $-1.118$ | $-2.605$ | $-0.239$ |
| CC+SN+BAO | $66.139 \pm 1.472$ | $-3.857$ | $-1.533$ | $-3.131$ | $-0.811$ |
| CC+R19 | $73.777 \pm 1.3760$ | $-0.1279$ | 1.707 | 0.214 | 4.356 |
| CC+SN+R19 | $72.016 \pm 1.082$ | $-1.127$ | 1.022 | $-0.623$ | 3.872 |
| CC+SN+BAO+R19 | $71.148 \pm 1.028$ | $-1.643$ | 0.629 | $-1.060$ | 3.276 |
| CC+TRGB | $69.629 \pm 1.759$ | $-1.946$ | $-0.066$ | $-1.479$ | 1.218 |
| CC+SN+TRGB | $68.457 \pm 1.232$ | $-2.96$ | $-0.597$ | $-2.262$ | 0.795 |
| CC+SN+BAO+TRGB | $67.772 \pm 1.152$ | $-3.422$ | $-0.920$ | $-2.638$ | 0.295 |
| CC+HW | $72.963 \pm 1.666$ | $-0.487$ | 1.259 | $-0.139$ | 3.196 |
| CC+SN+HW | $70.840 \pm 1.208$ | $-1.710$ | 0.465 | $-1.156$ | 2.631 |
| CC+SN+BAO+HW | $69.872 \pm 1.132$ | $-2.288$ | 0.033 | $-1.644$ | 1.996 |

Table 4.3: GP reconstructions of $H_0$ (in km/s/Mpc units) for the various datasets and prior combinations for the Matérn kernel function of Eq. 3.11 The last 4 columns show the distance (in units of $\sigma$) between $H_0$ and literature priors.

| Data set(s) | $H_0$ | $d(H_0, H_0^{\rm R19})$ | $d(H_0, H_0^{\rm TRGB})$ | $d(H_0, H_0^{\rm HW})$ | $d(H_0, H_0^{\rm P18})$ |
|---|---|---|---|---|---|
| CC | $70.672 \pm 5.491$ | $-0.592$ | 0.150 | $-0.456$ | 0.593 |
| CC+SN | $67.099 \pm 1.686$ | $-3.143$ | $-1.069$ | $-2.551$ | $-0.171$ |
| CC+SN+BAO | $66.195 \pm 1.465$ | $-3.839$ | $-1.512$ | $-3.112$ | $-0.778$ |
| CC+R19 | $73.851 \pm 1.376$ | $-0.090$ | 1.739 | 0.247 | 4.404 |
| CC+SN+R19 | $72.081 \pm 1.085$ | $-1.090$ | 1.051 | $-0.591$ | 3.917 |
| CC+SN+BAO+R19 | $71.620 \pm 1.085$ | $-1.348$ | 0.838 | $-0.816$ | 3.532 |
| CC+TRGB | $69.78 \pm 1.763$ | $-1.876$ | $-0.007$ | $-1.415$ | 1.299 |
| CC+SN+TRGB | $68.523 \pm 1.234$ | $-2.926$ | $-0.567$ | $-2.2303$ | 0.843 |
| CC+SN+BAO+TRGB | $67.810 \pm 1.146$ | $-3.407$ | $-0.903$ | $-2.623$ | 0.328 |
| CC+HW | $73.077 \pm 1.668$ | $-0.434$ | 1.304 | $-0.091$ | 3.259 |
| CC+SN+HW | $70.917 \pm 1.211$ | $-1.667$ | 0.499 | $-1.119$ | 2.683 |
| CC+SN+BAO+HW | $69.911 \pm 1.128$ | $-2.271$ | 0.050 | $-1.628$ | 2.034 |

Table 4.4: GP reconstructions of $H_0$ (in km/s/Mpc units) for the various datasets and prior combinations for the rational quadratic kernel function of Eq. 3.12. The last 4 columns show the distance (in units of $\sigma$) between $H_0$ and literature priors.

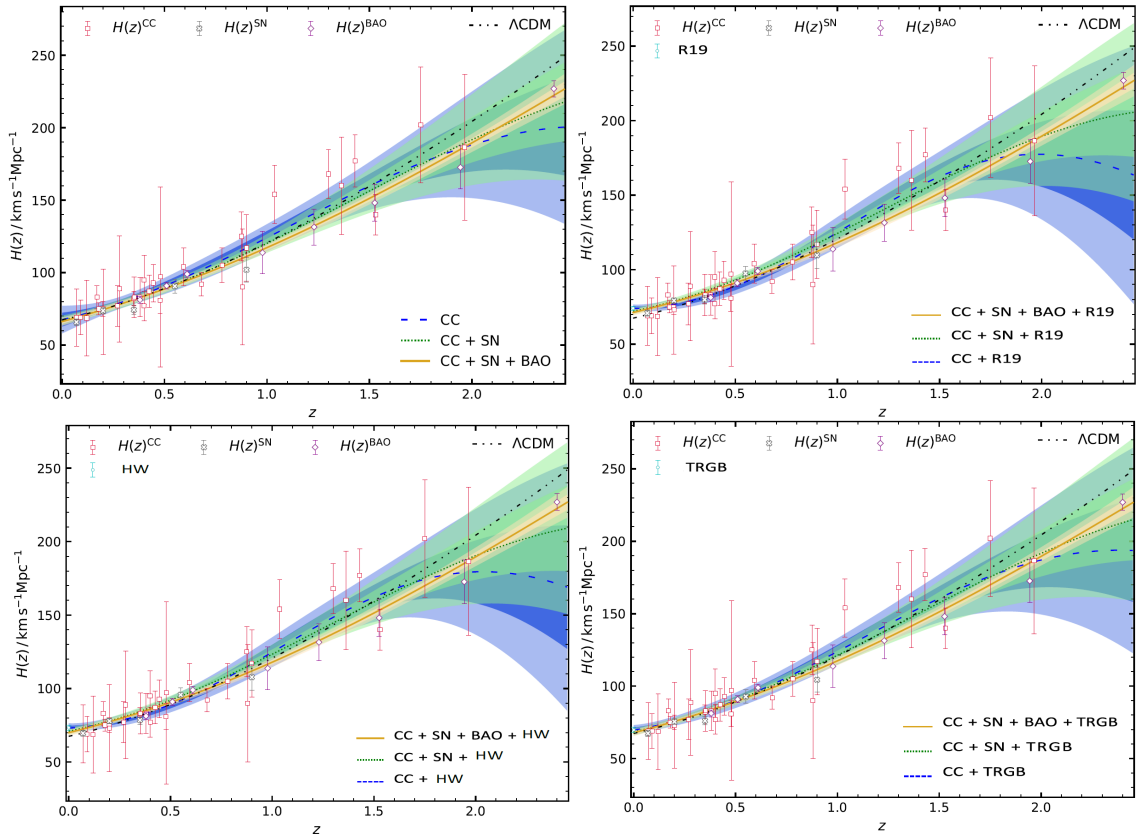


Figure 4.1: GP reconstruction of $H(z)$ using the square exponential kernel function in Eq. 3.9. For each panel a different $H_0$ prior is used for the different combinations of datasets.

can also be noticed that the errors, in this case are higher than those with combined datasets and this emerges due to the low number of data points this dataset has. Nonetheless, the $H_0$ results fall within the $1\sigma$ confidence band for all cases and kernel choices. The R19 prior results in the highest measurements of the Hubble constant, with the highest value achieved using the Rational Quadratic kernel on the CC data alone. This is because the R19 prior represents the highest measurement of $H_0$ considered. The HW prior produces results that are similar but slightly lower compared to those obtained with the R19 prior, as the prior values are close.

In contrast, the BAO data, which is situated at higher redshifts, favours lower Hubble constants. For all priors and kernels, the BAO data reduces the reconstructed value of $H_0$. Excluding the no-prior condition, the lowest values of $H_0$ with a prior are found for the combination CC + SN + BAO along with the TRGB prior, which is expected since the TRGB prior is the lowest value considered among the three priors. In fact, this prior exhibits the least tension with the Planck Collaboration's Hubble constant measurement.

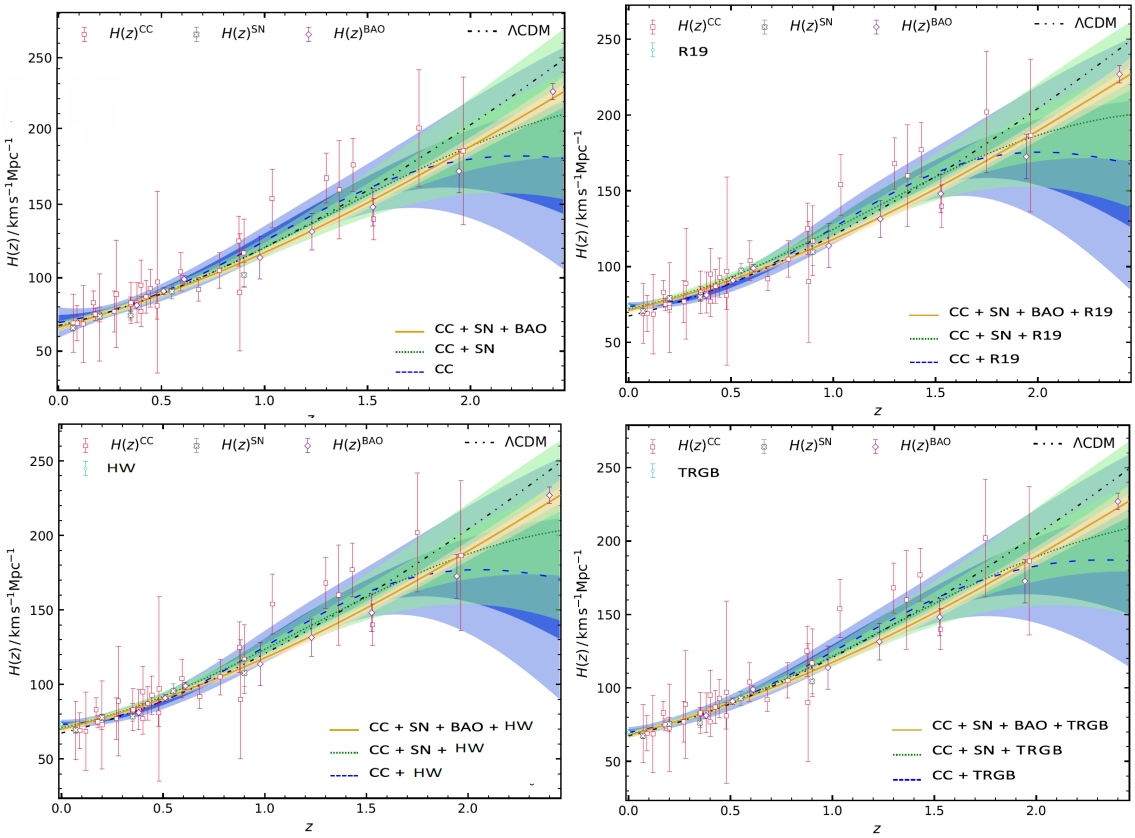


Figure 4.2: GP reconstruction of $H(z)$ using the Cauchy kernel function in Eq. 3.10. For each panel a different $H_0$ prior is used for the different combinations of datasets.

Figure 4.1 presents the reconstruction of the Hubble function for the Squared-Exponential kernel across the entire redshift range covered by the dataset. In all instances, the $1\sigma$ and $2\sigma$ uncertainties are reduced at higher redshifts when the BAO dataset is included. This reduction is attributable to the fact that the BAO data pertains to high-redshift points, which favours smaller uncertainties in this regime. Indeed, in the cases of CC and CC + SN, the ΛCDM line diverges from the $1\sigma$ uncertainty region at high redshifts and only deviates from the $2\sigma$ region when the BAO data is included. This deviation is anticipated as the BAO data is dependent on the cosmological model, whereas the other two datasets are independent. For the remaining redshift ranges, the reconstructed Hubble rate remains close to the ΛCDM line. This feature will be further examined in the diagnostic tests that follow this analysis.

For the remaining kernels—Cauchy, Matérn, and Rational Quadratic—the GP reconstructions exhibit behaviour similar to that of the Squared-Exponential kernel and are consistent with each other within $1\sigma$ confidence levels. A key aspect of this analysis is the model independence of the GP reconstructions. While the choice of covariance model does

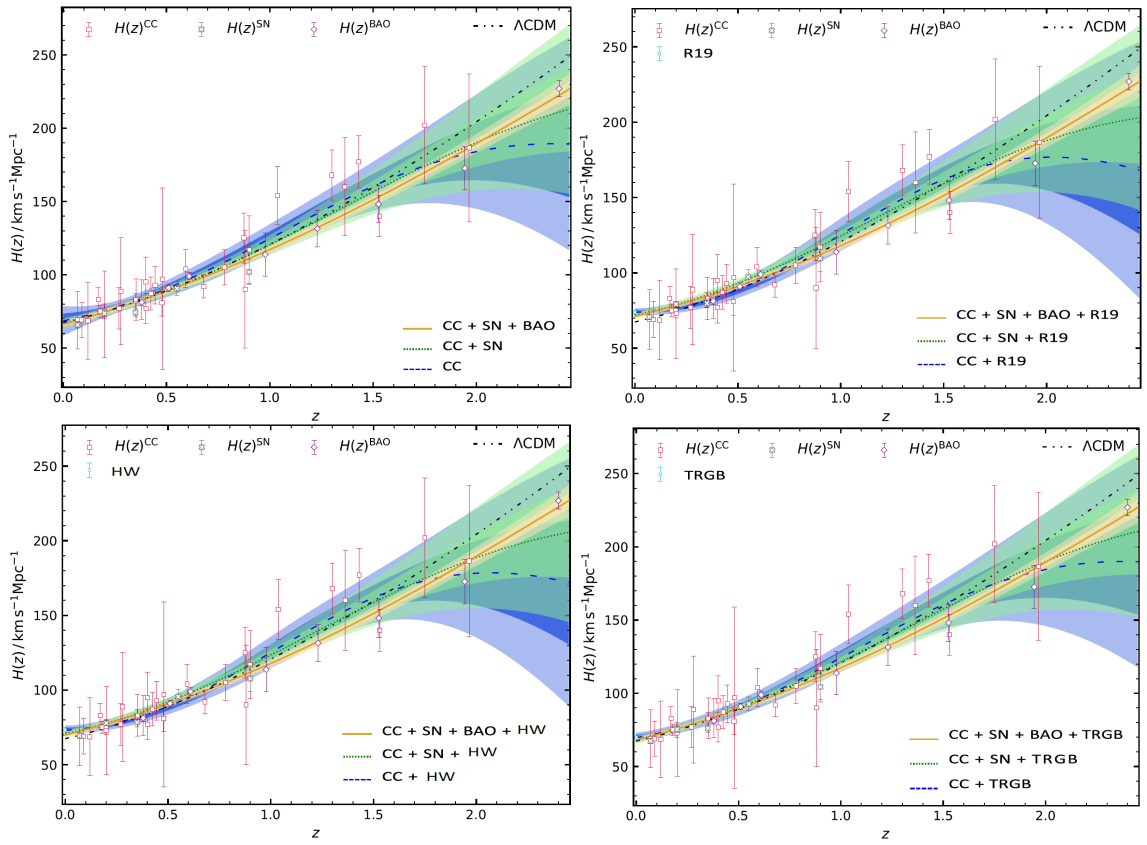


Figure 4.3: GP reconstruction of $H(z)$ using the Matérn kernel function in Eq. 3.11. For each panel a different $H_0$ prior is used for the different combinations of datasets.

influence the reconstructions, the impact is minimal.

### 4.1.1 | Diagnostic Tests

The results from the previous sections provided comprehensive insights into the reconstructions of the Hubble parameter $H(z)$ across various datasets and kernels. The GP approach, applied to different combinations of cosmic data, yielded reconstructions of $H_0$ and illustrated how the choice of kernel and prior influences the derived values. While the results showed a general agreement with the ΛCDM model, there were noteworthy variations depending on the data sources and the priors used. To further investigate the consistency of these reconstructions with the ΛCDM paradigm, diagnostic tests are employed. These tests offer a means to quantitatively evaluate how well the reconstructed models align with the predictions of ΛCDM and test the statistical strength of deviations from ΛCDM. In the subsequent analysis, the Equation of State (EoS) together with the consistency test $\mathcal{O}_m^{(1)}(z)$ and its derivative $\mathcal{L}^{(1)}(z)$ will be utilised to rigorously assess the fit of the reconstructed Hubble

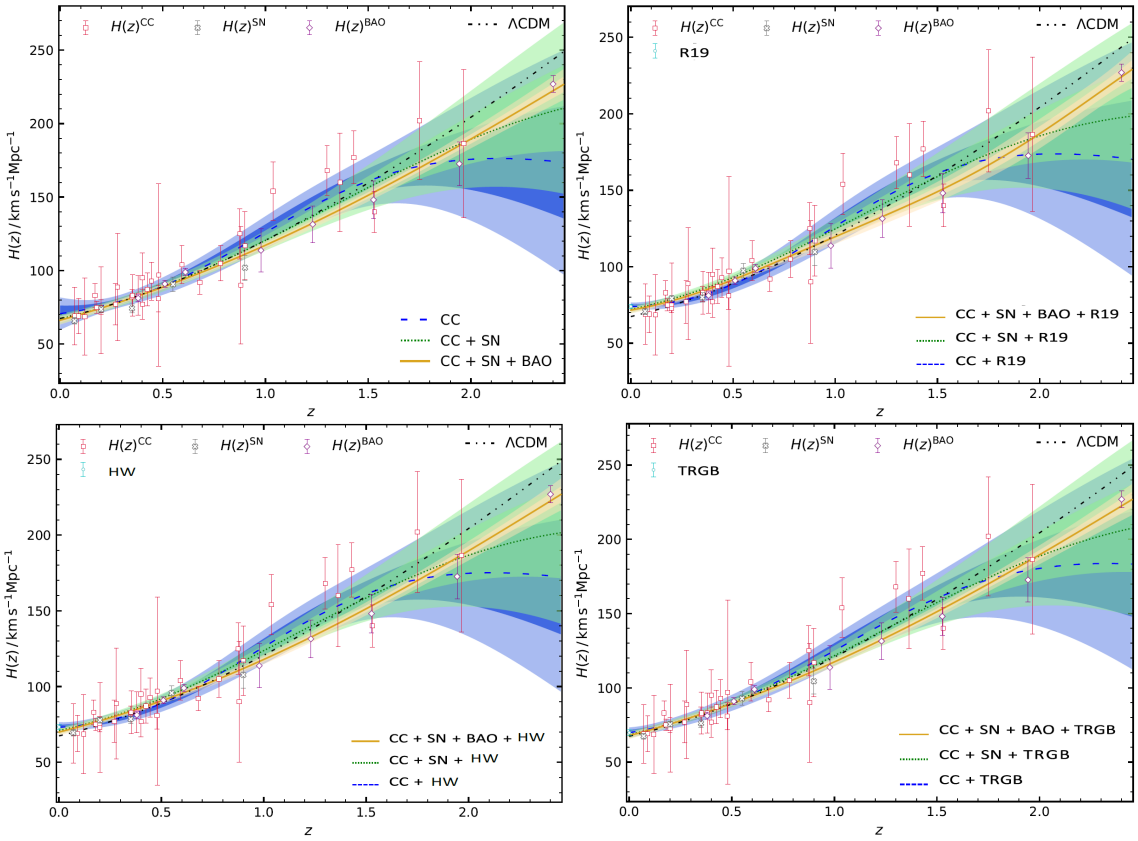


Figure 4.4: GP reconstruction of $H(z)$ using the rational quadratic kernel function in Eq. 3.12. For each panel a different $H_0$ prior is used for the different combinations of datasets.

parameter to the standard cosmological model [261, 262]. This approach will provide additional insights into the validity of the ΛCDM model in light of the reconstructed data and highlight any discrepancies that may suggest alternative cosmological scenarios.

Considering the GR Friedmann equation for a cosmos filled with a evolving dark fluid EoS

$$\frac{H^2(z)}{H_0^2} = \Omega_m^0\,(1+z)^3 + \Omega_k^0\,(1+z)^2 + \Omega_\Lambda^0 \exp\left[3\int_0^z \frac{1+w(z')}{1+z'}\mathrm{d}z'\right], \tag{4.2}$$

which can be rearranged to reconstruct the EoS of the dark fluid via

$$w(z) = \frac{2(1+z)E(z)E'(z) - 3E^2(z)}{3\left[E^2(z) - \Omega_m^0(1+z)^3\right]}, \tag{4.3}$$

The GP reconstructions plots of $w(z)$ can be found in Appendix A in Figs. A.1 andA.2. It is clear that $w = -1$ is not excluded by the currently available data, however, it is important to point out that this reconstruction is dependent on the matter density parameter, which restricts the construction of physical models.

On the other hand, one effective diagnostic tool is the consistency test for the flat ΛCDM model, which is formulated using the following diagnostic redshift function

$$\mathcal{O}_m^{(1)}(z) := \frac{E^2(z) - 1}{z(3 + 3z + z^2)}\,. \tag{4.4}$$

This diagnostic function is derived from the Friedmann equation specifically for the ΛCDM cosmological model. In deriving this, it is assumed that the contribution from radiation density, characterised by $\Omega_{r,0}$, is negligible at late cosmic times.

For the ΛCDM model, Eq. (4.4) simplifies to $\mathcal{O}_m^{(1)}(z) = \Omega_{m,0}$, where $\Omega_{m,0}$ denotes the current matter density parameter. This simplification serves as a null test of the ΛCDM model. Deviations of $\mathcal{O}_m^{(1)}(z) \neq \Omega_{m,0}$ indicate a potential falsification of the flat ΛCDM model. The reconstructed values of $\mathcal{O}_m^{(1)}(z)$ using the GP approach are detailed in Appendix A. Figs. A.3 through A.4 illustrate that the observational datasets generally align well with the predictions of the ΛCDM model. Nonetheless, a significant observation is the pronounced effect of the $H_0$ priors on this reconstruction. When $H_0$ priors are included, the reconstructed $\mathcal{O}_m^{(1)}(z)$ deviates more noticeably from the ΛCDM model, which raises questions about the robustness of the standard cosmological model.

To further explore these deviations, the evolution of $\mathcal{O}_m^{(1)}(z)$ with redshift by analysing its derivative is considered. This provides a more nuanced diagnostic tool

$$\mathcal{L}^{(1)}(z) = 3(1 - E^2(z))(1 + z)^2 + 2z(3 + 3z + z^2)E(z)E'(z)\,, \tag{4.5}$$

where $\mathcal{L}^{(1)}(z)$ denotes the derivative of $\mathcal{O}_m^{(1)}(z)$ with respect to redshift $z$.

The function $\mathcal{L}^{(1)}(z)$ is zero if and only if $\frac{\mathrm{d}\mathcal{O}_m^{(1)}(z)}{\mathrm{d}z} = 0$. Any deviation from $\mathcal{L}^{(1)}(z) = 0$ indicates a departure from the ΛCDM model. Figures A.5 through A.6 in Appendix A, display the reconstructed values of $\mathcal{L}^{(1)}(z)$, which continue to corroborate the previous analyses. Notably, these figures reveal significant deviations from zero, underscoring potential discrepancies with the ΛCDM model and highlighting areas where the model's predictions may not align with observed data.

### 4.1.2 | Transition Redshift

In the preceding analysis, the GP approach was employed to reconstruct the Hubble rate of the Universe across its evolutionary history. While the primary focus was on determining the Hubble constant via GP analysis, another significant parameter that warrants attention is the transition redshift $z_t$. This parameter denotes the redshift at which the transition from a decelerating to an accelerating expansion of the cosmos occurs [263]. The transition redshift is crucial as it offers insights into the nature of dark energy and its evolution over time.

Furthermore, it can provide valuable information regarding the changing ratio of matter to dark energy throughout cosmic history [264].

To understand this transition, consider the deceleration parameter $q(z)$, which is a dimensionless quantity that quantifies the rate of acceleration of the Universe. As defined in Eq. 2.30, it can be expressed as:

$$q(z) = (1+z)\frac{H'(z)}{H(z)} - 1\,. \tag{4.6}$$

Here, $'$ denotes differentiation with respect to $z$ [35]. The transition redshift $z_{\rm t}$ corresponds to the value of $z$ at which $q(z)$ transitions from positive to negative. This transition signifies a shift from decelerated to accelerated expansion, as a positive $\ddot{a}$ (the second derivative of the scale factor $a$) characterises an accelerating Universe, making $q(z)$ negative (as defined in Eq, 2.30). Consequently, for a flat FLRW cosmology, the transition redshift can be defined by the equation [265]:

$$z_{\rm t} = \left[\frac{2\,(1-\Omega_{m,0})}{\Omega_{m,0}}\right]^{1/3} - 1\,. \tag{4.7}$$

According to the Planck Collaboration 2018, the transition redshift is approximately $z_t \sim 0.63$ [16]. Given that the GP approach has been utilised to reconstruct $H(z)$ throughout cosmic history, it is also feasible to use the GP method to reconstruct $q(z)$ and thereby infer a value for $z_t$ beyond the indicative $\Lambda$CDM value. The reconstructions of $q(z)$ are depicted in Appendix A in Figures A.7 through A.8. Additionally, the reconstructed results for $z_t$ corresponding to each kernel function, for the various datasets and prior combinations, are presented in Table 4.5.

Tables 4.1 through 4.4 reveal that the highest values of $H_0$ are obtained from the CC dataset. Conversely, Table 4.5 indicates that this dataset generally yields the lowest values for $z_t$, suggesting that a higher Hubble constant corresponds to a lower redshift at which the acceleration of the Universe transitions. Specifically, the CC+PN and CC+PN+BAO datasets, which produce $H_0$ values in descending order, also result in ascending $z_t$ values, as the transition to accelerated expansion occurs closer to the present day. Notably, the lowest transition redshift is associated with the CC dataset, particularly when the Riess prior (R19) is applied, as this prior results in the highest $H_0$. The HW prior leads to the next lowest $z_t$ values, while the TRGB prior produces the highest values of $z_t$, which is consistent with the expected hierarchy of these priors (HW $>$ TRGB).

| Data set(s) | $z_t$ | | | |
|---|---|---|---|---|
| | Square exponential | Cauchy | Matérn | Rational quadratic |
| CC | $0.616^{+\text{nan}}_{-0.137}$ | $0.572^{+0.267}_{-0.118}$ | $0.591^{+\text{nan}}_{-0.129}$ | $0.553^{+0.211}_{-0.110}$ |
| CC+SN | $0.607^{+0.132}_{-0.084}$ | $0.600^{+0.132}_{-0.087}$ | $0.605^{+0.131}_{-0.089}$ | $0.598^{+0.133}_{-0.088}$ |
| CC+SN+BAO | $0.667^{+0.095}_{-0.075}$ | $0.658^{+0.105}_{-0.081}$ | $0.659^{+0.108}_{-0.082}$ | $0.664^{+0.101}_{-0.079}$ |
| CC+R19 | $0.551^{+0.112}_{-0.079}$ | $0.540^{+0.114}_{-0.081}$ | $0.546^{+0.115}_{-0.082}$ | $0.528^{+0.114}_{-0.082}$ |
| CC+SN+R19 | $0.702^{+0.246}_{-0.112}$ | $0.687^{+0.268}_{-0.114}$ | $0.694^{+0.263}_{-0.116}$ | $0.679^{+\text{nan}}_{-0.114}$ |
| CC+SN+BAO+R19 | $0.783^{+0.107}_{-0.088}$ | $0.770^{+0.119}_{-0.095}$ | $0.772^{+0.123}_{-0.097}$ | $0.783^{+0.118}_{-0.095}$ |
| CC+TRGB | $0.573^{+0.165}_{-0.096}$ | $0.552^{+0.161}_{-0.099}$ | $0.564^{+0.167}_{-0.102}$ | $0.537^{+0.159}_{-0.098}$ |
| CC+SN+TRGB | $0.633^{+0.149}_{-0.091}$ | $0.624^{+0.148}_{-0.094}$ | $0.629^{+0.148}_{-0.094}$ | $0.622^{+0.148}_{-0.094}$ |
| CC+SN+BAO+TRGB | $0.703^{+0.099}_{-0.079}$ | $0.693^{+0.109}_{-0.085}$ | $0.695^{+0.112}_{-0.087}$ | $0.699^{+0.106}_{-0.084}$ |
| CC+HW | $0.556^{+0.120}_{-0.083}$ | $0.544^{+0.122}_{-0.085}$ | $0.551^{+0.124}_{-0.087}$ | $0.531^{+0.121}_{-0.085}$ |
| CC+SN+HW | $0.679^{+0.196}_{-0.104}$ | $0.666^{+0.197}_{-0.107}$ | $0.671^{+0.200}_{-0.108}$ | $0.661^{+0.201}_{-0.107}$ |
| CC+SN+BAO+HW | $0.752^{+0.106}_{-0.085}$ | $0.740^{+0.116}_{-0.091}$ | $0.743^{+0.119}_{-0.094}$ | $0.745^{+0.113}_{-0.091}$ |

Table 4.5: Values of $z(t)$ obtained from the GP reconstructions of $q(z)$ for the different kernel functions and the different datasets and priors combinations.

## 4.2 | Reconstruction of $f(T)$ gravity

In the preceding section, the GP approach was utilised to reconstruct observational data pertaining to the Hubble rate, $H(z)$, together with some diagnostic tests. This reconstructed data will now be employed to formulate a data-driven $f(T)$ cosmological model. Specifically, the model-independent data obtained from the GP reconstruction will be integrated with a theoretical framework governed by $f(T)$ gravity, without assuming a particular form for the arbitrary Lagrangian as specified in Eq. 2.51.

The critical aspect of relating the reconstructed $H(z)$ with the $f(T)$ cosmological dynamics involves the connection between $H(z)$ and the torsion scalar $T$. As stated in Chapter 2, this chapter adopts the convention $T = 6H^2$, which is commonly used in the literature to align with the metric signature $(-,+,+,+)$ [266]. Alternatively, the convention $T = -6H^2$, can also be employed arising from a different choice of metric signature, as seen in previous sections and as will be employed in the next chapters.

It is important to emphasize that at the level of the Friedmann equations, both conventions yield equivalent results. Specifically, at the level of the Hubble parameter $H$, these

equations remain unchanged under either choice of $T$, ensuring consistency. This equivalence is well-established in the literature (Ref. [66]), where the Friedmann equations after evaluating the field equations under the above mentioned metric signature are expressed as

$$H^2 = \kappa^2 \left(\rho_{\rm m} + \tfrac{T}{3} f_T - \tfrac{f}{6}\right), \tag{4.8}$$

$$2\dot{H} = -\tfrac{\kappa^2(p_{\rm m}+\rho_{\rm m})}{1-f_T-2Tf_{TT}}, \tag{4.9}$$

In contrast, when the convention $T = -6H^2$ is adopted, the Friedmann equations are expressed as in Eqs. 2.56,2.57. Therefore, both formulations lead to identical expressions at the level of the Hubble parameter $H$, demonstrating that the choice of sign for $T$ does not alter the cosmological dynamics or the resulting physical predictions.

Consequently, the cosmological dynamics within the $f(T)$ framework can be expressed in terms of $H(z)$ and its derivatives, both of which were reconstructed in the prior section. The initial step toward achieving this goal involves expressing all $f(T)$ cosmological equations, including the Friedmann equation Eq. 2.56, in terms of redshift. To facilitate this, the $f(T)$ derivative in the modified Friedmann Equation, Eq. 2.56, must first be converted into a form that depends solely on redshift. This is achieved using the following relation, in order to convert the first derivative of $f$ w.r.t $T$

$$f_T = \frac{\mathrm{d}f/\mathrm{d}z}{\mathrm{d}T/\mathrm{d}z} = \frac{f'(z)}{T'(z)}, \tag{4.10}$$

where the redshift derivatives are defined as $f'(T) = \mathrm{d}f/\mathrm{d}z$ and $T'(z) = 12HH'$. To further elaborate, $f'(z)$ needs to be approximated because there is no explicit equation available to determine it directly. In this case, the central differencing method is employed to approximate $f'(z)$. One key benefit is that central differencing converges faster, providing a more accurate approximation of the derivative with fewer grid points. This is due to its higher-order accuracy, typically second-order ($\mathcal{O}(\Delta z^2)$), compared to the first-order accuracy of forward and backward ($\mathcal{O}(\Delta z)$), where $\Delta z = z_{i+1} - z_{i-1}$ [267]. Therefore, by central differencing method

$$f'(z_i) \simeq \frac{f(z_{i+1}) - f(z_{i-1})}{z_{i+1} - z_{i-1}}. \tag{4.11}$$

By utilising the modified Friedmann equation, Eq. 2.56, the numerical propagation equation for $f(z)$ is derived as follows

$$f(z_{i+1}) = f(z_{i-1}) + 2\,(z_{i+1} - z_{i-1})\,\frac{H'(z_i)}{H(z_i)}\left(3H^2(z_i) + \frac{f(z_i)}{2} - 3H_0^2\Omega_{m,0}\,(1+z_i)^3\right). \tag{4.12}$$

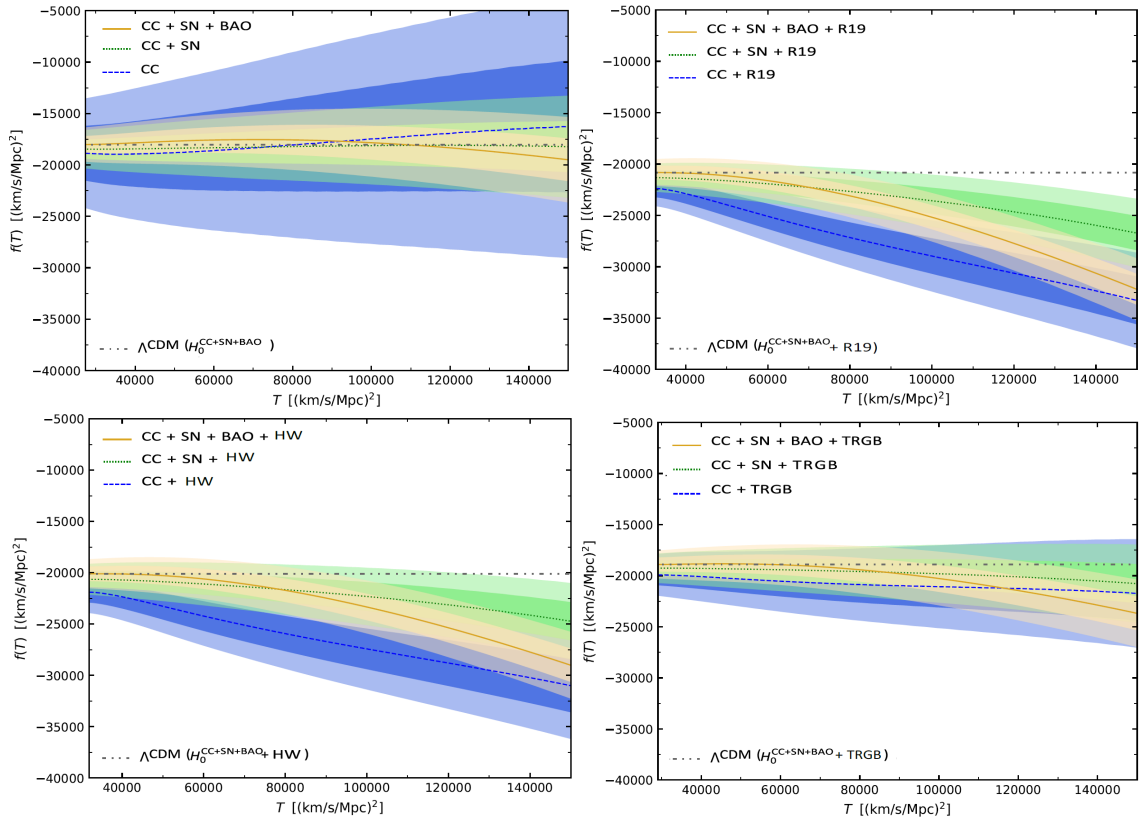


Figure 4.5: Propagation of the $f(T)$ function obtained using the Hubble parameter reconstructed with the square exponential kernel function of Eq. 3.9. Each panel displays a different $H_0$ for the different combinations of datasets.

In this equation, $H_0$ and $\Omega_{m,0}$ are taken from the previous GP reconstructions, corresponding to various datasets and $H_0$ priors. However, Eq. 4.12 necessitates two boundary conditions, which are established as follows

1. First Boundary Condition: This is obtained by evaluating the modified Friedmann equation Eq. 2.56 at $z = 0$, resulting in

$$f(z = 0) \simeq 6H_0^2 \left(\Omega_{m,0} - 1\right) , \tag{4.13}$$

   This assumption assumes that at the current time, ΛCDM is the dominant cosmological model, suggesting $f_T(z = 0) \simeq 0$. It is noteworthy that this boundary condition depends on the same parameters as those used in the propagation equation.

2. Second Boundary Condition: This condition is required because the propagation equation depends on both $z_{i-1}$ and $z_i$. To determine this, the forward differencing method

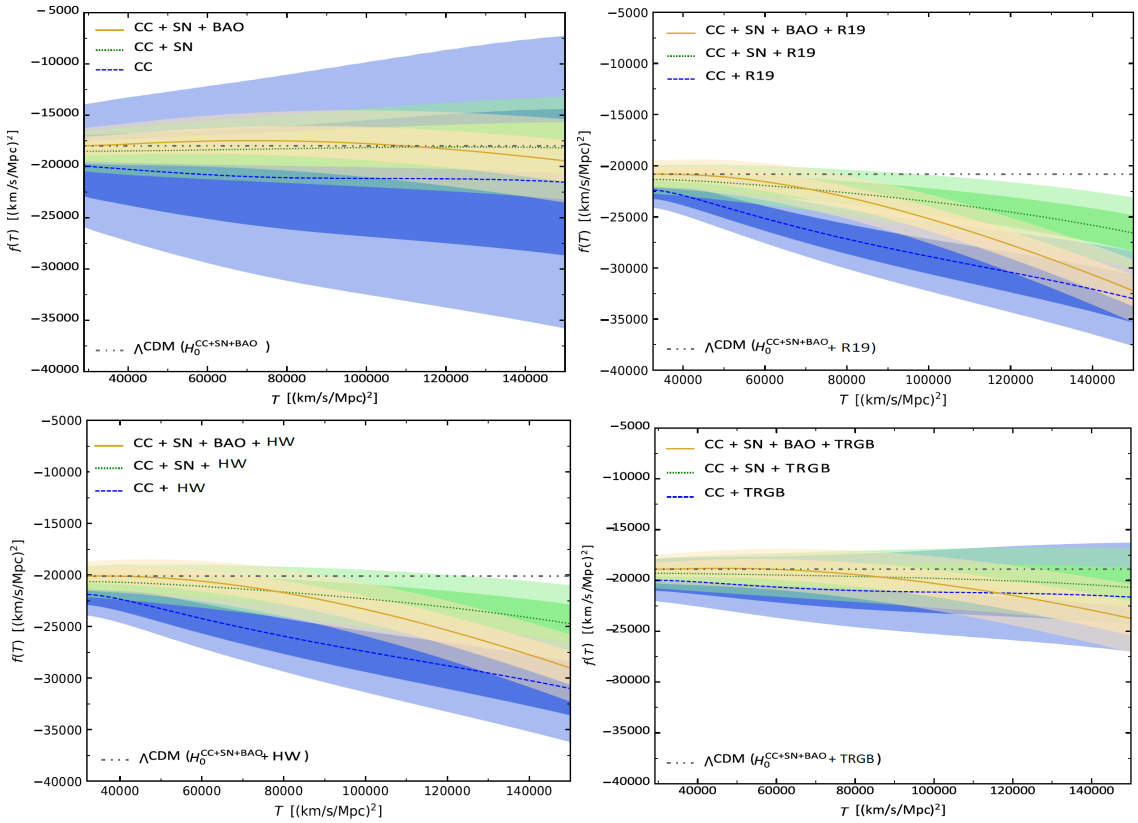


Figure 4.6: Propagation of the $f(T)$ function obtained using the Hubble parameter reconstructed with the Cauchy kernel function of Eq. 3.10. Each panel displays a different $H_0$ for the different combinations of datasets.

is used [267], leading to

$$f'(z_i) \simeq \frac{f(z_{i+1}) - f(z_i)}{z_{i+1} - z_i} \,. \tag{4.14}$$

By applying the Friedmann equation to Eq. 4.14, the following equation is obtained for the second boundary condition

$$f(z_{i+1}) = f(z_i) + 6\,(z_{i+1} - z_i)\,\frac{H'(z_i)}{H(z_i)}\left[H^2(z_i) + \frac{f(z_i)}{6} - H_0^2\Omega_{m,0}\,(1+z_i)^3\right] . \tag{4.15}$$

To ensure thoroughness, the propagation of $f(T)$ functions is accompanied by $1\sigma$ and $2\sigma$ uncertainty regions, determined through the Monte Carlo routine described previously.

With the propagation equation in Eq. 4.12 and the specified boundary conditions, $f(T)$ can be determined as a function of the redshift $z$, enabling the construction of $f(z)$ in a model-independent manner. Moreover, the torsion scalar $T$ can be related to the redshift $z$

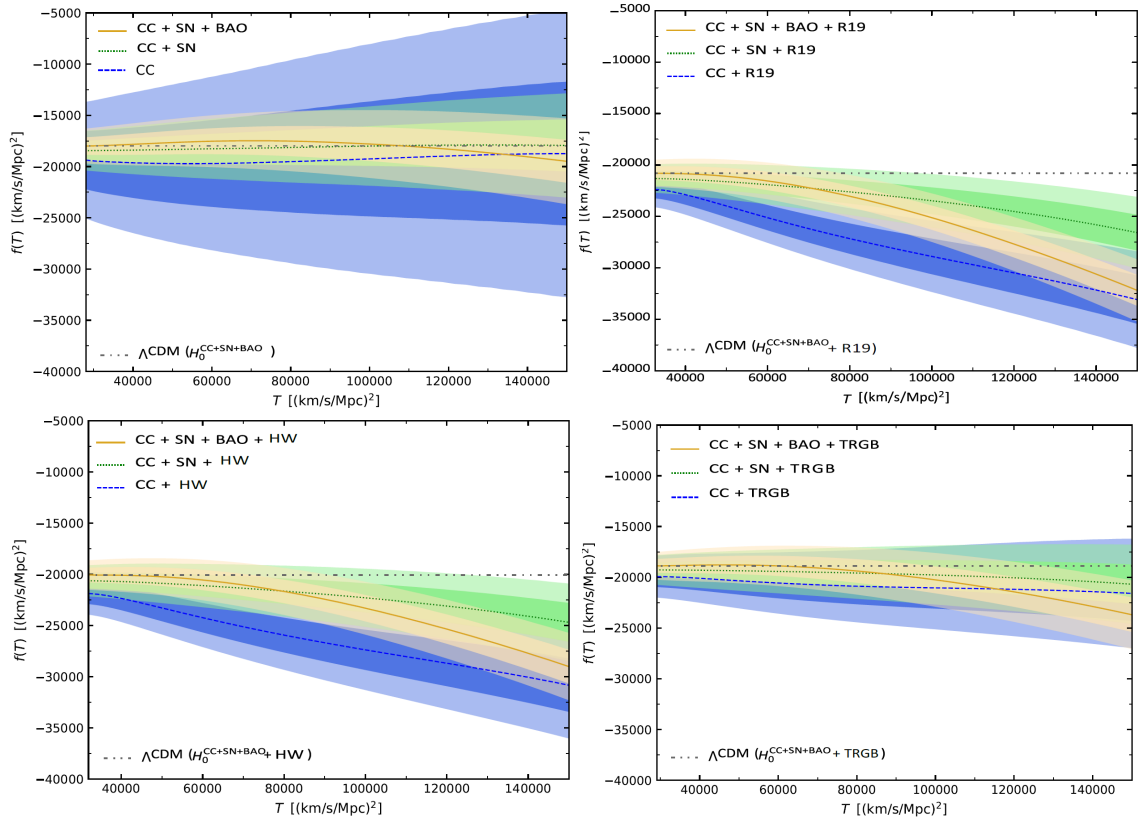


Figure 4.7: Propagation of the $f(T)$ function obtained using the Hubble parameter reconstructed with the Matérn kernel function of Eq. 3.11. Each panel displays a different $H_0$ for the different combinations of datasets.

using the equation $T = 6H^2(z)$. Thus, $f(T)$ can be expressed as a function of $T$, allowing for the creation of plots depicting $f(T)$ against $T$ for each kernel and for the various datasets and prior combinations, as illustrated in Figs. 4.5-4.8. Each plot is accompanied by $1\sigma$ and $2\sigma$ uncertainty regions. Additionally, a ΛCDM reference line is included, which corresponds to $f(T) \to 6H_0^2(\Omega_{m,0} - 1)$.

By and large, the ΛCDM scenario remains within the reconstructed regions for all choices of kernel, dataset, and prior combination. However, analysis of Figs. 4.5-4.8 reveals that the $f(T)$ reconstruction functions exhibit a slight decreasing trend with $T$, suggesting negative values of $f'(T)$. This result is significant and should be considered when developing $f(T)$ models.

The first panel of each figure in Figs. 4.5-4.8 presents the reconstructions for each dataset without priors, according to each kernel. Over the entire redshift range, ΛCDM remains primarily within the $1\sigma$ confidence region and consistently within the $2\sigma$ region. Notably, the $f(T)$ line derived from the Hubble parameter, including the BAO dataset, is observed

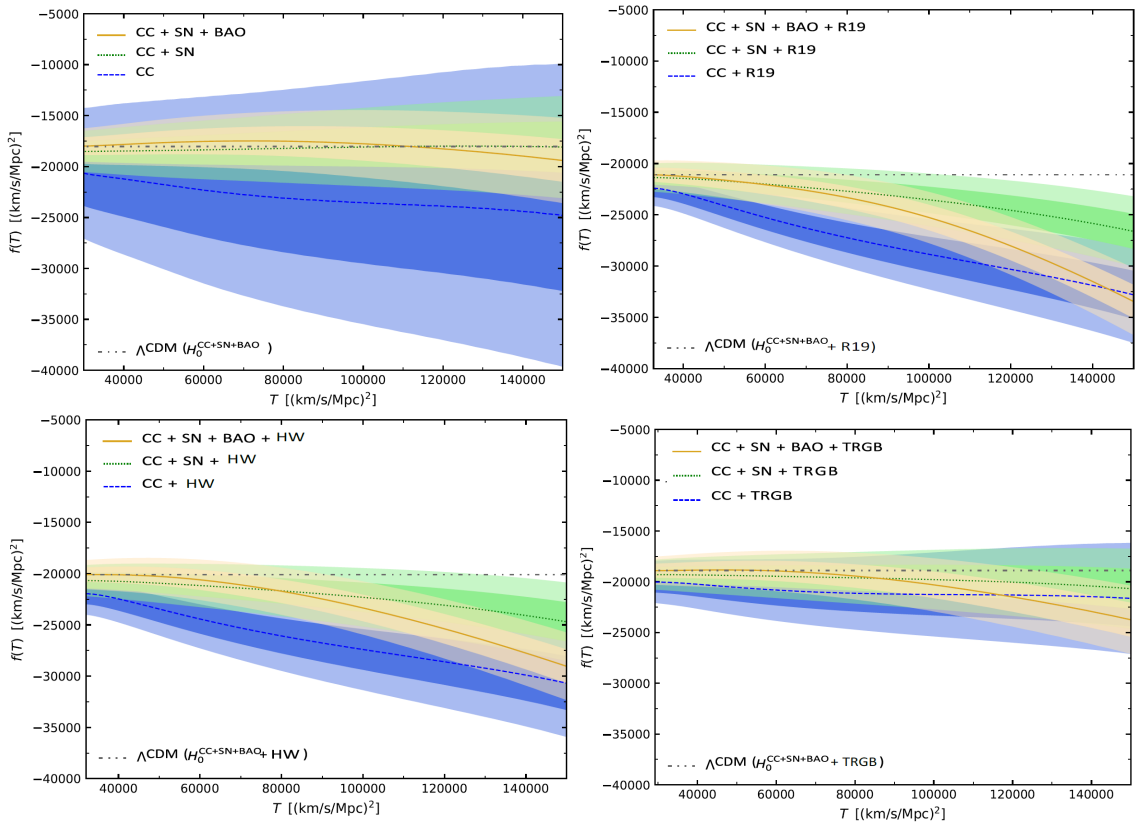


Figure 4.8: Propagation of the $f(T)$ function obtained using the Hubble parameter reconstructed with the rational quadratic kernel function of Eq. 3.12. Each panel displays a different $H_0$ for the different combinations of datasets.

to be the furthest from the ΛCDM line. When priors are incorporated, the propagation line exhibits a more pronounced negative slope, especially for the R19 prior, and to a lesser extent for the HW prior. Conversely, the TRGB prior has minimal effect on the propagation.

Overall, when no priors are included, $f(T)$ deviates only slightly from ΛCDM throughout the examined cosmic evolution. However, the inclusion of priors leads to a more notable divergence of the propagated $f(T)$ line from ΛCDM. This trend is consistent across the kernels analysed, further reinforcing the conclusion that $f(T)$ exhibits a slight deviation from the ΛCDM model within the probed redshift range.

## 4.3 | Conclusion

In this work, the GP approach has been effectively utilised to reconstruct key cosmological parameters, such as the Hubble constant $H_0$, which has been a focal point of exten-

sive scrutiny in modern cosmology. The application of the GP method provided a model-independent reconstruction of the $f(T)$ Lagrangian, distinguishing this analysis from previous studies that relied on predefined forms for the functions involved. By avoiding any initial assumptions about the functional form, this work allowed for the construction of theories extending beyond the ΛCDM model in a flexible and unbiased manner.

To apply this technique to $f(T)$ gravity, the Hubble function was first reconstructed using the GP method, applied to observational datasets from the CC, PN, and BAO methods, combined with three different $H_0$ priors. This resulted in the reconstruction of $H(z)$ and its derivatives across the redshift range of the datasets considered. Since the Friedmann equations in $f(T)$ gravity can be expressed in terms of $H(z)$ and its derivatives, the reconstructed $H(z)$ functions were employed to model $f(T)$ in a model-independent way.

The investigation included four different kernels to assess potential dependencies on the statistical model. Results showed that, within the $1\sigma$ confidence region, these kernels were consistent with each other, as detailed in Tables 4.1-4.4. The CC+SN+BAO datasets provided the most conservative estimates of $H_0$, which was expected due to the dependence of the BAO dataset on the ΛCDM model. Conversely, the highest $H_0$ values were obtained with the CC dataset alone, and the R19 prior yielded the highest values among the priors considered.

Diagnostic tests for the ΛCDM model revealed that while the reconstructions were consistent within the $1\sigma$ confidence region at low redshifts, deviations emerged at higher redshifts. Notably, the transition redshift, indicating the point at which the Universe shifted from a decelerating to an accelerating phase, was inferred from the deceleration parameter. This transition, along with the equation of state for dark energy detailed in Appendix A, highlights the dynamic evolution of the Universe.

The relationship between the Hubble function and the torsion scalar enabled the reconstruction of $f(T)$. With the necessary propagation equations and boundary conditions established, $f(T)$ was expressed as a function of $T$. The results demonstrated that the ΛCDM model lies within the reconstructed regions, although a slight trend for $f(T)$ to decrease with $T$, particularly at higher redshifts, was observed. This trend should be considered in future $f(T)$ model development.

In transitioning to the next chapter, the focus will shift from the GP approach to the MCMC analysis. While the GP method provided valuable insights into the model-independent reconstruction of $f(T)$, MCMC analysis offers a complementary approach for parameter estimation and model validation. The GP method excels in providing a smooth reconstruction of functions without assuming a specific model form, but it does not directly address the probabilistic evaluation of model parameters against observational data.

MCMC analysis, on the other hand, is well-suited for this purpose. It allows for the

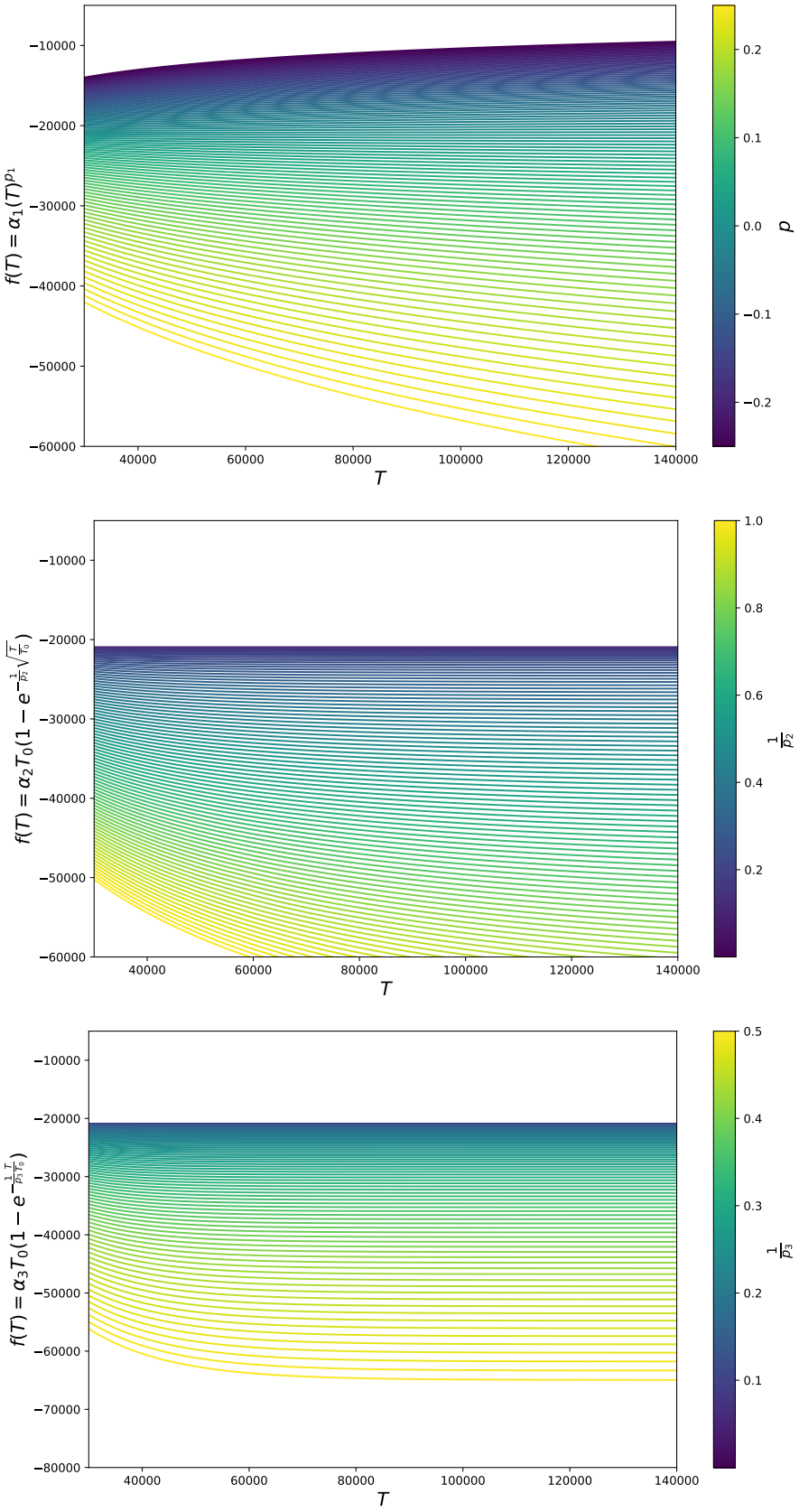


Figure 4.9: Propagation of three $f(T)$ functions –Power Law Model, Linder Model and Variant Model (top to bottom)– as functions of $T$.

exploration of parameter space and the quantification of uncertainties in a probabilistic framework. By applying MCMC techniques, the parameters of various $f(T)$ models can be constrained and thus, assess their viability more rigorously. This approach involves constructing a likelihood function based on observational data and iteratively sampling from the posterior distribution of model parameters. This will enable a detailed examination of how well different $f(T)$ models fit the data and provide insights into the robustness and reliability of the reconstructed function.

Therefore, in addition to the GP-based reconstructions discussed, the forthcoming chapter will delve into the analysis of parameters extracted from various $f(T)$ models (with a $\Lambda$CDM limit), specifically the power law model, the Linder model, and a variant of the Linder model with a varying parameter, as detailed in Sec. 3.4. As outlined in Sec. 3.2, the MCMC analysis requires a specified range of priors to initiate the parameter estimation process and such that the likelihood will explore this range of parameters.

To facilitate this analysis, the aforementioned $f(T)$ models were selected based on their alignment with the reconstructed $f(T)$ functions. Fig. 4.9 illustrates how these three $f(T)$ models vary with the torsion scalar, $T$ and therefore, gives the ability to compare them with the reconstructed functions. The comparison indicates that all three models are consistent with the reconstructed $f(T)$ values, thus providing a strong basis for further exploration. This alignment suggests that these models are promising candidates for a detailed examination through MCMC analysis and also give an indication for the prior range required in the MCMC algorithm.

The MCMC analysis will be instrumental in evaluating which of these models most accurately represents the observed data and in assessing their deviations from the $\Lambda$CDM benchmark. By constraining the model parameters and assessing their fit against observational data, this analysis will offer a comprehensive evaluation of the $f(T)$ models.

In summary, the next chapter will build upon the insights gained from the GP reconstructions by employing MCMC analysis to refine and validate $f(T)$ models. This transition marks a critical step in advancing our understanding of $f(T)$ gravity and its implications for the cosmological evolution of the Universe. The detailed MCMC analysis will provide a thorough assessment of these three $f(T)$ models (and two more which do not have a $\Lambda$CDM limit) and their impact on cosmological dynamics, offering valuable insights into the viability and accuracy of these models.

# 5

# Constraints on viable models of $f(T)$ gravity using late-time observations

The possibility of an observational mismatch in ΛCDM has prompted renewed efforts to determine the current value of the cosmological expansion, aiming to better assess any inconsistencies in the standard model. In modern cosmology, there is a drive for the pursuit of alternative approaches, such as $f(T)$ gravity. These theories aim to create self-consistent models that accurately depict the Universe's history. To this end, possible gravitational models that demonstrate validity are investigated in order to not only understand better the underlying physics, but which also offer insights into resolving, or alleviating the cosmological problems described in more detail in Chapter 2.

To begin, specific TG models will be implemented in numerical code, specifically in MCMC, whose architecture is described in Sec. 3.2. The starting point will be to use the fundamental background equations governing $f(T)$, from which a tailored form of $f(T)$ cosmological models can be deduced. Through the MCMC computational analysis, the opportunity is seized to utilise observational data and thereby, determining the model constraints in an efficient manner. This approach facilitates the study of late-time cosmic acceleration without the need for resorting to exotic components like dark energy. Indeed, in this case $f(T)$ gravity is used to model the effect of a dynamical $\Lambda$ whilst retaining the CDM component of the ΛCDM model.

In the previous chapter, the reconstruction of $f(T)$ gravity was explored to assess its viability in the context of that observational data. In addition, a series of $f(T)$ models were also analysed to assess their fit within the reconstructed $f(T)$ as seen in Fig. 4.9. Building on this, the current chapter extends this analysis to further investigate the same set of $f(T)$ cosmological models in the late-time Universe. These particular forms of $f(T)$ are confronted against late-time observational data such as CC, SNe Ia and BAO, by utilising MCMC code.

In recent years numerous cosmological independent measurements of the current value of Hubble parameter $H_0$ have also emerged, contributing to the growing Hubble tension. In this work, the impact of these priors on core $f(T)$ models is probed to gain a deeper insight into the viable parameter values. To explore the influence of these values of measurements of $H_0$, several background studies are conducted on these $f(T)$ models using various settings, aiming to better discern the impact of priors and $f(T)$ models. The findings of this work were published in Briffa et al. [187].

## 5.1 | Constraints of $f(T)$ late-time cosmology

In this section, five $f(T)$ models as described in Sec. 3.4 are presented on which the MCMC algorithm was implemented by using the observational data described in Sec. 3.3.2. Additionally, these $f(T)$ gravity models are investigated in order to examine the effect of recent cosmology model independent measurements particularly, $H_0$ and $\Omega_{m,0}$. Moreover, the MCMC analysis allowed the parameter stemming from the models themselves to be constrained, enabling a better definition of the models. Thus, this work aims to assess the truth value of the statement of whether these models predict the late-time expansion history of the observable Universe to a significant enough degree in $f(T)$ gravity.

The subsequent subsections will investigate the following five models:

- Power-Law Model - as described in Sec. 3.4.1
- Square Root Exponential Model - as described in Sec. 3.4.2
- Exponential Model - as described in Sec. 3.4.3
- Logarithmic Model - as described in Sec. 3.4.4
- Hyperbolic Tangent Model - as described in Sec. 3.4.5

These five models, will be constrained against a combination of datasets including CC combined with PN (CC + PN) and CC combined with PN and BAO datasets (CC + PN + BAO). Alongside these datasets the R19, HW, and TRGB $H_0$ priors will be employed, for which values can be found in Sec. 3.3.2.4. Furthermore, these models be analysed and compared with $\Lambda$CDM model, which is also presented as the first subsection for comparison purposes. To this end, the $\chi^2_{\text{min}}$, together with the AIC and BIC will be calculated and presented for each model. The main role of both these criterion is as a model selection criterion when analysing observational data as further explained in Sec. 3.5.

Therefore, $\Delta$AIC and $\Delta$BIC will be calculated for model comparison, representing the difference in AIC and BIC values between each model dataset ad prior combination, and the corresponding $\Lambda$CDM values. This difference can be defined from the equations describing AIC and BIC, in Eqs. 3.68,3.70. As a reminder, in this setting, smaller values of $\Delta$AIC and $\Delta$BIC signify that the specific model with the particular dataset and prior combination are closer to the $\Lambda$CDM model.

### 5.1.1 | $\Lambda$CDM Model

The first model presented is the $\Lambda$CDM model, referred to as $f_0$CDM, as previously indicated. This choice is significant because in all subsequent $f(T)$ models, comparison with $\Lambda$CDM can be made through the values of AIC and BIC. To this end, an MCMC run for the $\Lambda$CDM model was conducted using the Friedmann equation, Eq. 2.47. This equation reveals that the free parameters for this model are the Hubble parameter $H_0$ and the current matter density parameter $\Omega_{m,0}$, which were constrained using different combination datasets.

The posterior and confidence regions, obtained from the MCMC analysis are shown in Fig. 5.1. The two datasets combinations used, CC + PN and CC + PN + BAO, constrain the two parameters and are shown respectively in the top and bottom figures. In addition, the plots display the results of the priors on $H_0$ reported in Sec. 3.3.2.4. In the top figure, an anticorrelation between $\Omega_{m,0}$ and $H_0$ is evident. However, this relationship diminishes and becomes more degenerate when the BAO dataset is included in the bottom figure.

As expected, the constrained parameters converge quickly. In fact, the precision results obtained through the MCMC runs for the parameters are given in Table 5.1a which shows that by and large, the parameters have nearly Gaussian uncertainties. This is also reflected in the posterior distributions. The table demonstrates that reliable values have been obtained since the resultant $H_0$ parameters are within the range of observed Hubble constant values. Furthermore, Planck18 reports a value for the matter density parameter of $\Omega_{m,0}^{\mathrm{P18}} = 0.315 \pm 0.007$ [16].

Additionally, Table 5.1 not only gives the results of the constrained parameters, it also presents the minimum $\chi^2$ for each dataset and prior combination calculated through the respective $\chi^2$ equations. For comparison purposes, the values of AIC and BIC statistical indicators for $\Lambda$CDM are given in Table 5.1b. These values are used throughout the analysis to compare models with respect to the obtained values for $\Lambda$CDM.

A more thorough analysis will be carried out as the remaining subsections proceed. The objective of this subsection was solely to present the results obtained from the MCMC analysis of $\Lambda$CDM, thus enabling comparison in subsequent sections.

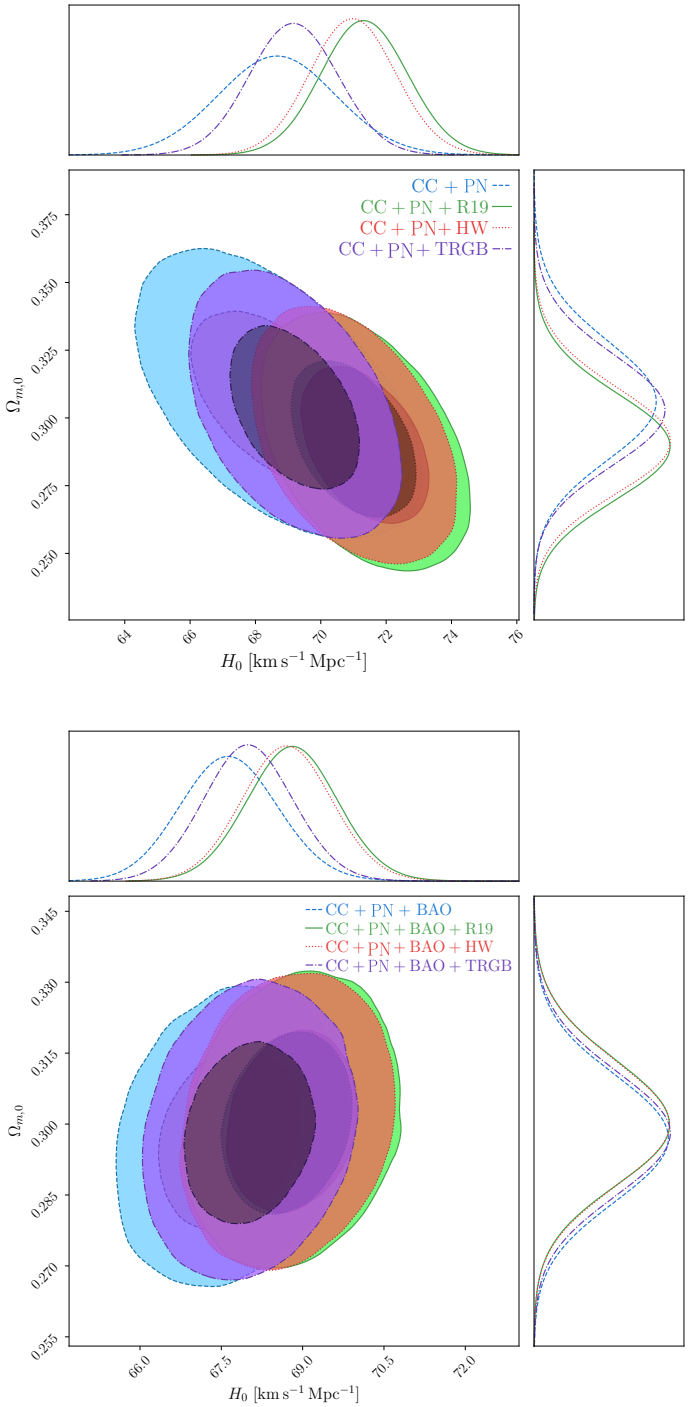


Figure 5.1: Contour plots for the ΛCDM model. *Top:* Confidence levels and posteriors for the model using the CC+PN setting combined with different priors denoted by R19 (green colour), HW (red colour), TRGB (purple colour) and no prior (blue colour). *Bottom:* Confidence levels and posteriors for the model using the CC+PN+BAO with the same parameters being implemented.

| Data Sets | $H_0$ [km/s/Mpc] | $\Omega_{m,0}$ | $M$ |
|---|---|---|---|
| CC + PN | $68.7 \pm 1.8$ | $0.306^{+0.022}_{-0.021}$ | $-19.383^{+0.052}_{-0.054}$ |
| CC + PN + R19 | $71.3^{+1.4}_{-1.3}$ | $0.290^{+0.019}_{-0.020}$ | $-19.310^{+0.038}_{-0.037}$ |
| CC + PN + HW | $71.0 \pm 1.3$ | $0.291^{+0.020}_{-0.019}$ | $-19.320^{+0.038}_{-0.037}$ |
| CC + PN + TRGB | $69.2 \pm 1.4$ | $0.303^{+0.021}_{-0.020}$ | $-19.371^{+0.040}_{-0.039}$ |
| CC + PN + BAO | $67.63 \pm 0.90$ | $0.297 \pm 0.013$ | $-19.403^{+0.037}_{-0.034}$ |
| CC + PN + BAO + R19 | $68.81^{+0.82}_{-0.84}$ | $0.300 \pm 0.013$ | $-19.328^{+0.027}_{-0.026}$ |
| CC + PN + BAO + HW | $68.70 \pm 0.83$ | $0.300^{+0.014}_{-0.013}$ | $-19.350^{+0.030}_{-0.029}$ |
| CC + PN + BAO + TRGB | $67.98^{+0.85}_{-081}$ | $0.298 \pm 0.013$ | $-19.370^{+0.031}_{-0.029}$ |

(a) Results for the constrained parameters for the $f_0$CDM model obtained from the MCMC runs.

| Data Sets | $\chi^2_{\text{min}}$ | AIC | BIC |
|---|---|---|---|
| CC + PN | 1041.49 | 1047.49 | 1062.44 |
| CC + PN + R19 | 1046.32 | 1052.32 | 1067.27 |
| CC + PN + HW | 1041.88 | 1047.88 | 1062.83 |
| CC + PN + TRGB | 1041.69 | 1047.69 | 1062.64 |
| CC + PN + BAO | 1057.46 | 1063.46 | 1078.45 |
| CC + PN + BAO + R19 | 1068.30 | 1074.30 | 1089.30 |
| CC + PN + BAO + HW | 1066.03 | 1072.03 | 1087.03 |
| CC + PN + BAO + TRGB | 1058.56 | 1064.56 | 1079.56 |

(b) Results for the minimum chi-squared together with the AIC and BIC values, Eqs. 3.68,3.70 for $f_0$CDM model.

Table 5.1: Output parameter results and statistical indicators for ΛCDM model. The first column of both sub-tables denote the different datasets and prior combinations.

### 5.1.2 | Power Law Model

The first $f(T)$ cosmological model considered in this analysis is the power law model (referred to as $f_1$CDM). As a reminder, within the action described by Eq. 2.51, the model function $f(T)$ evolves as a power law in the torsion scalar, denoted as $f_1(T) \propto T^{p_1}$. Its specific expression can be found in Eq. 3.52, which leads to the deduction that the two model parameters in this case are $\alpha_1$ and $p_1$. However, as demonstrated in Sec. 3.4.1, this can be reduced to one model parameter by evaluating the Friedmann equation at current times to obtain $\alpha_1$. Therefore, the only model parameter obtained for $f_1$CDM is the dimensionless constant $p_1$.

Furthermore, the modified Friedmann equations for this model become Eq. 3.54. It is useful to keep in mind that the model reduces to ΛCDM for $p_1 = 0$ and reaches the GR limit for $p_1 = 1$.

The posterior distributions and $1\sigma$ and $2\sigma$ confidence regions are depicted in Fig. 5.2 for the primary dataset combination of CC with PN at the top, and CC+PN+BAO at the bottom. These datasets are also combined with different $H_0$ priors. Precise results for these datasets are provided in Table 5.2. In this case, as indicated by the Friedmann equation Eq. 3.54, there are three primary parameters: $H_0$, $\Omega_{m,0}$, and the additional model parameter $p_1$. The additional parameter featured in Table 5.2a is the nuisance parameter, derived from the PN dataset, as elaborated in Sec. 3.3.2.2. Given its nature as a nuisance parameter, it is excluded from the posterior plots to maintain focus on the significantly constrained parameters.

The advantage of using these corner plots is that it does not only show you the the individual posteriors of the parameter but also the correlation between the parameters through the confidence levels of $1\sigma$ and $2\sigma$ regions. A similar relationship between $\Omega_{m,0}$ and $H_0$ as seen in ΛCDM is observed. Initially, this relationship is anticorrelated when CC+PN data are included, but it becomes more degenerate with the inclusion of the BAO dataset.

The posteriors for $H_0$ in both primary datasets reveal that introducing an $H_0$ prior primarily results in an elevation of the $H_0$ value compared to the results obtained without any prior (indicated by the dashed blue line). Similarly, but to a lesser extent, the parameter $\Omega_{m,0}$ exhibits a lower value when priors are incorporated into the datasets. This outcome is expected, as an increase in the current acceleration of the Universe (i.e. $H_0$) implies a greater distribution of matter throughout the Universe. Consequently, while most of the energy in this scenario would manifest as effective dark energy, the matter density parameter (i.e. $\Omega_{m,0}$) is anticipated to decrease.

Upon a careful review of the precise values in the table, it becomes evident that the highest value obtained for $H_0$ occurs with the CC+PN dataset when combined with the R19 prior, yielding $H_0 = 71.3^{+1.3}_{-1.4}\,\mathrm{km\ s^{-1}Mpc^{-1}}$. This outcome is anticipated, as the R19 prior

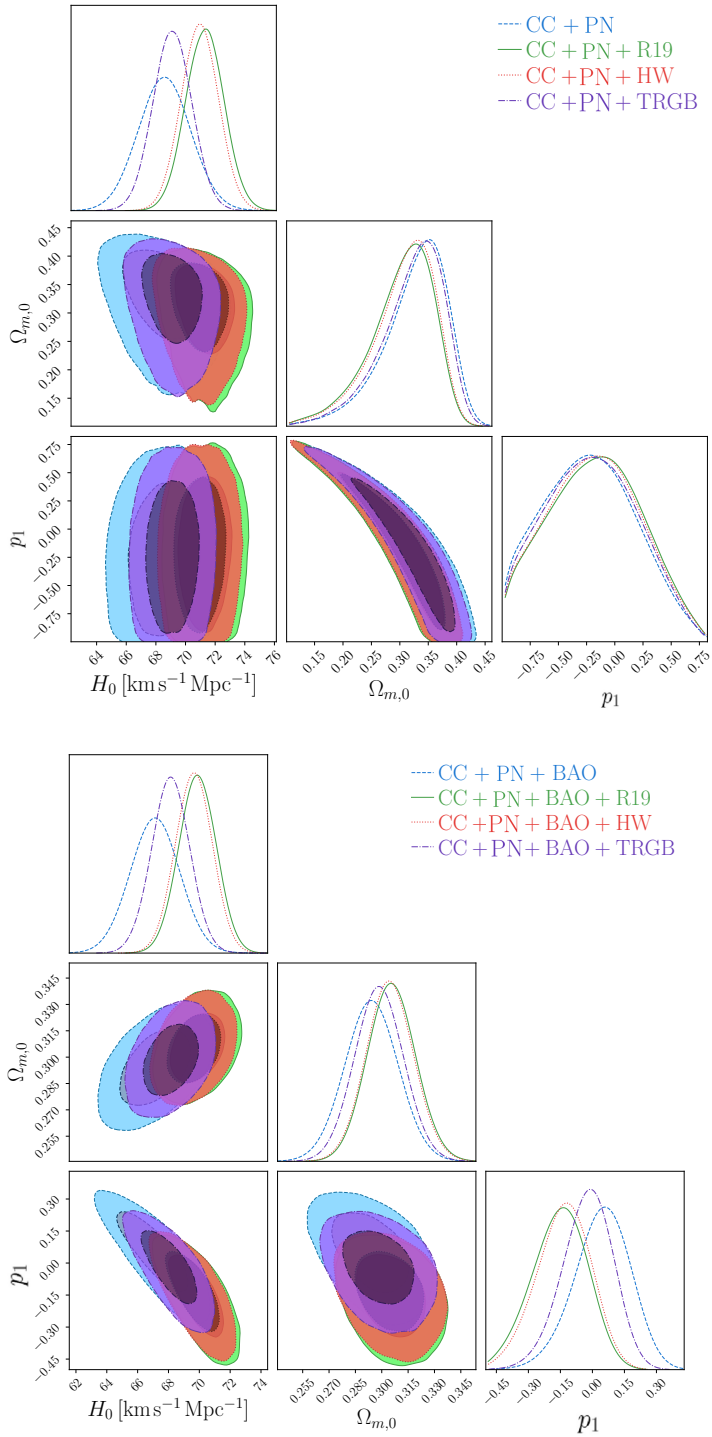


Figure 5.2: Contour plots for the Power Law model. *Top:* Confidence levels and posteriors for the model using the CC+PN setting combined with different priors denoted by R19 (green colour), HW (red colour), TRGB (purple colour) and no prior (blue colour). *Bottom:* Confidence levels and posteriors for the model using the CC+PN+BAO with the same parameters being implemented.

| Data Sets | $H_0$ [km/s/Mpc] | $\Omega_{m,0}$ | $p_1$ | $M$ |
|---|---|---|---|---|
| CC + PN | $68.5 \pm 1.8$ | $0.350^{+0.045}_{-0.064}$ | $-0.22^{+0.41}_{-0.48}$ | $-19.390^{+0.053}_{-0.055}$ |
| CC + PN + R19 | $71.3^{+1.3}_{-1.4}$ | $0.326^{+0.045}_{-0.065}$ | $-0.13^{+0.40}_{-0.50}$ | $-19.314^{+0.039}_{-0.038}$ |
| CC + PN + HW | $71.0 \pm 1.3$ | $0.329^{+0.045}_{-0.062}$ | $-0.16^{+0.41}_{-0.48}$ | $-19.324^{+0.038}_{-0.037}$ |
| CC + PN + TRGB | $69.1^{+1.4}_{-1.3}$ | $0.344^{+0.045}_{-0.063}$ | $-0.20^{+0.42}_{-0.47}$ | $-19.375 \pm 0.040$ |
| CC + PN + BAO | $67.1 \pm 1.6$ | $0.294 \pm 0.015$ | $0.06 \pm 0.13$ | $-19.435 \pm 0.047$ |
| CC + PN + BAO + R19 | $69.9 \pm 1.2$ | $0.305^{+0.014}_{-0.013}$ | $-0.14^{+0.12}_{-0.13}$ | $-19.359^{+0.035}_{-0.034}$ |
| CC + PN + BAO + HW | $69.7 \pm 1.2$ | $0.304^{+0.014}_{-0.012}$ | $-0.12^{+0.12}_{-0.13}$ | $-19.366^{+0.035}_{-0.033}$ |
| CC + PN + BAO + TRGB | $68.1 \pm 1.2$ | $0.298 \pm 0.014$ | $-0.01^{+0.11}_{-0.12}$ | $-19.407 \pm 0.036$ |

(a) Results for the constrained parameters for the $f_1$CDM model obtained from the MCMC runs.

| Data Sets | $\chi^2_{\text{min}}$ | AIC | BIC | $\Delta$AIC | $\Delta$BIC |
|---|---|---|---|---|---|
| CC + PN | 1040.94 | 1048.94 | 1068.88 | 1.45 | 6.43 |
| CC + PN + R19 | 1045.83 | 1053.83 | 1073.77 | 1.51 | 6.50 |
| CC + PN + HW | 1044.50 | 1052.50 | 1072.44 | 1.51 | 6.50 |
| CC + PN + TRGB | 1041.55 | 1049.55 | 1069.49 | 1.87 | 6.85 |
| CC + PN + BAO | 1057.13 | 1065.13 | 1085.13 | 1.68 | 6.68 |
| CC + PN + BAO + R19 | 1066.87 | 1074.87 | 1094.87 | 0.56 | 5.56 |
| CC + PN + BAO + HW | 1064.92 | 1072.92 | 1086.92 | 0.89 | 5.89 |
| CC + PN + BAO + TRGB | 1058.56 | 1066.56 | 1086.56 | 2.00 | 7.00 |

(b) Results for the minimum chi-squared together with the AIC and BIC values, Eqs. 3.68,3.70, for $f_1$CDM model. The last two columns denote the respective differences of the AIC and BIC values with the $\Lambda$CDM model

Table 5.2: Output parameter results and statistical indicators for Power Law Model. The first column of both sub-tables denote the different datasets and prior combinations.

is the most influential among those employed due to its high value, consequently leading to the greatest shift towards higher values of $H_0$ in the MCMC runs. Correspondingly, the minimum value of the $\Omega_{m,0}$ parameter is attained with this combination of datasets, aligning with the observation made for the posterior.

The values for $H_0$ exhibit a notable variation across different dataset combinations, with the CC+PN+BAO dataset configuration without priors yielding the lowest estimate of $H_0 = 67.1 \pm 1.6\,\mathrm{km\ s^{-1}Mpc^{-1}}$. The combination with the TRGB prior produces the next lowest value for $H_0$, influenced by the fact that this prior is the lowest among the three and consequently has the least impact on pushing $H_0$ upwards. The HW prior, conversely, falls somewhere in between the R19 and TRGB priors, leaning notably closer to the R19 prior in terms of value. This closeness is evident in the resulting output values, which tend to align more closely with those derived from the R19 prior. Additionally, Table. 5.2a also shows that the $H_0$ priors produce tighter constraints when compared to no prior values. The values become even more tighter when the BAO dataset is included.

Interestingly, the inclusion of the BAO dataset consistently leads to slightly lower $H_0$ values compared to scenarios where it is omitted. This discrepancy arises due to the nature of the BAO datasets, which primarily probe acoustic oscillations coming from the early Universe. Thus, the incorporation of the BAO dataset in conjunction with the absence of priors results in the lowest Hubble constant estimation. However, it is observed once more that the combination with the R19 prior results in the highest value obtained for $H_0$ when compared with the BAO dataset. The matter density parameter exhibits a slightly different behavior in the combination datasets involving BAO. However, this discrepancy arises solely due to the lower values of $H_0$.

Shifting focus to the $p_1$ parameter, it is notable that the values derived from the MCMC analysis remain consistently within approximately $1\sigma$ of the $\Lambda$CDM value. This suggests a close concordance between the $f_1$CDM model and the standard model of cosmology, with the uncertainties consistently encapsulating the $\Lambda$CDM. Of particular interest is the interplay between the $p_1$ parameter and other parameters. Although initially appearing degenerate in the CC+PN scenarios, the relationship between $p_1$ and $H_0$ transitions to being anti-correlated upon the addition of BAO to the combination. On the other hand, the relationship between $p_1$ and $\Omega_{m,0}$ begins as an anti-correlation but diminishes to a lesser extent when BAO is included. It is also worth noting that the $p_2$ values also tend to be in the negative range.

The second column of Table 5.2b presents the $\chi^2_{\mathrm{min}}$ values, calculated using the corresponding dataset's $\chi^2$ equations as detailed in the observational section discussing $\chi^2$ in Eq. 3.69. A higher $\chi^2_{\mathrm{min}}$ implies a larger deviation between the model-predicted values and the observed data. Thus, based on this metric, the combination of CC+PN appears to offer

the closest fit. However, it is important to consider that this assessment depends significantly on factors like the number of data points and the inclusion of different datasets. This explains why incorporating BAO datasets results in a higher $\chi^2_{\rm min}$. Therefore, for more robust model selection, it is worth examining $\Delta$AIC and $\Delta$BIC values, which serve as reliable statistical indicators. These values represent the difference between the model under consideration and the $\Lambda$CDM model.

From all the MCMC runs, the CC+PN+BAO+R19, gives the lowest values of both the $\Delta$AIC and $\Delta$BIC. Indeed, in this case, the evidence does not point strongly towards $\Lambda$CDM case, in both AIC and BIC. With all $\Delta$AIC values being less than 2, it remains inconclusive to assert robust support for $\Lambda$CDM over competing models based on this evidence alone. Nonetheless, it is important to highlight the effective explanatory power of the $\Lambda$CDM model in describing the late-time evolution of the Universe. Consequently, while the CC+PN+BAO+R19 model emerges as the preferred choice among this group of runs. Furthermore, the obtained results align with the confidence regions of previous studies in the literature [268, 237, 217, 269] for the closest prior value.

### 5.1.3 | Square-root Exponential Model

The second model under consideration is the Linder Model, referred to as the $f_2$CDM model, which was introduced earlier. This model, outlined in detail in Sec. 3.4.2, incorporates a square root within the exponential term, as illustrated in Eq. 3.55. Like the $f_1$CDM model, the $f_2$CDM model involves two model parameters, namely $\alpha_2$ and $p_2$. However, $\alpha_2$ can be directly derived from the Friedmann equation at present times, leaving $p_2$ as the only new model parameter for the $f_2$CDM model, in addition to the current matter density $\Omega_{m,0}$ and the functional form in the exponential term $H/H_0$. The corresponding modified Friedmann equation for this model is provided in Eq. 3.57. In this case, the model approaches $\Lambda$CDM as $p_2$ tends to infinity.

Clearly, the interpretation of the $p_2$ parameter changes in the current model compared to the previous $f_1$CDM model, given their distinct nature. However, in the limiting scenario where both parameters converge to $\Lambda$CDM cosmology, the $f_2$CDM parameter can be reformulated as $1/p_2$. This transformation ensures numerical stability, as the limit for $\Lambda$CDM now becomes $1/p_2 \to 0^+$.

The constrained parameter results for $H_0$, $\Omega_{m,0}$, and $1/p_2$ obtained from the MCMC runs are presented in Fig. 5.3, following the same configuration as the previous model. The exact outcomes are outlined in Table 5.3a. Upon comparing the $f_1$CDM model to the current one, it becomes apparent that certain similar trends emerge, such as priors on $H_0$ lead to elevated values of the Hubble constant in the MCMC runs. Indeed, the low-

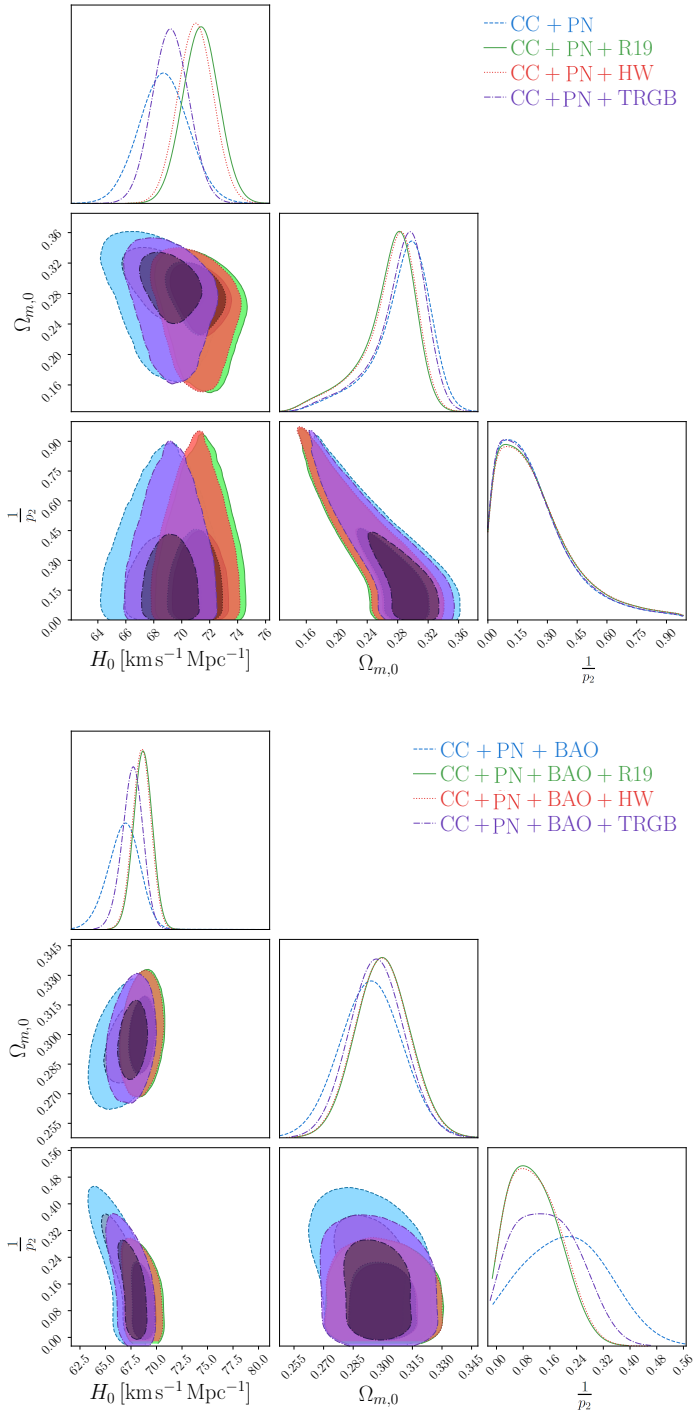


Figure 5.3: Contour plots for the Square-root exponential model. *Top:* Confidence levels and posteriors for the model using the CC+PN setting combined with different priors denoted by R19 (green colour), HW (red colour), TRGB (purple colour) and no prior (blue colour). *Bottom:* Confidence levels and posteriors for the model using the CC+PN+BAO with the same parameters being implemented.

| Data Sets | $H_0$ [km/s/Mpc] | $\Omega_{m,0}$ | $\frac{1}{p_2}$ | $M$ |
|---|---|---|---|---|
| CC + PN | $68.7^{+1.8}_{-1.7}$ | $0.298^{+0.031}_{-0.035}$ | $0.101^{+0.227}_{-0.098}$ | $-19.43^{+0.57}_{-0.47}$ |
| CC + PN + R19 | $71.4 \pm 1.3$ | $0.283^{+0.027}_{-0.036}$ | $0.088^{+0.252}_{-0.086}$ | $-19.28^{+0.50}_{-0.51}$ |
| CC + PN + HW | $71.0^{+1.3}_{-1.2}$ | $0.285^{+0.027}_{-0.036}$ | $0.096^{+0.245}_{-0.093}$ | $-19.37^{+0.45}_{-0.34}$ |
| CC + PN + TRGB | $69.2 \pm 1.3$ | $0.296^{+0.028}_{-0.035}$ | $0.088^{+0.239}_{-0.085}$ | $-19.36^{+0.36}_{-0.37}$ |
| CC + PN + BAO | $66.9^{+1.5}_{-1.6}$ | $0.294 \pm 0.016$ | $0.22^{+0.12}_{-0.15}$ | $-19.38^{+0.22}_{-0.35}$ |
| CC + PN + BAO + R19 | $68.71^{+0.88}_{-0.96}$ | $0.300 \pm 0.014$ | $0.079^{+0.098}_{-0.064}$ | $-19.35^{+0.19}_{-0.24}$ |
| CC + PN + BAO + HW | $68.58^{+0.89}_{-0.92}$ | $0.300^{+0.013}_{-0.014}$ | $0.076^{+0.105}_{-0.060}$ | $-19.39^{+0.05}_{-0.05}$ |
| CC + PN + BAO + TRGB | $67.7 \pm 1.0$ | $0.297 \pm 0.014$ | $0.128^{+0.111}_{-0.099}$ | $-19.46^{+0.37}_{-0.26}$ |

(a) Results for the constrained parameters for the $f_2$CDM model obtained from the MCMC runs.

| Data Sets | $\chi^2_{\text{min}}$ | AIC | BIC | $\Delta$AIC | $\Delta$BIC |
|---|---|---|---|---|---|
| CC + PN | 1041.49 | 1049.49 | 1069.43 | 2.00 | 6.98 |
| CC + PN + R19 | 1046.32 | 1054.32 | 1074.25 | 2.00 | 6.99 |
| CC + PN + HW | 1044.99 | 1052.99 | 1072.93 | 2.00 | 6.99 |
| CC + PN + TRGB | 1041.69 | 1049.69 | 1069.62 | 2.00 | 6.99 |
| CC + PN + BAO | 1056.52 | 1064.62 | 1084.52 | 1.06 | 6.06 |
| CC + PN + BAO + R19 | 1068.31 | 1076.31 | 1096.31 | 2.00 | 7.00 |
| CC + PN + BAO + HW | 1066.03 | 1074.03 | 1094.03 | 2.00 | 7.00 |
| CC + PN + BAO + TRGB | 1058.47 | 1066.47 | 1086.47 | 1.90 | 6.90 |

(b) Results for the minimum chi-squared together with the AIC and BIC values, Eqs. 3.68,3.70, for $f_2$CDM model. The last two columns denote the respective differences of the AIC and BIC values with the $\Lambda$CDM model

Table 5.3: Output parameter results and statistical indicators for Linder Model. The first column of both sub-tables denote the different datasets and prior combinations.

est $H_0$ value is observed for the CC+PN+BAO dataset, attributed to the inclusion of the BAO dataset and the absence of any priors, yielding $H_0 = 66.9^{+1.5}_{-1.6}$ km s$^{-1}$Mpc$^{-1}$. Although marginally higher, the CC+PN combined with the R19 dataset still gives the highest value at $H_0 = 71.4 \pm 1.3$ km s$^{-1}$Mpc$^{-1}$. Following similar reasoning as in $f_1$CDM, this outcome is expected, and similarly, the CC+PN+R19 attains the lowest value for the current matter density. Analogous to $f_1$CDM, the values obtained when incorporating the R19 and HW priors into the MCMC runs generate relatively consistent outcomes for these respective parameters. This consistency arises due to the comparable values of these two priors.

As previously indicated, the active model parameter in this case is $1/p_2$, which was chosen for numerical stability. In contrast to the previous model, most datasets fall within the $2\sigma$ region of the $\Lambda$CDM rather than $1\sigma$ as in $f_1$CDM. This suggests that in this case, the values are slightly further away from favouring the $\Lambda$CDM model. Additionally, it can be observed that when the BAO dataset is added, the values of this parameter are marginally lowered, especially when the R19 and HW priors are included. Furthermore, especially in the CC+PN cases, there is some anti-correlation between the parameters of $\Omega_{m,0}$ and $1/p_2$. The $\chi^2_{\rm min}$ values are outlined in the second row of Table 5.3b. As before, combinations such as CC+PN+BAO and CC+PN+BAO+TRGB exhibit the lowest values, indicating relatively good fits. However, it is important to interpret these results with caution and consider the broader context using $\Delta$AIC and $\Delta$BIC for a more comprehensive comparison across models and datasets. Among the various MCMC runs, the CC+PN+BAO combination, without any prior, emerges as the closest match to $\Lambda$CDM. This aligns with expectations, considering the reliance of BAO datasets on early Universe data. An interesting observation in the last two columns of Table 5.3b is that the values are around 2.00 and 6.99, respectively, which are slightly higher than the previous model. This indicates a slight deviation from $\Lambda$CDM compared to the previous model.

As in $f_1$CDM, the results are consistent with literature [268, 237, 217, 269] for the closest prior value, however, the priors add more detail to the impact of the priors on $H_0$. They also provide a more detailed evaluation of the effect on each MCMC run and the resulting parameter values. In fact, to a certain extent, the priors tend to narrow the uncertainty regions in the parameter values, which provides an interesting feature when compared to the $\Lambda$CDM model.

### 5.1.4 | Exponential Model

The third $f(T)$ cosmological model being examined is the Exponential model, described in Sec. 3.4.3, in particular, Eq. 3.59, hereafter referred to as $f_3$CDM. Similar to previous models, two model parameters, $\alpha_3$ and $p_3$, are involved. However, through the evaluation of

the Friedmann equation at the present time, $\alpha_3$ can be derived, leaving only $p_3$ as the remaining model parameter. Consequently, the modified Friedmann equation takes the form of Eq. 3.61. Similar to the analysis conducted for $f_2$CDM, as $p_3 \to +\infty$, this model tends towards $\Lambda$CDM. For a more stable analysis, constraints are applied to $1/p_3$, ensuring the model converges towards $\Lambda$CDM as $1/p_3 \to 0^+$.

The confidence regions and posteriors for this model and for all dataset combinations are presented in Fig 5.4. This model is an intriguing one, since the only difference between $f_2$CDM and $f_3$CDM is the square-root in the exponential index. However, Fig. 5.4, shows that this difference has a clear effect on the confidence regions of the density parameter which now has stricter confidence regions. On the other hand, the $H_0$ parameter is mostly unaffected, although there are still marginal increases depending on the dataset and prior combination setting.

The precise results of the MCMC runs are shown in Table 5.4a, providing insights for the parameters $H_0$, $\Omega_{m,0}$, $1/p_3$ and also the nuisance parameter $M$. The tighter confidence regions in the $\Omega_{m,0}$ parameter are more evident, making the predictions of the model less ambiguous. As anticipated, similar to previous models, the inclusion of $H_0$ priors tends to exert a push effect on the $H_0$ results, leading to higher values. Specifically, the highest $H_0$ output is generated by the same dataset and prior settings, albeit slightly higher this time, with a value of $H_0 = 72.0^{+1.3}_{-1.4}\,\mathrm{km\ s^{-1}\,Mpc^{-1}}$. It is also notable that the $H_0$ parameters have an almost Gaussian error in this case. Consistently, the lowest value of $\Omega_{m,0}$ is for the same CC+PN+R19. Furthermore, it is interesting to observe that the values of this parameter are marginally lower across all dataset combinations. Notably, the anti-correlation between $H_0$ and $\Omega_{m,0}$ is particularly evident in the CC+PN dataset combinations, gradually becoming more degenerate with the inclusion of the BAO dataset.

Comparing the model parameter $1/p_i$ between $f_2$CDM and $f_3$CDM offers valuable insights. Notably, the best fit values for $1/p_3$ in the $f_3$CDM model are generally closer to the $\Lambda$CDM limit. Despite this proximity, the confidence regions still reveal a noticeable $2\sigma$ distinction between $\Lambda$CDM and the $f_3$CDM model. Additionally, due to the smaller values, the previously observed anti-correlation between this parameter and $\Omega_{m,0}$ in the $f_2$CDM diminishes and becomes more degenerate.

However, despite $1/p_3$ parameter being close to the $\Lambda$CDM model, the $\Delta$AIC and $\Delta$BIC present a contrasting scenario. Both statistical indicators exhibit comparatively higher values, suggesting a stronger preference for the $\Lambda$CDM model in this case compared to other models. Across various MCMC runs, these indicators range around $\sim$ 4.5, indicating a significant deviation from previous models. Upon closer examination, it becomes evident that the datasets without priors, namely CC+PN and CC+PN+BAO, are less favoured in this analysis. On the other hand, the CC+PN+R19 setting emerges as the most favoured

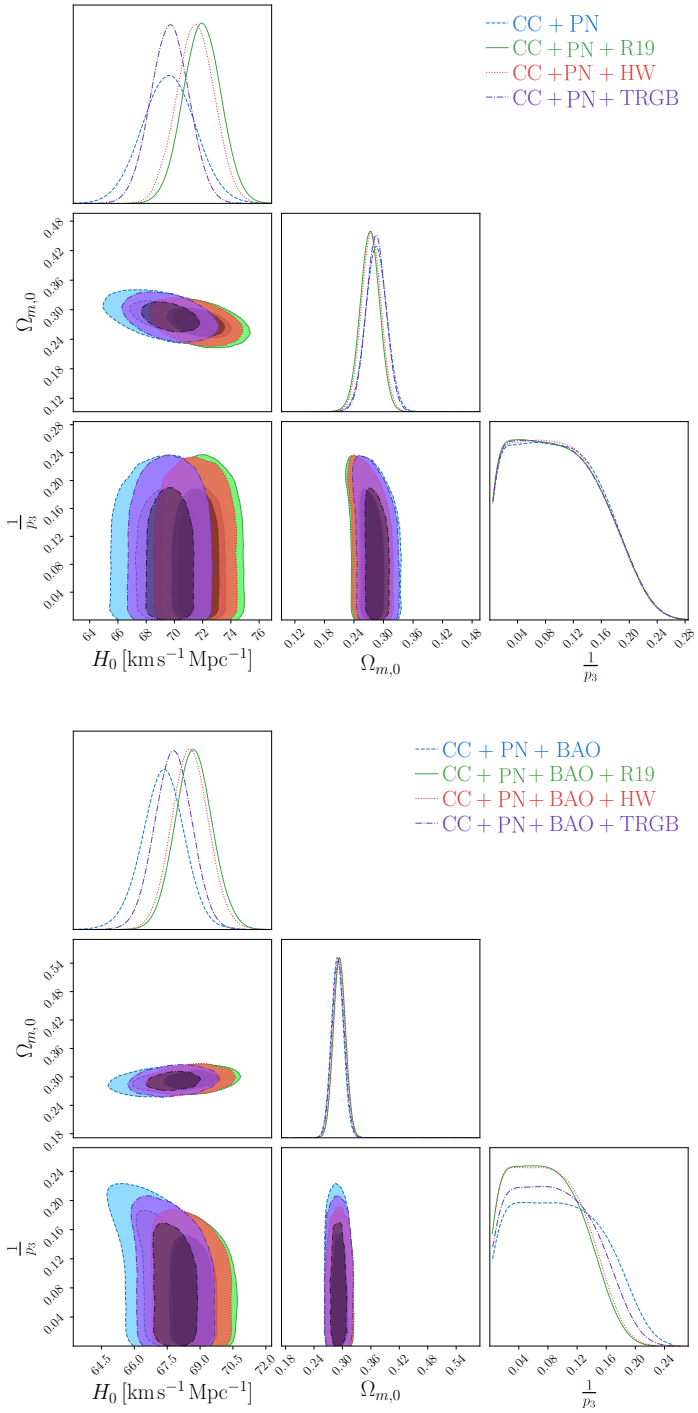


Figure 5.4: Contour plots for the Exponential model. *Top:* Confidence levels and posteriors for the model using the CC+PN setting combined with different priors denoted by R19 (green colour), HW (red colour), TRGB (purple colour) and no prior (blue colour). *Bottom:* Confidence levels and posteriors for the model using the CC+PN+BAO with the same parameters being implemented.

| Data Sets | $H_0$ [km/s/Mpc] | $\Omega_{m,0}$ | $\frac{1}{p_3}$ | $M$ |
|---|---|---|---|---|
| CC + PN | $69.6^{+1.8}_{-1.9}$ | $0.286^{+0.021}_{-0.023}$ | $0.067^{+0.078}_{-0.054}$ | $-19.367^{+0.053}_{-0.056}$ |
| CC + PN + R19 | $72.0^{+1.3}_{-1.4}$ | $0.273 \pm 0.020$ | $0.042^{+0.099}_{-0.032}$ | $-19.302^{+0.037}_{-0.039}$ |
| CC + PN + HW | $71.5 \pm 1.4$ | $0.275^{+0.019}_{-0.020}$ | $0.070^{+0.072}_{-0.058}$ | $-19.317^{+0.039}_{-0.038}$ |
| CC + PN + TRGB | $69.7^{+1.3}_{-1.4}$ | $0.285^{+0.020}_{-0.021}$ | $0.048^{+0.094}_{-0.037}$ | $-19.366 \pm 0.040$ |
| CC + PN + BAO | $67.35^{+0.94}_{-0.97}$ | $0.289 \pm 0.013$ | $0.043^{+0.101}_{-0.026}$ | $-19.441^{+0.032}_{-0.031}$ |
| CC + PN + BAO + R19 | $68.70^{+0.84}_{-0.85}$ | $0.293^{+0.013}_{-0.012}$ | $0.059^{+0.056}_{-0.047}$ | $-19.397^{+0.029}_{-0.028}$ |
| CC + PN + BAO + HW | $68.52^{+0.85}_{-0.82}$ | $0.295^{+0.011}_{-0.014}$ | $0.034^{+0.089}_{-0.024}$ | $-19.401^{+0.028}_{-0.029}$ |
| CC + PN + BAO + TRGB | $67.79 \pm 0.85$ | $0.292^{+0.012}_{-0.014}$ | $0.074^{+0.057}_{-0.059}$ | $-19.425^{+0.027}_{-0.030}$ |

(a) Results for the constrained parameters for the $f_3$CDM model obtained from the MCMC runs.

| Data Sets | $\chi^2_{\text{min}}$ | AIC | BIC | $\Delta$AIC | $\Delta$BIC |
|---|---|---|---|---|---|
| CC + PN | 1045.04 | 1053.04 | 1072.97 | 5.55 | 10.53 |
| CC + PN + R19 | 1048.16 | 1056.16 | 1076.10 | 3.84 | 8.82 |
| CC + PN + HW | 1047.06 | 1055.07 | 1075.01 | 4.08 | 9.06 |
| CC + PN + TRGB | 1045.04 | 1053.04 | 1072.98 | 5.36 | 10.34 |
| CC + PN + BAO | 1060.55 | 1068.55 | 1088.55 | 5.09 | 10.09 |
| CC + PN + BAO + R19 | 1071.71 | 1079.71 | 1099.71 | 5.41 | 10.41 |
| CC + PN + BAO + HW | 1069.03 | 1077.03 | 1097.03 | 4.99 | 9.10 |
| CC + PN + BAO + TRGB | 1061.78 | 1069.78 | 1089.78 | 5.21 | 10.21 |

(b) Results for the minimum chi-squared together with the AIC and BIC values, Eqs. 3.68,3.70, for $f_3$CDM model. The last two columns denote the respective differences of the AIC and BIC values with the $\Lambda$CDM model

Table 5.4: Output parameter results and statistical indicators for the exponential model. The first column of both sub-tables denote the different datasets and prior combinations.

among the analysed configurations. Additionally, these outputs, Fig 5.4 and Table 5.4 are also consistent with previous literature [268, 237, 217, 269].

### 5.1.5 | Logarithmic Model

The fourth $f(T)$ model under consideration is the Logarithmic model, referred to as $f_4$CDM, characterised by $f_4(T) \propto \log(qT)$, where $q$ is a constant as described in Eq. 3.62. Similar to previous models, this model also involves two parameters, $\alpha_4$ and $p_4$. Interestingly, after obtaining $\alpha_4$ through the current Friedmann Equation, the modified Friedmann equation, Eq. 3.64, lacks the inclusion of both parameters. Therefore, in the modified Friedmann equation, neither $\alpha_4$ nor $p_4$ are present. This implies that the same constrained parameters are required in this model as those in $\Lambda$CDM. However, $f_4$CDM is quite intriguing as it cannot show a confirmation bias with $\Lambda$CDM, given that $p_4$ does not appear in the equation.

The posterior distributions and confidence regions for the parameters $H_0$ and $\Omega_{m,0}$ are depicted in Fig. 5.5. Notably, an anti-correlation between these parameters is evident in the figure, in particular for the CC+PN setting, a pattern also reflected in the precise results provided in the upper section of Table 5.5a.

A difference also emerges in the output results between the CC+PN and CC+PN+BAO settings. In the former scenario, $H_0$ values fall within a reasonable range, while the $\Omega_{m,0}$ parameter has significantly lower values. Consequently, the combination of CC+PN+R19 yields a maximum value of $H_0$ at $71.4 \pm 1.3\,\mathrm{km\ s^{-1}Mpc^{-1}}$, as anticipated. Conversely, upon incorporating the BAO dataset, both the $H_0$ and $\Omega_{m,0}$ parameter values notably decrease. Specifically, the minimum $H_0$ value is observed at $H_0 = 60.89^{+0.75}_{-0.71}\,\mathrm{km\ s^{-1}Mpc^{-1}}$ for the CC+PN+BAO combination, as expected. However, upon closer examination, these values are deemed low.

In this case, the statistical indicators provide a deeper insight on this model. As depicted in the upper section of Table 5.5b, both the $\Delta$AIC and $\Delta$BIC values appear relatively low. However, it is important to recognize that these values are influenced by the number of free parameters, and in this case, the model under consideration and the $\Lambda$CDM model have an equal number of such parameters. On the other hand, upon studying the lower section of Table 5.5b, the values of $\Delta$AIC and $\Delta$BIC are exceptionally high. As evidenced in Table 5.5a, the inclusion of the BAO dataset leads to deviations of both the Hubble constant and the matter density parameter from their respective confidence regions. Consequently, the statistical indicators in this case consistently point away from $\Lambda$CDM, due to their exceptionally high values.

These results, as depicted in Fig. 5.5 and summarised in Table 5.3, align with previous research findings [237, 217]. It is evident that the $f_4$CDM model faces challenges in aligning

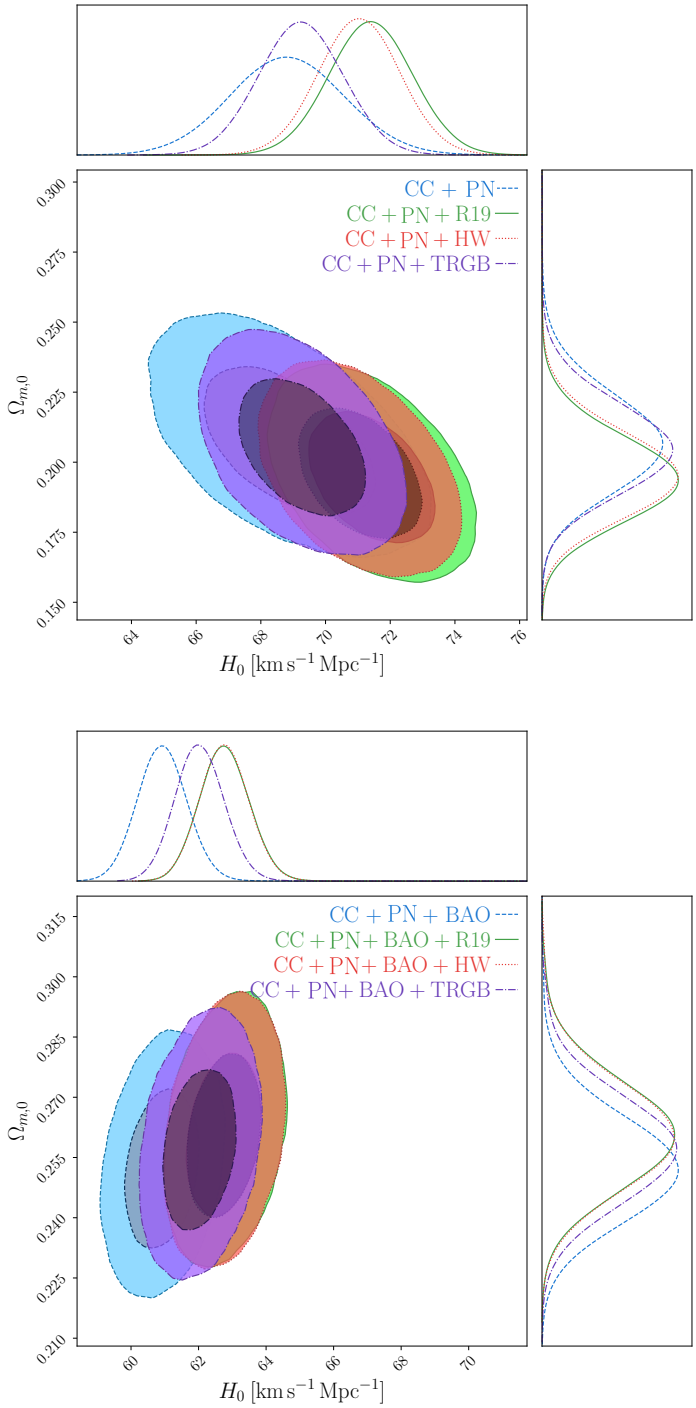


Figure 5.5: Contour plots for the Logarithmic model. *Top:* Confidence levels and posteriors for the model using the CC+PN setting combined with different priors denoted by R19 (green colour), HW (red colour), TRGB (purple colour) and no prior (blue colour). *Bottom:* Confidence levels and posteriors for the model using the CC+PN+BAO with the same parameters being implemented.

| Data Sets | $H_0$ [km/s/Mpc] | $\Omega_{m,0}$ | $M$ |
|---|---|---|---|
| CC + SN | $68.8^{+1.8}_{-1.7}$ | $0.207^{+0.018}_{-0.017}$ | $-19.371^{+0.051}_{-0.052}$ |
| CC + PN + R19 | $71.4 \pm 1.3$ | $0.194^{+0.016}_{-0.015}$ | $-19.301^{+0.038}_{-0.035}$ |
| CC + PN + HW | $69.2 \pm 1.3$ | $0.205 \pm 0.016$ | $-19.358^{+0.037}_{-0.040}$ |
| CC + PN + TRGB | $69.2 \pm 1.3$ | $0.205 \pm 0.016$ | $-19.358^{+0.037}_{-0.040}$ |
| CC + PN + BAO | $60.89^{+0.75}_{-0.71}$ | $0.252^{+0.014}_{-0.013}$ | $-19.611^{+0.027}_{-0.031}$ |
| CC + PN + BAO + R19 | $62.77^{+0.72}_{-0.76}$ | $0.261^{+0.013}_{-0.014}$ | $-19.543^{+0.028}_{-0.029}$ |
| CC + PN + BAO + HW | $62.77^{+0.70}_{-0.76}$ | $0.260^{+0.014}_{-0.013}$ | $-19.544^{+0.029}_{-0.028}$ |
| CC + PN + BAO + TRGB | $62.02^{+0.72}_{-0.73}$ | $0.257^{+0.013}_{-0.014}$ | $-19.567^{+0.026}_{-0.033}$ |

(a) Results for the constrained parameters for the $f_4$CM model obtained from the MCMC runs.

| Data Sets | $\chi^2_{\text{min}}$ | AIC | BIC | $\Delta$AIC | $\Delta$BIC |
|---|---|---|---|---|---|
| CC + PN | 1043.46 | 1042.46 | 1064.41 | 1.97 | 1.97 |
| CC + PN + R19 | 1047.98 | 1053.98 | 1068.94 | 1.67 | 1.67 |
| CC + PN + HW | 1046.70 | 1052.70 | 1067.65 | 1.70 | 1.70 |
| CC + PN + TRGB | 1043.60 | 1049.60 | 1064.55 | 1.91 | 1.91 |
| CC + PN + BAO | 1078.52 | 1084.52 | 1099.52 | 21.07 | 21.07 |
| CC + PN + BAO + R19 | 1124.87 | 1130.87 | 1145.87 | 56.56 | 56.56 |
| CC + PN + BAO + HW | 1121.49 | 1127.49 | 1142.49 | 55.47 | 55.46 |
| CC + PN + BAO + TRGB | 1097.80 | 1103.80 | 1118.80 | 39.23 | 39.23 |

(b) Results for the minimum chi-squared together with the AIC and BIC values, Eqs. 3.68,3.70, for $f_4$CDM model.

Table 5.5: Output parameter results and statistical indicators for Logarithmic model. The first column of both sub-tables denote the different datasets and prior combinations.

with observational data, particularly when considering datasets sensitive to early Universe effects such as the BAO dataset. As a result, it appears that the $f_4$CDM model lacks substantial support from observational data.

### 5.1.6 | Hyperbolic-tangent Model

The hyperbolic-tangent model, hereafter refereed to as $f_5$CDM, model stands out as quite different from the others, offering an intriguing avenue to explore $f(T)$. Defined by the equation $f_5(T) \propto \tanh(kT)$, with $k$ being just a constant, it introduces the $\alpha_5$ and $p_5$ parameter. The $\alpha_5$ parameter is determined as usual through the current Friedmann equation, leading to the modified Friedmann equation specific to this model, as shown in Sec. 3.4.5, specifically Eq. 3.67. Unlike the $f_4$CDM model, here the $p_5$ parameter appears in Eq. 3.67, yet it does not have a corresponding $\Lambda$CDM limit for any value of $p_5$. Therefore, there are no predefined expectations for this additional model parameter.

The posteriors and confidence regions are depicted in Fig. 5.6, illustrating similar relationships between the parameters as observed previously. For instance, in the CC+PN scenario, an anti-correlation between $\Omega_{m,0}$ and $H_0$ is apparent. The precise results are shown in Table 5.6a. This $f_5$CDM model presents entirely different outcomes compared to $f_4$CDM. The range of values for $H_0$ is broader, and the $\Omega_{m,0}$ parameter tends to favor larger values than those obtained in $f_4$CDM, thereby having more confidence in the model's predictions.

In line with previous models, the highest Hubble constant is obtained from the combination CC+PN+R19, yielding $H_0 = 71.8 \pm 1.3$km, s$^{-1}$Mpc$^{-1}$. This value falls between the highest values obtained in $f_2$CDM and $f_3$CDM models. Conversely, the minimum value is achieved for the CC+PN+BAO combination, resulting in $H_0 = 68.4^{+1.5}_{-1.4}$km, s$^{-1}$Mpc$^{-1}$, which represents the highest minimum value across all the models. The TRGB prior consistently yields results closer to those without prior, while the HW prior tends to produce outcomes closer to the R19 prior combinations.

In this scenario, unlike the preceding model, the $p_5$ parameter plays a significant role in background cosmology, yet no value of this parameter can accurately replicate $\Lambda$CDM. An interesting observation arises when comparing the CC+PN and CC+PN+BAO combinations: $p_5$ has positive values in the former while transitioning to negative values in the latter. Remarkably, the highest and lowest values are observed in configurations without any prior inclusion, with other combinations falling between these extremes. However, it is worth noting that uncertainties are notably large.

The statistical indicators presented in Table 5.6b highlight the distinction between $f_4$CDM and $f_5$CDM models. In this context, the values appear more realistic and promising. However, despite this, the $\Delta$AIC and $\Delta$BIC still suggest a marginal deviation from the $\Lambda$CDM

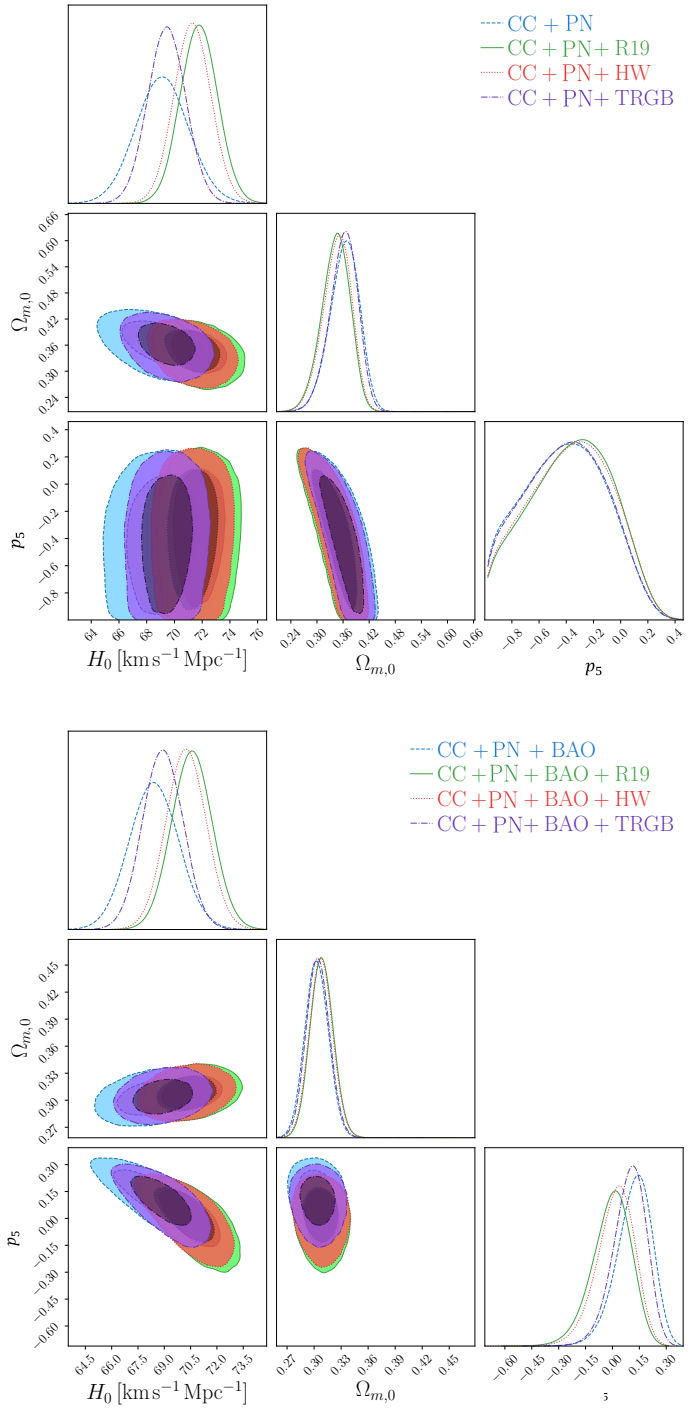


Figure 5.6: Contour plots for the Hyperbolic-tangent model. *Top:* Confidence levels and posteriors for the model using the CC+PN setting combined with different priors denoted by R19 (green colour), HW (red colour), TRGB (purple colour) and no prior (blue colour). *Bottom:* Confidence levels and posteriors for the model using the CC+PN+BAO with the same parameters being implemented.

| Data Sets | $H_0$ [km/s/Mpc] | $\Omega_{m,0}$ | $p_5$ | $M$ |
|---|---|---|---|---|
| CC + PN | $69.2^{+1.9}_{-2.0}$ | $0.369^{+0.031}_{-0.036}$ | $-0.36^{+0.29}_{-0.38}$ | $-19.390^{+0.056}_{-0.058}$ |
| CC + PN + R19 | $71.8 \pm 1.3$ | $0.349^{+0.029}_{-0.035}$ | $-0.28^{+0.28}_{-0.38}$ | $-19.314^{+0.038}_{-0.041}$ |
| CC + PN + HW | $71.3 \pm 1.3$ | $0.353^{+0.029}_{-0.036}$ | $-0.29^{+0.28}_{-0.38}$ | $-19.329 \pm 0.040$ |
| CC + PN + TRGB | $69.5^{+1.3}_{-1.4}$ | $0.366^{+0.030}_{-0.034}$ | $-0.35^{+0.29}_{-0.37}$ | $-19.381^{+0.041}_{-0.042}$ |
| CC + PN + BAO | $68.4^{+1.5}_{-1.4}$ | $0.302^{+0.014}_{-0.012}$ | $0.144^{+0.087}_{-0.107}$ | $-19.400^{+0.039}_{-0.037}$ |
| CC + PN + BAO + R19 | $70.6^{+1.1}_{-1.2}$ | $0.308 \pm 0.013$ | $0.079^{+0.098}_{-0.064}$ | $-19.342^{+0.031}_{-0.033}$ |
| CC + PN + BAO + HW | $70.2 \pm 1.1$ | $0.308^{+0.012}_{-0.013}$ | $0.039^{+0.095}_{-0.112}$ | $-19.351^{+0.032}_{-0.031}$ |
| CC + PN + BAO + TRGB | $68.9^{+1.1}_{-1.2}$ | $0.304 \pm 0.013$ | $0.115^{+0.082}_{-0.100}$ | $-19.386^{+0.032}_{-0.031}$ |

(a) Results for the constrained parameters for the $f_5$CDM model obtained from the MCMC runs.

| Data Sets | $\chi^2_{\rm min}$ | AIC | BIC | $\Delta$AIC | $\Delta$BIC |
|---|---|---|---|---|---|
| CC + PN | 1044.44 | 1052.44 | 1072.38 | 4.95 | 9.93 |
| CC + PN + R19 | 1048.13 | 1056.13 | 1076.06 | 3.81 | 8.79 |
| CC + PN + HW | 1046.94 | 1054.94 | 1074.87 | 3.94 | 8.93 |
| CC + PN + TRGB | 1044.50 | 1052.50 | 1072.44 | 4.81 | 9.80 |
| CC + PN + BAO | 1062.88 | 1070.88 | 1090.88 | 7.43 | 12.43 |
| CC + PN + BAO + R19 | 1069.77 | 1077.77 | 1097.77 | 3.47 | 8.47 |
| CC + PN + BAO + HW | 1067.90 | 1075.90 | 1095.90 | 3.88 | 8.88 |
| CC + PN + BAO + TRGB | 1063.34 | 1071.34 | 1091.34 | 6.78 | 11.78 |

(b) Results for the minimum chi-squared together with the AIC and BIC values, Eqs. 3.68,3.70, for $f_5$CDM model. The last two columns denote the respective differences of the AIC and BIC values with the $\Lambda$CDM model

Table 5.6: Output parameter results and statistical indicators for the exponential model. The first column of both sub-tables denote the different datasets and prior combinations.

cosmology, particularly in combinations where no prior information is incorporated. This prompts the question of whether the hyperbolic tangent model is a viable consideration for cosmological studies.

## 5.2 | Conclusion

In this study, a late-time analysis was conducted to explore the behavior of different $f(T)$ cosmological models in conjunction with the impact of $H_0$ priors. Five distinct models were carefully selected and tested using recent observational datasets, including CC, SNe Ia using the PN dataset, and BAO, along with three cosmology-independent priors sourced from the literature. The objective was to assess how various cosmological parameters are impacted by different forms of $f(T)$ gravity and their compatibility with observational data as well as $\Lambda$CDM cosmology.

To facilitate a comprehensive cross-analysis of the different $f(T)$ models, datasets, and priors, a whisker plot illustrating each cosmological parameter against the others is presented in Fig. 5.7. The shaded regions in the $H_0$ column represented the values of each prior, providing clear insights into the direct influence of these priors on cosmological parameters.

The initial three models, $f_{1-3}$CDM, have the capacity to reduce to the $\Lambda$CDM model. However, they introduce an additional model parameter, $p_i$ ($i = 1, 2, 3$), which plays a pivotal role. A specific $p_i$ value will reduce the model to $\Lambda$CDM. Therefore, to facilitate, comparison and for statistical analysis purposes, an MCMC run for $\Lambda$CDM was also performed as discussed in Sec. 5.1.1.

Furthermore, the cosmological parameters derived from these three models align with findings in previous literature [237, 217, 269], falling within $1-2\sigma$ regions of $\Lambda$CDM. Notably, both the Hubble constant and the matter density parameter closely resemble those obtained in $\Lambda$CDM. The value at which the models reduce to $\Lambda$CDM, denoted by $p_i = 0$, is represented by an orange dashed line. It is observed that, for the most part, the obtained $p_i$ values for the first three models fall within the $1\sigma$ range of $\Lambda$CDM.

Focusing on the $H_0$ parameter for $f_{1-3}(T)$, the green, red, and violet regions in Fig. 5.7 represent the R19, HW, and TRGB prior values, respectively. Notably, the green whiskers, reflecting datasets with the R19 prior, consistently extend above their corresponding blue whisker counterparts, indicating a tendency towards higher $H_0$ values. This suggests that the R19 prior tends to push the value of $H_0$ towards higher values, albeit not quite to the extent of the R19 prior itself. The same observation holds true for the HW prior, though to a lesser extent, given that the value of the HW prior is slightly lower than that of the R19. In contrast the, the violet markers, representing datasets with the TRGB prior obtained

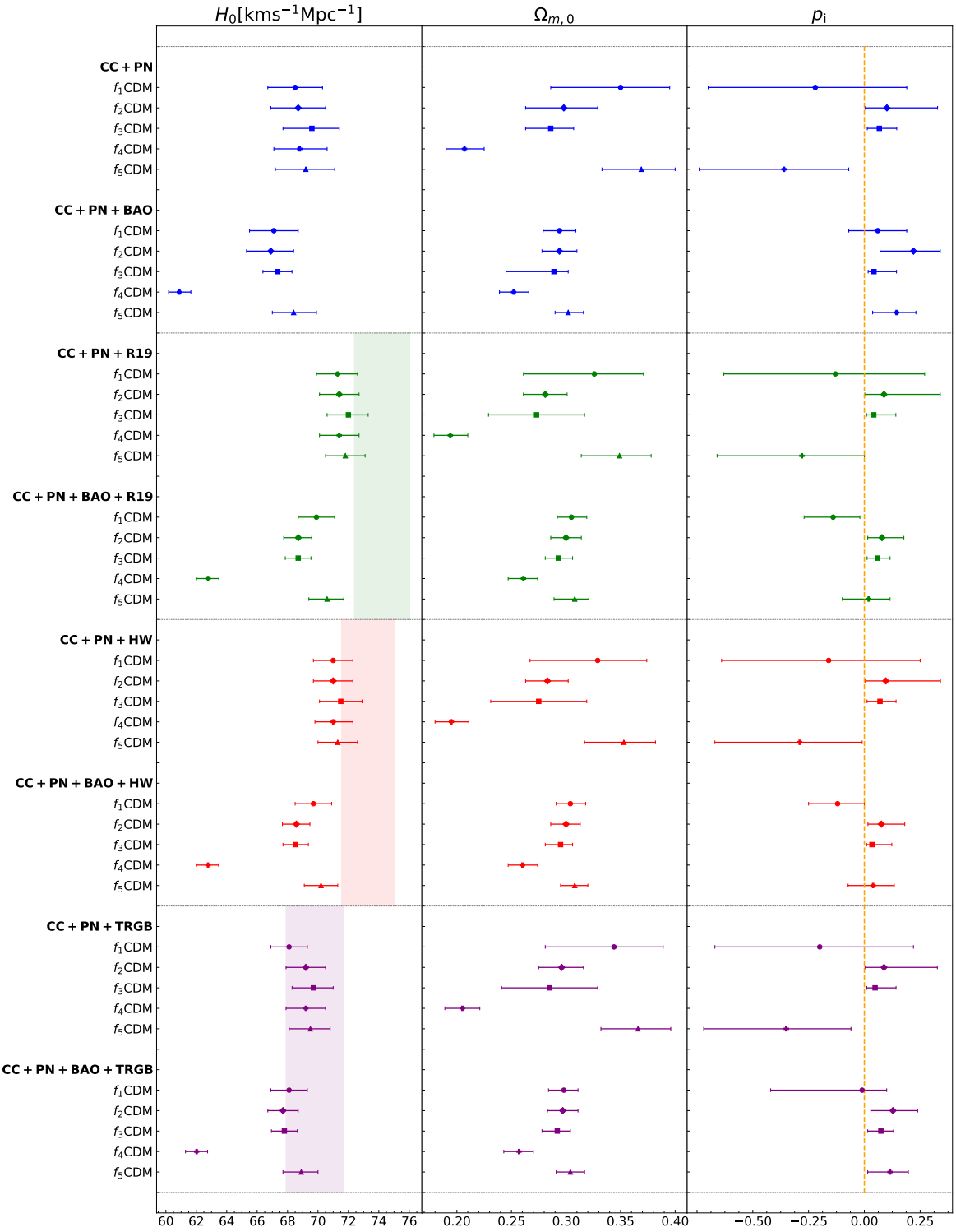


Figure 5.7: A whisker plot showing the three parameters $\{H_0, \Omega_{m,0}, p_i\}$ The $p_i$ parameter represents $p_1$ for $f_1$CDM, $\frac{1}{p_2}$ for $f_2$CDM, $\frac{1}{p_3}$ for $f_3$CDM, $p_4$ for $f_4$CDM and $p_5$ for $f_5$CDM. Each section represents the best fits for CC+PN and CC+PN+BAO together with the different priors where blue, green, red and purple correspond to: no prior, R19 prior, HW prior and TRGB prior. The shaded bands represent the priors with their $1\sigma$ uncertainty whilst the orange dashed line denotes the $\Lambda$CDM model.

from the MCMC results, are much closer to the TRGB prior itself. This suggests that the TRGB prior has a more subdued impact on the $H_0$ best fit values compared to the R19 and HW priors, as seen by the closer alignment of the violet markers with the blue markers in Fig. 5.7.

The extra freedom parameter in the $f(T)$ models ($p_i$), offers more flexibility in fitting observational data. While these models can better approximate the data, they are punished by the statistical indicators, when compared to $\Lambda$CDM model. Indeed these models produce higher AIC and BIC. Indeed, the $\Delta$AIC and $\Delta$BIC values for these models show that the $\Lambda$CDM still remains favoured however in certain instances, particularly in $f_{1-2}$CDM, the preference to the standard model of cosmology is not decisive or strong, prompting further investigation and analysis.

The latter two models, $f_{4-5}$CDM, are of particular interest as they do not converge to the $\Lambda$CDM model for any parameter values. In the case of the $f_4$CDM model, the absence of the $p_4$ parameter at the background level distinguishes it from the others. A significant observation regarding the $H_0$ parameter obtained from the MCMC runs is that the values tend to be significantly lower, indicating potential issues with the model's performance. This is reinforced when also including the BAO dataset and obtaining low values for the matter density parameter there as well. Moreover, the $f_4$CDM model lacks the $p_4$ parameter at background level, and is therefore not included in the last column of Fig. 5.7. In this context, the MCMC runs had one less parameter to consider and thus, the statistical indicators will not be severely punished by the number of parameters. In this sense, for the CC+PN dataset this turns out to be a great benefit as the $\Delta$AIC and $\Delta$BIC have low values in comparison with $\Lambda$CDM cosmology. However, this favorable outcome is not mirrored in the CC+PN+BAO dataset combinations, where the model has exceptionally large statistical indicator values, such that the viability of the model comes into question.

On the other hand, the $f_5$CDM model, has cosmological parameter values that align reasonably well with those of the other models. However, the statistical quantifiers still indicate large values, such that the $\Lambda$CDM has strong preference. Thus, similar to the $f_4$CDM, this model is brought into question whether it should be a competitive framework for cosmology.

In light of these findings, the pivotal question that emerges becomes: are these models cosmologically viable models within the broader framework of $f(T, B)$ gravity? Can these models effectively replicate the late-time cosmological dynamics observed in $f(T, B)$ gravity? The next chapter attempts to answer these questions by constraining cosmological parameters in $f(T, B)$ cosmology.

# 6

# $f(T,B)$ cosmological models in the late-time Universe

A noteworthy aspect of the relationship between GR and its teleparallel equivalent, the TEGR, is the equivalence between the Ricci scalar $\mathring{R}$ and the torsion scalar $T$, along with a boundary scalar $B$. This equivalence facilitates the generalisation of the $f(T)$ framework, leading to the formulation of $f(T,B)$ gravity, in which both the torsion scalar and the boundary term appear through an arbitrary function $f$. This generalisation is inspired by the extended forms of $f(\mathring{R})$ gravity [70, 153, 270, 271], as in the limit where $f(T,B) \to f(-T+B) = f(\mathring{R})$, yielding equivalent equations of motion.

In this chapter, which was presented and published in Briffa et al. [188], $f(T,B)$ gravity is strategically employed as a tool to model the effects of a dynamical cosmological constant, $\Lambda$, while retaining the CDM aspect of the standard cosmological model. The objective is to replicate the behaviours attributed to dark energy, thereby addressing prominent cosmological tensions, particularly the Hubble tension.

To further this exploration, three distinct $f(T,B)$ models have been identified, building on the groundwork laid in the previous chapter, which focused on $f(T)$. Among these models, two are designed to exhibit a $\Lambda$CDM limit, while the third is deliberately chosen to deviate from this limit across all parameter values. This selection allows for an assessment of each model's predictive capabilities regarding the late-time expansion history of the observable Universe within the $f(T,B)$ gravity framework, facilitating a comparative analysis of how well these models align with current observational data.

To achieve this, the MCMC technique will be employed to effectively constrain the cosmological parameters. This statistical approach will enable a rigorous evaluation of the models' fit to observational data, probing their viability in accurately describing the dynamics of the Universe. Through this analysis, valuable insights into the implications of

$f(T,B)$ gravity for addressing cosmological tensions will be uncovered.

## 6.1 | Formulation of the $H(z)$ Equation in $f(T,B)$ Cosmology

Constraining parameters for viable $f(T,B)$ models entails employing algorithms like the MCMC technique. However, for efficient utilisation of this technique, having an $H(z)$ equation that is computationally tractable is essential. Nevertheless, when examining the modified Friedmann equation for $f(T,B)$, as depicted in Eq. 2.73, directly deriving an equation for $H(z)$ presents challenges. Instead, as will be illustrated shortly, a second-order differential equation of $H$ with respect to $z$ can be formulated, thus providing a pathway to solving for $H(z)$.

Consider the first modified Friedman Equation for $F(B)$, Eq. 2.73 which can be re-written as follows

$$-F + BF_B - T + 6H\dot{F}_B = 2\kappa^2\rho\,, \tag{6.1}$$

where the dot derivative is again referring to a derivative with respect to time. The initial step to derive a differential equation involves expressing all components in the equation in terms of redshift. The chain rule is therefore applied, yielding,

$$\dot{F} = \frac{\mathrm{d}F(B)}{\mathrm{d}t} = \frac{\mathrm{d}F}{\mathrm{d}B}\frac{\mathrm{d}B}{\mathrm{d}t} = F_B\dot{B}\,, \tag{6.2}$$

and thus, $\dot{F}_B = F_{BB}\dot{B}$. Consequently, Eq. 6.1 becomes

$$-F + Bf_B - T + 6H(F_{BB}\dot{B}) = 6H_0^2(\Omega_{m,0}(1+z)^3 + \Omega_{r,0}(1+z)^4)\,, \tag{6.3}$$

where $\rho = \frac{3}{8\pi G}H_0^2(\Omega_{m,0}(1+z)^3 + \Omega_{r,0}(1+z)^4)$. Additionally, given that $B = -6(3H^2 + \dot{H})$, $\dot{B}$ is evaluated as

$$\dot{B} = -6(6H\dot{H} + \ddot{H})\,. \tag{6.4}$$

Substituting this expression in Eq. 6.3, the following second order differential equation is obtained

$$\ddot{H} = \frac{-1}{36HF_{BB}}\left[6H_0^2\left(\Omega_{m,0}(1+z)^3 + \Omega_{r,0}(1+z)^4\right) + F - BF_B + T\right] - 6H\dot{H}\,. \tag{6.5}$$

However, it is noteworthy to mention that the above second order differential equation is with respect to time. Hence, using the relations between the scale factor and redshift, together with $H(z)$ one can deduce that

$$\dot{H} = -(1+z)H(z)H'(z) \quad \text{and} \tag{6.6}$$

$$\ddot{H} = H^2(z)H'(z)(1+z) + H(z)H'^2(z)(1+z)^2 + H^2(z)H''(z)(1+z)^2\,, \tag{6.7}$$

which leads to the following Friedmann equation

$$H''(z) = \frac{-1}{36(1+z)^2 H^3(z) F_{BB}} \Big[ 6H_0^2 \left( \Omega_{m,0}(1+z)^3 + \Omega_{r,0}(1+z)^4 \right) + F - BF_B + T \\ -216H^3(z)H'(z)(1+z)F_{BB} \Big] - \frac{H'(z)}{(1+z)} - \frac{H'^2(z)}{H(z)} . \quad (6.8)$$

This differential equation will be the general Friedman equation used in the subsequent sections (except for the ΛCDM model), which is then solved for $H(z)$ in order to be able to constrain the $f(T, B)$ model parameters.

## 6.2 | Constraints on viable $f(T, B)$ cosmological models

In this section the MCMC algorithm is applied to three $f(T, B)$ models using observational data. Similar to how constraints were placed on the $f(T)$ models, recent data surveys are utilised. Essential baseline datasets, including the CC, PN, and BAO datasets, are employed, which are described in further detail in Sec. 3.3.2.

The subsequent sections will present and explore the constrained parameters for the following three $f(T, B)$ models:

- Power Law Model (detailed in Sec. 6.2.2 further on)
- Square Root exponential (detailed in Sec. 6.2.3 further on)
- Logarithmic Model (detailed in Sec. 6.2.4 further on)

These models will undergo constraints against two primary observational settings: CC+PN and CC+PN+BAO, provided CC alone is not sufficiently reliable, primarily due to its limited sample size. Additionally, an assessment will be made regarding the consistency of these three models and dataset combinations with two significant Hubble constant priors. Specifically, the updated versions of the SH0ES Collaboration prior (R21) and measurements from the TRGB (F21) are implemented, detailed further Table 3.1. These observational datasets, along with the priors, will be utilised in the MCMC algorithm, to determine the maximum likelihood or, equivalently, the minimum $\chi^2$ for each respective dataset combination.

In addition to the fundamental analysis of each $f(T, B)$ model against observational data, an integral aspect of this study involves comparing these models to the well-established ΛCDM model. The introduction of the ΛCDM model into the analysis serves as a crucial reference point. By establishing a baseline with the ΛCDM model, the relative performance of the $f(T, B)$ models can be assessed. This comparative analysis allows us to determine

whether the $f(T, B)$ models offer improvements over the traditional ΛCDM framework or if they are surpassed by it in terms of their ability to accurately describe the observed Universe.

To perform this comparison, the two widely-used model selection criteria, namely AIC and BIC, are employed. By computing these values for each $f(T, B)$ model as well as for the ΛCDM model, an assessment can be made regarding which model offers the best balance between explanatory power and model complexity. The comparison with ΛCDM model provides valuable insights into the viability and efficacy of the $f(T, B)$ and discern whether the $f(T, B)$ models provide a more accurate and better description of cosmological phenomena or if they fall short compared to the well-established ΛCDM model.

### 6.2.1 | ΛCDM model – $f_0(T, B)$CDM model

With the intention of comparing to the ΛCDM model and similar to the $f(T)$ models, the initial MCMC run is performed for the standard model of cosmology, using Eq. 2.49. This section will thus present the results for ΛCDM, with a more detailed analysis provided for the other models as they are compared with it.

The posteriors together with the confidence regions for the resulting constrained parameters are shown in Fig. 6.1. Similar to $f(T)$, the constrained parameters for combined datasets CC+PN are at the top and for CC+PN+BAO are at the bottom of the figure. Being the ΛCDM model, the MCMC chains converge quickly, with Gaussian errors. This is more enhanced in Table. 6.1a, in which precise results for the chains are shown and errors are shown to be almost Gaussian.

Upon examining these results closely, one can observe their similarity to those obtained in the previous chapter, Sec. 5.1.1. Specifically, $H_0$ adn $\Omega_{m,0}$ exhibit an anticorrelation with CC+PN, but show a more degenerate, almost correlated, relationship with CC+PN+BAO. While certain alterations are attributable to the updated prior values, the consistency observed in the results underscores their reliability.

The second part of Table 6.1 pertains to the statistical metrics. Specifically, Table 6.1b displays the minimum $\chi^2$ value, alongside the statistical indicators of AIC and BIC, against which the subsequent models will be compared.

### 6.2.2 | Power Law Model – $f_1(T, B)$CDM model

Inspired by the power law model within the $f(T)$ framework, a similar model is proposed for $f(T, B)$, which is defined as follows

$$F_1(B) = r_1(-B)^{p_1}\,, \tag{6.9}$$

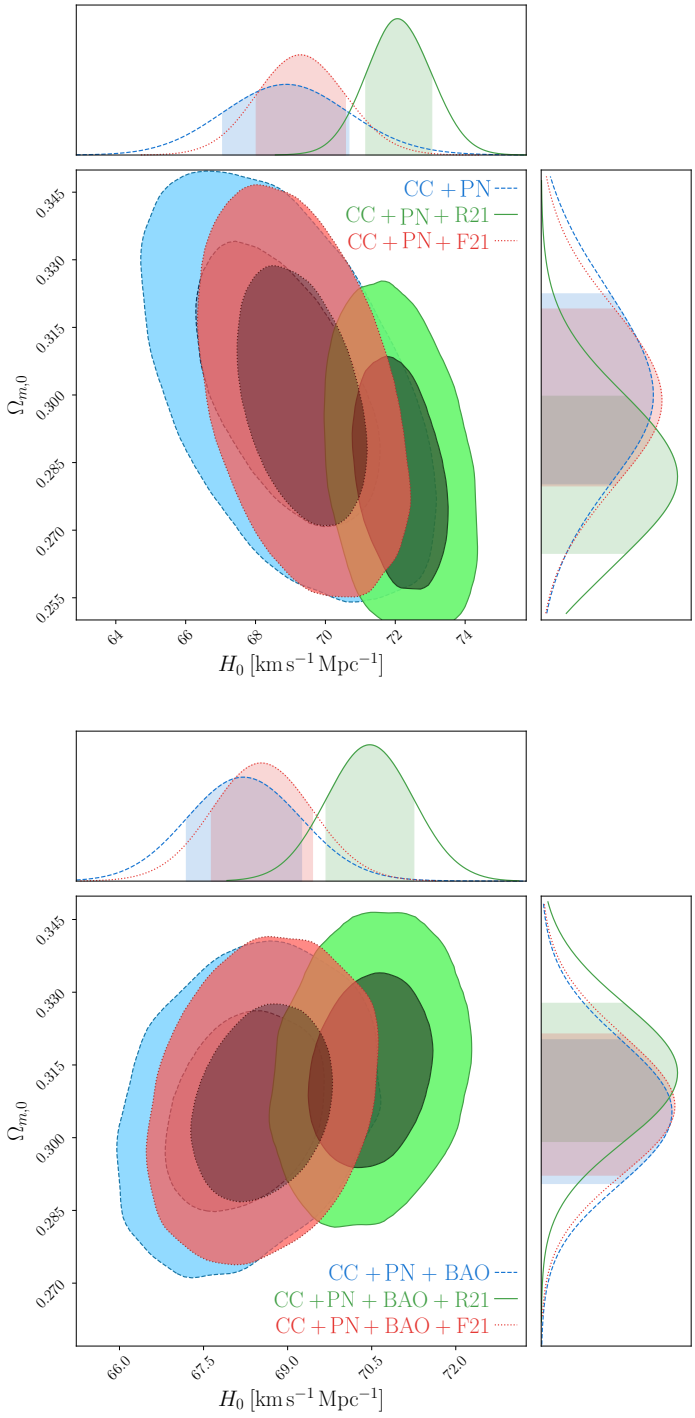


Figure 6.1: Contour plots for the ΛCDM model. *Top:* Confidence levels and posteriors for the model using the CC+PN setting combined with different priors denoted by R21 (green colour), F21 (red colour) and no prior (blue colour). *Bottom:* Confidence levels and posteriors for the model using the CC+PN+BAO with the same priors being implemented.

| Data Sets | $H_0$ [km/s/Mpc] | $\Omega_{m,0}$ | $M$ |
|---|---|---|---|
| CC + PN | $68.8 \pm 1.8$ | $0.300^{+0.023}_{-0.019}$ | $-19.381^{+0.051}_{-0.054}$ |
| CC + PN + R21 | $72.05^{+0.99}_{-0.90}$ | $0.282^{+0.018}_{-0.017}$ | $-19.292^{+0.028}_{-0.027}$ |
| CC + PN + F21 | $69.3 \pm 1.3$ | $0.299^{+0.020}_{-0.019}$ | $-19.370 \pm 0.038$ |
| CC + PN + BAO | $68.2 \pm 1.0$ | $0.305 \pm 0.015$ | $-19.403^{+0.037}_{-0.034}$ |
| CC + PN + BAO + R21 | $70.46^{+0.80}_{-0.77}$ | $0.313 \pm 0.014$ | $-19.328^{+0.027}_{-0.026}$ |
| CC + PN + BAO + F21 | $68.54 \pm 0.90$ | $0.306^{+0.015}_{-0.014}$ | $-19.389^{+0.030}_{-0.032}$ |

(a) Results for the constrained parameters for the $f_1(T, B)$ model obtained from the MCMC runs.

| Data Sets | $\chi^2_{\text{min}}$ | AIC | BIC |
|---|---|---|---|
| CC + PN | 1041.74 | 1047.74 | 1062.83 |
| CC + PN + R21 | 1046.45 | 1052.45 | 1067.41 |
| CC + PN + F21 | 1041.88 | 1047.88 | 1062.83 |
| CC + PN + BAO | 1050.01 | 1056.01 | 1071.00 |
| CC + PN + BAO + R21 | 1063.44 | 1069.44 | 1084.45 |
| CC + PN + BAO + F21 | 1050.68 | 1056.68 | 1077.69 |

(b) Results for the minimum chi-squared together with the AIC and BIC values, Eqs. 3.68,3.70, for $f_1(T, B)$CDM model.

Table 6.1: Output parameter results and statistical indicators for ΛCDM Model. The first column of both sub-tables denote the different datasets and prior combinations.

where $r_1$ and $p_1$ are the model parameters, analogous to the $f(T)$ case. Given the computational complexity inherent from Eq. 6.8, it is best to minimise the number of parameters to streamline the computational efficiency. Consequently, as previously done, determining the constant term $r_1$ in Eq. 6.9 the number of model parameters are minimised. This process involves evaluating the Friedmann equation at the present epoch ($t = t_0$). By computing all requisite derivatives from Eq. 6.9, the constant parameter $r_1$ in $\mathrm{km/s/Mpc}^{2-2p_1}$ can be expressed as follows

$$r_1 = \frac{6H_0^2(\Omega_{m,0} + \Omega_{r,0} - 1)}{(p_1 - 1)(-B_0)^{p_1} + 6H_0\left(p_1(p_1 - 1)(-B_0)^{p_1 - 2}\dot{B}|_{t=t_0}\right)}\,, \tag{6.10}$$

where $B_0$ refers to the boundary term (Eq. 2.55), evaluated at current times whilst $\dot{B}|_{t=t_0}$ is its derivative with respect to time evaluated at current times. Therefore, the only model parameter, left for this model is the $p_1$ constant.

Consequently, the differential equation for obtaining $H(z)$ can be calculated using Eq. 6.8. Substituting the necessary derivatives from Eq. 6.9, it is expressed as

$$\begin{aligned} H'' = \frac{-1}{36r_1(1+z)^2H^3p_1(p_1-1)(-B)^{p_1-2}} + \Big[6H_0^2\left(\Omega_{m,0}(1+z)^3 + \Omega_{r,0}(1+z)^4\right) \\ -6H_0^2 + r_1(1-p_1)(-B)^{p_1} - 216r_1p_1(p_1-1)H^3H'(1+z)(-B)^{p_1-2}\Big] \\ - \frac{H'}{1+z} - \frac{H'^2}{H}\,. \end{aligned} \tag{6.11}$$

Studying the equation for the power law model, Eq. 6.9, more closely reveals that TEGR is replicated when $r_1 = -1$ and $p_1 = 1$, thereby setting an upper bound for $p_1 < 1$ to describe an accelerating Universe. Contrastingly, akin to the $f_1$CDM scenario in the $f(T)$ framework, when $p_1 = 0$, the $\Lambda$CDM limit is achieved.

The posteriors, along with the confidence regions for the two different dataset combinations, namely CC+PN (top) and CC+PN+BAO (bottom) , are depicted in Fig. 6.2. Additionally, the figure includes confidence level plots for the R21 and F21 priors, illustrated by the green and red colours, respectively.

The figures highlight a significant trend: the inclusion of priors leads to an upward shift in the $H_0$ value, especially notable with the R21 prior as expected. The F21 prior also influences this trend, although to a lesser extent, with its impact falling between those without any prior and those with R21 prior. A similar pattern to the $f(T)$ cases is observed for the CC+PN dataset combination, where an increase in $H_0$ coincides with a slight decrease in the matter density parameter. However, the confidence regions suggest a more simplistic and degenerate relationship between these parameters. Conversely, in the CC+PN+BAO dataset combination, there is a subtle shift towards a correlation between the parameters, albeit minor.

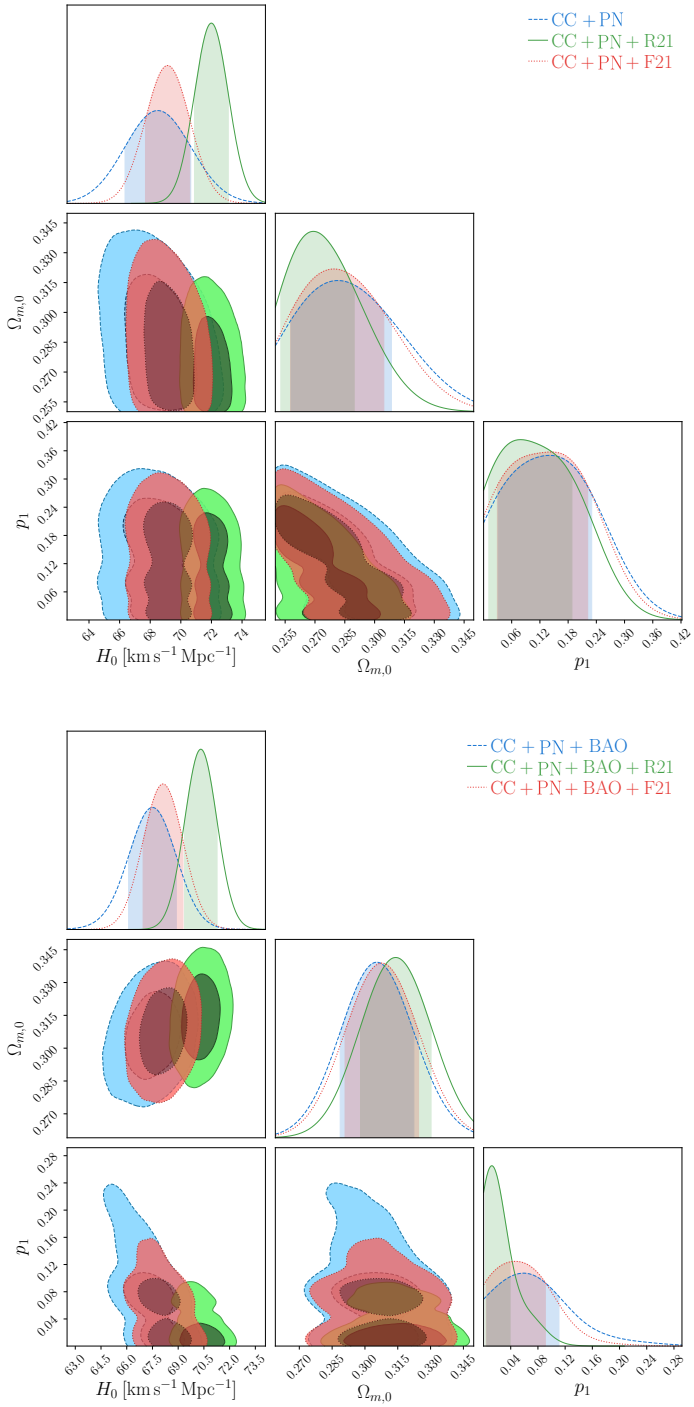


Figure 6.2: Contour plots for the Power Law model in the $f(T, B)$ framework. *Top:* Confidence levels and posteriors for the model using the CC+PN setting combined with different priors denoted by R21 (green colour), F21 (red colour) and no prior (blue colour). *Bottom:* Confidence levels and posteriors for the model using the CC+PN+BAO with the same priors being implemented.

| Data Sets | $H_0$ [km/s/Mpc] | $\Omega_{m,0}$ | $p_1$ | $M$ |
|---|---|---|---|---|
| CC + PN | $68.5^{+2.1}_{-2.2}$ | $0.281^{+0.027}_{-0.023}$ | $0.140^{+0.090}_{-0.109}$ | $-19.381^{+0.063}_{-0.064}$ |
| CC + PN + R21 | $72.0 \pm 1.1$ | $0.269^{+0.021}_{-0.016}$ | $0.080^{+0.108}_{-0.068}$ | $-19.27^{+0.19}_{-0.22}$ |
| CC + PN + F21 | $69.1^{+1.5}_{-1.4}$ | $0.279^{+0.025}_{-0.022}$ | $0.143^{+0.079}_{-0.113}$ | $-19.362^{+0.075}_{-0.078}$ |
| CC + PN + BAO | $67.5 \pm 1.4$ | $0.305 \pm 0.017$ | $0.058 \pm 0.053$ | $-19.396^{+0.090}_{-0.136}$ |
| CC + PN + BAO + R21 | $70.32^{+0.95}_{-0.94}$ | $0.314 \pm 0.016$ | $0.012^{+0.027}_{-0.0094}$ | $-19.327^{+0.029}_{-0.034}$ |
| CC + PN + BAO + F21 | $68.1 \pm 1.2$ | $0.308 \pm 0.017$ | $0.046^{+0.045}_{-0.042}$ | $-19.35^{+0.69}_{-0.78}$ |

(a) Results for the constrained parameters for the $f_1(T, B)$ model obtained from the MCMC runs.

| Data Sets | $\chi^2_{\text{min}}$ | AIC | BIC | $\Delta$AIC | $\Delta$BIC |
|---|---|---|---|---|---|
| CC + PN | 1040.94 | 1048.94 | 1068.88 | 1.21 | 6.19 |
| CC + PN + R21 | 1040.50 | 1053.50 | 1076.10 | 1.04 | 6.02 |
| CC + PN + F21 | 1040.98 | 1048.98 | 1068.92 | 1.10 | 6.08 |
| CC + PN + BAO | 1047.97 | 1055.97 | 1075.97 | $-0.04$ | 4.96 |
| CC + PN + BAO + R21 | 1062.23 | 1070.23 | 1090.24 | 0.79 | 5.79 |
| CC + PN + BAO + F21 | 1048.81 | 1056.81 | 1076.81 | 0.13 | 5.12 |

(b) Results for the minimum chi-squared together with the AIC and BIC values, Eqs. 3.68,3.70, for $f_1(T, B)$CDM model. The last two columns denote the respective differences of the AIC and BIC values with the $\Lambda$CDM model

Table 6.2: Output parameter results and statistical indicators for Power Law Model. The first column of both sub-tables denote the different datasets and prior combinations.

A common feature, similar to what occurred in the $f_1$CDM within the $f(T)$ framework, is the degeneracy between the $H_0$ parameter and the model parameter $p_1$. This degeneracy becomes slightly more anti-correlated with the addition of the BAO dataset. Interestingly, in this dataset combination, there appear to be two feasible sets of values for the $p_1$ parameter. Consequently, if one were to construct a Hubble diagram of $H(z)$ against redshift $z$, these two values of $p_1$ would influence the tilt of the graph, resulting in a similar range of $H_0$ values. Comparably, a similar relationship between the $p_1$ and $\Omega_{m,0}$ parameters emerges. In contrast, for CC+PN, the relationship between these parameters exhibits an anti-correlation in the conventional sense.

The specific values for the parameters $H_0$ in km s$^{-1}$Mpc$^{-1}$, $\Omega_{m,0}$, $p_1$, and the nuisance parameter $M$ are detailed in Table 6.2a. Notably, the values of $p_1$ are relatively lower compared to those obtained in the $f(T)$ framework. This trend is highlighted in the CC+PN+BAO combination, where the minimum value is reached for the combination with the F21 prior, yielding $p_1 = 0.046^{+0.045}_{-0.042}$. However, the highest value is obtained for the same F21 prior without the BAO dataset. Overall, there is a slight deviation from $\Lambda$CDM as the $p_1$ parameter falls within $2\sigma$ of such a model.

The maximum $H_0$ value is achieved for CC+PN+R21 with $H_0 = 72.0 \pm 1.1$ km s$^{-1}$ Mpc$^{-1}$, which is expected as R21 is the highest prior considered. Conversely the BAO dataset reflects influences from the early Universe and hence, the lowest $H_0$ value is obtained for CC+PN+BAO, with $H_0 = 67.5 \pm 1.4$, km, s$^{-1}$ Mpc$^{-1}$. Another interesting characteristic is that the value of $\Omega_{m,0}$ seems to be lower for CC+PN compared to CC+PN+BAO, and even relative to the general values of this parameter.

The second half of Table 6.1b includes $\chi^2_{\rm min}$, AIC, BIC, and their comparison with $\Lambda$CDM values. Notably, the $\Delta$AIC values appear relatively small, lacking significant evidence to favour the $\Lambda$CDM model over this one. Conversely, the $\Delta$BIC values suggest a different scenario, indicating a potential preference for the $\Lambda$CDM model. However, these results must be interpreted cautiously, especially considering the negative $\Delta$AIC value for CC+PN+BAO, technically implying a preference for this model over $\Lambda$CDM, although the significance is minimal. This observation arises from the lower $\chi^2_{\rm min}$ for this model with this specific dataset compared to $\Lambda$CDM. Similarly, the relatively low $\Delta$BIC suggests that $\Lambda$CDM is not strongly favoured over this model. Indeed, this observation should be considered within the broader context of the analysis, especially given the lack of clear definition in the 2D joint probability regions within the $f(T, B)$ framework.

### 6.2.3 | Square Root Exponential Model – $f_2(T, B)$CDM model

The subsequent model under consideration is the square-root exponential model, denoted as $f_2(T, B)$CDM, defined by the equation

$$f_2(B) = r_2 \,\mathrm{Exp}\left[-p_2\sqrt{\frac{B}{B_0}}\right], \tag{6.12}$$

where, $r_2$ and $p_2$ represent constant model parameters. The distinction from the $f(T)$ model lies in the fact that the exponential function is now a function of $B$. Following a similar approach as before, $r_2$ can be derived by evaluating the Friedmann equation at the present epoch. Thus, utilising Eq. 6.3 and computing the requisite derivatives from the model equation, $r_2$ in $\mathrm{km/s/Mpc^2}$ can be expressed as

$$r_2 = \frac{e^{p_2} 6H_0^2(\Omega_{m_o} + \Omega_{r,0} - 1)}{-1 - \frac{p_2}{2} + \frac{6H_0 p_2}{4B_0^2}(1+p_2)\dot{B}|_{t=t_0}}, \tag{6.13}$$

This leaves $p_2$ as the only new model parameter, which will be determined using the MCMC algorithm. This also allows for the determination of the differential equation

$$\begin{aligned} H'' = \frac{-BB_0\mathrm{Exp}\left[p_2\sqrt{\frac{B}{B_0}}\right]}{9r_2p_2(1+z)^2H^3\left(p_2\sqrt{\frac{B_0}{B}}\right)}\Bigg[6H_0^2\Big(\Omega_{m,0}(1+z)^3 + \Omega_{r,0}(1+z)^4\Big) - 6H_0^2 \\ + r_2\mathrm{Exp}\left[p_2\sqrt{\frac{B}{B_0}}\right]\left(1 - \frac{54p_2(1+z)H^3H'}{BB_0}\left(p_2 + \sqrt{\frac{B_0}{B}}\right)\right)\Bigg] \\ - \frac{H'}{1+z} - \frac{H'^2}{H}. \end{aligned} \tag{6.14}$$

Studying Eq. 6.12 in more detail, one can note that this model reduces to the ΛCDM for $p_2 = 0$.

The MCMC constraint analysis was therefore executed to constrain the parameters $H_0$, $\Omega_{m,0}$, and $p_2$, along with the nuisance parameter $M$, for various datasets and different priors. The resulting posteriors and $1\sigma$ and $2\sigma$ regions are shown in Fig. 6.3.

As expected and consistent with previous findings, priors on $H_0$ tend to elevate its values. Consequently, the density matter parameter tends to decrease accordingly, revealing an anti-correlation relationship, particularly pronounced in the CC+PN case. Notably, the highest $H_0$ value is observed in the dataset combination including the R21 prior, specifically CC+PN+R21 with $H_0 = 72.1^{+1.1}_{-1.0}$ km s$^{-1}$ Mpc$^{-1}$. Correspondingly, the lowest $\Omega_{m,0}$ value is attained for the same dataset and prior, registering $\Omega_{m,0} = 0.307 \pm 0.016$.

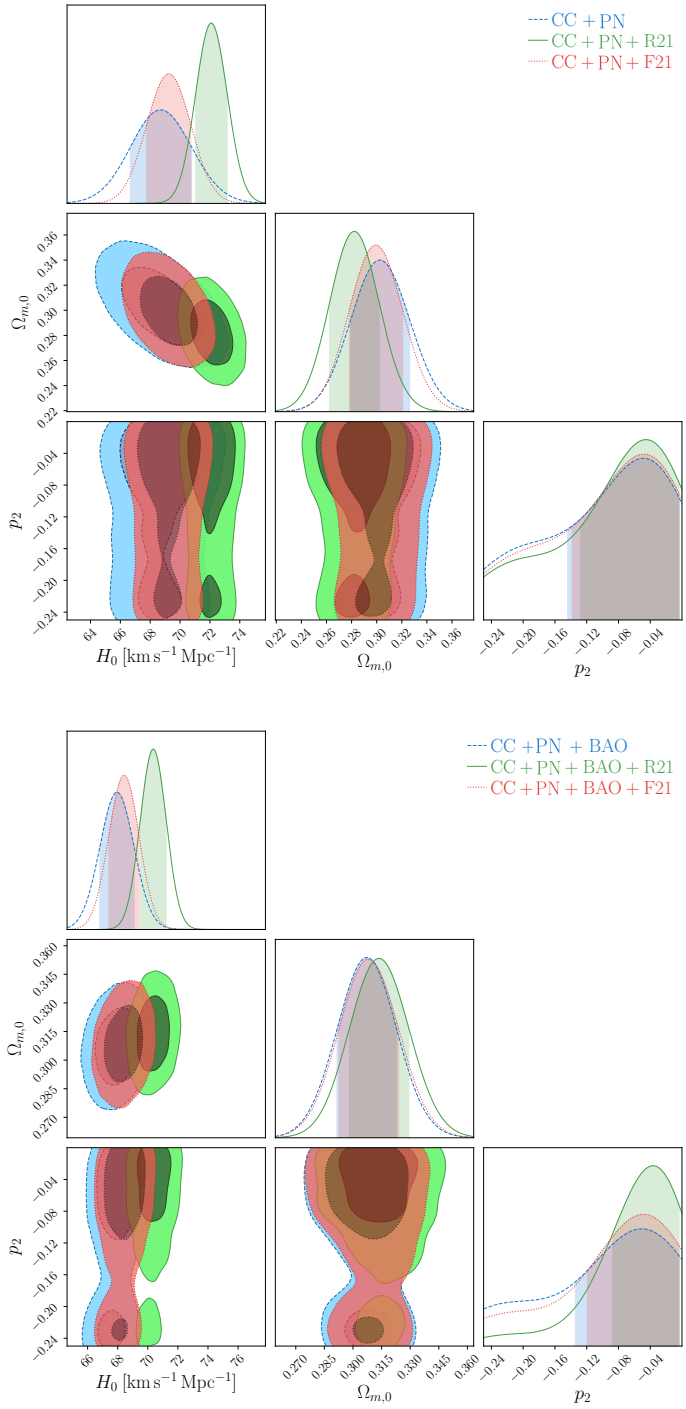


Figure 6.3: Contour plots for the Square-root Exponential model in the $f(T, B)$ framework. *Top:* Confidence levels and posteriors for the model using the CC+PN setting combined with different priors denoted by R21 (green colour), F21 (red colour) and no prior (blue colour). *Bottom:* Confidence levels and posteriors for the model using the CC+PN+BAO with the same priors being implemented.

| Data Sets | $H_0$ [km/s/Mpc] | $\Omega_{m,0}$ | $p_2$ | $M$ |
|---|---|---|---|---|
| CC + PN | $68.7^{+2.1}_{-2.0}$ | $0.302^{+0.024}_{-0.023}$ | $-0.049^{+0.045}_{-0.095}$ | $-19.398^{+0.115}_{-0.051}$ |
| CC + PN + R21 | $72.1^{+1.1}_{-1.0}$ | $0.282 \pm 0.020$ | $-0.045^{+0.041}_{-0.082}$ | $-19.288^{+0.030}_{-0.031}$ |
| CC + PN + F21 | $69.3 \pm 1.5$ | $0.299 \pm 0.021$ | $-0.048^{+0.044}_{-0.090}$ | $-19.368^{+0.043}_{-0.044}$ |
| CC + PN + BAO | $68.0^{+1.1}_{-1.2}$ | $0.307 \pm 0.016$ | $-0.050^{+0.046}_{-0.084}$ | $-18.95^{+0.25}_{-0.00}$ |
| CC + PN + BAO + R21 | $70.38^{+0.85}_{-0.87}$ | $0.314 \pm 0.016$ | $-0.037^{+0.033}_{-0.051}$ | $-19.329^{+0.053}_{-0.052}$ |
| CC + PN + BAO + F21 | $68.4^{+1.1}_{-1.2}$ | $0.307^{+0.016}_{-0.014}$ | $-0.044^{+0.046}_{-0.071}$ | $-18.7^{+7.7}_{-0.0}$ |

(a) Results for the constrained parameters for the $f_2(T,B)$CDM model obtained from the MCMC runs.

| Data Sets | $\chi^2_{\text{min}}$ | AIC | BIC | $\Delta$AIC | $\Delta$BIC |
|---|---|---|---|---|---|
| CC + PN | 1040.70 | 1048.70 | 1068.64 | 0.96 | 5.95 |
| CC + PN + R21 | 1045.69 | 1053.69 | 1073.63 | 1.23 | 6.22 |
| CC + PN + F21 | 1040.89 | 1048.89 | 1068.83 | 1.01 | 6.00 |
| CC + PN + BAO | 1048.31 | 1056.31 | 1076.31 | 0.30 | 5.30 |
| CC + PN + BAO + R21 | 1062.46 | 1070.46 | 1090.46 | 1.02 | 6.02 |
| CC + PN + BAO + F21 | 1049.22 | 1057.23 | 1077.23 | 0.54 | 5.54 |

(b) Results for the minimum chi-squared together with the AIC and BIC values, Eqs. 3.68,3.70, for $f_2(T,B)$CDM model. The last two columns denote the respective differences of the AIC and BIC values with the $\Lambda$CDM model

Table 6.3: Output parameter results and statistical indicators for the Exponential Model. The first column of both sub-tables denote the different datasets and prior combinations.

The detailed numerical results for all dataset combinations are provided in Table 6.3a. Regarding $p_2$, the non-Gaussianity of its values is notable in the errors, which, despite being predominantly negative, exhibit relatively high uncertainty. However, it is worth noting that the ΛCDM limit falls within $2\sigma$ of the observed values. Additionally, the apparent anti-correlation observed in the $f_1$(T,B)CDM model between the $p_i$ parameter($i = 1, 2$) and $\Omega_{m,0}$ is absent in this scenario, across both cases.

The statistical indicators, as displayed in Table 6.3b alongside the minimum $\chi^2$ values, offer insights into the model's fit relative to ΛCDM. Compared to the standard model (ΛCDM), the relative indicators, namely ΔAIC and ΔBIC, exhibit lower values. Specifically, all ΔAIC values are below 1.23, while ΔBIC values remain under 6.02. This suggests a lack of strong preference for the ΛCDM framework based on these metrics alone, although this is on the verge of limits according to Jeffrey's limits. In addition, it is also crucial to consider the broader context. Similar to the $f_1(T,B)$CDM case, the presence of dual valid regions for the $p_2$ parameter is noteworthy, accompanied by considerable uncertainties in its values. Thus, while the statistical measures suggest a certain neutrality towards ΛCDM, the intricate uncertainties in the parameter underscores the complexity of the model.

### 6.2.4 | Logarithmic Model – $f_3(T,B)$CDM model

The final model under consideration is the logarithmic model, denoted as $f_3(T,B)$CDM, expressed by the equation

$$f_3(B) = r_3 \ln\left[p_3 \frac{B_0}{B}\right], \tag{6.15}$$

where $r_3$ and $p_3$ are model parameters. Determining $r_3$ involves evaluating the Friedmann equation at the present time ($t = t_0$), using Eq.6.3

$$r_3 = \frac{6H_0^2\left(\Omega_{m,0} + \Omega_{r,0} - 1\right)}{\frac{6H_0}{B_0^2}\dot{B}|_{t=t_0} - 1 - \ln p_3}. \tag{6.16}$$

Therefore, since $r_3$ can be determined using the above equation, the only model parameter left is $p_3$. Consequently, the differential equation can be derived using Eq.6.8, where the necessary derivatives are substituted to obtain

$$H'' = \frac{-B^2}{36r_3(1+z)^2H^3}\left[6H_0^2\left(\Omega_{m,0}(1+z)^3 + \Omega_{r,0}(1+z)^4\right) - 6H_0^2 + r_3\ln\left[p_3\frac{B_0}{B}\right] + r_3 - \frac{216r_3}{B^2}H^3H'(1+z)\right] - \frac{H'}{1+z} - \frac{H'^2}{H}. \tag{6.17}$$

An intriguing characteristic for this model is that no value of $p_3$ can reproduce the ΛCDM model. From the three models considered, this feauture is unique to $f_3(T, B)$CDM .

The probability distributions depicted in Fig. 6.4 provide a view of the $1D$ and $2D$ joint probability regions. Interestingly, this model diverges notably in its value of the Hubble constant ($H_0$) when compared to previous models, despite lacking a well-defined ΛCDM limit. The dataset CC+PN+R21 yields the highest $H_0$ value as in previous models, with a value of $72.09^{+0.97}_{-0.98}$ km s$^{-1}$ Mpc$^{-1}$. Furthermore, when BAO data is included but without any prior, the $H_0$ value drops to its lowest value in this model, at $66.0^{+1.3}_{-1.4}$ km s$^{-1}$ Mpc$^{-1}$ as detailed in Table 6.4a. This particular value aligns with the lower end of the spectrum observed across models.

Moreover, a similar trend of lower values is observed in the values of the matter density parameter as shown in Table 6.4a. This is especially evident within the CC+PN dataset, regardless of the inclusion of priors, although an improvement is noted when including BAO. These observations prompt a reassessment of the model's validity and predictive capability. It highlights the need for further investigation into the underlying framework and parameters driving the model's predictions, particularly regarding the observed lower values of the matter density parameter.

Despite the absence of a specific value for the $p_3$ parameter anticipated from the MCMC runs, it consistently converges to small values, approaching zero. This tendency persists across all dataset combinations, with a more pronounced effect observed when incorporating the BAO dataset. Furthermore, an evident anti-correlation emerges between this parameter and both the Hubble constant and the matter density parameter, particularly evident with the inclusion of the BAO dataset.

The statistical indicators present a contrasting perspective compared to the previous models. The $\chi^2_{\text{min}}$ values are slightly elevated for this model, consequently resulting in higher ΔAIC and ΔBIC values. When considering datasets comprising of CC+PN, the statistical indicators exhibit similar values irrespective whether a prior is added or not. However, with the inclusion of BAO, a more variant scenario emerges, with different values obtained upon the specific prior utilised. Overall, the indications suggest a preference for the ΛCDM model over this logarithmic model. This further reinforces the discussion on the model's viability and its comparability to established cosmological frameworks.

## 6.3 | Conclusion

The previous chapters, Chapters 4 and 5, sparked an interest in exploring the viability of various models established in the literature within the realm of $f(T)$ gravity. This led to

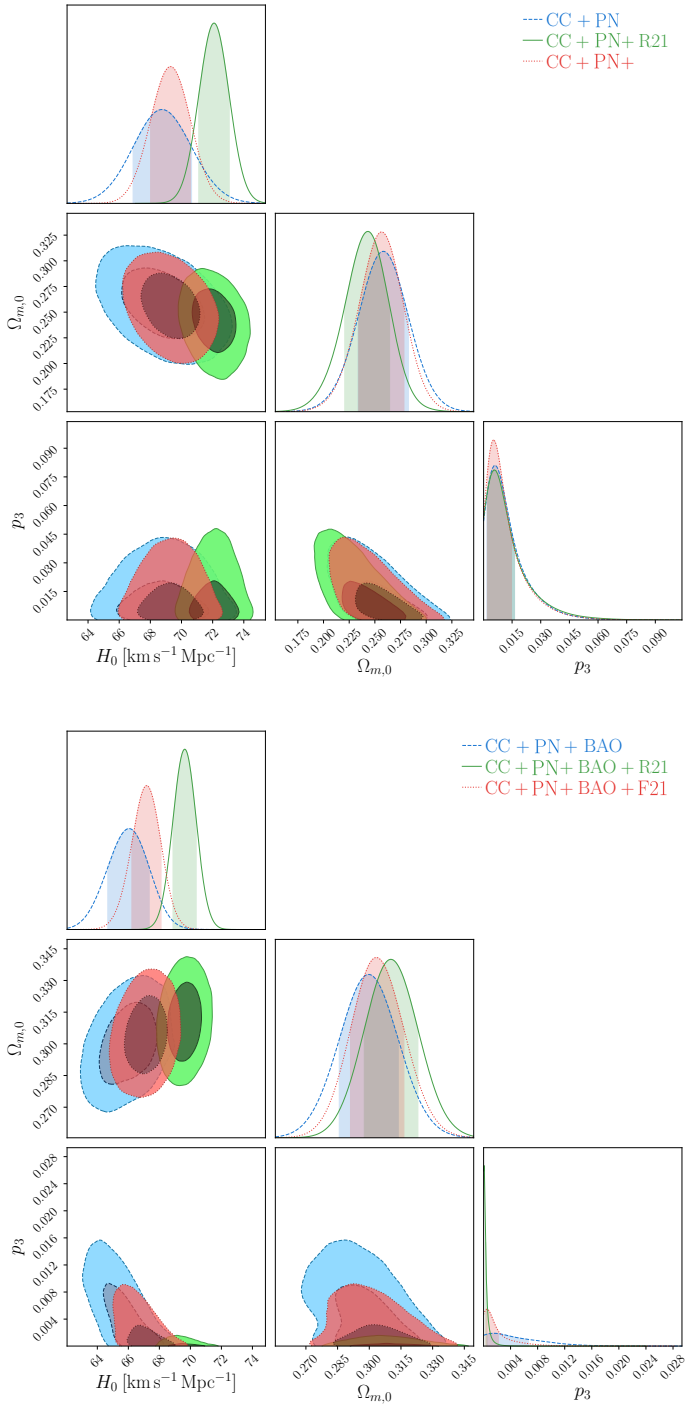


Figure 6.4: Contour plots for the Logarithmic model in the $f(T, B)$ framework. *Top:* Confidence levels and posteriors for the model using the CC+PN setting combined with different priors denoted by R21 (green colour), F21 (red colour) and no prior (blue colour). *Bottom:* Confidence levels and posteriors for the model using the CC+PN+BAO with the same priors being implemented.

| Data Sets | $H_0$ [km/s/Mpc] | $\Omega_{m,0}$ | $p_3/10^{-3}$ | $M$ |
|---|---|---|---|---|
| CC + PN | $68.8 \pm 1.9$ | $0.258^{+0.025}_{-0.024}$ | $5.9^{+10.4}_{-4.0}$ | $-19.370^{+0.059}_{-0.056}$ |
| CC + PN + R21 | $72.09^{+0.97}_{-0.98}$ | $0.243^{+0.021}_{-0.022}$ | $5.5^{+10.8}_{-3.4}$ | $-19.274 \pm 0.028$ |
| CC + PN + F21 | $69.3 \pm 1.3$ | $0.257 \pm 0.022$ | $5.3^{+9.4}_{-3.2}$ | $-19.355^{+0.039}_{-0.036}$ |
| CC + PN + BAO | $66.0^{+1.3}_{-1.4}$ | $0.300 \pm 0.014$ | $1.53^{+5.13}_{-1.00}$ | $-19.442^{+0.035}_{-0.049}$ |
| CC + PN + BAO + R21 | $69.64^{+0.73}_{-0.76}$ | $0.310 \pm 0.013$ | $0.32^{+0.19}_{-0.0}$ | $-19.340^{+0.023}_{-0.024}$ |
| CC + PN + BAO + F21 | $67.17 \pm 0.94$ | $0.303^{+0.013}_{-0.012}$ | $0.49^{+1.7}_{-0.12}$ | $-19.429^{+0.047}_{-0.019}$ |

(a) Results for the constrained parameters for the $f_3(T,B)$CDM model obtained from the MCMC runs.

| Data Sets | $\chi^2_{\text{min}}$ | AIC | BIC | $\Delta$AIC | $\Delta$BIC |
|---|---|---|---|---|---|
| CC + PN | 1042.08 | 1050.08 | 1070.02 | 2.35 | 7.33 |
| CC + PN + R21 | 1046.93 | 1054.93 | 1074.87 | 2.48 | 7.46 |
| CC + PN + F21 | 1042.23 | 1050.23 | 1070.17 | 2.35 | 7.33 |
| CC + PN + BAO | 1049.21 | 1057.21 | 1077.20 | 1.20 | 6.20 |
| CC + PN + BAO + R21 | 1066.77 | 1074.77 | 1094.77 | 5.33 | 10.33 |
| CC + PN + BAO + F21 | 1049.78 | 1057.78 | 1077.78 | 1.09 | 6.09 |

(b) Results for the minimum chi-squared together with the AIC and BIC values, Eqs. 3.68,3.70, for $f_3(T,B)$CDM model. The last two columns denote the respective differences of the AIC and BIC values with the $\Lambda$CDM model

Table 6.4: Output parameter results and statistical indicators for the Logarithmic Model. The first column of both sub-tables denote the different datasets and prior combinations.

a deeper investigation and a generalisation by incorporating both the torsion scalar $T$ and the boundary scalar $B$, which together form the Ricci scalar. Hence, $f(T, B)$ constitutes a more general framework of gravity. In this regard, three models of $f(T, B)$ were examined to assess their their performance against $\Lambda$CDM with the data samples used. Two of these models were specifically chosen to reproduce the standard cosmological model for certain values of the model parameter $p_i$ for $i = 1, 2$, including the Power Law Model discussed in Sec. 6.2.2 and the Square-Root Exponential outlined in Sec. 6.2.3. On the other hand, the Logarithmic Model detailed in Sec. 6.2.4 was selected with the aim of diversification, as no specific value of $p_3$ leads to the $\Lambda$CDM case.

These models were evaluated against cosmological observations using the MCMC algorithm. The baseline analysis relied on the CC+PN dataset, which was later supplemented with BAO data in order to incorporate early Universe effects. Additionally, two updated priors, derived from the SH0ES Collaboration and the F21 TRGB Calibration Update, were incorporated. The primary aim of this investigation was to assess the framework's suitability at late times and gauge its performance against observational datasets. The analysis focused on key cosmological parameters, including the Hubble constant $H_0$, the matter density parameter, and the model parameter $p_i$ for $i = 1, 2, 3$.

To assess the performance of these models, a visualisation of the constrained parameters is shown in the whisker plot in Fig. 6.5 for easy interpretation. The plot is divided into three sections: the first displays the models without any priors, the second incorporates the R21 prior with the datasets, and the third section illustrates the inclusion of the F21 prior. This arrangement facilitates comparison across different models, within the same dataset combinations.

Notably, the inclusion of the R21 prior tends to elevate the constrained $H_0$ values, although not to the extent of the R21 prior itself, depicted by the blue shaded region representing the $1\sigma$ range. In cases where BAO data is combined with the R21 prior, $H_0$ values tend to be closer to those without prior, albeit slightly higher. The density parameter exhibits more variability, particularly when BAO data is included with the R21 prior, where $\Omega_{m,0}$ tends towards higher values and are more consistent with each other.

In the third section of the whisker plot, the data incorporating the F21 prior are presented for the different models. The $1\sigma$ F21 prior value is indicated by the red shaded region. Similar to the previous section, introducing the F21 prior nudges the $H_0$ value slightly higher compared to the scenario without any prior. However, these adjusted values demonstrate a closer alignment with the prior itself, particularly notable for the baseline dataset combination (CC+PN). Regarding the density parameter, a consistent trend similar to the previous section is observed, highlighting the influence of incorporating the F21 prior.

The analysis extends to examining the model parameter $p_i$ for $i = 1, 2, 3$, which plays a

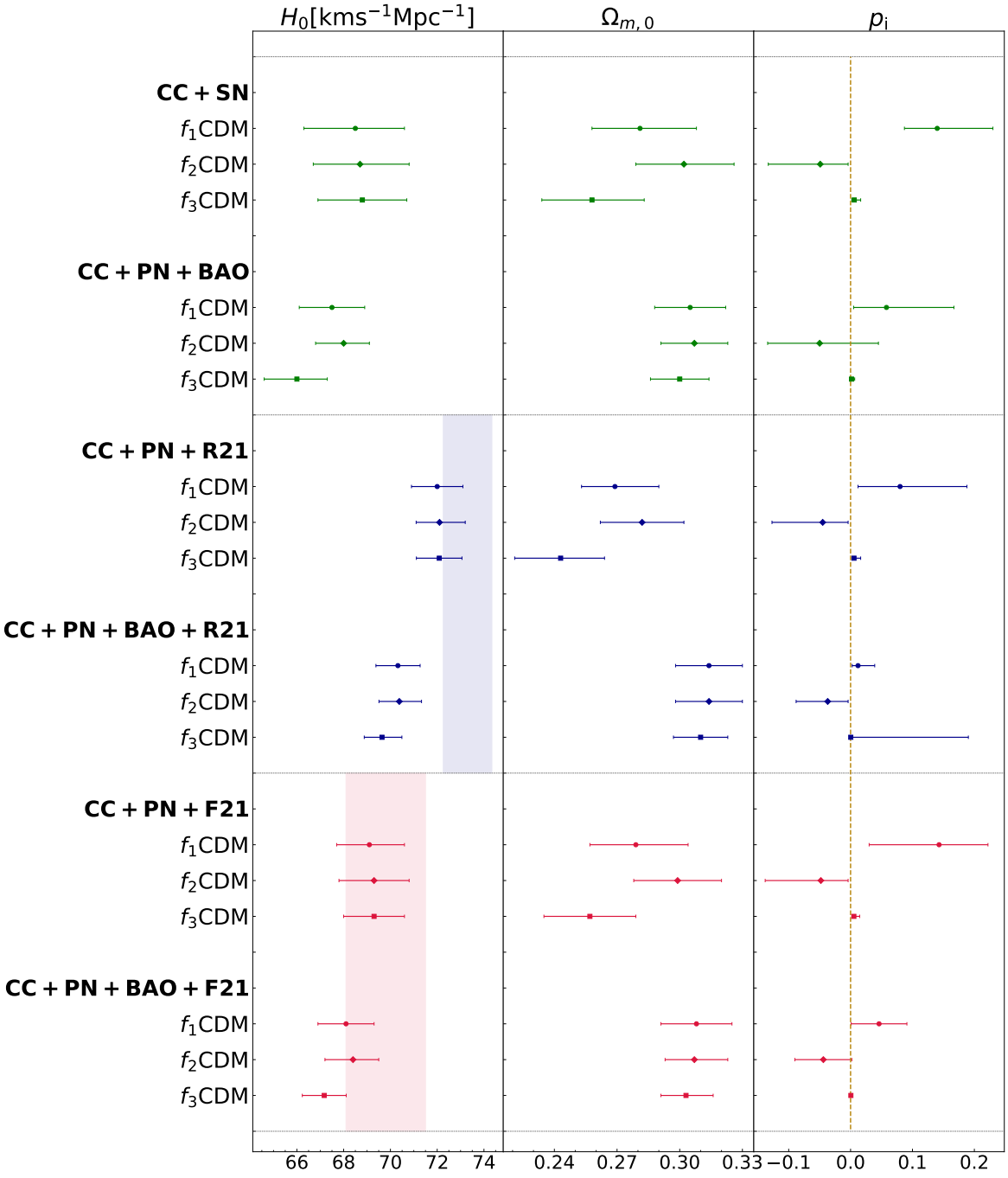


Figure 6.5: Whisker plot for the parameters $H_0$, $\Omega_{m0}$ and $p_i$, respectively. Each section represents the output results of the parameters for CC+PN and CC+PN+BAO where the green colour represents no prior, the blue colour represents the R21 prior and the red colour represents the F21 colour. The shaded bands denote the 1-$\sigma$ measurements of each prior whilst the dashed orange line in $p_i$ denotes the $\Lambda$CDM model.

crucial role in determining the behaviour of the models. With $f_3(T, B)$ as an exception, the first two models can exhibit ΛCDM behaviour when certain configurations of the additional model parameter are applied. By reviewing Eqs. 6.9 and 6.12, one can discern whether the extra Lagrangian terms favour a non-zero evolution. The orange dotted line in the last column of the whisker plot represents the ΛCDM limit, revealing that for $f_1$ and $f_2$, the parameter values fall within $2\sigma$ of $p = 0$. This observation underscores the proximity of these models to the established ΛCDM framework.

The last model, $f_3(T, B)$, diverges from a ΛCDM limit due to the absence of a specific value for the additional model parameter. Similar to observations made in the previous chapter, such models present an intriguing alternative to ΛCDM without necessitating extreme amendments. Generally, the resultant values for both the Hubble constant and the matter density tend to be towards the lower end of the spectrum as shown in the first and second column of Fig. 6.5. Moreover, while the additional model parameter $p_3$ lacks an expected value, the model generates values with minimal magnitudes and negligible uncertainties, providing an interesting insight into its behaviour.

Given the observations from the analysis, it becomes apparent that the $f(T)$ framework exhibits certain advantages over the $f(T, B)$ models. This conclusion is drawn from several key findings. Firstly, in the $f(T, B)$ models, most statistical indicators, in particular the BIC, which is the most robust indicator, tend to have higher values,indicating a preference towards the Λ over these models. Additionally, upon examining the 2D joint probability regions, it becomes evident that they are not as well-defined in the $f(T, B)$ models compared to the $f(T)$ framework. Consequently, these discrepancies prompt a shift in focus towards the $f(T)$ models for further investigation and analysis. By emphasising the robustness and reliability of the $f(T)$ framework, future studies can delve deeper into its implications for cosmology with greater confidence and clarity. By doing so, the aim is to extend the redshift range under consideration, thereby enhancing the comprehensiveness and accuracy of the cosmological models. This approach ensures that investigations into the $f(T)$ framework are conducted with a broader scope, allowing for a more extensive understanding of the Universe's dynamics across different epochs.

# 7

# Updating late-time $f(T)$ cosmology with Pantheon+ catalogue

SNe Ia were pivotal in the discovery of the Universe's accelerating expansion in 1998 by the Supernova Cosmological Project and the High-z Supernova Search Teams [34, 33]. Since then, transient surveys have continuously identified many more SNe Ia, significantly advancing the optimisation of their detection and measurement across various redshift ranges. Over the past decades, the statistical power of large samples of SNe Ia has grown considerably. These well-calibrated and standardised samples have facilitated the constraint of cosmological parameters through the compilation and analysis of multiple datasets. For example, measurements of the Hubble constant ($H_0$) require very nearby SNe in galaxies that host calibrated primary indicators such as Cepheids and the TRGB. However, combining different sub-samples of SNe is not straightforward due to the need for rigorous cross-calibration, self-consistent analysis of their light curves and redshifts, and characterisation of the covariance arising from various sources. Therefore, as sample sizes increase, it is essential to control systematic uncertainties meticulously.

This is where the latest compilation of confirmed SNe Ia comes into play. The Pantheon+ Compilation data set (PN+) dataset, which serves as the direct successor to the PN analysis, will be discussed in detail in the following sections and will be analysed within the framework of $f(T)$ gravity. The objective is to highlight how the new data impacts the constraints on $f(T)$ gravity models and to provide an understanding of their viability in explaining cosmological observations. This comparison will also elucidate the improvements introduced by the PN+ dataset and its significance.

Indeed, this chapter aims to constrain leading models of $f(T)$ gravity using the latest PN+ dataset in Sec. 7.2 and to compare the results with the previous PN release in Sec. 7.3. These analyses will be considered within the context of late-time datasets extensively stud-

ied in previous chapters. The findings of this work were presented and published in Briffa et al. [189].

## 7.1 | The Pantheon+ Data Set

As previously discussed, two SNe Ia datasets were used in this analysis: the PN and the PN+ compilations, with the latter being a successor to the original Pantheon analysis. The main difference between the original PN and the PN+ in cosmology lies in the addition of new measurements at various redshifts. While the original PN analysis used 1048 supernovae, the PN+ includes 1701 cosmologically viable SN light curves of 1550 distinct supernovae, representing a significant increase in data, particularly at low redshift. In addition, unlike the PN analysis, the PN+ dataset includes light curves with redshifts $z < 0.01$, allowing for analysis over the entire redshift range from $z = 0.001$ to $z = 2.26$.

This expansion in the PN+ dataset is complemented by the contributions from the SH0ES team. A companion paper Riess et al. 2021 [4], R22, uses observations from the HST to combine data from 277 Hubble flow SNe Ia (with redshifts $0.023 < z < 0.15$) and 42 SNe Ia in Cepheid-calibrator hosts. These combined datasets utilise their relative distances and covariances with the absolute distances of primary distance anchors (Cepheids and TRGB) to calibrate the Hubble constant, resulting in a value of $H_0^{\mathrm{R22}} = 73.3 \pm 1.04$ km s$^{-1}$ Mpc$^{-1}$.

The primary distance indicators from the SH0ES Cepheid host galaxies were incorporated into the PN+ dataset. This incorporation is instrumental for accurately determining distances, providing a robust calibration of SNe Ia luminosity via Cepheid distances, therefore improving the precision of the low-redshift sample. This helps to break the degeneracy between the absolute magnitude $M$ and the Hubble constant $H_0$ when analysing SNe Ia alone. Hence, the PN+ dataset is, henceforth, referred to as 'PN+& SH0ES', reflecting the integration of the SH0ES Cepheid's host distance anchors, which enhances the robustness of the dataset by improving distance measurements and reducing systematic uncertainties.

In addition to these improvements, the PN+& SH0ES dataset compilation includes more advanced systematic techniques compared to the PN dataset. These advancements encompass refined calibration procedures, enhanced light-curve fitting models, and comprehensive treatments of systematic uncertainties, such as those arising from peculiar velocities and intrinsic scatter. The PN+& SH0ES dataset also incorporates updated host-galaxy property analyses and improved redshift measurements, leading to more accurate cosmological constraints. These enhancements make PN+& SH0ES a more robust and precise dataset for cosmological studies, enabling better insights into the expansion history of the Universe and the determination of fundamental cosmological parameters.

In this case, the associated $\chi^2_{\rm PN}$ is still represented by

$$\chi^2_{\rm PN+}(\Theta) = (\Delta\mu(z_i, \Theta))^T C^{-1}_{\rm PN+} \Delta\mu(z_i, \Theta) \tag{7.1}$$

where $C_{\rm PN+}$ is the total covariance matrix, and $\Delta\mu(z_i, \Theta) = \mu(z_i, \Theta) - \mu_{\rm obs}(z_i)$, with $\mu(z_i, \Theta)$ being the theoretical value of the distance modulus and $\mu_{\rm obs}(z_i)$ obtained from the PN+& SH0ES dataset.

## 7.2 | Constraints in $f(T)$ cosmology: PN vs. PN+

In the context of the previous section, this next analysis examines the constraints on cosmological parameters derived from the PN and PN+& SH0ES datasets within the $f(T)$ framework. This section will focus on the specific parameters obtained from both datasets, comparing their implications and highlighting any significant differences. The key parameters under investigation include the Hubble constant ($H_0$), the matter density parameter ($\Omega_{m,0}$), and the model parameters specific to the $f(T)$ models. These models include the Power Law Model, the Linder Model, and the Exponential Model, as detailed in Sec. 3.4, for which the posterior distributions and confidence regions derived from the MCMC runs will be illustrated, providing an initial overview of the datasets' impact.

By analysing these parameters, a better understanding of how the updated and expanded data in the PN+ dataset impact the constraints and whether they provide more precise and reliable cosmological insights compared to the original PN+& SH0ES dataset, can be obtained. This comparison is crucial for evaluating the robustness of the $f(T)$ models and their consistency with the observational data. A comparative analysis, providing a overview of the fit quality for each dataset combination, will be discussed in more detail in the next section.

### 7.2.1 | ΛCDM Model: PN vs PN+

As in previous chapters, the first model being presented is the ΛCDM model to facilitate comparisons with all subsequent $f(T)$ models. With this in mind, an MCMC run was conducted, yielding constrained parameters for $H_0$ and $\Omega_{m,0}$. These results are illustrated in Fig. 7.1, where the posteriors and confidence regions are shown.

The calibration of the BAO is achieved through the calculation of the sound horizon at the drag epoch, which provides a critical scale for measuring cosmic distances. Similarly, the PN+& SH0ES dataset is calibrated using the absolute magnitude $M$, a key parameter in the distance ladder. Importantly, the values of $M$ used in these calibrations are consistent across all datasets. This consistency demonstrates the reliability of the calibration processes

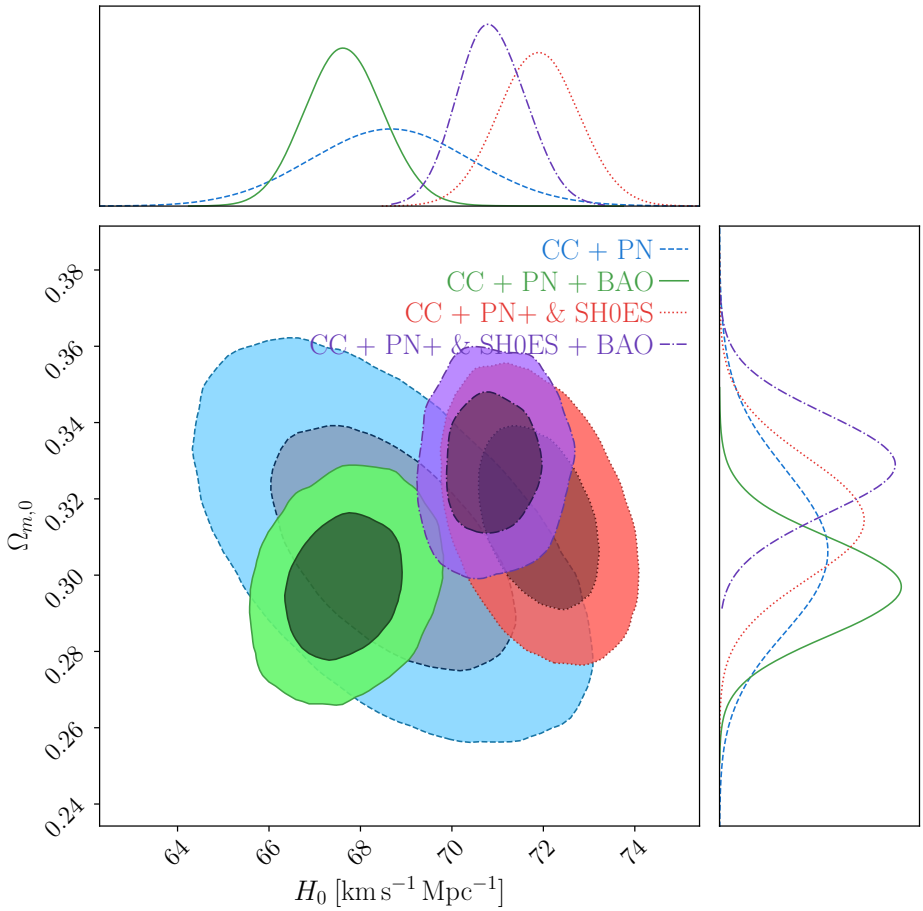


Figure 7.1: Confidence contours and posteriors for ΛCDM for the parameters $H_0$ and $\Omega_{m,0}$. The blue and green contours represent dataset combinations that include PN dataset, while the red and purple contours show combinations that also include the PN$^+$ & SH0ES datasets.

and ensures that the results remain comparable and coherent, regardless of the dataset being analysed.

It is immediately apparent that certain combinations of datasets that include the PN+& SH0ES (the red and purple contours), provide tighter constraints for both parameters and higher values for the Hubble constant parameter. A more detailed explanation and analysis of this will follow as the models are discussed in subsequent sections. The purpose of this section is to present the posteriors and the corresponding Table 7.1 for comparison purposes only. Nevertheless, the influence of PN+& SH0ES is immediately evident, as it consistently pushes $H_0$ to higher values. Additionally, the Gaussian-like errors in the $\Omega_{m,0}$ parameter indicate its rapid convergence within the ΛCDM framework, whereas the errors in though

| Data Sets | $H_0$ [km s$^{-1}$ Mpc$^{-1}$] | $\Omega_{m,0}$ | $M$ |
|---|---|---|---|
| CC + PN | $68.6^{+1.8}_{-1.7}$ | $0.306 \pm 0.021$ | $-19.383^{+0.050}_{-0.053}$ |
| CC + PN + BAO | $67.59^{+0.89}_{-0.81}$ | $0.297 \pm 0.013$ | $-19.419^{+0.026}_{-0.033}$ |
| CC + PN$^+$ & SH0ES | $71.88^{+0.88}_{-0.87}$ | $0.315 \pm 0.016$ | $-19.298 \pm 0.025$ |
| CC + PN$^+$ & SH0ES + BAO | $70.76^{+0.80}_{-0.64}$ | $0.329 \pm 0.013$ | $-19.326^{+0.024}_{-0.022}$ |

Table 7.1: Results for the ΛCDM model, where the first column lists the datasets used to constrain the parameters. The second to fourth columns display the constrained parameters, namely $H_0$, $\Omega_{m,0}$, and the nuisance parameter $M$.

not perfectly Gaussian, still display a close approximation.

### 7.2.2 | Power Law Model: PN vs PN+

The first cosmological model considered is the Power Law Model, with the specific Friedmann equation, Eq. 3.54 as detailed in Sec. 3.4.1. This model, designed to describe the late-time acceleration of the Universe, introduces an additional parameter compared to the standard ΛCDM model, $p_1$

The constraints on the specified parameters for this Power Law Model model are shown in Fig. 7.2. The figure illustrates the confidence regions and posteriors for the different combinations of observational datasets. Specifically, it shows results for datasets that include either the PN catalogue or the PN+& SH0ES together with CC data or BAO data. The blue and green contours in the figure represent combinations of datasets that include the PN sample, while the red and purple contours correspond to combinations incorporating the PN+& SH0ES samples. The results clearly demonstrate that dataset combinations incorporating the PN+& SH0ES dataset exhibit significantly tighter constraints, indicating higher precision. This improvement is particularly evident in the 1- and 2-$\sigma$ contour regions, which are notably smaller compared to those derived from datasets that include only PN. Specifically, the $H_0$ parameter shows a notable enhancement in precision.

The contour plots for the CC+PN and CC+PN+& SH0ES dataset combinations display a degeneracy between the $H_0$ and $p_1$ parameters. However, this degeneracy is broken when the BAO dataset is included, revealing an anti-correlation between these parameters. Notably, the CC+PN+& SH0ES dataset combination shows a degeneracy between $\Omega_{m,0}$ and $H_0$, while an anti-correlation is observed between $p_1$ and $\Omega_{m,0}$ for all dataset combinations. The strength of this anti-correlation is less pronounced for datasets that include BAO.

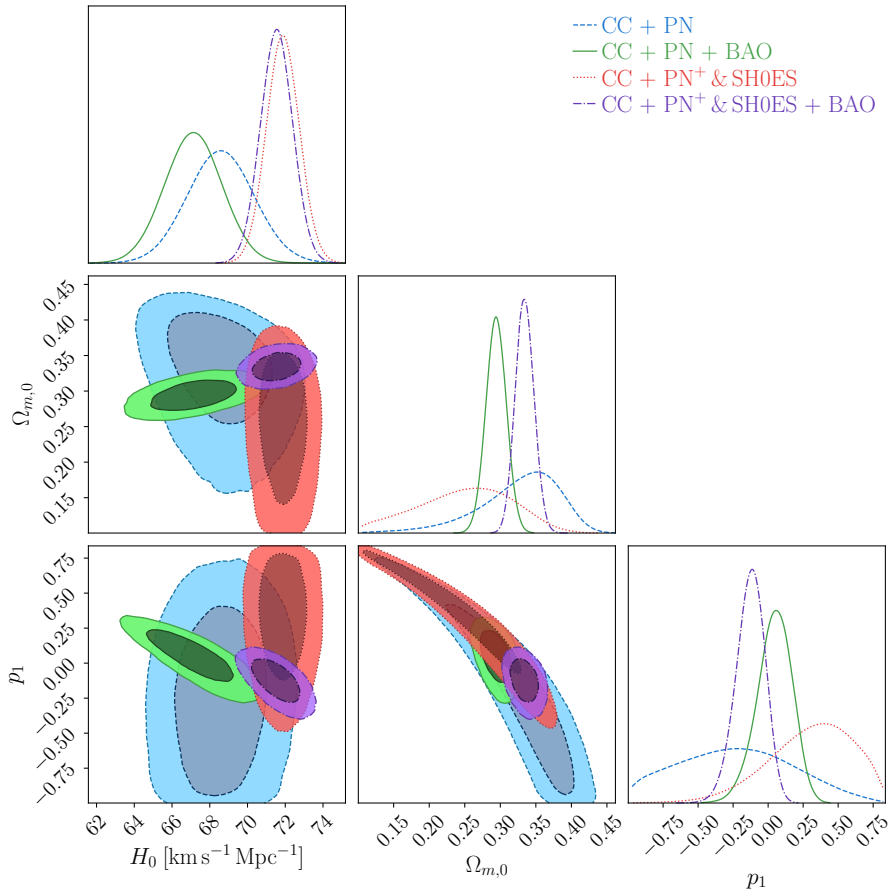


Figure 7.2: Confidence contours and posteriors for $f_1$CDM for the parameters $H_0$, $\Omega_{m,0}$, and $p_1$. The blue and green contours represent dataset combinations that include the PN dataset, while the red and purple contours show combinations that also include the PN$^+$ & SH0ES datasets.

| Data sets | $H_0$ [km s$^{-1}$Mpc$^{-1}$] | $\Omega_{m,0}$ | $p_1$ | $M$ |
|---|---|---|---|---|
| CC + PN | $68.6^{+1.7}_{-1.8}$ | $0.352^{+0.042}_{-0.063}$ | $-0.22^{+0.41}_{-0.48}$ | $-19.390^{+0.052}_{-0.053}$ |
| CC + PN + BAO | $67.1 \pm 1.5$ | $0.294^{+0.015}_{-0.014}$ | $0.06^{+0.12}_{-0.13}$ | $-19.435 \pm 0.044$ |
| CC + PN$^+$ & SH0ES | $71.88^{+0.87}_{-0.89}$ | $0.266^{+0.062}_{-0.076}$ | $0.40^{+0.28}_{-0.33}$ | $-19.295 \pm 0.025$ |
| CC + PN$^+$ & SH0ES + BAO | $71.55^{+0.85}_{-0.86}$ | $0.334^{+0.014}_{-0.013}$ | $-0.113^{+0.098}_{-0.108}$ | $-19.309^{+0.024}_{-0.025}$ |

Table 7.2: Results for the $f_1$CDM (Power law) model, where the first column lists the datasets used to constrain the parameters. The second to fourth columns display the constrained parameters, namely $H_0$, $\Omega_{m,0}$, and $p_1$, while the last column shows the nuisance parameter $M$.

The precise values for the cosmological and model parameters, including the nuisance parameter $M$, for the power law model are shown in Table 7.2. It is evident that the $H_0$ values for dataset combinations including PN+& SH0ES are relatively higher than their corresponding $H_0$ values. This is also reflected in the posteriors , where the red and purple posteriors are pushed towards higher values of $H_0$, than the blue and green contours (which include the PN dataset. The highest $H_0$ value is obtained for the CC+PN+& SH0ES combination, with $H_0 = 71.88^{+0.87}_{-0.89}\,\mathrm{km\,s^{-1}Mpc^{-1}}$. This result is consistent with the high $H_0$ value reported by the SH0ES team, ($H_0^{\mathrm{R22}} = 73.30 \pm 1.04\,\mathrm{km\,s^{-1}Mpc^{-1}}$ [4]). In this scenario, the $\Omega_{m,0}$ parameter reaches a minimum value, indicating that most of the Universe's energy appears as effective dark energy, aligning with the high $H_0$ value. The CC+PN+& SH0ES+BAO combination results in a lower $H_0$ value due to the influence of BAO data, which is sensitive to early Universe effects and tends to lower the resulted value of $H_0$.

With regards to value of $p_1$, the values seem to vary. The values of CC+PN and CC+PN+& SH0ES are not tight-constrained, however, as soon as the BAO is included the $p_1$ value becomes well-constrained. In this case, the $p_1$ parameter is also found to be within $1\sigma$ of $\Lambda$CDM value (i.e $p_1 = 0$).

Overall, it is evident that the purple contours demonstrate substantially tighter constraints, indicating a more precise value. This implies that the PN+& SH0ES dataset significantly contributes to the accuracy of the model. The subsequent section, Sec. 7.3 will provide a more detailed statistical analysis of these findings, including a comparison with the $\Lambda$CDM model.

### 7.2.3 | Square-Root Exponential Model: PN vs PN+

The second cosmological model considered is the Linder Model, explained in more detail in Sec. 3.4.2 and having the Friedmann Equation as Eq. 3.57. The posterior distributions and confidence levels for the constrained parameters of the Linder model are illustrated in Fig. 7.3.

This model exhibits trends similar to those observed in the first model. However, the constraints are notably tighter when the PN+& SH0ES samples are included, particularly for the Hubble constant $H_0$. The inclusion of BAO data further refines these constraints, resulting in the most precise parameter constrained when the combined CC+PN+& SH0ES+BAO dataset is utilised ($H_0 = 70.79 \pm 0.71\,\mathrm{km\,s^{-1}Mpc^{-1}}$). This highlights the significant impact of including the SH0ES data, which provided the local measurement of the Hubble constant (R22), thereby reducing the overall uncertainty.

Table 6.4 provides the exact numerical values of the parameters derived from the Linder model using various dataset combinations. These parameters include the Hubble constant

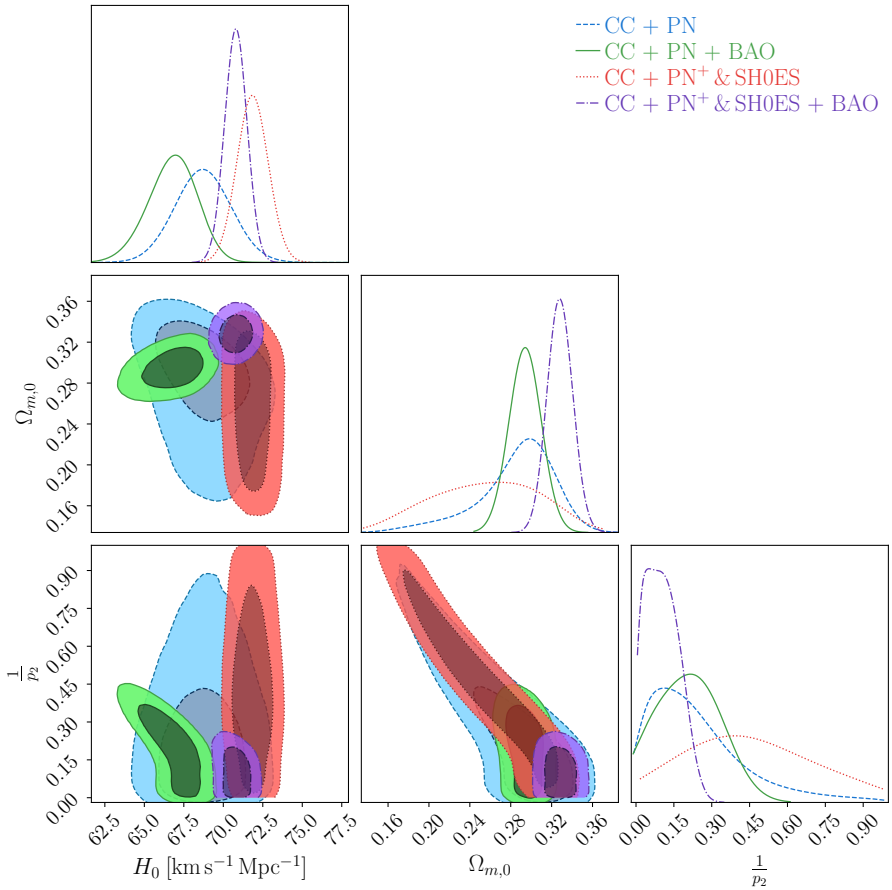


Figure 7.3: Confidence contours and posteriors for $f_2$CDM for the parameters $H_0$, $\Omega_{m,0}$ and $\frac{1}{p_2}$. The blue and green contours represent dataset combinations that include PN dataset, while the red and purple contours show combinations that also include the PN$^+$ & SH0ES datasets.

| Data sets | $H_0$ [km s$^{-1}$ Mpc$^{-1}$] | $\Omega_{m,0}$ | $\frac{1}{p_2}$ | $M$ |
|---|---|---|---|---|
| CC + PN | $68.7^{+1.8}_{-1.7}$ | $0.298^{+0.031}_{-0.036}$ | $0.11^{+0.22}_{-0.11}$ | $-19.433^{+0.117}_{-0.083}$ |
| CC + PN + BAO | $66.9^{+1.5}_{-1.6}$ | $0.294 \pm 0.016$ | $0.22^{+0.12}_{-0.15}$ | $-19.38^{+0.22}_{-0.35}$ |
| CC + PN$^+$ & SH0ES | $71.86^{+0.97}_{-0.99}$ | $0.269^{+0.046}_{-0.065}$ | $0.39^{+0.29}_{-0.25}$ | $-19.287^{+0.048}_{-0.032}$ |
| CC + PN$^+$ & SH0ES + BAO | $70.79 \pm 0.71$ | $0.328^{+0.013}_{-0.012}$ | $0.052^{+0.104}_{-0.038}$ | $-19.322^{+0.026}_{-0.033}$ |

Table 7.3: Results for the $f_2$CDM (Linder) model, where the first column lists the datasets used to constrain the parameters. The second to fourth columns display the constrained parameters, namely $H_0$, $\Omega_{m,0}$, and $\frac{1}{p_2}$, while the last column shows the nuisance parameter $M$.

($H_0$), the matter density parameter ($\Omega_{m,0}$), and the parameter $\frac{1}{p_2}$ from the model's exponential term, alongside the nuisance parameter $M$. The values of $H_0$ obtained from this model are comparable to those from the Power Law model. Notably, this model is explicitly designed to account for an accelerating Universe in the late-time regime, which is reflected in the slightly lower inferred values of $\Omega_{m,0}$ compared to the first model. For instance, the combination of CC+PN+& SH0ES yields the lowest $\Omega_{m,0}$ value of $0.269^{+0.046}_{-0.065}$. Concurrently, this combination provides the highest $H_0$ value at $71.86^{+0.97}_{-0.99}\,\mathrm{km\,s^{-1}Mpc^{-1}}$.

The $\frac{1}{p_2}$ parameter in this model allows for a more flexible description of the Universe's expansion history. This second model also ensures that the parameter $\frac{1}{p_2}$ remains positive. Compared to the previous model, this model's parameters tend to fall within $2\sigma$ of the $\Lambda$CDM values, rather than within $1\sigma$. This indicates that while the Linder model does not strongly support the $\Lambda$CDM model, it is still within reasonable proximity, highlighting its viability as an alternative. In addition, the anti-correlation remains evident between the $\Omega_{m,0}$ and the mode parameter $\frac{1}{p_2}$, in particular for the datasets that include the PN+& SH0ES catalogue.

Incorporating the PN+& SH0ES dataset significantly influences the MCMC runs and the resulting parameter estimates. Although the outcomes remain consistent with those derived from the PN dataset alone, the uncertainties in the parameters, especially $H_0$, are considerably reduced. This makes the PN+& SH0ES dataset invaluable for comparative purposes with the $\Lambda$CDM model. The detailed statistical comparisons and analyses with the $\Lambda$CDM model are further elaborated in Section 7.3.

### 7.2.4 | Exponential Model: PN vs PN+

The third model evaluated is the Exponential Model, also referred to as a Variant of the Linder Model, as detailed in Sec. 3.4.3. The core of this model is the Friedmann Equation, represented by Eq. 3.61.

The behaviour of the this model parallels that of the second one. It is a variant of the Linder model, with a significant modification: the removal of the square root term, which substantially impacts the constraints, particularly for the matter density parameter $\Omega_{m,0}$ as showcased in Fig. 7.4. This figure also illustrates the posterior distributions and confidence levels for all constrained parameters of the Exponential model. Unlike previous models, this model shows no significant degeneracy between the parameters $H_0$ and $\Omega_{m,0}$. Instead, the correlation between $\Omega_{m,0}$ and $\frac{1}{p_3}$ is emphasised.

Table 7.4 presents the precise numerical values of the parameters constrained within the Exponential model, based on various dataset combinations. Notably, the highest $H_0$ value is derived from the CC+PN+& SH0ES dataset combination, with $H_0 = 71.80 \pm 0.89\,\mathrm{km\,s^{-1}Mpc^{-1}}$.

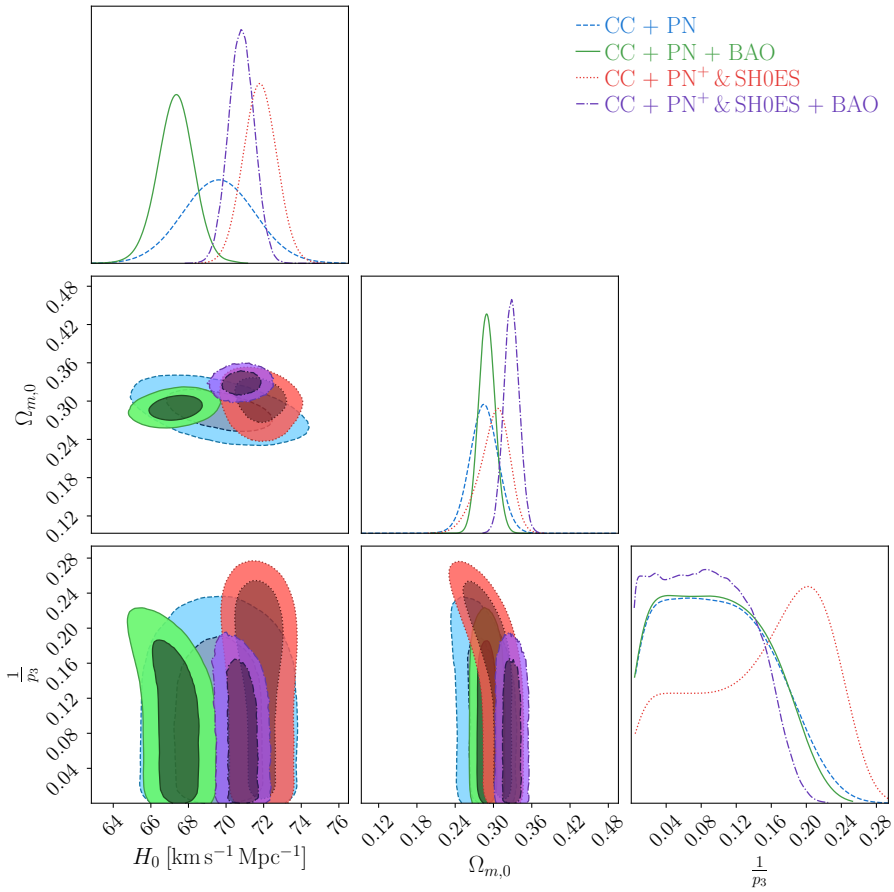


Figure 7.4: Confidence contours and posteriors for $f_3$CDM for the parameters $H_0$, $\Omega_{m,0}$ and $\frac{1}{p_3}$. The blue and green contours represent dataset combinations that include the PN dataset, while the red and purple contours show combinations that also include the PN$^+$ & SH0ES datasets.

| Data Sets | $H_0$ [km s$^{-1}$ Mpc$^{-1}$] | $\Omega_{m,0}$ | $\frac{1}{p_3}$ | $M$ |
|---|---|---|---|---|
| CC + PN | $69.6^{+1.9}_{-2.0}$ | $0.286 \pm 0.022$ | $0.065^{+0.082}_{-0.050}$ | $-19.367^{+0.054}_{-0.057}$ |
| CC + PN + BAO | $67.35^{+0.94}_{-0.97}$ | $0.289 \pm 0.013$ | $0.043^{+0.101}_{-0.026}$ | $-19.441^{+0.032}_{-0.031}$ |
| CC + PN$^+$ & SH0ES | $71.80 \pm 0.89$ | $0.307^{+0.020}_{-0.026}$ | $0.201^{+0.045}_{-0.114}$ | $-19.302^{+0.033}_{-0.021}$ |
| CC + PN$^+$ & SH0ES + BAO | $70.80^{+0.70}_{-0.66}$ | $0.329 \pm 0.012$ | $0.086^{+0.035}_{-0.081}$ | $-19.259 \pm 0.077$ |

Table 7.4: Results for the $f_3$CDM model, where the first column lists the datasets used to constrain the parameters. The second to fourth columns display the constrained parameters, namely $H_0$, $\Omega_{m,0}$, and $\frac{1}{p_3}$, while the last column shows the nuisance parameter $M$.

The value of $H_0$ obtained from the this dataset combination in the Exponential model is consistent with corresponding values from previous models. However, the discrepancy between $H_0$ values for the CC+PN+& SH0ES and CC+PN+& SH0ES+BAO combinations is slightly larger in the this model than in the Power Law model, indicating a marginally lower $H_0$ value when BAO data is included. Regarding the $p_3$ parameter, the resulting values are closer to the ΛCDM limit compared to previous models. Nevertheless, the uncertainties indicate a deviation at the $2\sigma$ level from the ΛCDM model.

In general, the third model, a variant of the Linder model, exhibits unique behaviour due to the removal of the square root term, which significantly impacts parameter constraints. These results will be further analysed and statistically compared with the ΛCDM model in the subsequent section.

## 7.3 | Comparative Analysis using PN and PN+ Data Sets

In this section, the constrained parameters from the ΛCDM model will be compared with those from various $f(T)$ models, using both the PN and PN+& SH0ES datasets. A detailed discussion will highlight the differences, strengths, and implications of each model based on the results obtained from these datasets.

To compare the performance of various models using different combinations of datasets, the differences in AIC and BIC are calculated between each model and the ΛCDM model. Using ΛCDM as the standard model of cosmology and as the reference model allows for a clear comparison between each model and this benchmark. Smaller values of ΔAIC and ΔBIC indicate a model's performance is more comparable to the ΛCDM model, suggesting better fit.

The comparison values for all models using the CC+PN datasets with those using the CC+PN+& SH0ES datasets are tabulated in Table 7.5, while Table 7.6 compares the models using the CC+PN+BAO datasets with those using the CC+PN$^+$ & SH0ES+BAO datasets.

Upon initial examination, the results indicate that the PN$^+$ & SH0ES datasets yield significantly lower values of ΔAIC and ΔBIC, despite a higher $\chi^2_{\text{min}}$ due to the increased number of data points. It is notable that the $\chi^2_{\text{min}}$ values for the $f(T)$ models considered are slightly lower than those of the ΛCDM model for the CC+PN+& SH0ES datasets. However, these $f(T)$ models are penalised by the AIC and BIC due to the larger dataset size. Additionally, the values of ΔAIC and ΔBIC for the CC+PN+& SH0ES datasets are very close to each other, indicating a strong dataset with constrained parameters similar to each other. While CC+PN observations generally support the ΛCDM model, the inclusion of PN+& SH0ES data does not provide strong evidence in favour of the ΛCDM model over the $f(T)$ cos-

| Model | CC + PN | | | CC+ PN$^+$ & SH0ES | | |
|---|---|---|---|---|---|---|
| | $\chi^2_{\rm min}$ | $\Delta$AIC | $\Delta$BIC | $\chi^2_{\rm min}$ | $\Delta$AIC | $\Delta$BIC |
| $\Lambda$CDM | 1041.49 | 0 | 0 | 1548.30 | 0 | 0 |
| Power Law | 1040.94 | 1.44 | 6.43 | 1546.64 | 0.34 | 5.80 |
| Square-root Exponential | 1041.49 | 2.00 | 6.98 | 1546.67 | 0.37 | 5.82 |
| Exponential | 1045.04 | 5.54 | 10.53 | 1546.77 | 0.47 | 5.93 |

Table 7.5: Results for each model, including $\chi^2_{\rm min}$, AIC, BIC, and their differences relative to the $\Lambda$CDM model (i.e., $\Delta$AIC and $\Delta$BIC). The left side of the table presents the results obtained from the CC+PN datasets, while the right side shows the results from the CC+PN$^+$ & SH0ES datasets.

| Model | CC+ PN + BAO | | | CC+ PN$^+$ & SH0ES + BAO | | |
|---|---|---|---|---|---|---|
| | $\chi^2_{\rm min}$ | $\Delta$AIC | $\Delta$BIC | $\chi^2_{\rm min}$ | $\Delta$AIC | $\Delta$BIC |
| $\Lambda$CDM | 1057.46 | 0 | 0 | 1560.68 | 0 | 0 |
| Power Law | 1057.13 | 1.68 | 6.68 | 1559.24 | 0.55 | 6.02 |
| Square-root Exponential | 1056.52 | 1.06 | 6.06 | 1560.68 | 1.99 | 7.46 |
| Exponential | 1060.55 | 5.09 | 10.09 | 1560.68 | 1.99 | 7.47 |

Table 7.6: Results for each model, including $\chi^2_{\rm min}$, AIC, BIC, and their differences relative to the $\Lambda$CDM model (i.e., $\Delta$AIC and $\Delta$BIC). The left side of the table presents the results obtained from the CC+PN+BAO datasets, while the right side shows the results from the CC+PN$^+$ & SH0ES+BAO datasets.

mological models, given that both $\Delta$AIC and $\Delta$BIC are statistically comparable. Incorporating the BAO dataset reveals a similar trend, albeit to a lesser extent. For the Exponential (i.e the third) model, however, the values of both $\Delta$AIC and $\Delta$BIC are higher for the CC+PN+& SH0ES+BAO combination, indicating less support for this model compared to $\Lambda$CDM.

Figure 7.5 further supports this analysis by comparing the constrained $H_0$ values from the $f(T)$ models to those from the $\Lambda$CDM model, using Eq. 4.1. This radar plot compares the constraints on parameters from different dataset combinations in relation to the $\Lambda$CDM model. The plot shows the relative spread for four different data combinations: CC + PN (blue),CC + PN + BAO (red), CC + PN+& SH0ES (green), CC + PN+& SH0ES + BAO (purple). The shaded regions represent the distances in $\sigma$ units for each dataset combination, with the $\Lambda$CDM model as the reference point. On the horizontal axis, the radial distances indicate the level of difference between the $H_0$ value for each specific dataset combination and the $\Lambda$CDM model, expressed in $\sigma$ units. Larger radial distance reflect a higher $\sigma$ value, meaning a larger difference between the obtained $H_0$ value and the $\Lambda$CDM value.

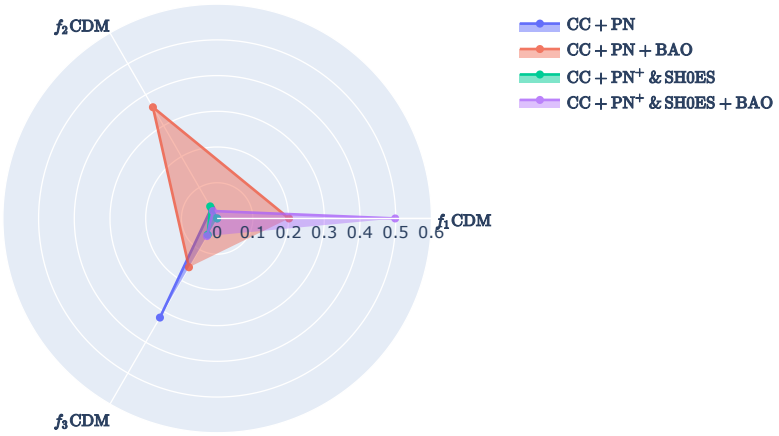


Figure 7.5: Distances, in units of standard deviations ($\sigma$), between the constrained values of $H_0$ and the $\Lambda$CDM value for different combinations of datasets, represented by different colours.

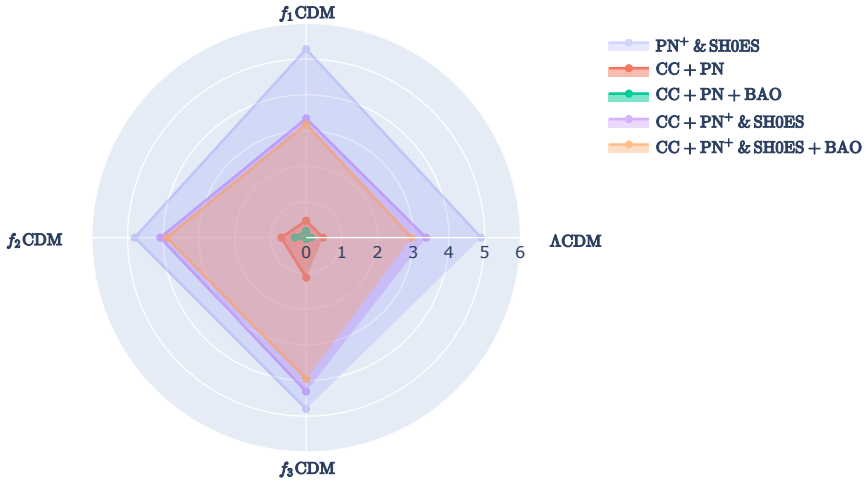


Figure 7.6: Distances, in units of standard deviations ($\sigma$), between the constrained values of $H_0$ for different combinations of datasets, represented by different colours and the P18 value.

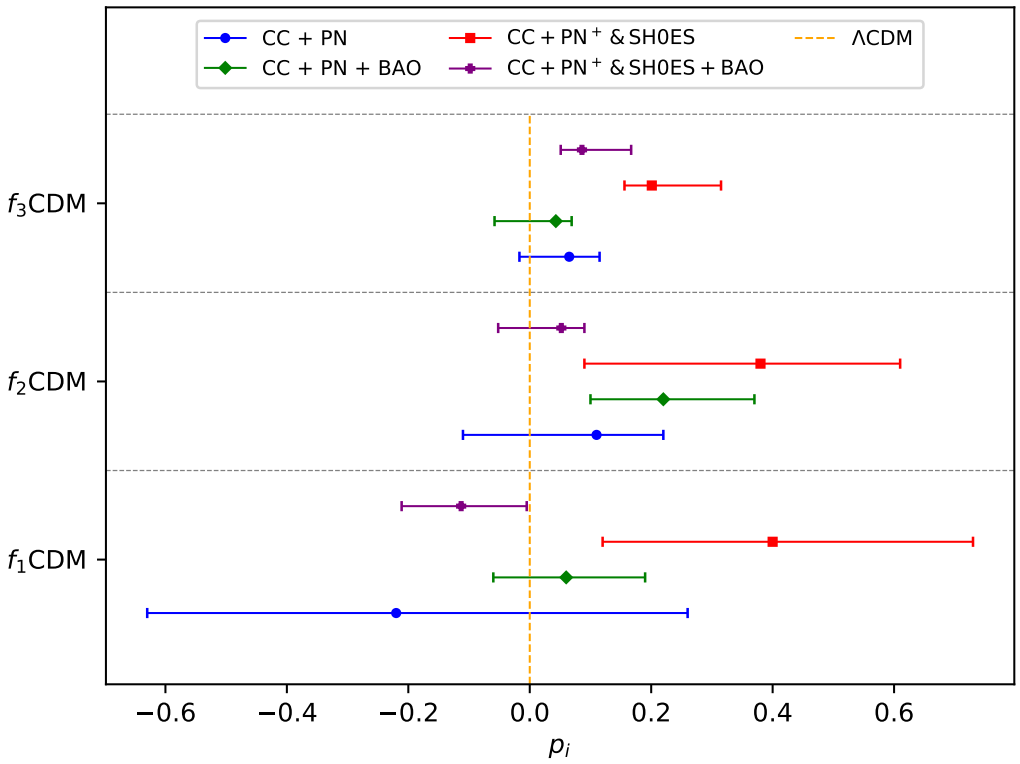


Figure 7.7: Values of the constrained model parameter $p_i$, corresponding to $p_1$ for $f_1$CDM, $\frac{1}{p_2}$ for $f_2$CDM, and $\frac{1}{p_3}$ for $f_3$CDM. Each colour represents a different dataset combination, while the orange line represents the ΛCDM value, i.e., $p_i = 0$.

For each dataset combination, represented by different colours, the $H_0$ values obtained from the $f(T)$ models are within $1\sigma$ of the corresponding ΛCDM values. This visualisation illustrates the variations in $H_0$ estimates across different datasets, with greater distances indicating larger discrepancies between the constrained and ΛCDM values of $H_0$. Thus, the plot suggests that the $H_0$ values obtained using the $f(T)$ models are comparable to those obtained using the ΛCDM model.

In contrast, Figure 7.6 displays the differences in $\sigma$ units between the constrained $H_0$ values obtained from the MCMC analysis and the Planck 18 value of $H_0^{\rm P18} = 67.4 \pm 0.5\,{\rm km\,s^{-1}Mpc^{-1}}$ [16]. In this case, the PN+& SH0ES dataset alone is also considered, with constrained $H_0$ values for each model shown in Table B in Appendix B [9]. The plot clearly illustrates the

[9] An MCMC analysis was run for the PN+& SH0ES dataset only for which the tabulated results are shown in Appendix B as indicated above.

$5\sigma$ tension between the PN+& SH0ES dataset and the P18 value under the $\Lambda$CDM model. However, the inclusion of the CC dataset at late times reduces the tension to around $3-4\sigma$ for all models. The inclusion of the BAO dataset significantly reduces this tension, as expected, since the BAO data captures early Universe effects in agreement with the Planck CMB dataset.

Finally, Figure 7.7 illustrates the effects of the PN+& SH0ES dataset on the model parameter $p_i$. The results indicate that the use of PN+& SH0ES leads to a more tightly constrained estimate of $p_i$ compared to other methods. Notably, the CC+PN and CC+PN+BAO methods produce $p_i$ values that fall within $1\sigma$ of the $\Lambda$CDM value. However, for CC+PN+& SH0ES, the estimated $p_i$ values do not consistently fall within $1\sigma$ of the $\Lambda$CDM value, indicating a deviation from the standard model.

## 7.4 | Conclusion

In this chapter, a constraints analysis was conducted to examine the behaviour of cosmological parameters using the PN+& SH0ES dataset compared to the PN dataset. Three prominent models in $f(T)$ gravity were evaluated, assessing their performance against three combinations of observational datasets. The primary aim was to compare the outcomes derived from the PN+& SH0ES datasets with those from the PN catalogue, focusing on the differences in results and their impact on the performance of the $f(T)$ gravity models under investigation.

For each model, an MCMC analysis was performed, obtaining observational constraints on the cosmological parameters for all data combinations. Additionally, the performance of each model and dataset was compared against the standard model of cosmology using statistical indicators such as AIC and BIC as in Sec. 7.3. Furthermore, the increasing tensions between cosmological observations were addressed by comparing the $H_0$ value with the corresponding $\Lambda$CDM value and the P18 value.

The performance of three models, namely Power Law Model, Square-root Exponential Model and the Exponential Model, was evaluated, where a continuous $\Lambda$CDM component is present, and a specific setting of an additional model parameter recovers a constant cosmological constant contribution. For all models, the posteriors and confidence contours revealed that the PN+& SH0ES dataset produced tighter constraints on the model parameters compared to the PN dataset. Additionally, the PN+& SH0ES dataset consistently yielded higher values of $H_0$, consistent with previous SH0ES team results (R22). This is due to its composition of the PN+& SH0ES catalogue and the SH0ES Cepheid host distance anchors.

Consistent $H_0$ values were obtained across all models and data combinations. However,

for the $\Omega_{m,0}$ parameter, both Exponential models produced lower values than the Power Law model. The additional model parameter $p_i$, for the PN dataset, mostly fell within $1\sigma$ of the $\Lambda$CDM model. However, for the PN+& SH0ES dataset, they were mostly outside the $1\sigma$ but within the $2\sigma$ range.

In Sec. 7.2.1, the results obtained from the $\Lambda$CDM model are presented, which were used for statistical comparisons. The analysis in Sec. 7.3 indicated that the models under consideration are generally consistent with the $\Lambda$CDM model. The statistical indicators clearly show that the PN+& SH0ES is a stronger dataset, as the constrained parameters are close to those produced by the $\Lambda$CDM model. Additionally, the information criteria $\Delta$AIC and $\Delta$BIC suggest that the CC+PN data support the $\Lambda$CDM model, whereas the PN+& SH0ES dataset does not provide strong evidence favouring the $\Lambda$CDM model over the $f(T)$ cosmological models, as indicated by their relatively small values.

Finally, incorporating the CC data with the PN+& SH0ES dataset reduces the $H_0$ tension to around $3-4\sigma$ (as illustrated in Fig. 7.6). Additionally, including the BAO dataset impacts the $H_0$ values, slightly reducing them due to the early Universe effects. However, the contour plots in the triangular plots reveal an interesting point: when the BAO dataset is included, the degeneracy between the parameters $H_0$ and $\Omega_{m,0}$ is broken, as shown by the green and purple contours. Instead, a correlation between these parameters is revealed. The core source of the correlation between these parameters stems from how the matter density of the Universe correlates with the expansion velocity.

In conclusion, insights into the behaviour of the PN and the PN+& SH0ES datasets and the performance of different models in $f(T)$ gravity were provided in this analysis. The results suggest that the PN+& SH0ES dataset produces tighter constraints on model parameters and higher values of $H_0$ compared to the PN dataset, and the inclusion of the CC and BAO datasets has a significant impact on parameter degeneracies and $H_0$ tension. Overall, the analysis suggests that the $f(T)$ gravity models considered in this study provide a valuable framework for further investigations of modified gravity theories and highlights the importance of incorporating varied datasets to achieve more precise and reliable cosmological parameter estimations.

Moving forward, in the next chapter, the focus will be on exploring $f(T)$ cosmology using RSD data by including density fluctuations. By incorporating RSD data, it will be possible to further constrain the model parameters and assess their compatibility with large-scale structure observations. The inclusion of scalar perturbations will provide a better understanding of the growth of cosmic structures and also give insight into the $S_{8,0}$ tension with the $f(T)$ framework. This approach will offer deeper insights into the viability of $f(T)$ gravity as a potential alternative to the standard $\Lambda$CDM model and its implications for the evolution of the Universe.

# 8

# Model constraints using Growth of Structures through RSD data

In the preceding chapters, the focus was on incorporating late-time datasets into the MCMC analyses. These analyses included combinations of CC, PN+& SH0ES and BAO datasets, which provided valuable insights into the behaviour of the $f(T)$ framework. However, to achieve a more thorough understanding of this framework and the models within it, it is essential to extend the testing to more robust and extensive datasets. This expansion will enable a more detailed investigation into critical cosmological parameters, specifically the $H_0$ tension and in this chapter the $S_{8,0}$ parameter as well [63, 57]. By utilising a broader range of data, the goal is to obtain and refine the constraints on these parameters and assess the viability of the $f(T)$ models in explaining the current discrepancies observed in cosmological measurements. This chapter will, therefore, build on the previous findings by integrating additional datasets and exploring their implications for $f(T)$ cosmology.

Whilst the status of the $S_{8,0}$ tension is less clear than that of the $H_0$ tension, the discrepancy between the values of the amplitude of matter fluctuations derived from observations of the late-time Universe and those predicted by the standard model of cosmology, based on the CMB as previously described, is still evident. It is important to note, however, that while this discrepancy is evident from a data perspective, from a model perspective, the $H_0$ tension can push $S_{8,0}$ either up or down, impacting its consistency with the data. This is precisely why such analyses remain essential, as they explore the interplay between these tensions and their implications for cosmological models.

The above discrepancy, known as the $S_{8,0}$ tension, relates to the clustering of matter in the Universe [18]. Specifically, the values obtained from cosmic shear surveys are found to be lower than those predicted by the ΛCDM cosmology. Recently, KiDS reported the value of $S_{8,0}^{\mathrm{KiDS}} = 0.766^{+0.020}_{-0.014}$ [142] a $\sim 3\sigma$ tension with Planck value, $S_{8,0}^{\mathrm{P18}} = 0.834 \pm 0.016$ [16].

As detailed in Chapter 2, addressing this tension is crucial for understanding the LSS of the Universe and therefore constraining values for $S_{8,0}$ parameter in $f(T)$ gravity becomes one of the primary goals.

The $S_{8,0}$ parameter, defined as $S_{8,0} \equiv \sigma_8(\Omega_{m,0}/0.3)^{1/2}$, where $\sigma_8$ represents the amplitude of matter density fluctuations on an 8 Mpc/h scale, can be probed through various observational techniques. One effective method for determining the value of this growth parameter combination is through the use of RSD data [272, 273, 274, 112, 144], which will be discussed in detail in the subsequent sections .

In this chapter, which builds upon the work which has been presented and published in Ref.[190], the $f(T)$ framework is constrained using RSD data, providing insights into the large-scale structure of the Universe. By analysing RSD data, the growth rate of cosmic structures is examined, serving as a crucial test for the viability of $f(T)$ gravity. This approach aims to evaluate the framework's consistency and robustness in describing the distribution and dynamics of matter on cosmic scales. This investigation will not only contribute to our understanding of the $H_0$ tension but also address the $S_{8,0}$ discrepancy, thereby offering a better assessment of the $f(T)$ proposal within the context of modern cosmology.

## 8.1 | Growth Rate Data

The peculiar velocities of galaxies lead to characteristic distortions in the observed large-scale structure of the Universe when measured through spectroscopic redshifts. On small scales, high-density regions such as galaxy clusters appear elongated along the line of sight due to the increased velocity dispersion of galaxies within these clusters. Conversely, on larger scales, the gravitational infall of galaxies into overdense regions causes these areas to appear flattened in the line of sight. These anisotropic distortions arise because the measured redshifts of galaxies combine both the Hubble expansion and their peculiar velocities. Consequently, redshift-space maps of galaxies show deviations from the true isotropic distribution of galaxies in real space, a phenomenon known as Redshift Space Distortion (RSD). This important probe of Large Scale Structure (LSS) provides critical insights into the dynamics of cosmic structure formation and can be used to constrain the growth rate of cosmic structures [275, 276, 277].

Indeed, RSD data is sensitive to measurements of the growth rate of matter density perturbations $f(z)$, which can be estimated using RSD cosmological probes as a way to constrain cosmological models [278, 279, 280]. The growth rate of structure $f$, which depends on the theory of gravity, is defined as in Eq. 2.36.

However different, LSS surveys such as the 2-degree Field Galaxy Redshift Survey (2dFGRS)

[281], eBOSS [282], WiggleZ Dark Energy Survey (WiggleZ) [283] and Galaxy and Mass Assembly (GAMA) [229] surveys, amongst others, typically report a value for $f\sigma_8(z) \equiv f(z) \times \sigma_8(z)$ [112], which as a reminder is defined as

$$f\sigma_8(z) = -(1+z)\frac{\sigma_{8,0}}{\delta_0}\delta'(z)\,. \tag{8.1}$$

Furthermore, the Alcock-Paczyński effect [284] must also be acknowledged. This effect occurs because converting redshifts into distances requires the assumption of a specific cosmological model. However, recent research, including the findings in Ref. [285], has shown that the impact of this effect is minimal, allowing it to be safely disregarded in our studies.

The final RSD data compilation used in this work is presented in Table II of appendix A in Ref. [286]. The corresponding $\chi^2_{\rm min}$ is given by

$$\chi^2_{\rm RSD} = \Delta Q(z_i,\Theta)^T C^{-1}_{\rm RSD}\Delta Q(z_i,\Theta)\,, \tag{8.2}$$

where $Q(z_i,\Theta) = (f\sigma_8(z_i,\Theta)_{\rm theo} - f\sigma_{8\rm obs}(z_i))$ and $C^{-1}_{\rm RSD}$ is the inverse covariance matrix. This covariance matrix is assumed to be a diagonal matrix except for the WiggleZ subset data which can be found in Table 2 of Ref. [287]. Hence, the total covariance can be written as

$$C_{\rm RSD} = \begin{pmatrix} \sigma_1^2 & 0 & 0 & \dots \\ 0 & C_{\rm WiggleZ} & 0 & \dots \\ 0 & 0 & \dots & \sigma_N^2 \end{pmatrix}\,, \tag{8.3}$$

where $C_{\rm WiggleZ}$ is the corresponding covariance matrix and $\sigma_i$ are the uncertainties of the remaining RSD observational values.

The expression for $f\sigma_8(z_i,\Theta)_{\rm theo}$ in Eq. 8.2, which represents the theoretical predictions for specific $f(T)$ models, can be derived using Eq. 8.1 (as detailed in Chapter 2) in combination with the solution to $\delta'$ in Eq. 2.66, which as a reminder reads

$$\delta''(z) + \left(\frac{H'(z)}{H(z)} - \frac{1}{1+z}\right)\delta'(z) = \frac{3}{2}\frac{G_{\rm eff}(z)}{G_N}\left(\frac{H_0}{H(z)}\right)^2 \Omega_{m,0}\,(1+z)\,\delta(z)\,, \tag{8.4}$$

where $G_{\rm eff}(z) = \frac{1}{1+f_T(z)}$ for $f(T)$ and for which $\delta_0$ was obtained from Ref. [285].

The three $f(T)$ models analysed in this chapter are the Power Law Model, Square-root Exponential Model, and Exponential Model. Indeed, Fig. 8.1 illustrates how the growth rate $f\sigma_8$ varies with redshift for each of these models, for different values of the model parameters, $p_i$. Alongside these functions, the dotted represents the Planck18/$\Lambda$CDM model for comparison. The data points with error bars represent observational $f\sigma_8$ values. The colour gradient indicates the parameter $p_i$ as shown in the colour bar, providing a visual

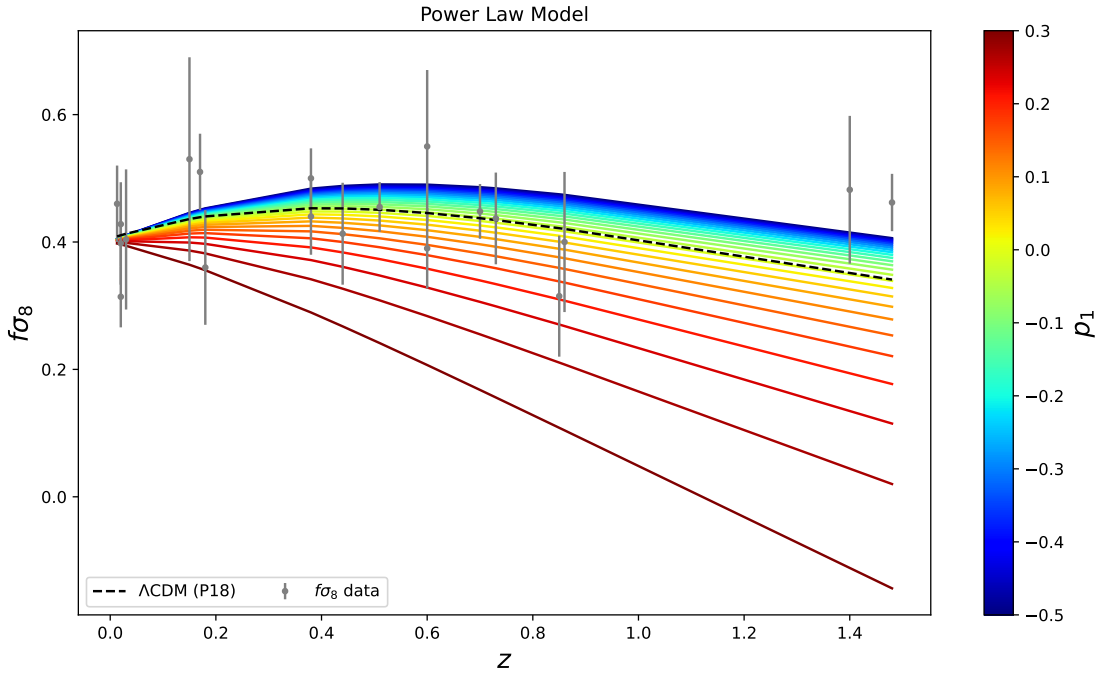
Power Law Model
$f\sigma_8$
$z$
ΛCDM (P18)
$f\sigma_8$ data
$p_1$

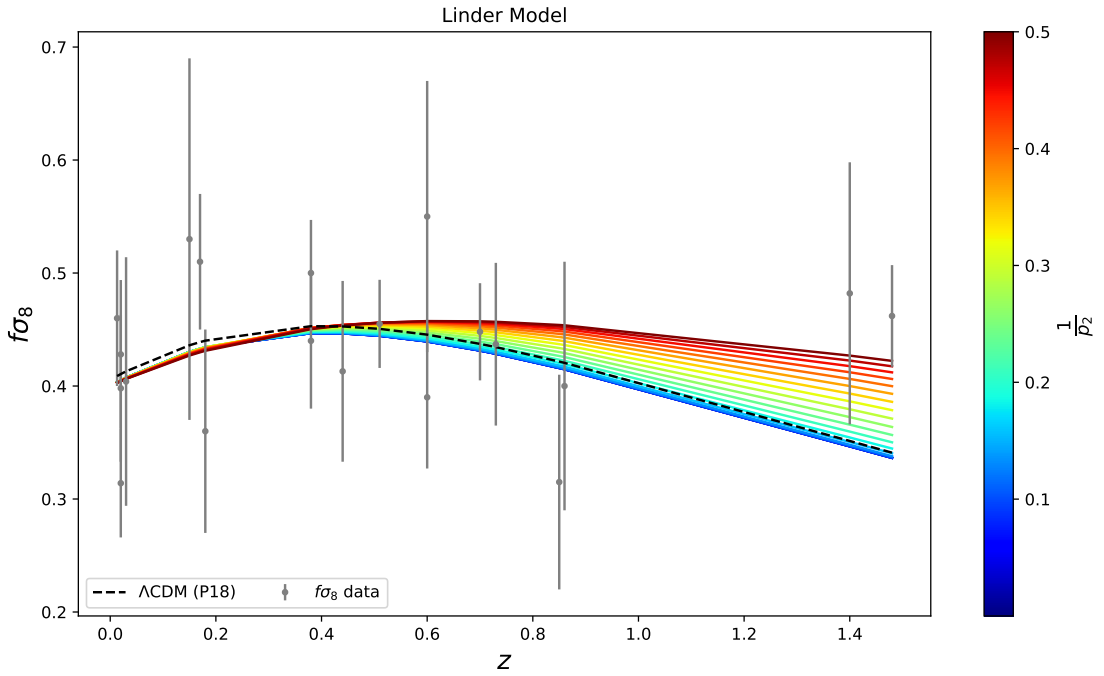
Linder Model
$f\sigma_8$
$z$
ΛCDM (P18)
$f\sigma_8$ data
$\frac{1}{p_2}$

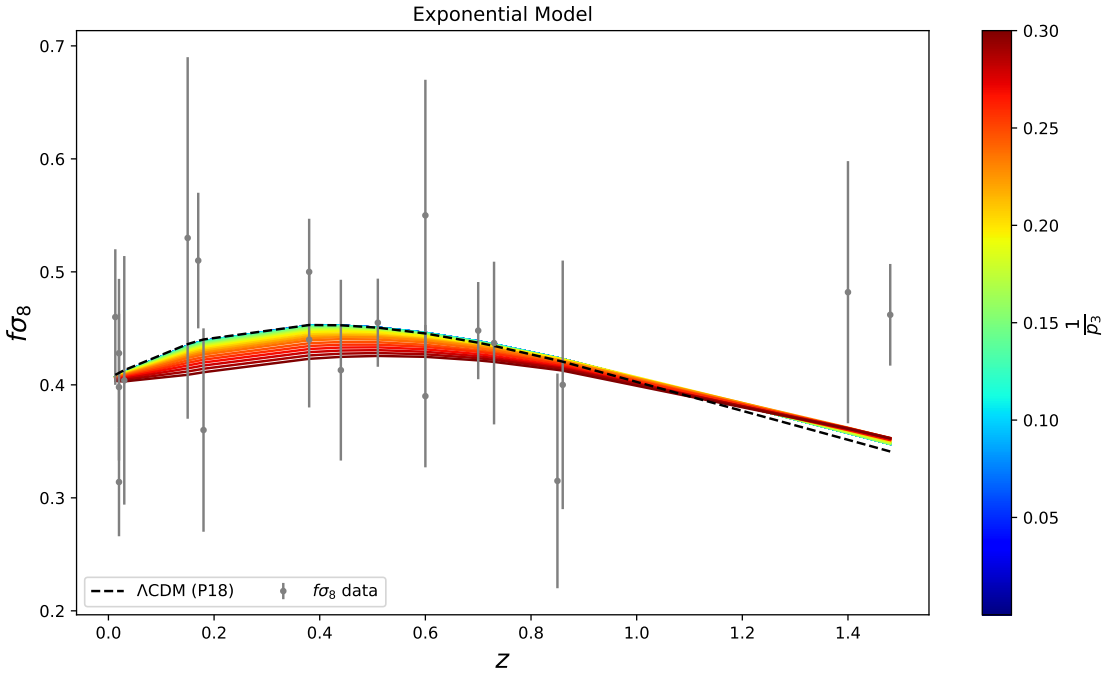


Figure 8.1: Plots of $f\sigma_8$ for the growth rate dataset for the three different models, that is Power Law Model, Linder Model and Exponential Model, respectively. The black dashed line in all figures correspond to the Planck18/ΛCDM models, whilst the error bars represent the $f\sigma_8$ data used.

representation of how different parameter values affect the predictions of the $f(T)$ models. These three sub-figures give an indication and validate the values of the model parameters $p_i$ chosen for the MCMC prior range.

Furthermore, certain differences between the models, in Fig. 8.1 become apparent. The Power Law Model exhibits the most variation in shape, as the parameter $p_1$ has a significant impact on the curve's behaviour. In contrast, the Linder Model shows a notable turning point around redshift 0.4, after which the range of curves expands moderately. The Exponential Model, however, appears more constrained, with its parameter having a less pronounced effect on the overall shape. Despite these differences, it is worth noting that all models bear a close resemblance to the shape predicted by Planck, suggesting a positive alignment with ΛCDM.

Therefore, this approach enables for the use of the above RSD data to constrain cosmological parameters for these three models, particularly $\sigma_{8,0}$. In turn, constraining such

parameter facilitates for the exploration of the [288, 289, 290, 291, 292, 293, 294]

$$S_{8,0} \equiv \sigma_{8,0}\sqrt{\Omega_{m,0}/0.3}\,. \tag{8.5}$$

## 8.2 | Constraining parameters using RSD data

As demonstrated throughout the chapters, constraining cosmological parameters is a pivotal aspect of modern cosmology. It enables the testing of theoretical models against observational data, refining our understanding of the Universe's fundamental properties. This section focuses on constraining the parameters of various $f(T)$ gravity models using RSD data. By comparing the theoretical predictions of these models with observational data, their viability can be evaluated and potentially uncover new insights into the nature of cosmic acceleration and structure formation.

The primary objective is to evaluate how well the $f(T)$ models can reproduce the observed growth rate of cosmic structures, encapsulated in the quantity $f\sigma_8$. Indeed, Fig. 8.1, already gives a positive indication. This process involves solving Eq. 8.1, together with Eq. 8.4 and fitting these predictions to the RSD data using MCMC analysis. By continuing rigorously testing these models against observations with the RSD dataset, our understanding of the Universe's large-scale structure and the underlying physics driving its evolution can be enhanced.

### 8.2.1 | ΛCDM Model

In this section, the ΛCDM model is presented as a reference point to facilitate comparisons with the $f(T)$ models. The posterior distributions and confidence regions resulting from the MCMC analysis for the ΛCDM model are illustrated in Fig. 8.2. In addition to the standard cosmological parameters for this model, namely $H_0$ and $\Omega_{m,0}$, the inclusion of the RSD dataset allows for the constraint of $\sigma_{8,0}$.

The purple, red, and orange contours, which incorporate RSD data in their dataset combinations, demonstrate the ability to constrain $\sigma_{8,0}$ effectively, as shown in Fig. 8.2. Conversely, the blue and green contours, which exclude RSD data, highlight the impact of growth rate data on the constraints.

The precise parameter values for the different dataset combinations are detailed in Table 8.1, providing information on $H_0$, $\Omega_{m,0}$, $\sigma_{8,0}$ and $M$. Additionally, the constraints on $\sigma_{8,0}$ and $\Omega_{m,0}$ facilitate the exploration of the $S_{8,0}$ tension through Eq. 8.5. Indeed, the results and posterior distributions for the parameter $S_{8,0}$ are presented in Fig. 8.3 and Table 8.2, respectively, which will allow for direct comparison of the values. Notably, the highest value is

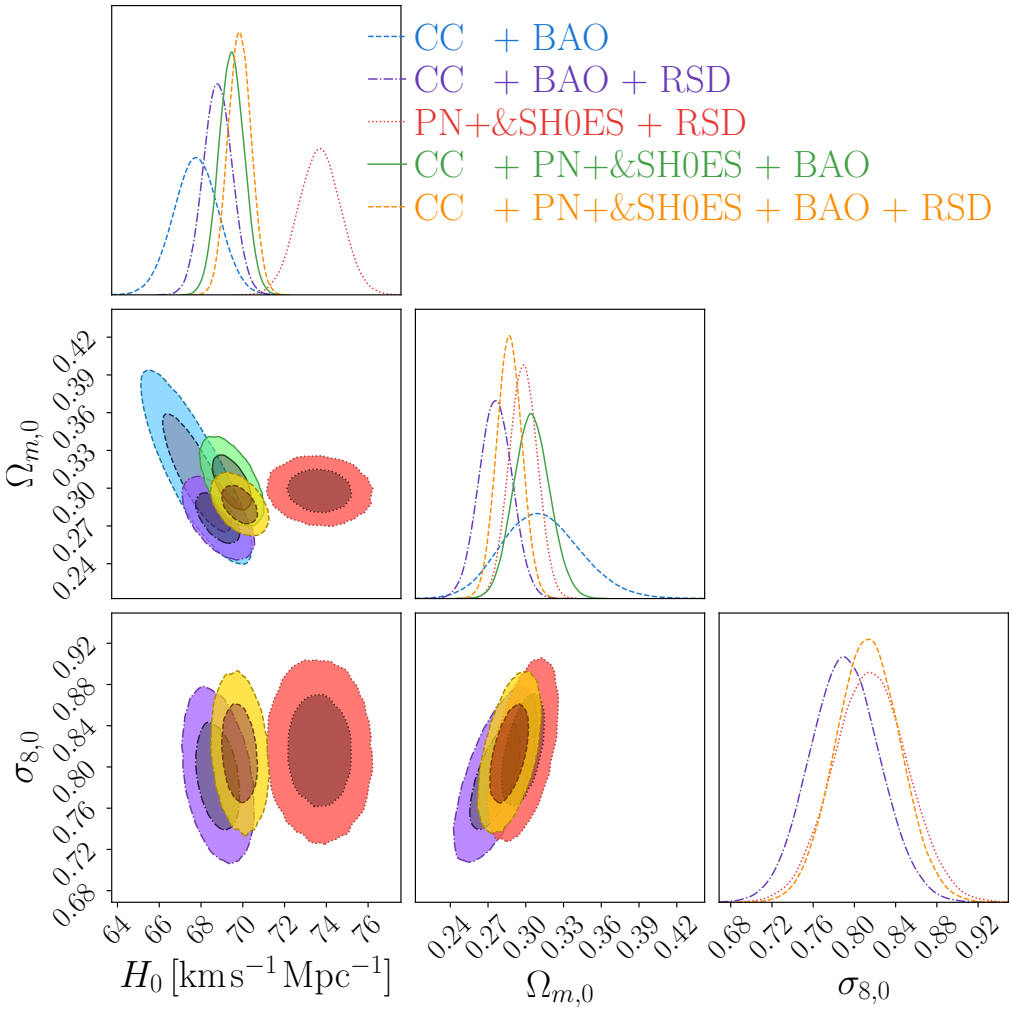


Figure 8.2: Confidence contours and posterior distributions for the ΛCDM model parameters, including $H_0$ and $\Omega_{m,0}$. In cases where the RSD data is incorporated (purple, red, and yellow contours), the $\sigma_{8,0}$ parameter is also displayed.

observed when PN+& SH0ES is combined with RSD data, bringing it closer to the P18 estimate. For comparison, the values derived from RSD data alone are also provided, showing a result on the lower end of the spectrum, indeed, even lower than the value obtained by KiDS-1000. Therefore, the values derived from these different dataset combinations exhibit some variation but remain consistent with those reported in the literature.

In fact, the values obtained for this model are found to align well with those reported by Nunes et al. in Ref. [295], which presents results for the ΛCDM model using the CC+PN+BAO+RSD dataset combinations. The primary difference between the results in Table 8.1 and those in

| Data Sets | $H_0$ [km s$^{-1}$ Mpc$^{-1}$] | $\Omega_{m,0}$ | $\sigma_{8,0}$ | $M$ |
|---|---|---|---|---|
| CC + BAO | $67.8 \pm 1.1$ | $0.308^{+0.032}_{-0.029}$ | – | – |
| CC + BAO + RSD | $68.77^{+0.71}_{-0.67}$ | $0.276^{+0.013}_{-0.014}$ | $0.789^{+0.035}_{-0.033}$ | – |
| PN$^+$ & SH0ES + RSD | $73.71^{+0.97}_{-1.06}$ | $0.298^{+0.011}_{-0.012}$ | $0.814^{+0.037}_{-0.034}$ | $-19.249^{+0.027}_{-0.032}$ |
| CC + PN$^+$ & SH0ES + BAO | $69.47^{+0.59}_{-0.63}$ | $0.304^{+0.015}_{-0.014}$ | – | $-19.375 \pm 0.017$ |
| CC + PN$^+$ & SH0ES + BAO + RSD | $69.84^{+0.55}_{-0.56}$ | $0.288^{+0.010}_{-0.010}$ | $0.815^{+0.030}_{-0.033}$ | $-19.369^{+0.016}_{-0.017}$ |

Table 8.1: Exact results for ΛCDM model that include the parameters $H_0$ and $\Omega_{m,0}$. The $\sigma_{8,0}$ parameter and the nuisance parameter $M$, are provided for datasets that include RSD or PN$^+$ & SH0ES, respectively otherwise, they are left empty.

Nunes et al. is attributed to the update from the PN dataset to the PN+& SH0ES dataset. This change allows for a direct comparison between the two sets of results. Additionally, the $H_0$ parameter is included in the current analysis, providing a broader context for the constrained parameters derived from the dataset combinations. This inclusion offers a more comprehensive perspective on the results and enhances the overall understanding of the constrained values. Specifically, the parameters $\Omega_{m,0}$, $\sigma_{8,0}$, and $S_{8,0}$ obtained in this work are within less than $1\sigma$ of those reported by Nunes et al., considering the only difference being the updated PN+& SH0ES dataset used in this study.

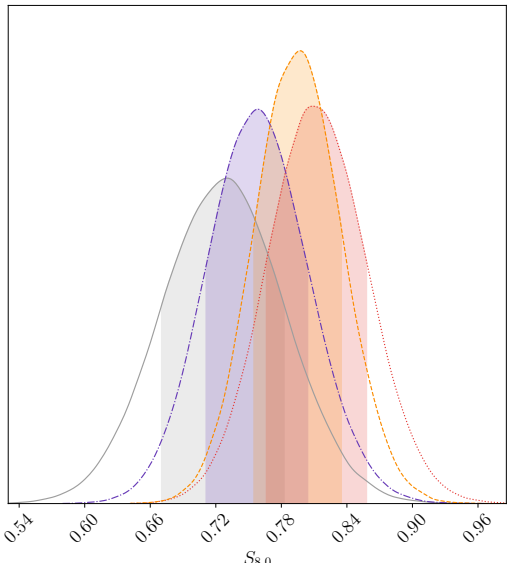


Figure 8.3: Posterior distribution for the $S_{8,0}$ parameter in the ΛCDM model. Legend: Grey denotes the RSD data, purple corresponds to CC+BAO+RSD data, red represents the PN$^+$ & SH0ES + RSD dataset, while orange indicates CC + PN$^+$ & SH0ES + BAO + RSD data.

| Model | $S_{8,0}$ |
|---|---|
| RSD | $0.729^{+0.053}_{-0.059}$ |
| CC + BAO + RSD | $0.758^{+0.046}_{-0.047}$ |
| PN$^+$ & SH0ES + RSD | $0.809^{+0.050}_{-0.042}$ |
| CC + PN$^+$ & SH0ES + BAO + RSD | $0.797^{+0.038}_{-0.042}$ |

Table 8.2: Exact $S_{8,0}$ values corresponding to various datasets for the ΛCDM model.

### 8.2.2 | Power Law Model: $f_1$CDM

Throughout the chapters, the Power Law Model, or $f_1$CDM model, has been a prominent focus, utilising Eq. 3.54 as its Friedmann Equation. In this context, apart from the three standard parameters, the mass fluctuations $\sigma_{8,0}$ can also be constrained when the RSD data is incorporated into the dataset combinations. The contour plots and posterior distributions for this model are presented in Fig. 8.4. Here, the blue and green contours represent the CC+BAO and CC+PN+& SH0ES+BAO datasets, respectively, while the remaining colours include the RSD data. These contours align with previous results, demonstrating continuity in the findings. However, a prominent feature from the posteriors is the impact of the RSD data. The posteriors show tighter constraints, which is further confirmed in Table 8.3, detailing the precise values corresponding to each dataset.

The posteriors and the values in the table confirm that the PN+& SH0ES+RSD combination achieves the highest $H_0$ value at $73.7 \pm 1.0\,\mathrm{km\,s^{-1}\,Mpc^{-1}}$. The lowest $H_0$ value, consistent with previous results, is found with the CC+BAO combination, yielding $68.1^{+1.4}_{-1.2}\,\mathrm{km\,s^{-1}\,Mpc^{-1}}$. Additionally, the anti-correlation between the Hubble parameter $H_0$ and the matter density $\Omega_{m,0}$, evident in previous results, is even more pronounced with the PN+& SH0ES+RSD data, indicating that the Universe predominantly manifests as an effective dark energy driven by an elevated $H_0$ parameter. This relationship is further supported by the values in Table 8.3.

Regarding the model parameter $p_1$, it is crucial to remember that as $p_1$ approaches 0, the model converges to the standard cosmological model. The resultant values of $p_1$ are close to 0, and this limit falls within the $1\sigma$ range. Furthermore, the inclusion of the new dataset leads to tighter constraints on the $p_1$ parameter. This effect is not exclusive to $p_1$ but extends to other parameters as well, as evidenced by both the contour plots in Fig. 8.4 and the error margins in Table 8.3.

The RSD data has been instrumental in constraining $\sigma_{8,0}$. At first glance, there appears to be a correlation between the Hubble parameter $H_0$ and the mass fluctuations $\sigma_{8,0}$. However, the contour plots reveal a more complex and degenerate relationship between these parameters.

Given that the growth rate $f\sigma_8$ depends on the matter perturbation $\delta(z)$, which can be obtained using Eq. 2.66, it is important to note that this equation depends on $G_{\mathrm{eff}}$. For $f(T)$ gravity, $G_{\mathrm{eff}}$ can be defined as in Eq. 2.65 [285]. Specifically, for the Power Law Model, this equation becomes

$$G_{\mathrm{eff}} = \frac{G_N}{1 - \alpha_1 p_1 (-T)^{p_1 - 1}}\,, \tag{8.6}$$

where specific values for the free parameters can be extracted from the table. Under these

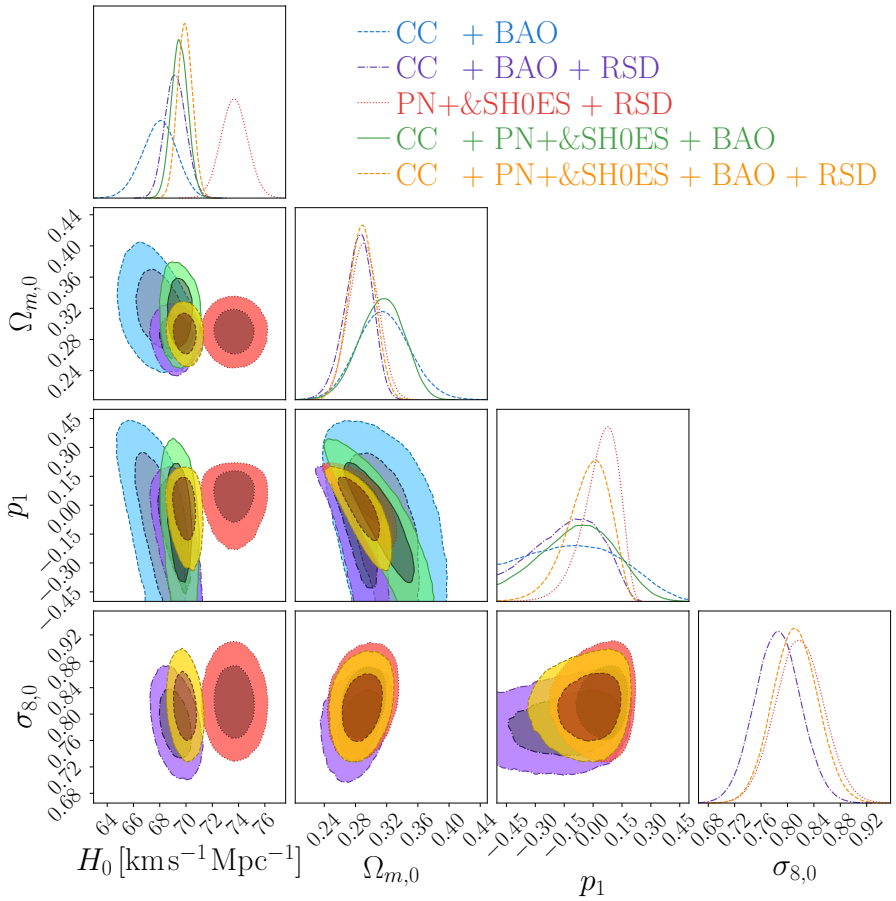


Figure 8.4: Confidence contours and posterior distributions for the $f_1$CDM model (Power Law Model) parameters, including $H_0$, $\Omega_{m,0}$, and $p_1$. In cases where the RSD data is incorporated (purple, red, and yellow contours), the $\sigma_{8,0}$ parameter is also displayed.

| Data sets | $H_0$ [km s$^{-1}$ Mpc$^{-1}$] | $\Omega_{m,0}$ | $p_1$ | $\sigma_{8,0}$ | $M$ |
|---|---|---|---|---|---|
| CC + BAO | $68.1^{+1.2}_{-1.4}$ | $0.314^{+0.034}_{-0.033}$ | $-0.09^{+0.24}_{-0.30}$ | – | – |
| CC + BAO + RSD | $69.17 \pm 0.81$ | $0.287^{+0.016}_{-0.020}$ | $-0.09^{+0.17}_{-0.20}$ | $0.785 \pm 0.035$ | – |
| PN$^+$ & SH0ES + RSD | $73.7 \pm 1.0$ | $0.290^{+0.019}_{-0.018}$ | $0.076^{+0.075}_{-0.102}$ | $0.817^{+0.037}_{-0.035}$ | $-19.252^{+0.029}_{-0.030}$ |
| CC + PN$^+$ & SH0ES + BAO | $69.45^{+0.69}_{-0.58}$ | $0.316^{+0.028}_{-0.029}$ | $-0.06^{+0.19}_{-0.22}$ | – | $-19.375 \pm 0.017$ |
| CC + PN$^+$ & SH0ES + BAO + RSD | $69.90 \pm 0.58$ | $0.289^{+0.016}_{-0.018}$ | $0.014^{+0.091}_{-0.125}$ | $0.810^{+0.036}_{-0.033}$ | $-19.367^{+0.016}_{-0.017}$ |

Table 8.3: Exact results for $f_1$ model that include the parameters $H_0$, $\Omega_{m,0}$ and $p_1$. The $\sigma_{8,0}$ parameter and the nuisance parameter $M$, are provided for datasets that include RSD or PN$^+$ & SH0ES, respectively otherwise, they are left empty.

conditions, $G_{\text{eff}}$ approximates $G_N$.

Additionally, the values for the $S_{8,0}$ parameter, derived from the $\Omega_{m,0}$ and $\sigma_{8,0}$ parameters, are presented in Table 8.4, while the posterior distributions are depicted in Fig. 8.5. The highest observed value for $S_{8,0}$, consistent with the values obtained for $\sigma_{8,0}$, was achieved with the PN+& SH0ES+RSD combination, measuring $S_{8,0} = 0.801^{+0.052}_{-0.046}$. It is noteworthy that values for the RSD dataset alone are also provided to isolate the impact of RSD data on this parameter. In this case, the value for the RSD dataset reaches a minimum. Furthermore, it is evident that the constraints for $S_{8,0}$ across all datasets are notably tight.

The effect of the model parameter on the $S_{8,0}$ parameter is also important to investigate, in order to check if the value of the model parameter impacts on the value of $S_{8,0}$. Therefore, the relationship between these two parameters is examined, and depicted in Fig.C.1 in Appendix C. A significant anti-correlation between these two parameters is observed, suggesting that changes in the power-law exponent $p_1$ may directly impact the amplitude of mass fluctuations $S_{8,0}$.

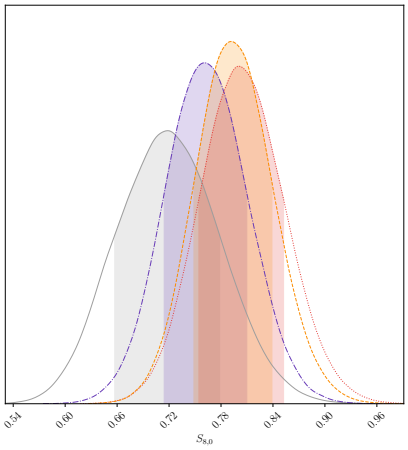


Figure 8.5: Posterior distribution for the $S_{8,0}$ parameter in the $f_1$CDM model. Legend: Grey denotes the RSD data, purple corresponds to CC+BAO+RSD data, red represents the PN$^+$ &,SH0ES + RSD dataset, while orange indicates CC + PN$^+$ & SH0ES + BAO + RSD data.

| Data sets | $S_{8,0}$ |
|---|---|
| — RSD | $0.718^{+0.061}_{-0.060}$ |
| ···-CC + BAO + RSD | $0.761^{+0.049}_{-0.046}$ |
| ····· PN$^+$ & SH0ES + RSD | $0.801^{+0.052}_{-0.046}$ |
| - - -CC + PN$^+$ & SH0ES + BAO + RSD | $0.792^{+0.047}_{-0.043}$ |

Table 8.4: Exact $S_{8,0}$ values corresponding to various datasets for the $f_1$CDM model.

### 8.2.3 | Linder Model: $f_2$CDM

The second model under consideration, as examined in other works, is the Linder model, or $f_2$CDM model, with its Friedmann equation represented by Eq. 3.57. The posterior distributions and confidence levels for the constrained parameters are illustrated in Fig. 8.6. Similar to the Power Law model, the highest value for the $H_0$ parameter is obtained when combining PN+& SH0ES with RSD data, as indicated by the precise values in Table 8.5. In contrast, the lowest $H_0$ value, specifically $H_0 = 66.5^{+2.2}_{-1.3}\,\mathrm{km\,s^{-1}Mpc^{-1}}$, is observed for the CC+BAO+RSD combination. Overall, in this scenario, the parameter values trend slightly lower compared to the $f_1$CDM model.

Regarding the $\Omega_{m,0}$ parameter, a similar trend to that of the $H_0$ parameter is observed, with lower values being reported. The consistent pattern persists, where datasets that include RSD values yield lower values for $\Omega_{m,0}$ compared to those that do not incorporate RSD data. The anti-correlation between the $H_0$ parameter and the $\Omega_{m,0}$ parameter remains visible. However, compared to the $f_1$CDM model, the anti-correlation between $\Omega_{m,0}$ and the model parameter is less pronounced, resulting in a higher degree of degeneracy between these two parameters.

The values obtained for the $1/p_2$ parameter are slightly higher than those in the $f_1$CDM model. Additionally, in contrast to the previous model, the $\Lambda$CDM limit does not fall within the $1\sigma$ region, indicating a slight deviation from the $\Lambda$CDM model. This deviation suggests that the Linder model might exhibit characteristics distinct from the standard $\Lambda$CDM model.

The parameter $\sigma_{8,0}$ continues to exhibit the same trend observed previously, with consistently lower values. A correlation between this parameter and $\Omega_{m,0}$ is observed across all datasets, while the degeneracy between $\sigma_{8,0}$ and $H_0$ remains valid in this model. Similar to the previous model, the trend in $G_{\mathrm{eff}}$ is observed, where $G_{\mathrm{eff}} \approx G_N$ as given by

$$G_{\mathrm{eff}} = \frac{G_N}{1 + \frac{1}{2}\alpha_2 p_2 \sqrt{\frac{T_0}{T}}\,\mathrm{Exp}\left[-p_2\sqrt{\frac{T}{T_0}}\right]}\,. \tag{8.7}$$

| Data Sets | $H_0$ [km s$^{-1}$ Mpc$^{-1}$] | $\Omega_{m,0}$ | $\frac{1}{p_2}$ | $\sigma_{8,0}$ | M |
|---|---|---|---|---|---|
| CC + BAO | $67.2^{+1.2}_{-1.6}$ | $0.302^{+0.035}_{-0.030}$ | $0.00^{+0.37}_{-0.00}$ | – | – |
| CC + BAO + RSD | $66.5^{+2.2}_{-1.3}$ | $0.286^{+0.016}_{-0.015}$ | $0.39^{+0.21}_{-0.22}$ | $0.784^{+0.038}_{-0.032}$ | – |
| PN$^+$ & SH0ES + RSD | $73.2 \pm 1.0$ | $0.287 \pm 0.013$ | $0.359^{+0.077}_{-0.071}$ | $0.770^{+0.042}_{-0.039}$ | $-19.26^{+0.33}_{-0.31}$ |
| CC + PN$^+$ & SH0ES + BAO | $69.35^{+0.61}_{-0.63}$ | $0.299^{+0.017}_{-0.021}$ | $0.167^{+0.080}_{-0.154}$ | – | $-19.40^{+0.21}_{-0.16}$ |
| CC + PN$^+$ & SH0ES + BAO + RSD | $69.38^{+0.67}_{-0.68}$ | $0.282 \pm 0.011$ | $0.275^{+0.083}_{-0.096}$ | $0.793 \pm 0.035$ | $-19.37^{+0.31}_{-0.30}$ |

Table 8.5: Exact results for $f_2$ model that include the parameters $H_0$, $\Omega_{m,0}$ and $\frac{1}{p_2}$. The $\sigma_{8,0}$ parameter and the nuisance parameter $M$, are provided for datasets that include RSD or PN$^+$ & SH0ES, respectively otherwise, they are left empty.

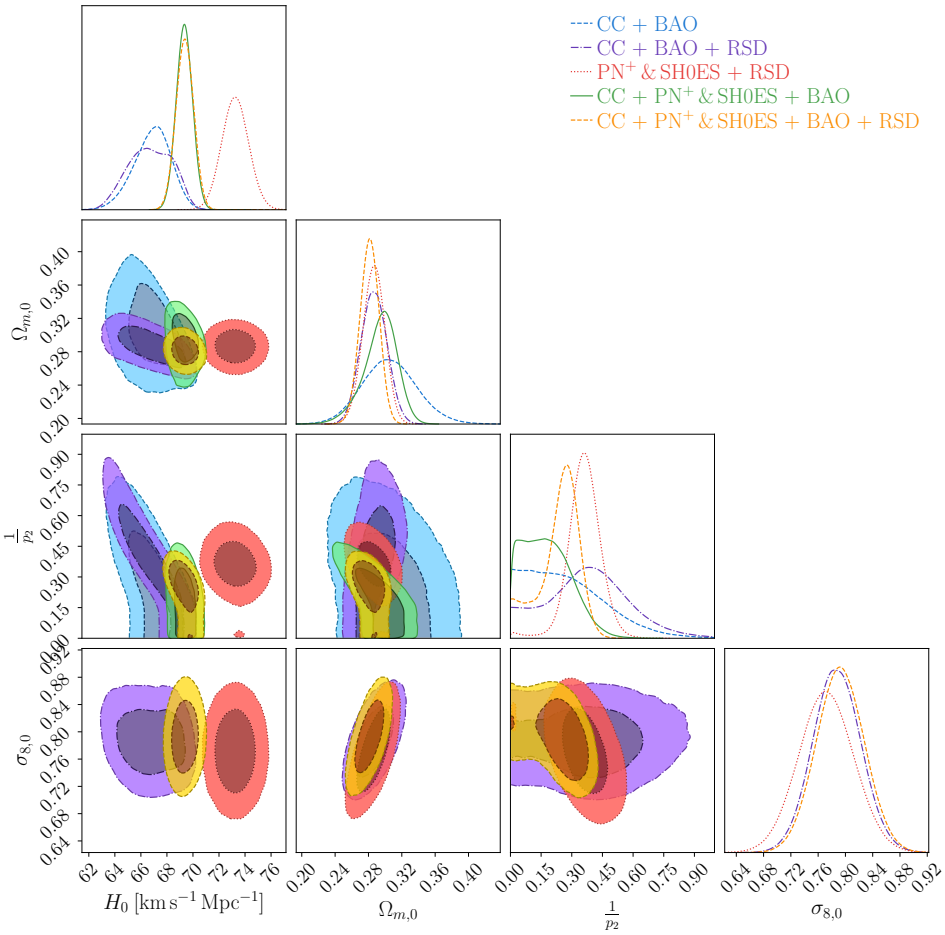


Figure 8.6: Confidence contours and posterior distributions for the $f_2$CDM model (Linder Model) parameters, including $H_0$, $\Omega_{m,0}$, and $\frac{1}{p_2}$. In cases where the RSD data is incorporated (purple, red, and yellow contours), the $\sigma_{8,0}$ parameter is also displayed.

When RSD data is included, the quantity $S_{8,0}$ is calculated, yielding slightly different results compared to the previous model, as shown in Table 8.6 and Fig. 8.7. Similar results are obtained for the CC+BAO+RSD datasets, but a lower value is observed for the PN+& SH0ES+RSD combination. Conversely, higher values are obtained for the RSD dataset alone and for the CC+PN+& SH0ES+BAO+RSD combination, with the maximum value achieved for the former dataset, whereas previously it exhibited the minimum value.

Finally, the correlation between the parameters $p$ and $S_{8,0}$ is examined. The degeneracy in the RSD data persists; however, when the PN+& SH0ES data is combined with the RSD data, an anti-correlation is now evident. These findings are visually represented in Appendix C, specifically in Fig. C.2.

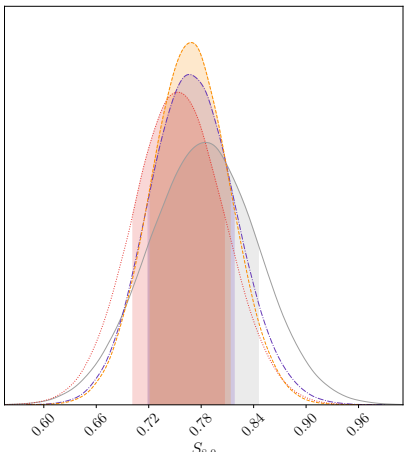


Figure 8.7: Posterior distribution for the $S_{8,0}$ parameter in the $f_2$CDM model. Legend: Grey denotes the RSD data, purple corresponds to CC+BAO+RSD data, red represents the PN$^+$ &,SH0ES + RSD dataset, while orange indicates CC + PN$^+$ & SH0ES + BAO + RSD data.

| Data sets | $S_{8,0}$ |
|---|---|
| RSD | $0.784^{+0.061}_{-0.065}$ |
| CC + BAO + RSD | $0.765^{+0.052}_{-0.046}$ |
| PN$^+$ & SH0ES + RSD | $0.753^{+0.054}_{-0.051}$ |
| CC + PN$^+$ & SH0ES + BAO + RSD | $0.768^{+0.045}_{-0.046}$ |

Table 8.6: Exact $S_{8,0}$ values corresponding to various datasets for the $f_2$CDM model.

### 8.2.4 | Exponential Model: $f_3$CDM

The next model considered in this chapter is the Exponential Model, or $f_3$CDM model, characterised by the Friedmann Equation given in Eq. 3.61. This model behaves similarly to the Linder Model, approaching the ΛCDM limit as $p_3 \to \infty$. To maintain numerical stability, the analyses are conducted using $1/p_3$, consistent with the approach used for the previous model. In this context, $G_{\text{eff}}$ is defined as

$$G_{\text{eff}} = \frac{G_N}{1 + \alpha_3 p_3 \text{Exp}\left[-p_3 \frac{T}{T_0}\right]}, \tag{8.8}$$

demonstrating a similar trend to the previously discussed models.

The confidence levels and posterior distributions of the constrained parameters are shown in Fig. 8.8, with the exact constrained values detailed in Table 8.7. Notably, removing the square root component has significantly affected the constraints, particularly on the parameter $\sigma_{8,0}$. This model reports significantly higher $\sigma_{8,0}$ values compared to the $f_2$CDM model.

Consistent with the $f_1$CDM model, the $f_3$CDM model achieves the highest constrained value for $H_0$ using the PN+& SH0ES+RSD data combination. Specifically, $H_0$ is constrained to $73.2^{+1.1}_{-1.14}\,\text{km}\,\text{s}^{-1}\,\text{Mpc}^{-1}$, while the lowest value is obtained from the CC+BAO data combination, yielding $H_0 = 67.5^{+1.7}_{-2.3}\,\text{km}\,\text{s}^{-1}\,\text{Mpc}^{-1}$. Similarly, the density parameter $\Omega_{m,0}$ reaches

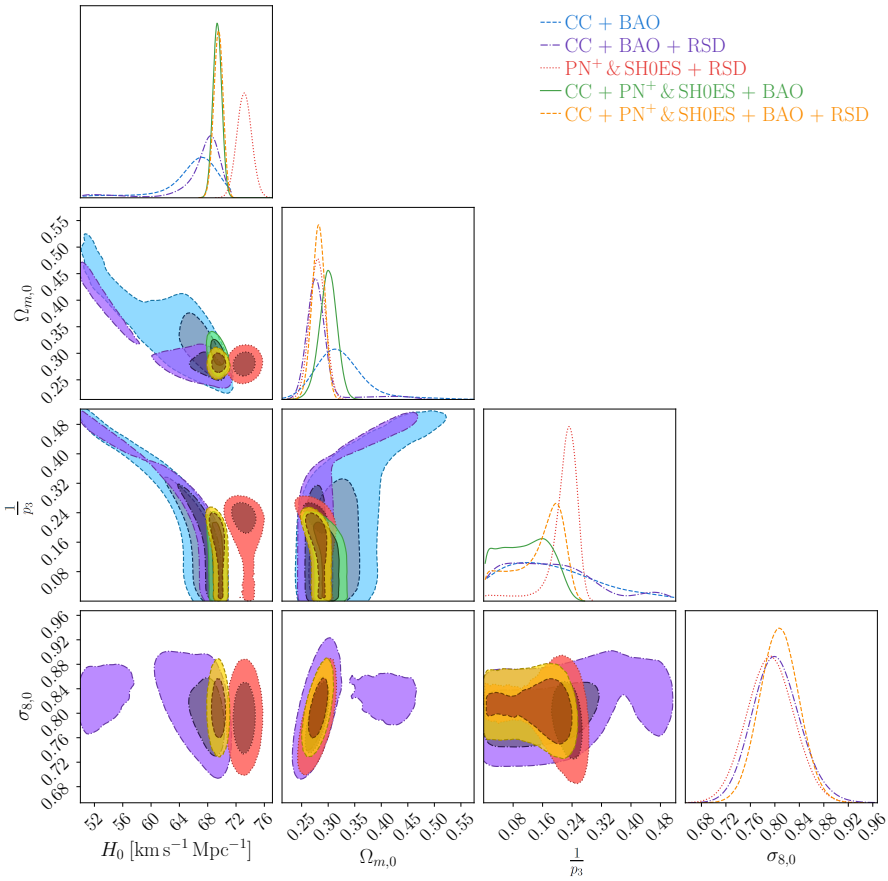


Figure 8.8: Confidence contours and posterior distributions for the $f_3$CDM model (Exponential Model) parameters, including $H_0$, $\Omega_{m,0}$, and $\frac{1}{p_3}$. In cases where the RSD data is incorporated (purple, red, and yellow contours), the $\sigma_{8,0}$ parameter is also displayed.

| Data Sets | $H_0$ [km s$^{-1}$ Mpc$^{-1}$] | $\Omega_{m,0}$ | $\frac{1}{p_3}$ | $\sigma_{8,0}$ | $M$ |
|---|---|---|---|---|---|
| CC + BAO | $67.5^{+1.7}_{-2.3}$ | $0.311^{+0.039}_{-0.034}$ | $0.058^{+0.182}_{-0.056}$ | – | – |
| CC + BAO + RSD | $68.6^{+1.3}_{-1.9}$ | $0.276^{+0.016}_{-0.015}$ | $0.026^{+0.214}_{-0.025}$ | $0.798^{+0.040}_{-0.036}$ | – |
| PN$^+$ & SH0ES + RSD | $73.2^{+1.0}_{-1.1}$ | $0.280^{+0.014}_{-0.015}$ | $0.232^{+0.027}_{-0.031}$ | $0.793^{+0.038}_{-0.039}$ | $-19.25 \pm 0.11$ |
| CC + PN$^+$ & SH0ES + BAO | $69.34^{+0.65}_{-0.64}$ | $0.300^{+0.017}_{-0.016}$ | $0.160^{+0.029}_{-0.126}$ | – | $-19.34^{+0.24}_{-0.31}$ |
| CC + PN$^+$ & SH0ES + BAO + RSD | $69.54^{+0.64}_{-0.66}$ | $0.282 \pm 0.012$ | $0.197^{+0.038}_{-0.092}$ | $0.807 \pm 0.032$ | $-19.38^{+0.20}_{-0.19}$ |

Table 8.7: Exact results for $f_3$ model that include the parameters $H_0$, $\Omega_{m,0}$ and $\frac{1}{p_3}$. The $\sigma_{8,0}$ parameter and the nuisance parameter $M$, are provided for datasets that include RSD or PN$^+$ & SH0ES, respectively otherwise, they are left empty.

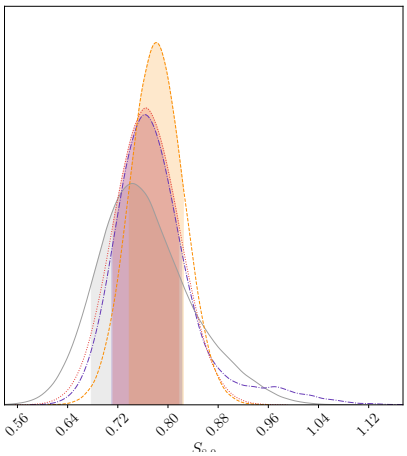


Figure 8.9: Posterior distribution for the $S_{8,0}$ parameter in the $f_3$CDM model. Legend: Grey denotes the RSD data, purple corresponds to CC+BAO+RSD data, red represents the PN$^+$ &,SH0ES + RSD dataset, while orange indicates CC + PN$^+$ & SH0ES + BAO + RSD data.

| Data Sets | $S_{8,0}$ |
|---|---|
| — RSD | $0.744^{+0.079}_{-0.066}$ |
| ·-·-CC + BAO + RSD | $0.762^{+0.059}_{-0.052}$ |
| ·····PN$^+$ & SH0ES + RSD | $0.765^{+0.053}_{-0.052}$ |
| - - -CC + PN$^+$ & SH0ES + BAO + RSD | $0.782 \pm 0.043$ |

Table 8.8: Exact $S_{8,0}$ values corresponding to various datasets for the $f_3$CDM model.

its highest value for CC+BAO, where $\Omega_{m,0} = 0.311^{+0.039}_{-0.034}$. Including RSD data leads to tighter constraints on these parameters, particularly on the density parameter.

The model parameter, $1/p_3$ has a range within the $1\sigma$ and $2\sigma$ confidence intervals is narrower compared to the $f_2$CDM model. Here, the $2\sigma$ interval extends from 0 to a maximum of 0.5, but, similar to $f_2$CDM, it remains within $2\sigma$ of the $\Lambda$CDM limit.

A significant difference in this model is observed in the $\sigma_{8,0}$ parameter, which reports a higher value. Additionally, a correlation between $\Omega_{8,0}$ and $\sigma_{8,0}$ is now evident, unlike in the $f_1$CDM model but similar to the $f_2$CDM model. The degeneracy between the $H_0$ and $\sigma_{8,0}$ parameters remains consistent with previous observations.

The highest value for $S_{8,0}$ is obtained for the CC+PN+& SH0ES+BAO+RSD combination, yielding $S_{8,0} = 0.782 \pm 0.043$, as detailed in Table 8.8 and illustrated in Fig. 8.9. Conversely, reflecting the values obtained for $\sigma_{8,0}$ the lowest value for $S_{8,0}$ is achieved with the PN+& SH0ES+RSD data combination, as shown in the tables presenting the $\sigma_{8,0}$ and $S_{8,0}$ values, respectively. Consistent with previous models, the value for $S_{8,0}$ obtained using the RSD data alone is relatively low, similar to the $f_1$CDM model.

Additionally, the final analysis for the $f_3$CDM model is depicted in Fig. C.3 in Appendix C. This figure illustrates a degenerate relationship between the parameters $p_3$ and $S_{8,0}$, which transitions into an anti-correlation at higher values of $p_3$. This effect is particu-

larly noticeable for datasets that incorporate BAO measurements, highlighting the complex interplay between these parameters under different data combinations.

## 8.3 | Analysis and Tension metrics

To evaluate the effectiveness of these three cosmological models using different dataset combinations, the differences in the AIC and BIC between each model ($f_i$CDM) and the reference $\Lambda$CDM model are calculated, as has been previously done. These differences, represented as $\Delta$AIC and $\Delta$BIC defined by Eqs. 3.71,3.72, help determine how closely each model aligns with the standard model. And as has been indicated multiple times throughout the chapters, lower values of $\Delta$AIC and $\Delta$BIC suggest that a model, along with its dataset, better approximates the $\Lambda$CDM model, indicating improved performance. Table 8.9 provides a comparison of these metrics, together with the $\chi^2_{\rm min}$ for the CC+BAO and CC+BAO+RSD datasets, in order to highlight the effect of the RSD dataset on these statistical indicators. Similarly, Table 8.10 allows for a comparison of $\Delta$AIC and $\Delta$BIC values across three dataset combinations: PN+& SH0ES+RSD, CC+PN+& SH0ES+BAO, and CC+PN+& SH0ES+BAO+RSD.

Table 8.9 demonstrates that the CC+BAO dataset typically has a lower $\chi^2_{\rm min}$, indicating a better fit in the absence of RSD. However, the $\Delta$AIC values for CC+BAO+RSD show a notable decrease, suggesting the increased suitability of this dataset in some instances. The $\Delta$BIC values for CC+BAO+RSD are slightly higher due to the inclusion of additional data points. In terms of overall model performance, the $f_2$CDM model consistently has the lowest $\Delta$AIC and $\Delta$BIC values, highlighting its dependable performance. The $f_1$CDM and $f_3$CDM models also perform well, demonstrating their suitability for this dataset.

Table 8.10 offers intriguing insights. For the PN+& SH0ES+RSD dataset combinations, the models are preferred over $\Lambda$CDM, as indicated by negative AIC and BIC values. This preference is not consistently observed across all models for the CC+PN+& SH0ES+BAO dataset but reappears for CC+PN+& SH0ES+BAO+RSD, especially for the $f_2$CDM and $f_3$CDM models. This highlights the effect that the RSD had on these three models and suggests that these two models, within the CC+PN+& SH0ES+BAO+RSD dataset, are favoured over $\Lambda$CDM. However, the evidence is not strong enough to definitively favour these models over $\Lambda$CDM. To further emphasise this point, one can look at the BIC values, where although not negative, the values are close to zero, indicating an inconclusive preference.

Further support for this analysis is provided by Fig. 8.10, which compares the $H_0$ values obtained from $f_i(T)$CDM ($i = 1, 2, 3$) models to those from the $\Lambda$CDM model for the same datasets, as detailed in Sec. 8.2.1 using Eq. 4.1. This visualisation highlights the variations in $H_0$ across different datasets, expressed in $\sigma$ units, with each dataset represented by a

| | CC+BAO | | | CC+BAO+RSD | | |
|---|---|---|---|---|---|---|
| | $\chi^2_{\rm min}$ | $\Delta$AIC | $\Delta$BIC | $\chi^2_{\rm min}$ | $\Delta$AIC | $\Delta$BIC |
| $\Lambda$CDM | 20.93 | 0 | 0 | 37.14 | 0 | 0 |
| $f_1$CDM | 20.87 | 1.94 | 1.61 | 37.04 | 1.91 | 3.15 |
| $f_2$CDM | 20.93 | 2.00 | 1.66 | 35.41 | 0.28 | 1.52 |
| $f_3$CDM | 20.93 | 2.00 | 1.66 | 37.21 | 2.08 | 3.32 |

Table 8.9: Comparison of $\chi^2_{\rm min}$ and differences in AIC and BIC between the models and $\Lambda$CDM (i.e $\Delta$AIC and $\Delta$BIC). On the left-hand side, results are presented for CC+BAO, while the right-hand side includes RSD.

| | PN$^+$ & SH0ES+RSD | | | CC+PN$^+$ & SH0ES+BAO | | | CC+PN$^+$ & SH0ES+BAO+RSD | | |
|---|---|---|---|---|---|---|---|---|---|
| | $\chi^2_{\rm min}$ | $\Delta$AIC | $\Delta$BIC | $\chi^2_{\rm min}$ | $\Delta$AIC | $\Delta$BIC | $\chi^2_{\rm min}$ | $\Delta$AIC | $\Delta$BIC |
| $\Lambda$CDM | 1550.20 | 0 | 0 | 1572.60 | 0 | 0 | 1590.71 | 0 | 0 |
| $f_1$CDM | 1549.52 | 1.32 | 2.56 | 1572.56 | 1.96 | 1.78 | 1590.56 | 1.85 | 3.10 |
| $f_2$CDM | 1541.46 | $-6.74$ | $-5.50$ | 1572.50 | 1.89 | 1.72 | 1587.49 | $-1.21$ | 0.04 |
| $f_3$CDM | 1543.13 | $-5.07$ | $-3.84$ | 1572.31 | 1.71 | 1.53 | 1588.33 | $-0.37$ | 0.88 |

Table 8.10: Comparison of $\chi^2_{\rm min}$ and differences in AIC and BIC between the models and $\Lambda$CDM (i.e $\Delta$AIC and $\Delta$BIC). On the left-hand side, results are presented for PN$^+$ & SH0ES+RSD, whilst in the middle CC+PN$^+$ & SH0ES+BAO. On the right-hand side the results for CC+PN$^+$ & SH0ES+BAO+RSD are displayed.

distinct colour. For each $f(T)$ model, the $H_0$ values fall within $1\sigma$ of the corresponding $\Lambda$CDM values, indicating consistency with the $\Lambda$CDM model.

The discrepancy between the locally measured expansion rate of the Universe and values inferred from CMB observations prompted further investigation into the performance of these models with different $H_0$ values. Specifically, the P18 value and the R22 value [4] were considered, as shown in Fig. 8.11, which includes the $\Lambda$CDM values from Sec. 8.2.1. In Fig. 8.11, on the left, the $H_0$ values are within $3.5\sigma$ of the P18 value, except for the PN+& SH0ES+RSD dataset. The high $\sigma$ value for the PN+& SH0ES+RSD dataset is expected, as it is included within the R22 value itself. On the right, the $H_0$ values are within approximately $3.5\sigma$ of the R22 value, suggesting that the $H_0$ values obtained from this analysis fall roughly midway between the P18 and R22 values.

Since, the parameters $\Omega_m$ and $S_{8,0}$ were constrains, the next goal was to quantify the agreement (or disagreement) between the dataset combinations and the $S_{8,0}$ values from the Planck Collaboration ($S^{\rm P18}_{8,0} = 0.834 \pm 0.016$) [16] or the KiDS-1000 value ($S^{\rm KiDS}_{8,0} = 0.766^{+0.020}_{-0.014}$) [142]. This concordance (or discordance) between these values was evaluated in a similar

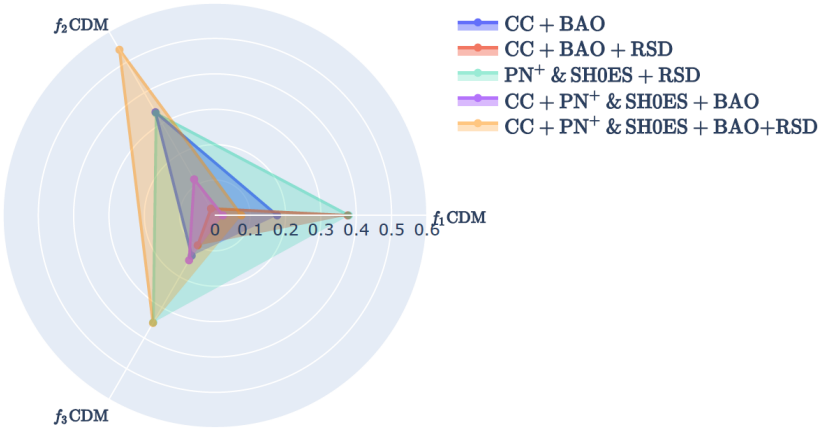


Figure 8.10: Distances measured in standard deviations ($\sigma$ units) between the constrained $H_0$ values obtained from the $f_{1-3}$CDM models and their corresponding values in the $\Lambda$CDM model. Different colours represent different datasets.

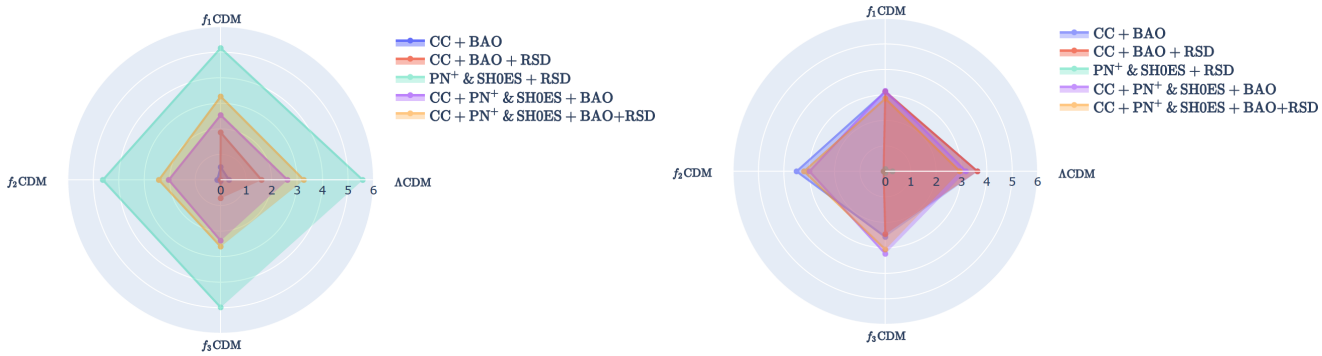


Figure 8.11: Distances measured in standard deviations ($\sigma$ units) between the constrained $H_0$ values obtained from the $f_{1-3}$CDM models together with $\Lambda$CDM and the $H_0^{\rm P18}$ value on the left-hand side and $H_0^{\rm R22}$ on the right-hand side. Different colours represent different datasets.

fashion as the $H_0$ distance values, where

$$T_{S_{8,0}} \equiv \frac{S_{8_0,i} - S_{8_0,j}}{\sqrt{\sigma^2_{S_{8_0,i}} + \sigma^2_{S_{8_0,j}}}}\,, \tag{8.9}$$

for inferred values of $S_8$.

The $S_{8,0}$ values in the $f_1 - f_3$CDM models are compared with those in $\Lambda$CDM using different dataset combinations, as shown in Fig. 8.12. Additionally, a comparison of $S_{8,0}^{\rm P18}$ and $S_{8,0}^{\rm KiDS}$ with values derived from $f_{1-3}$CDM models in $\sigma$ units is presented in Fig. 8.13. To provide more context, the RSD dataset values are included in these figures. On the left-hand side of Fig. 8.13, there is a maximum discrepancy of $2\sigma$ between the values derived from

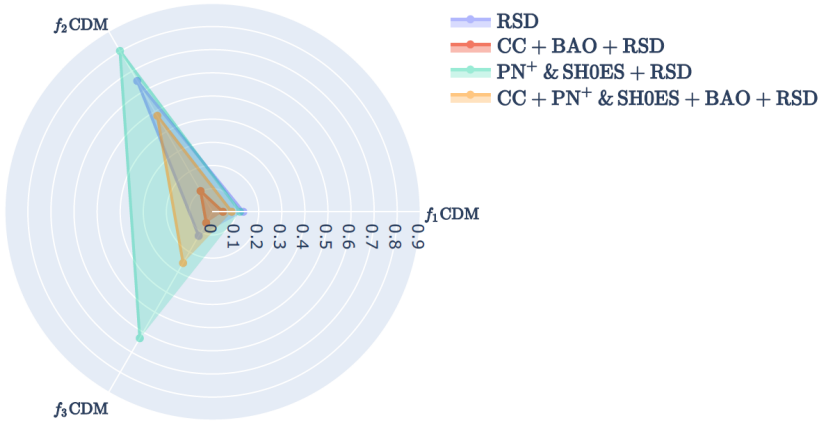


Figure 8.12: Distances measured in standard deviations ($\sigma$ units) between the constrained $S_{8,0}$ values obtained from the $f_{1-3}$CDM models and their corresponding values in the $\Lambda$CDM model. Different colours represent different datasets.

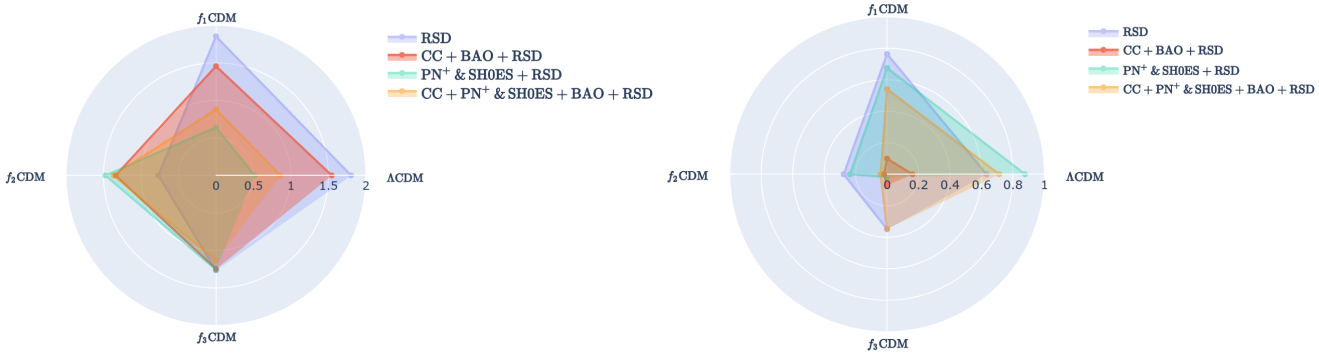


Figure 8.13: Distances measured in standard deviations ($\sigma$ units) between the constrained $S_{8,0}$ values obtained from the $f_{1-3}$CDM models together with $\Lambda$CDM and the $S_{8,0}^{\rm P18}$ value on the left-hand side and $S_{8,0}^{\rm KiDS}$ on the right-hand side. Different colours represent different datasets.

$\Lambda$CDM and the $f_i(T)$CDM models when compared to $S_{8,0}^{\rm P18}$, primarily when considering the RSD dataset alone. However, this discrepancy diminishes as more datasets are included, particularly CC+PN+& SH0ES+BAO+RSD.

On the right of Fig. 8.13, where a comparison with $S_{8,0}^{\rm KiDS}$ is made, the discrepancy is further reduced to $1\sigma$, indicating that the values obtained from this analysis are closer to the KiDS measurements than the Planck values. Notably, the CC+PN+& SH0ES+BAO+RSD dataset performs well, significantly reducing the $\sigma$ values. Thus, the combination of available datasets and the $f_{1-3}(T)$ models appears to help in mitigating tensions between CMB

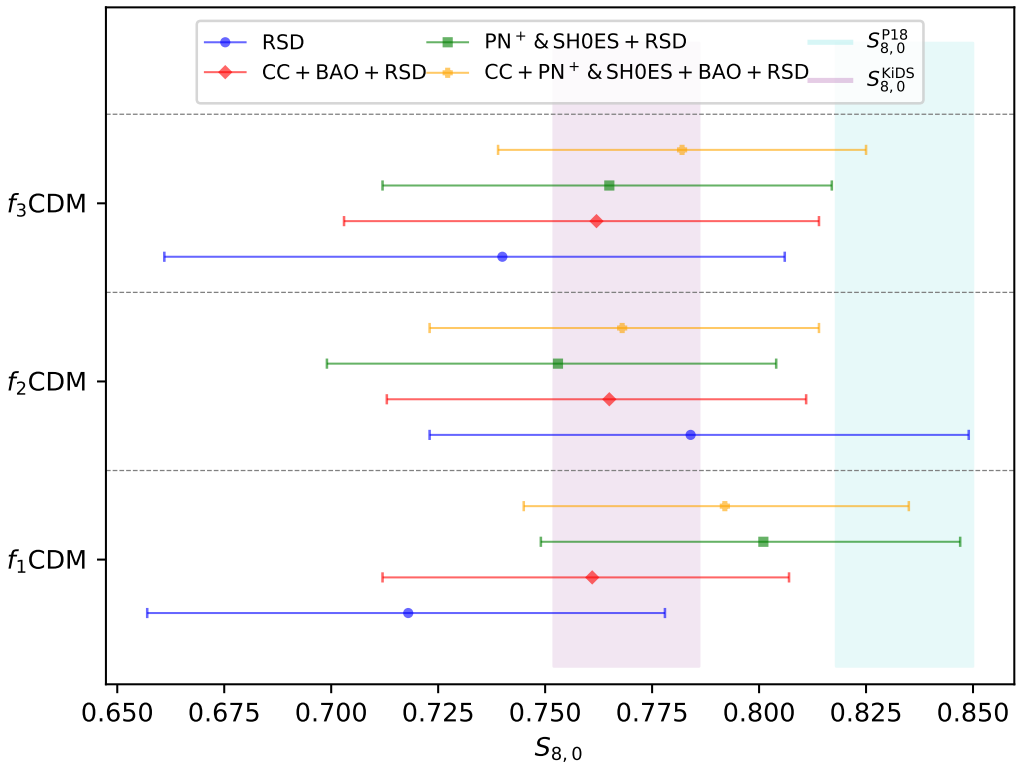


Figure 8.14: A whisker plot illustrating the constrained values of $S_{8,0}$ as derived from the $f_{1-3}$CDM models. The cyan and purple vertical bands depict the respective $1\sigma$ ranges of $S_{8,0}^{P18}$ and $S_{8,0}^{KiDS}$, whilst the coloured error bars illustrate the inferred model dependent $1\sigma$ constraints from each respective dataset.

and locally determined values, particularly for $S_{8,0}$. It is also noteworthy that these findings align with results reported in the literature, such as those presented by [295].

To provide additional context and a clearer visualisation of the $S_{8,0}$ values, Fig. 8.14 offers a detailed summary of the results, demonstrating the influence of different datasets on the models. This figure uses a whisker plot to depict the variability and distribution of $S_{8,0}$ values, showcasing how each dataset contributes to the overall performance and comparison of the models. The whisker plot effectively highlights the range and deviations in $S_{8,0}$ values, allowing for a comprehensive understanding of how the datasets impact the model outcomes and their alignment with the $\Lambda$CDM model.

## 8.4 | Conclusion

Despite the substantial success of the ΛCDM model, persistent hints in the form of cosmological tensions suggest that this model might be encountering limitations. However, before definitively claiming new hints of physics and cliaming that TG is the pathway to go, it is crucial to determine if these hints persist when examined from different perspectives.

To this end, in addition to assessing the $H_0$ tension as discussed in previous chapters, this study investigates the $S_{8,0}$ discrepancy between values obtained from CMB data and those derived from weak lensing probes of the amplitude of matter fluctuations. This discrepancy, or tension, is further examined through the lens of RSD data, specifically measurements of the growth rate, particularly $f\sigma_8$. Additionally, the analysis incorporates baseline local data using combinations of CC, PN+& SH0ES, and BAO datasets. These datasets are not only highly populated and precise but also span a wide range of redshifts, which is crucial for constraining $\Omega_{m,0}$ to obtain $S_{8,0}$. Notably, the PN+& SH0ES sample represents the largest SNe Ia collection in the literature and serves as a principal late-time indicator of the cosmic tension problem concerning the Hubble constant. The RSD data, which are sensitive to the growth of structure formation, have been employed to constrain the matter perturbative sector of the models under consideration, thereby obtaining $S_{8,0}$.

A full MCMC analysis was performed for each model and dataset combination to obtain constraints on all cosmological parameters. Additionally, the performance of each model was compared to the standard ΛCDM model using the $\chi^2_{\rm min}$, AIC, and BIC statistical indicators. In light of the increasing tension reported by various studies regarding the value of the Hubble constant, this study not only investigates its constrained value but also examines how the parameters such as the Hubble constant, the matter density parameter and the model parameter impact parameters related to the growth of structure formation, namely $\sigma_{8,0}$ and $S_{8,0}$.

For reference, the ΛCDM constraint values for each of the considered dataset combinations are provided first. These values are essential for estimating the statistical indicators in the model sections. The analysis generally indicates consistency with ΛCDM, although some differences do emerge, which may become more pronounced as measurement precision improves. The PN+& SH0ES sample continued to prove to be the strongest dataset in the analysis as has been indicated in the previous chapter, consistently reducing statistical errors for any baseline dataset. Conversely, the statistical metrics demonstrate that the expansion data combination of CC+PN+& SH0ES+BAO supports ΛCDM, while the inclusion of RSD data suggests a marginal preference for the $f(T)$ model under consideration. Additionally, these models offer best fits for cosmic parameters more aligned with a higher Hubble constant. The $S_{8,0}$ parameter values obtained are largely consistent with the most

recent reports in the literature.

In more detail, the statistical analysis involving AIC and BIC indicators revealed that certain $f(T)$ models can closely mimic the performance of ΛCDM. However, it was observed that the inclusion of RSD data tends to marginally favour the $f(T)$ models, indicating a warrant for further investigation. The use of the PN+& SH0ES datasets, which are pivotal in understanding late-time cosmic acceleration, significantly sharpens the constraints on the Hubble constant and other parameters, underscoring the importance of comprehensive dataset combinations.

The robustness of the models was then tested by comparing the constrained values of the Hubble constant against the established P18 and R22 values. This comparison illustrated that the models' predictions for $H_0$ fall between these two reference values, suggesting that while the models align with observed trends, they also highlight the ongoing tension between different measurement approaches. The impact on the $S_{8,0}$ parameter, reflecting the amplitude of matter fluctuations, was similarly examined, with results indicating general consistency with both the Planck Collaboration's findings and the KiDS-1000 results, albeit with slight variations that could hint at new physics or unaccounted systematic effects.

The findings from this analysis provide precise insights into the behaviour of TG models and their viability in explaining observed cosmic phenomena. The results suggest that these models hold promise as frameworks for modified cosmological scenarios, offering potential pathways to reconcile current tensions in cosmological measurements.

In summary, this chapter explored the impact of RSD data, combined with other observational datasets, on cosmological parameters and, in particular, the Hubble and $S_{8,0}$ tensions. This investigation underscored the significance of further constraining cosmological models, especially in the early and perturbative stages of the Universe. Moving forward, the next chapter will shift focus to a different approach for addressing these cosmological tensions and constraining parameters. Attention will be directed towards Horndeski in the Cosmic Linear Anistropy Solving System (HiCLASS), a Boltzmann code designed to evaluate cosmological models across both early and late cosmology. Specifically, the focus will be on tensor perturbations, expanding the investigation to primordial gravitational waves and their impact on CMB anisotropies and B-mode polarisation. Through the use of HiCLASS, this chapter aims to gain a better understanding of whether cosmological $f(T)$ models can provide a viable alternative to current models in explaining the fundamental dynamics of the Universe.

# 9

# Confronting Primordial Gravitational Waves with $f(T)$ gravity

Building on the analysis of previous chapters, this chapter delves deeper into $f(T)$ gravity by extending the analysis beyond late-time cosmology, reaching into the early Universe. While prior focus has been on its implications at later cosmic stages, particularly through the lens of parameter constraints at late redshifts, this chapter shifts toward earlier epochs. In addition, the previous inclusion of RSD significantly enhanced the understanding of the theory's effects on large-scale structure. The findings indicated that $f(T)$ gravity could serve as a promising framework for explaining observational data and exploring the evolution of the Universe at later stages

Therefore, this broader exploration is essential, in which $f(T)$ gravity's analysis is extended to earlier cosmic epochs. In this context, the CMB holds within it delicate and profound signals that date back to the Universe's beginning [296]. These signals offer a unique opportunity to investigate the early conditions and dynamics that shaped the cosmos. Primordial perturbations, which encompass both scalar and tensor modes, provide a fundamental framework for understanding these early conditions, with primordial GWs (arising from tensor perturbations) emerging from the inflationary period shortly after the Big Bang. These waves are predicted by inflationary theory to have a specific spectrum characterised by their wavelength and amplitude [16]. Detecting primordial GWs, particularly through their B-mode polarisation imprinted in the CMB, offers an unparalleled opportunity to explore the inflationary era and test underlying gravitational theories [297]. Ongoing experiments like BICEP/Keck are dedicated to detecting these signals, which could provide significant insights into the inflationary process and the physics of the early Universe [49].

In addition to the focus on primordial GWs, this chapter will provide an updated analysis of late-time cosmological datasets, with particular emphasis on the BAO measurements

from Dark Energy Spectroscopic Instrument (DESI) and the most recent CC data. The inclusion of these revised datasets is essential for refining our understanding of $f(T)$ gravity's behaviour across both early and late epochs. By examining the revised CC and BAO data alongside the study of primordial GWs, this chapter aims to present an investigation that bridges early- and late-time cosmology within the $f(T)$ framework.

Through this approach, the Power Law model in $f(T)$, This approach allows for a thorough evaluation of the Power Law model in $f(T)$ gravity, which, based on prior analyses, strikes a balance between simplicity and yet, a strong model, making it a compelling candidate for further investigation. This study will assess the model's influence on both late-time cosmological phenomena and the primordial gravitational wave spectrum. By expanding upon previous analyses, this broader investigation aims to provide deeper insights into the applicability of $f(T)$ gravity across various cosmic epochs, from the Universe's earliest stages to its ongoing expansion.

## 9.1 | Primordial Perturbations and Tensor Modes in $f(T)$ Gravity

Primordial perturbations are the seeds from which cosmic structure grows, and their effects are captured and analysed through the use of power spectra. These spectra provide a quantitative description of how the amplitude of perturbations, whether scalar or tensor, varies with scale, offering insight into the early Universe's dynamics. Typically, the power spectra are expressed as a power law, which reflects the distribution of power across different wavelengths or spatial scales.

For scalar perturbations, which drive the formation of large-scale structures like galaxies and clusters, the power spectrum $P_s(k)$ is given by [15]

$$P_s(k) = A_s \left(\frac{k}{k_s}\right)^{n_s - 1}, \tag{9.1}$$

where $A_s$ is the amplitude of the scalar perturbations at the pivot scale $k_s$, and $n_s$ is the scalar spectral index that describes how the amplitude changes with wavenumber $k$, which corresponds to different scales in the Universe. A spectral index $n_s = 1$ would imply a scale-invariant spectrum, meaning that the strength of the perturbations is uniform across all scales. However, observational data, particularly from the CMB experiments such as the Planck satellite, show that the scalar spectral index is slightly less than 1, with $n_s = 0.9665 \pm 0.0038$ [16]. This deviation from scale invariance implies that fluctuations are slightly stronger on larger scales than on smaller ones.

On the other hand, the power spectrum for tensor perturbations (which describe the power of primordial GWs), $P_t(k)$, is described similarly by [298]

$$P_t(k) = A_t \left(\frac{k}{k_t}\right)^{n_t}, \tag{9.2}$$

where $A_t$ is the amplitude of the tensor perturbations at the pivot scale $k_t$, and $n_t$ is the tensor spectral index. In the context of inflationary cosmology, the tensor spectral index $n_t$ is predicted to be slightly negative, suggesting that the amplitude of primordial GWs decreases at smaller scales (i.e. larger wavenumbers). This power law form encodes how the energy carried by GWs—produced during inflation—changes with the wavelength of the perturbation.

The power spectrum of both scalar and tensor perturbations is crucial for understanding the initial conditions of the Universe and the physics of inflation. In a power law spectrum, the wavenumber $k$ corresponds to the inverse of the wavelength, meaning that larger $k$ values represent smaller scales. The power spectra, therefore, tell us how much power (or amplitude) the perturbations have at different physical scales [299].

- For scalar perturbations, this is directly linked to the formation of large-scale structures, such as galaxies, by gravitational collapse.

- For tensor perturbations, the power spectrum provides information about the strength of primordial GWs, which can be probed indirectly through the B-mode polarisation of the CMB.

One of the key observational parameters that connects scalar and tensor perturbations is the tensor-to-scalar ratio, $r$. This ratio compares the amplitude of GW (tensor perturbations) to the amplitude of scalar perturbations [298, 300]

$$r = \frac{P_t(k)}{P_s(k)}\,. \tag{9.3}$$

This parameter is particularly important in inflationary cosmology because it provides insights into the energy scale at which inflation occurred.

Since this chapter focuses on GWs (tensor perturbations), it is necessary to consider how they evolve in the context of $f(T)$ gravity. The evolution of tensor perturbations in modified gravity theories, such as $f(T)$, is governed by an equation that generalises the standard propagation equation for GWs. In $f(T)$ gravity, the equation for tensor perturbations can be written as in Eq. 2.67, where both $\alpha_m$ and $\alpha_T$ are involved.

In the Power Law model of $f(T)$ gravity, GWs are predicted to propagate at the speed of light, implying $\alpha_T = 0$. The parameter $\alpha_m$, on the other hand, takes the form

$$\alpha_m = \frac{1}{H}\frac{\dot{f}_T}{f_T} = \frac{-12H' f_{TT}}{a f_T}, \tag{9.4}$$

where, as a reminder, $f_T$ and $f_{TT}$ represent the first and second derivatives of the $f(T)$ function with respect to the torsion scalar $T$, and the prime denotes differentiation with respect to redshift $z$. Specifically, for the Power Law model, these derivatives are given by

$$f_T = -1 - \alpha_1 p_1 (-T)^{p_1 - 1} \tag{9.5}$$

$$f_{TT} = \alpha_1 p_1 (p_1 - 1)(-T)^{p_1 - 2}, \tag{9.6}$$

where $\alpha_1$ and $p_1$ are parameters of the model that dictate how the torsion scalar contributes to the gravitational action.

By incorporating these modifications into the tensor perturbation equation, the evolution of GWs can be analysed in $f(T)$ gravity compared to standard GR. In particular, the Power Law model introduces a non-trivial dependence of the perturbations on redshift, allowing for a more complex evolution of GWs over cosmic time. This provides a potential avenue for distinguishing $f(T)$ gravity from GR through the observation of primordial GWs and their effects on the CMB polarisation.

## 9.2 | Revised Datasets

Having established the necessary theoretical framework, attention is now directed toward the revised datasets. In this case, the latest CC and Dark Energy Spectroscopic Instrument (DESI) data (which is an updated dataset for the BAO) have been incorporated to improve constraints on cosmological parameters. Additionally, to constrain the tensor-to-scalar ratio $r$ and the spectral index $n_t$, the BB spectrum from BICEP/Keck has been included. This, in turn, necessitates an updated likelihood analysis for these datasets, ensuring that the most recent observational data are accurately reflected in the parameter estimations.

### 9.2.1 | Revised CC Likelihood

The first dataset utilised is the CC dataset. It is important to note that the likelihood function for the CC dataset implemented in the code required updating to reflect the most recent data. Specifically, the covariance matrix for the CCs, as introduced by Moresco et al. [208], represents a significant advancement. Their work incorporated a full covariance matrix, $C_{\mathrm{H(z)}}$ to account for systematic uncertainties affecting the CC method, enhancing the precision of

the likelihood computation. This update replaced the previously used $\chi^2_{\mathrm{H(z)}}$ in Eq. 3.43 such that,

$$\chi^2_{\mathrm{H(z)}} = \Delta R(z_i, \Theta)^T C^{-1}_{H(z)} \Delta R(z_i, \Theta)\,, \tag{9.7}$$

where $R(z_i, \Theta) = (H(z)_{\mathrm{theo}(z_i,\Theta)} - H(z)_{\mathrm{obs}}(z_i))$ and $C^{-1}_{H(z)}$ is the inverse covariance matrix. [10]

### 9.2.2 | Incorporation of Pantheon+ and Revised BAO Likelihoods

The PN+ likelihood, as described in Sec. 7.1, is the next likelihood utilised in this chapter. Furthermore, the commencement of Stage IV cosmology has been marked by the release of the latest BAO measurements from the DESI. The Stage IV surveys represents a significant advancement in the field of observational cosmology, characterised by a suite of next-generation surveys and experiments designed to explore the Universe with unprecedented precision and depth. This includes DESI [301, 302, 303], Euclid [304], and the anticipated launches of several CMB missions [122, 305, 306], which are expected to revolutionise our understanding of the Universe.

The most recent DESI BAO dataset has been incorporated into this study. This dataset provides updated measurements of BAO in galaxies, quasars, and the Lyman-$\alpha$ forest from the initial year of DESI observations. Precise measurements of the transverse comoving distance and the Hubble rate, or their combination, relative to the sound horizon, have been obtained across seven redshift bins from over 6 million extragalactic objects within the redshift range $0.1 < z < 4.2$. These measurements are derived from various Large Scale Structure (LSS) tracers, such as galaxies [201].

The DESI BAO data include measurements from different LSS tracers: the Bright Galaxy Sample (BGS) at an effective redshift $z_{\mathrm{eff}} = 0.295$, three Luminous Red Galaxy (LRG) samples at $z_{\mathrm{eff}} = 0.510, 0.706, 0.930$, two Emission Line Galaxy (ELG) samples at $z_{\mathrm{eff}} = 0.930, 1.317$, the Quasar (QSO) sample at $z_{\mathrm{eff}} = 1.491$, and the Lyman-$\alpha$ (Ly$\alpha$) forest sample at $z_{\mathrm{eff}} = 2.330$. Some of the LRG and ELG samples have been combined, as detailed in Table 1 of Ref. [303], which provides the statistics for the DESI DR1 BAO measurements. The revised dataset includes values for $D_M/r_d$, $D_H/r_d$, and $D_V/r_d$, with detailed equations found in Sec. 3.3. For correlated measurements, the coefficient $r$ is provided, from which the covariance matrix can be calculated and the minimum $\chi^2$ determined using Eq. 3.51. [11]

[10] https://gitlab.com/mmoresco/CCcovariance
[11] https://github.com/cosmodesi/desilike/tree/hmc/desilike/likelihoods

### 9.2.3 | BICEP/Keck 2014 Dataset

The BICEP/Keck 2014 dataset, commonly known as BK14, represents a pivotal set of observations from the BICEP and Keck Array collaborations, designed to probe the B-mode polarisation of the CMB. The data, derived from the 2014 observing season, are detailed in the publication by the BICEP2 collaboration [49]. This dataset plays a crucial role in constraining key cosmological parameters related to primordial GWs.

BK14 provides high-precision measurements of the B-mode polarisation power spectrum. As has been said, B-mode polarisation, characterised by a specific pattern in the CMB, is a signature of primordial GWs generated during the inflationary epoch. The dataset captures detailed observational data that are instrumental in evaluating the power spectrum of these B-modes, which is crucial for understanding the inflationary dynamics of the Universe.

The BK14 dataset is specifically valuable for its ability to constrain the tensor-to-scalar ratio $r$ and the tensor spectral index $n_t$. As a reminder, the tensor-to-scalar ratio $r$ is a key parameter in cosmological models as it reflects the ratio of primordial GWs to scalar perturbations in the early Universe. On the other hand, the tensor spectral index $n_t$ provides additional details about the nature of these GWs across different scales.

## 9.3 | Boltzmann Code Architecture and MCMC integration

To investigate primordial GWs and explore $f(T)$ gravity further with the revised datasets, a Boltzmann code is employed, which encompasses the equations of motion for various components such as photons, neutrinos, CDM, baryons, and more. This code is primarily written in the *C* programming language, with the most commonly used code in the precision cosmology community being the publicly available Cosmic Linear Anistropy Solving System (CLASS) [12] code [307, 308, 309, 310]. An advanced extension of CLASS, known as Horndeski in the Cosmic Linear Anistropy Solving System (HiCLASS)[13] [311, 312], has been developed specifically to handle models involving Horndeski gravity.

Horndeski models are a class of theories that extend GR by introducing a scalar field with specific interactions to modify gravitational dynamics while avoiding instabilities. In this case, the focus is on $f(T)$ gravity and this is based on teleprallelism, which is a specific case within the broader Horndeski framework, known as teleparallel Horndeski Models

[12] https://github.com/lesgourg/class_public
[13] https://github.com/miguelzuma/hi_class_public

[81]. A useful visual representation of how $f(T)$ gravity fits into the broader context of teleparallel Horndeski models can be found in Ref. [66], Fig. 11.

CLASS is widely utilised for computing both the background evolution and the linear perturbations of cosmological models. The integration of Horndeski models into CLASS, achieved through HiCLASS, enables the examination of a broad range of scalar-tensor theories that extend beyond GR. This integration allows for the exploration of various modifications to gravity while maintaining theoretical consistency and compatibility with observational data. HiCLASS facilitates the investigation of different models by leveraging the dynamics described in terms of $\alpha$ functions, as illustrated in Eq. 2.70.

HiCLASS was designed with a common routine for all Horndeski models, offering the flexibility to choose specific models. In this context, the focus will be on the power-law model in $f(T)$, in particular on the GW propagation, which were not previously implemented in HiCLASS for $f(T)$ and thus, certain modifications had to be made to the code in order to implement this model. However, the use of $\alpha$ functions as specified in Eq. 2.67 allows for a more straightforward and smoother integration of this model into the code. Ultimately, this process involves describing the cosmological background evolution and employing the $\alpha$ functions for a broader analysis.

The general workflow of HiCLASS begins with the background module, which computes the background evolution of the Universe. This module iteratively solves for the evolution after specifying which background parameters are to be varied. The code then assesses stability conditions and checks for consistency before moving on to the perturbations module. HiCLASS is particularly advantageous because it retains the full dynamics across cosmic history without resorting to further simplifications when solving the linear perturbation equations.

Following this overview of the HiCLASS architecture and its capabilities in accommodating various cosmological models, it is important to discuss the principal modifications made to the codebase to support the analysis of $f(T)$ gravity models.

1. *Theoretical Input* `[source]`: This segment of the code encompasses all theoretical inputs essential for defining and implementing the cosmological model. Consequently, both the background and perturbations modules required substantial modifications. Specifically, the *background.c* file was updated to integrate the Friedmann equations for the $f(T)$ Power Law Model, by using Eqs. 2.56,2.57. *perturbations.c* was modified to include the gravitational wave equation, Eq. 2.67, where the forms of the $\alpha$ functions are explicitly defined. As has been mentioned in Sec.2.4.2, $\alpha_T$ for $f(T)$ gravity is 0, whilst for $\alpha_m$ is defined as in Eq. 2.69, which turns out to be dependant on background equations and the $p_1$ parameter as will be shown in subsequent sections. Addition-

ally, changes were made to the *input.c* file to explicitly define the power parameter, specifying the nature and type of the parameter within the model.

2. *Parameter Information* `[include]`: This part of the architecture manages the definitions of cosmological parameters. To incorporate the $f(T)$ Power Law Model, new parameters related to this model were introduced into the system (which include the $b$ parameter. These additions were primarily made in the *background.h* file, ensuring that the newly defined parameters were properly integrated into the model's framework.

Following the in-depth discussion of HiCLASS and its integration of various cosmological models, it is crucial to emphasise the role of MontePython, a sophisticated Python wrapper designed for use with both CLASS and HiCLASS. MontePython [14] significantly augments the functionality of HiCLASS by offering a high-level interface for executing MCMC analyses and performing advanced statistical computations. This wrapper streamlines the parameter estimation process, enabling the exploration of parameter spaces and fitting cosmological models to observational data with greater ease. It complements the computational power of CLASS and HiCLASS, extending their capabilities and providing a valuable tool for modern cosmological research. MontePython is particularly advantageous for extracting precise cosmological parameters from complex models, as it includes the likelihoods for the latest experimental data.

The workflow and the integration process between HiCLASS and MontePython is depicted in Fig. 9.1. Initially, specific modifications are made to the modules in HiCLASS, as highlighted in red, which are crucial for adapting the code to handle the new cosmological model. These modifications enable HiCLASS to compute the necessary background and perturbation data. The resulting outputs are then processed by MontePython, which performs MCMC analyses to generate the parameter chains and log likelihoods. The diagram also shows the data surveys and corresponding likelihoods utilised by MontePython. This integrated approach ensures a streamlined process from theoretical model adjustments to statistical analysis and result interpretation.

Following this integration, significant updates were made to ensure accurate representation of the latest observational data. Specifically, advancements documented by Moresco et al. [313] necessitated the implementation of an updated covariance matrix, which was not initially available in MontePython. This led to the full implementation and integration of the updated likelihood functions with HiCLASS, ensuring precise and current analyses.

Additionally, the likelihood function for DESI was not originally included in MontePython. Thus, its integration into HiCLASS was crucial for accurately reflecting and analysing the

[14] https://github.com/mtristram/montepython_public/tree/3.6/montepython

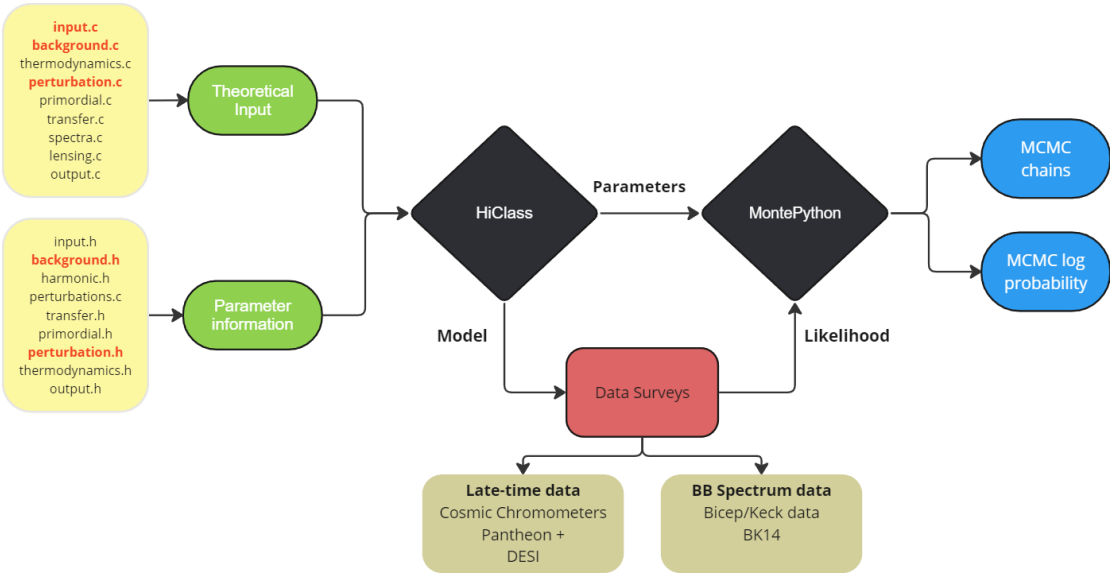


Figure 9.1: This diagram depicts the integration of HiCLASS with MontePython. Modifications to the red-highlighted HiCLASS modules lead to computations that are fed into MontePython. MontePython then performs MCMC analyses to generate chains and log probabilities. The bottom of the diagram shows the data surveys and likelihoods used in MontePython.

latest data. In MontePython, the BK14 dataset is integrated through its B-mode polarisation likelihood function, known as the BB likelihood. This integration enhances MontePython's capability to incorporate high-precision constraints from BK14, improving the parameter estimation process and refining the estimates of the tensor-to-scalar ratio $r$ and the spectral index $n_t$. The inclusion of these datasets, therefore, significantly advances our ability to test and validate theoretical models such as the $f(T)$ power-law model.

Regarding the convergence of chains, the Gelman-Rubin test, commonly referred to as the $R-1$ statistic, is employed to assess the convergence of MCMC simulations [314]. This method compares the variance within each chain to the variance between different chains to determine whether the chains have converged to a stationary distribution. For reliable parameter estimation, convergence is typically indicated when $R-1$ is less than a threshold, commonly 0.01, while values significantly above this value suggest that further iterations are necessary. This test is vital for ensuring that the MCMC chains have sufficiently explored the parameter space, leading to robust and trustworthy estimates.

The final step in this process involves visualising the parameters through corner plots, which offer insights into the posterior distributions and confidence levels of the parame-

ters. This visualisation was accomplished using the `GetDist` code [15] [315], a Python package specifically designed for analysing and visualising the results from MCMC analyses. `GetDist` provides a suite of tools for interpreting MCMC chains, such that results can be presented in a clear and accessible manner. Its capabilities for generating detailed plots and statistical summaries are essential for understanding the parameter estimates and their implications within the context of cosmological models.

## 9.4 | Integrating Late-Time Acceleration Data and Gravitational Wave Observations: Results from CC, PN+, DESI, and Gravitational Waves

In this section, an integrated analysis of late-time acceleration data and GW constraints is conducted. Revised datasets from CC, PN+& SH0ES and DESI are utilised, alongside data from GW observations (BK14). This combined approach facilitates a thorough evaluation of cosmological models, assessing their compatibility with current observational data and their alignment with theoretical predictions. The results provide insights into the effectiveness of these models in describing the Universe's expansion history and primordial GWs.

The goal of this analysis is not only to assess $f(T)$ gravity with the newly revised datasets but also, as previously mentioned, to examine two additional parameters that describe B-mode polarisation. These include the tensor-to-scalar ratio, $r$, which quantifies the amplitude of primordial tensor perturbations at a reference scale, and the spectral tilt, $n_t$, which captures the scale dependence of the primordial tensor spectrum. In essence, the tensor power spectrum is parameterised similarly to the scalar spectrum as a power law, as discussed in Eq. 9.2.

### 9.4.1 | Constraints in $f(T)$ gravity: Exploring revised late-time data

Given the recent updates to the late-time datasets, it is crucial to examine their individual contributions and assess the constraints they provide. Fig. 9.2 presents the results from various combinations of these datasets: CC+PN+& SH0ES (blue), PN+& SH0ES+DESI (red), and the full combination of CC+PN+& SH0ES+DESI (green). As illustrated, the blue contours corresponding to the CC+PN+& SH0ES combination are noticeably broader, indicating that these datasets alone offer less stringent constraints. This highlights the significant

[15] https://getdist.readthedocs.io/en/latest/intro.html

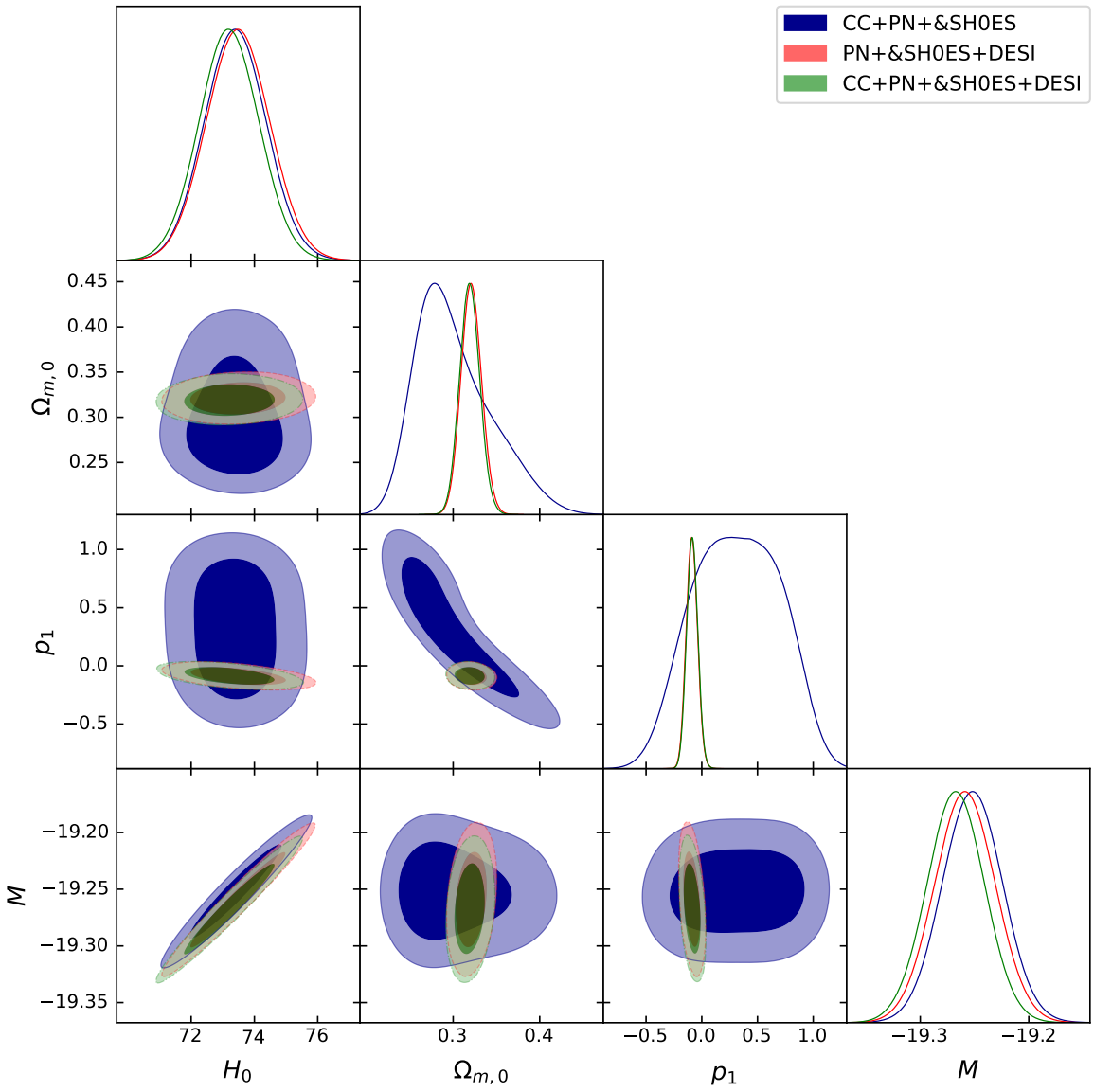


Figure 9.2: The 68% and 95% confidence level intervals, along with the posterior distributions for the parameters $H_0$, $\Omega_{m,0}$, $p_1$, and $M$ for the Power Law Model are presented. These results are based on the analysis of late-time data, including the CC, PN$^+$&SH0ES, and DESI datasets.

influence of the DESI dataset, which, when included, leads to much tighter parameter constraints.

Consistent with previous analyses, a degeneracy between $H_0$, $\Omega_{m,0}$, and $p_1$ is observed in the blue contours, with these parameters being strongly correlated. However, once the DESI BAO data is incorporated, this degeneracy is substantially reduced, leading to more

| Data Sets | $H_0$ [km s$^{-1}$ Mpc$^{-1}$] | $\Omega_{m,0}$ | $p_1$ |
|---|---|---|---|
| CC + PN$^+$ & SH0ES | $73.40 \pm 0.96$ | $0.300^{+0.036}_{-0.052}$ | $0.32 \pm 0.38$ |
| PN$^+$ & SH0ES + DESI | $73.2^{+1.3}_{-0.97}$ | $0.320 \pm 0.012$ | $-0.081^{+0.049}_{-0.058}$ |
| CC + PN$^+$ & SH0ES + DESI | $73.1^{+1.1}_{-0.92}$ | $0.318 \pm 0.012$ | $-0.081^{+0.049}_{-0.0.54}$ |

Table 9.1: Cosmological parameters derived using late-time datasets, highlighting the effect of updating BAO data with DESI. The combinations include CC, PN$^+$&SH0ES, and DESI. Shown are the Hubble constant ($H_0$), matter density ($\Omega_{m,0}$), and dark energy parameter ($p_1$), with uncertainties reflecting the impact of including DESI data.

precise constraints and an enhanced anti-correlation between these parameters. In particular, the inclusion of DESI data markedly tightens the anti-correlation between $\Omega_{m,0}$ and $p_1$, demonstrating the impact of DESI on resolving parameter uncertainties.

The constraints on $H_0$ across the different dataset combinations remain relatively similar, indicating that the inclusion of DESI has a more pronounced effect on the matter density parameter, $\Omega_{m,0}$. This effect is particularly noticeable, as DESI provides stronger constraints on $\Omega_{m,0}$, with a higher value but significantly reduced uncertainties. In addition, the parameter distributions are clearly consistent with the findings from the previous chapter, especially regarding the degeneracy between $H_0$ and $\Omega_{m,0}$. The relationship between $H_0$ and $p_1$ also aligns with earlier results for the Power Law Model, and the slight anticorrelation between $\Omega_{m,0}$ and $p_1$ is similarly evident. These consistencies underscore the reliability of the results.

The exact results are summarised in Table 9.1, which presents the exact parameter values and uncertainties for each dataset combination (Since this section focuses on the impact of the DESI likelihood, the values of $M$ has been omitted from the tables, although the posteriors are still presented in the plots). The table highlights the critical role of DESI in tightening the constraints, especially on the matter density, while the $H_0$ parameter remains largely consistent across different combinations. The notable improvement in constraints with the DESI dataset reaffirms its importance in late-time cosmological analyses, providing a more refined picture of the Universe's expansion and matter distribution.

### 9.4.2 | Constraints in $f(T)$ gravity: Exploring $r$ & $n_t$

Following the exploration of the revised datasets in late-time cosmology, the BICEP/Keck Array dataset will be utilised to constrain two additional parameters at $k_t = 0.01\,\mathrm{Mpc}^{-1}$ [120]: the tensor-to-scalar ratio $r$ and the spectral tilt $n_t$. Two scenarios will be considered: the first in which $n_t$ is fixed at a specified value, and the second in which $n_t$ is treated as a free parameter. This approach facilitates an extensive exploration of the parameters and

their impacts on both individual outcomes and their interrelationships.

### 9.4.3 | Case 1: Scale-invariant tensor spectrum $n_t = 0$

Several studies and models frequently set $n_t = 0$ as a simplification, particularly within the framework of slow-roll inflation [49, 120]. This choice is often justified by the fact that, during slow-roll inflation, the tensor spectral index $n_t$ is predicted to be small or nearly zero. (Slow-roll inflation describes a phase of accelerated expansion in the early Universe, driven by a scalar field known as the inflaton. During this phase, the potential energy of the inflaton dominates its kinetic energy, leading to a gradual, slow evolution of the field.)

Fixing $n_t = 0$ is a practical assumption, especially in contexts where precision constraints on the amplitude of tensor modes are more critical than resolving the scale-dependence of the tensor power spectrum. In the literature, such an approach has been used in studies like those from the BICEP/Keck Array, which set $n_t = 0$ to focus on constraining other cosmological parameters like the tensor-to-scalar ratio $r$ without the added complexity of a free $n_t$ parameter and studies have shows a strong pull toward a scale-invariance tensor spectrum [298, 300]. This simplification helps to reduce the number of free parameters in the analysis, allowing for clearer constraints on the tensor contribution to the CMB polarisation.

In this analysis, $n_t = 0$ is fixed, while other relevant parameters—such as $H_0$, $\Omega_{m,0}$, $p_1$, and $r$ (apart from nuisance parameters)—are left free to vary. Fig. 9.3 and Table 9.2 illustrate the resulting constraints, providing the 68% and 95% confidence intervals for these parameters, along with their exact values and uncertainties (at 68%).

To assess the impact of the updated DESI dataset, various combinations of data are tested: CC + PN$^+$ & SH0ES + BK14 (gray colour in Fig. 9.3), and CC + PN$^+$ & SH0ES + DESI + BK14 (teal colour). Consistent with previous findings, the most significant impact of the DESI dataset is observed on the matter density parameter $\Omega_{m,0}$ and the model parameter $p_1$. The Hubble constant $H_0$, though primarily influenced by the PN$^+$ & SH0ES dataset, is indirectly affected by the constraints on $\Omega_{m,0}$ due to the interdependence of these parameters. As shown in Fig. 9.3, while the contour shapes for the 2D parameter space remain similar across the different data combinations, the inclusion of DESI leads to noticeably tighter constraints, particularly in the $H_0$ and $\Omega_{m,0}$ parameters.

The value of $H_0$ for both data combinations that include DESI aligns closely with previous results, falling in the range of approximately $73\,\mathrm{km\,s^{-1}\,Mpc^{-1}}$. This suggests that while the primary driver of $H_0$ remains the PN$^+$ & SH0ES dataset, the inclusion of DESI provides additional support by significantly reducing uncertainties, further confirming the robustness of the results. The effect of DESI is most pronounced in the matter density parameter

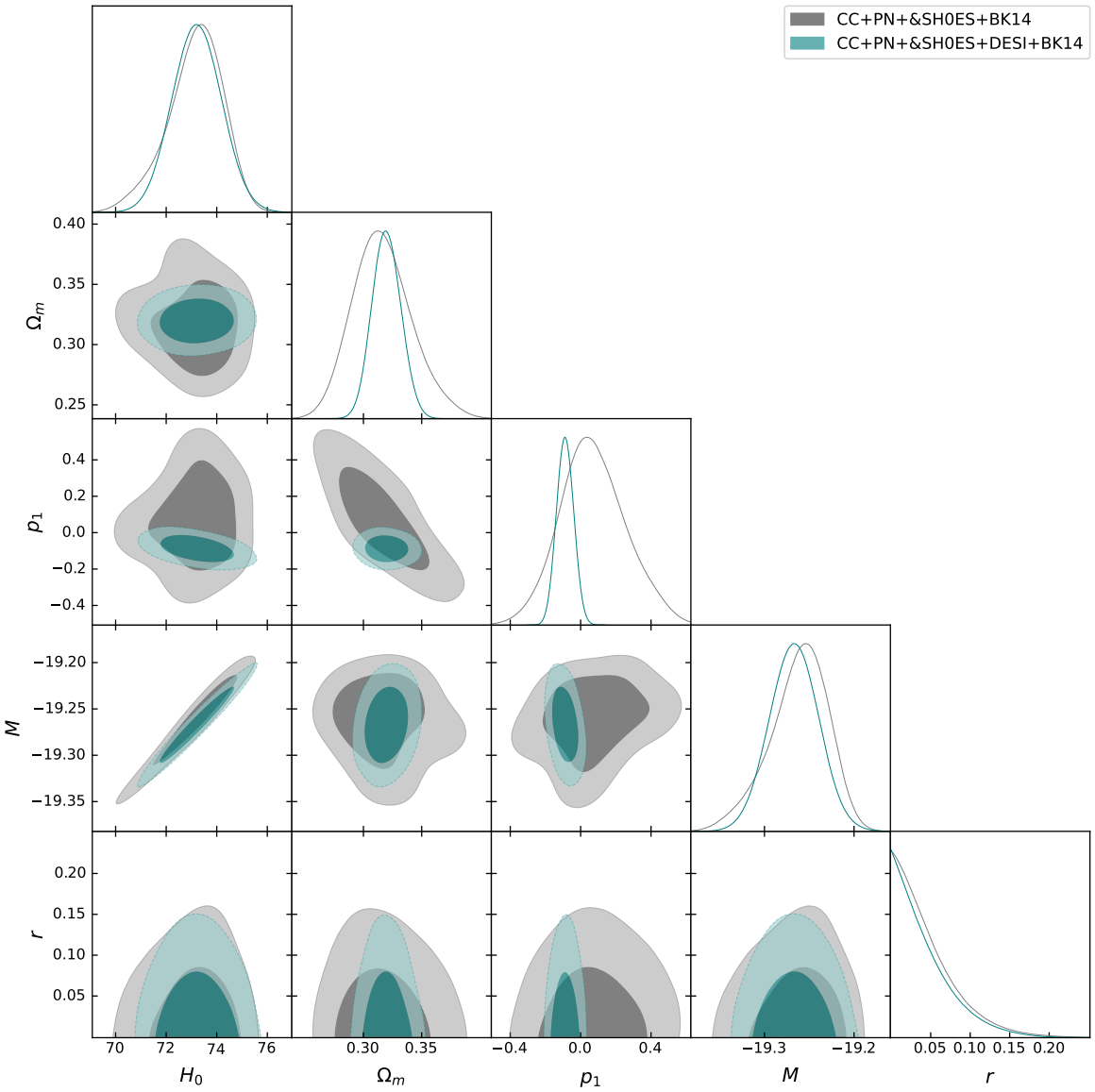


Figure 9.3: The 68% and 95% confidence level intervals, along with the posterior distributions for the parameters $H_0$, $\Omega_{m,0}$, $p_1$, and $M$ in the Power Law Model are displayed. These results are derived from the analysis of late-time data sets, including CC, PN$^+$&SH0ES, DESI, and the BB spectrum from BK14, where $n_t$ was set to 0.

| Data Sets | $H_0$ [km s$^{-1}$ Mpc$^{-1}$] | $\Omega_{m,0}$ | $p_1$ | $r$ |
|---|---|---|---|---|
| CC + PN$^+$ & SH0ES + BK14 | $73.16^{+1.23}_{-0.96}$ | $0.315^{+0.028}_{-0.023}$ | $0.07^{+0.20}_{-0.17}$ | $0.045^{+0.011}_{-0.044}$ |
| CC + PN$^+$ & SH0ES + DESI + BK14 | $73.21 \pm 0.95$ | $0.320 \pm 0.012$ | $-0.08^{+0.047}_{-0.0.48}$ | $0.043^{+0.012}_{-0.042}$ |

Table 9.2: Cosmological parameters derived from dataset combinations, with the tensor spectral index fixed at $n_t = 0$. The datasets include CC, PN$^+$&SH0ES, DESI, and BK14. The parameters shown are the Hubble constant ($H_0$), matter density ($\Omega_{m,0}$), model parameter ($p_1$), and tensor-to-scalar ratio ($r$) at 68% confidence level, with associated uncertainties.

$\Omega_{m,0}$, where the inclusion of this dataset not only shifts the central value but also dramatically tightens the constraints, as demonstrated in both the Fig 9.3 and Table 9.2 provided.

The values of the model parameter $p_1$ are found to be close to the $\Lambda$CDM limit, with the parameter lying within 1 to 2 sigma of the $\Lambda$CDM value in both cases. As observed in previous results, the inclusion of the DESI dataset exerts a significant influence, shifting the parameter from a slightly positive value to a marginally negative one. However, the constraints tighten considerably when combining CC + PN$^+$ & SH0ES + DESI + BK14, as reflected in the parameter contours shown in Fig. 9.3. This figure also highlights the correlations between $p_1$ and other cosmological parameters. A noticeable anti-correlation between $p_1$ and $H_0$, seen in earlier dataset combinations, remains evident here. Additionally, a similar correlation is observed between $p_1$ and $\Omega_{m,0}$, reinforcing the trend seen with the other data combinations. The improved constraints offered by the DESI dataset significantly impact both $H_0$ and $\Omega_{m,0}$, contributing to a more precise understanding of the model's parameter space.

Turning to the value of $r_{0.01}$ at the 68% confidence level (CL), the analysis shows that for the combination of CC + PN$^+$ & SH0ES + BK14, the value is $r_{0.01} = 0.0455^{+0.0091}_{-0.046}$, with an upper limit of $r_{0.01} < 0.12$ at 95% CL. In contrast, when DESI data is added to the combination (CC + PN$^+$ & SH0ES + DESI + BK14), the value is slightly lower at $r_{0.01} = 0.043^{+0.012}_{-0.042}$, with an upper bound of $r_{0.01} < 0.11$ at 95% CL.

When these results are compared to recent findings from Galloni et al. [298], which use new and revised datasets and multiple combinations, including the BICEP/Keck array, Planck 3 and 4, and collaborations like LIGO-Virgo-Kagra, our results offer a slightly higher upper bound on $r_{0.01}$ at the 95% CL. Galloni et al. provide some of the most stringent constraints on the tensor-to-scalar ratio $r$ and the tensor spectral index $n_t$, yet despite the higher upper limit found here, the results remain in line with other data combinations.

It is important to note that Galloni et al.'s work combines multiple datasets to derive these limits, which could explain the tighter constraints. In contrast, the analysis presented here relies on fewer datasets, specifically Bicep/Keck array which likely accounts for the relatively higher upper bound. Nevertheless, these findings are a significant step toward

constraining $r_{0.01}$, and they align with the general trend in the literature towards more precise bounds. The inclusion of future datasets and further refinements to the analysis will likely continue to push the upper limits lower, providing even more stringent tests of inflationary models.

In addition, these results are in agreement with the upper bound on $r_{0.001} < 0.076$ provided by Akrami et al. (Planck 2018) [120] when combining both CMB and GW data. This consistency further highlights the reliability of the constraints derived here and underscores the importance of combining diverse observational data to improve the precision of cosmological parameter estimates.

### 9.4.4 | Case 2: $n_t$ free parameter

In the second scenario, greater flexibility is introduced by allowing the spectral tilt $n_t$ to vary as a free parameter. The same two dataset combinations are analysed, and the 68% and 95% confidence levels are illustrated in Fig. 9.4. The grey contours correspond to the combination of CC+PN+& SH0ES+BK14, while the teal contours represent the addition of the DESI dataset, i.e., CC + PN+& SH0ES+DESI+ BK14. These results exhibit trends similar to those observed in the previous fixed $n_t$ case.

For instance, the value of $H_0$ is found to remain on the higher end of the spectrum, primarily driven by the PN+& SH0ES data, which consistently pushes the value upwards. Conversely, $\Omega_{m,0}$ is more sensitive to the inclusion of different datasets, reflecting the influence of DESI, as seen in earlier analyses. The tighter constraints on the matter density parameter are evident in the results, particularly in Table 9.3, where the combination CC + PN+& SH0ES+BK14 yields $\Omega_{m,0} = 0.317^{+0.035}_{-0.048}$, while CC+PN+& SH0ES+DESI+BK14 provides a significantly more constrained $\Omega_{m,0} = 0.318 \pm 0.011$. This demonstrates the substantial impact of the DESI dataset in tightening the bounds on the matter density parameter.

Moreover, the relationship between $H_0$ and $\Omega_{m,0}$ shifts between the two combinations. Initially, the first dataset combination shows a more degenerate correlation, which transitions to a stronger anti-correlation when DESI is included, as anticipated and in line with previous interpretations. A similar, yet more pronounced effect, is observed with the model parameter $p_1$. In the case of CC+PN+& SH0ES+BK14, $p_1$ is positive, albeit with large uncertainties that encompass the $\Lambda$CDM limit, specifically $p_1 = 0.13^{+0.20}_{-0.17}$. However, upon the inclusion of DESI, the constraint on $p_1$ tightens significantly, shifting to the negative region, with a value of $p_1 = -0.082 \pm 0.049$. In this scenario, BK14 appears to have a limited influence on the constraints for $p_1$, while DESI plays a critical role in refining the parameter space. The 2D confidence levels presented in Fig. 9.4 exhibit consistency with the trends identified in previous chapters, particularly in the slight anti-correlation between $\Omega_{m,0}$ and

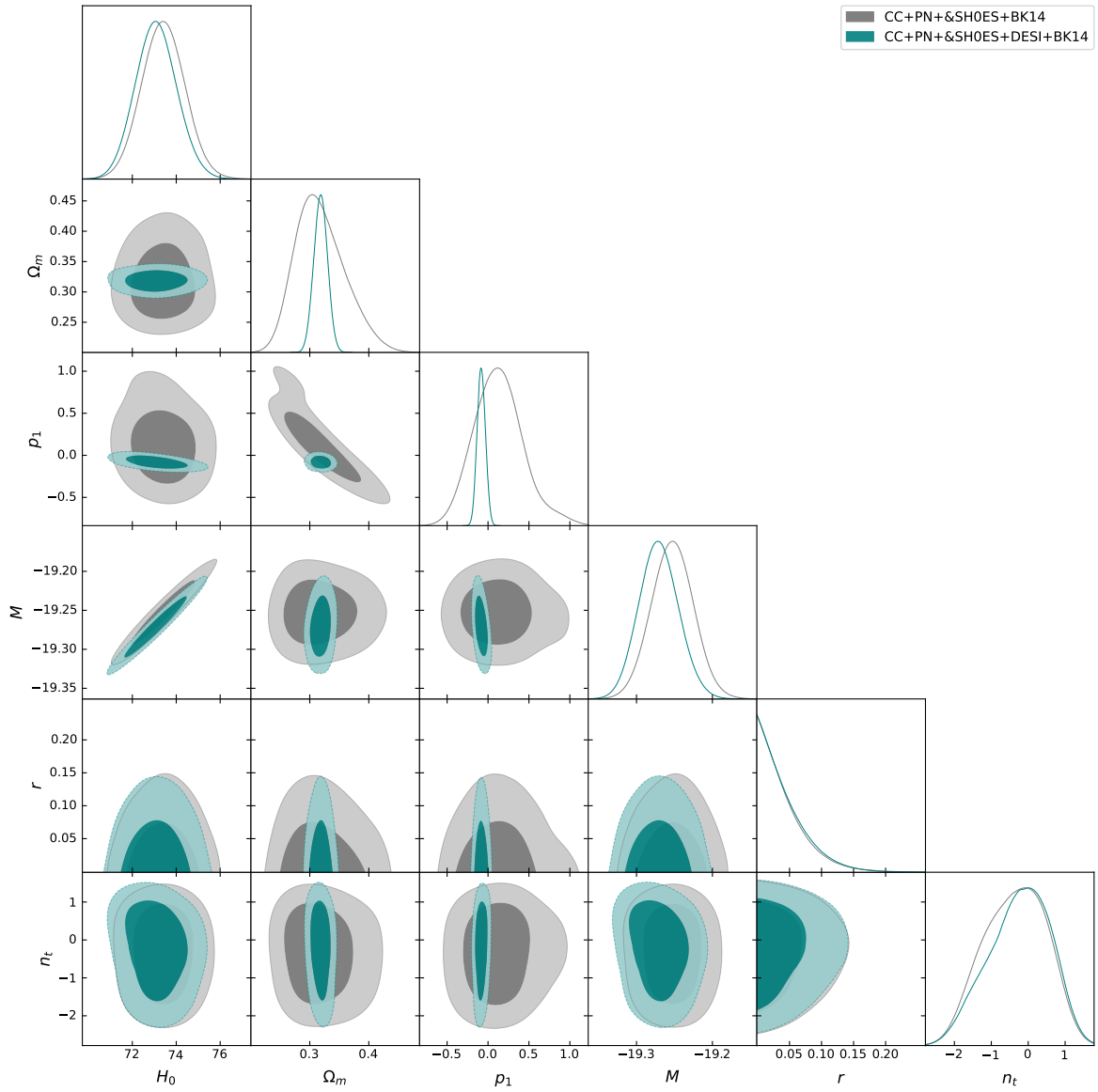


Figure 9.4: The 68% and 95% confidence level intervals, along with the posterior distributions for the parameters $H_0$, $\Omega_{m,0}$, $p_1$, and $M$ in the Power Law Model are displayed. These results are derived from the analysis of late-time data sets, including CC, PN$^+$&SH0ES, DESI, and the BB spectrum from BK14, where $n_t$ was left as a free parameter.

| Data Sets | $H_0$ [km s$^{-1}$ Mpc$^{-1}$] | $\Omega_{m,0}$ | $p_1$ | $r$ | $n_t$ |
|---|---|---|---|---|---|
| CC + PN$^+$ & SH0ES + BK14 | $73.41 \pm 0.95$ | $0.317^{+0.035}_{-0.048}$ | $0.13^{+0.20}_{-0.17}$ | $0.0410^{+0.008}_{-0.040}$ | $-0.35^{+0.94}_{-0.81}$ |
| CC + PN$^+$ & SH0ES + DESI + BK14 | $73.08 \pm 0.92$ | $0.318 \pm 0.011$ | $-0.082 \pm 0.049$ | $0.0415^{+0.01}_{-0.041}$ | $-0.23^{0.99}_{-0.70}$ |

Table 9.3: Cosmological parameters derived from various dataset combinations, including CC, PN$^+$&SH0ES, DESI, and BK14. The table shows the Hubble constant ($H_0$), matter density ($\Omega_{m,0}$), model parameter ($p_1$), tensor-to-scalar ratio ($r$), and tensor spectral index ($n_t$), with associated uncertainties at 1 $\sigma$.

$p_1$, and the relationship between $H_0$ and $p_1$.

On the other hand, the inclusion of the BK14 dataset now enables both $n_t$ and $r$ to be constrained and evaluated alongside other cosmological parameters. The exact values, as shown in Table 9.3, indicate a slight reduction in the $r_{0.01}$ value within the 68% confidence levels for both dataset combinations. For instance, in the case of CC+PN+& SH0ES+BK14, $r_{0.01}$ is constrained to $0.041^{+0.0082}_{-0.04}$ (with $r_{0.01} < 0.113$ at 95% CL). However, the inclusion of DESI does not significantly impact the constraints on $r$, as shown by the result $r_{0.01} = 0.0415^{+0.010}_{-0.041}$ (with $r_{0.01} < 0.112$ at 95% CL) for CC+PN+& SH0ES+DESI+BK14. These results remain consistent with those previously obtained in the literature, particularly with the findings from Planck18 [120] and the corresponding values from different dataset combinations referenced in Ref. [298]. Furthermore, they align with recent research by Galloni et al. [300], which reports $r_{0.01} < 0.030$ and $-1.35 < n_t < 3.40$ (at 95% confidence level using multiple datasets), closely matching the bounds obtained in this study. The constraints on $r$ in both cases are well-aligned with current cosmological limits, further reinforcing the reliability of this Power Law Model in $f(T)$ gravity.

In this case, $n_t$ is treated as a free parameter, in which the BK14 dataset allows for its constraint alongside the tensor-to-scalar ratio $r$. As shown in Fig. 9.4, the inclusion of BK14 consistently demonstrates that it has minimal effect on the shape of the posterior distribution and the contour plots for $n_t$, provided that BK14 is included. The precise values, as presented in Table 9.3, are $n_t = -0.35^{+0.94}_{-0.81}$ (with $-1.7 < n_t < 1.0$ at the 95% confidence level) for the combination CC+PN+& SH0ES+BK14. For the combination CC+PN+& SH0ES+DESI+BK14, $n_t$ is constrained to $-0.23^{+0.99}_{-0.70}$ (with $-1.7 < n_t < 1.1$ at the 95% confidence level). In addition, Eq. 9.2, shows that a negative $n_t$ implies that the power spectrum at larger scales will have lower amplitude. On the other hand when one looks at GWs, the ones on smaller scales are stronger or have higher amplitude tan the ones on larger scales.

While these results exhibit a broader range—particularly with the higher upper bounds—they remain largely consistent with those reported in the literature. Planck18, for instance, constrained $n_t$ within the range $-0.76 < n_t < 0.52$, and Fig. 2 of Ref. [298] presents a range of

$n_t$ values from various dataset combinations that overlap with the findings of this analysis. Despite the slightly larger uncertainty in this study, this is attributable to the fact that the BK14 dataset is not as constraining as Planck18, which results in looser bounds, particularly in the upper limits of $n_t$. Nevertheless, these results still provide valuable insight into the behaviour of $n_t$ when constrained by current BB polarisation data. Indeed, these results also confirm that the scale-invariant scenario remains well within the obtained range, further reinforcing the case presented in the previous section.

## 9.5 | Conclusion

In this chapter, a thorough investigation was undertaken to constrain primordial GWs within the framework of $f(T)$ gravity, utilising both early- and late-time cosmological datasets. One of the objectives was to confront the theoretical predictions of $f(T)$ gravity with observational data, particularly focusing on the B-mode polarisation of the CMB and its associated parameters: the tensor-to-scalar ratio $r$ and the spectral tilt $n_t$. This was achieved by modifying parts of HiCLASS to incorporate the power law in $f(T)$ gravity.

In parallel, revisions to key late-time cosmological datasets were incorporated to refine the parameter space. The CC dataset, reflecting the expansion history of the Universe, was reviewed, and the BAO dataset was enhanced through the inclusion of the DESI likelihood. The inclusion of these revised datasets allowed for more accurate constraints on cosmological parameters at late times, complementing the constraints derived from early-time observations. These refinements were necessary to capture the dynamics of the $f(T)$ model more accurately, as it modifies both the background expansion and the evolution of cosmological perturbations.

To constrain the two additional parameters—$r$ and $n_t$—that characterise the B-mode polarisation, the BICEP/Keck Array (BK14) [49] dataset was employed. This dataset, which is sensitive to the primordial GWs, was crucial in constraining the tensor perturbations of the Universe. The analysis involved two case studies: one where the spectral tilt $n_t$ was fixed to zero, and another where $n_t$ was treated as a free parameter, allowing for a broader exploration of its impact on the model.

The theoretical framework of $f(T)$ gravity was implemented using the Boltzmann code, HiCLASS [311, 312], which was adapted to account for both the background evolution and the linear perturbations under the Horndeski models. The code was modified to accommodate for the power law model in $f(T)$ gravity at both the background and tensor perturbation levels, in which a detailed workflow was provided in Fig. 9.1. The modifications allowed for the exploration of how the $f(T)$ model behaves under different parameter con-

straints, leading to a more comprehensive understanding of its predictions.

MontePython was employed as the MCMC tool to perform parameter constraints. The MCMC algorithm allowed for the exploration of the posterior distributions of the model parameters, providing constraints on $r$, $n_t$, and other cosmological parameters such as $H_0$, $\Omega_{m,0}$ and $p_1$. A Gelman-Rubin convergence criterion of less than 0.01 was used, ensuring that the chains were well converged and that the resulting parameter estimates were reliable. This level of precision was particularly important for the exploration of the late-time datasets and also at the perturbative level.

The results of the analysis demonstrated that the inclusion of these datasets, such as DESI, led to tighter constraints on the cosmological parameters. Specifically, the addition of DESI played a critical role in refining the bounds on $\Omega_{m,0}$, providing clearer insights into the matter content and expansion rate of the Universe. Otherwise, the parameters were well constrained and remained consistent with previous results obtained in the previous chapters.

In this chapter the use of both early- and late-time data in conjunction provided a more extensive picture of the $f(T)$ framework and the Universe's evolution. Indeed, the BK14 dataset was then added to these late-time combinations in order to provide more insight. In the case where $n_t$ was fixed to zero, the BK14 dataset allowed for the constraint of the tensor-to-scalar ratio $r < 0.11$ (at 95% confidence level) for the dataset CC+ PN+& SH0ES + DESI + BK14, providing results that were consistent with those reported in the literature. The constraints obtained in this analysis were found to be in agreement with the results from Planck18, confirming the reliability of the approach. The inclusion of BK14 also demonstrated that the dataset's ability to constrain $r$ was comparable to other studies, despite the broader uncertainty range observed due to the limited sensitivity of BK14 compared to Planck18 [120, 298].

In the second case, where $n_t$ was treated as a free parameter, the analysis allowed for a deeper exploration of the possible deviations from the scale-invariant scenario. The posterior distributions for $n_t$ and $r$ showed that the inclusion of BK14 provided meaningful constraints on both parameters, although the upper bounds were less stringent than those provided by Planck18 [120] and Galloni et al. [298]. The results obtained in this case demonstrated that the scale-invariant scenario was well within the allowed range, further reinforcing the findings from previous case. The impact of including different dataset combinations on the posterior distributions was also minimal, as long as BK14 was included, confirming the dataset's validity in constraining the primordial tensor modes.

The results also highlighted the importance of using both the CC and DESI datasets in combination with the BK14 likelihood. While the DESI dataset did not directly impact the constraints on $r$ and $n_t$, it significantly improved the constraints on $\Omega_{m,0}$, which in turn

influenced the overall cosmological model and its compatibility with the $f(T)$ framework both at late-time and early-times. The tighter constraints on $\Omega_{m,0}$ provided by DESI allowed for a more accurate exploration of how the $f(T)$ model behaves under different assumptions for $n_t$.

Overall, the results of this chapter have provided a detailed exploration of the interplay between early- and late-time cosmological data in constraining primordial GWs within the $f(T)$ framework, specifically the power law model. By utilising the HiCLASS Boltzmann code and MontePython for MCMC sampling, it was possible to derive reliable constraints on the tensor-to-scalar ratio $r$ and the spectral tilt $n_t$, while also refining the constraints on late-time parameters such as $H_0$,$\Omega_{m,0}$ and the model parameter $p_1$. The analysis demonstrates the power of combining the revised datasets with the BK14 likelihood to probe the fundamental properties of the Universe, and it lays the groundwork for future studies involving additional BB spectrum datasets to further tighten the constraints on $n_t$ and $r$.

# 10

# Conclusion

Modifications to gravity theories beyond General Relativity (GR) provide new perspectives on the fundamental nature of gravitational interactions. In particular, Teleparallel Gravity (TG) introduces torsion as the primary geometric quantity, replacing curvature. In this framework, the Einstein-Hilbert Lagrangian of GR is replaced by the torsion scalar $T$. A key formulation within this context is the Teleparallel Equivalent of General Relativity (TEGR), where the field equations are dynamically equivalent to those in GR. The distinction between TEGR and GR lies in a boundary term, $B$, which separates the curvature scalar from the torsion scalar, expressed as $\mathring{R} = -T + B$. Extending this framework, one can generalise the action to include arbitrary functions of the torsion scalar and the boundary term, leading to $f(T)$ and $f(T, B)$ gravity.

Given the ongoing challenges in cosmology—particularly the $H_0$ and $S_{8,0}$ tensions—torsion gravity provides a compelling avenue for exploration. Indeed, this study mainly focuses on $f(T)$ gravity, examining whether this approach can resolve the pressing cosmological discrepancies observed today, while remaining aligned with existing observational data. This research marks one of the most extensive investigations into the $f(T)$ gravity model as a strong alternative to the $\Lambda$CDM framework. Through in-depth analysis and comparison with observational data, it highlights the potential of $f(T)$ gravity to offer new insights into both early and late-time cosmological phenomena.

Central to this investigation is the application of GPs, which allows for the non-parametric reconstruction of the Hubble parameter $H(z)$. GP analysis is a powerful tool that facilitates the reconstruction of underlying cosmological functions without imposing a prior form on them. One key parameter reconstructed through this method is the Hubble constant, $H_0$, which has drawn significant attention due to the observed mismatch between early- and late-Universe measurements within the $\Lambda$CDM scenario.

In a cosmological context, GP techniques can reconstruct arbitrary Lagrangian functions

beyond the standard cosmological model, relying solely on observational datasets without prior assumptions about their functional form. However, the accuracy of these reconstructions hinges on the choice of kernel function. In this study, four kernel functions were considered: squared exponential, Cauchy, Matérn, and rational quadratic, each tested for dependency. The analysis confirmed, at the $1\sigma$ confidence level, that kernel selection can moderately influence results, but are still consistent with each other.

The GP analysis incorporated various datasets, including CC, CC+sn, and CC+SN+BAO, alongside three different $H_0$ priors (R19, HW, and TRGB). The reconstruction of $H(z)$, illustrated in Figs. 4.1 – 4.4, indicated that theCC+SN+BAO dataset combination consistently produced lower $H_0$ values, while the highest $H_0$ estimates arose from datasets that included the R19 prior.

Diagnostic tests were conducted to assess deviations from the $\Lambda$CDM model. The diagnostic redshift function, $\mathcal{O}_m^{(1)}(z)$, indicated consistency between the dataset combinations and $\Lambda$CDM predictions, though slight deviations were observed at higher redshifts. These deviations became more pronounced in the analysis of the derivative of $\mathcal{O}_m^{(1)}(z)$, denoted as $\mathcal{L}_m^{(1)}(z)$. Furthermore, a reconstruction of the deceleration parameter allowed for the estimation of the transition redshift $z_t$, the point at which the Universe transitioned from deceleration to acceleration. Consistent with the $H_0$ results, the Riess prior (R19) yielded the lowest $z_t$ values, while the CC+SN+BAO dataset combination resulted in the highest values.

These reconstructions of the Hubble parameter provided a foundation for model-independent evaluations of $f(T)$ gravity. The assessment of numerical propagation, alongside the initial conditions, facilitated the construction of the arbitrary Lagrangian. Consequently, the functional form of $f(T)$ as a function of the torsion scalar $T$ for each kernel and dataset combination was presented in Figs. 4.5 – 4.8. In these figures, the $\Lambda$CDM scenario was overlaid on the reconstructed regions, demonstrating that $\Lambda$CDM lies well within the reconstructed range. Moreover, $f(T)$ exhibited a slight decrease at higher redshifts, a feature that could inform the development of future $f(T)$ models.

This groundwork enabled a probabilistic evaluation of model parameters against observational data using MCMC analysis, which allows for exploration of parameter space and quantification of uncertainties in a probabilistic framework. Thus, the MCMC technique was employed throughout various analyses, building on one another. Five different models within the $f(T)$ framework were evaluated: Power Law, Square-root Exponential, Exponential, Logarithmic, and Hyperbolic-tangent models, to assess their performance in explaining cosmic acceleration and later on structure growth. These models were rigorously compared to the $\Lambda$CDM model to evaluate their alignment with the latest observational data, continually revising the datasets to remain current.

The results of our analysis in Chapter 5 indicate that $f(T)$ gravity models can indeed

serve as alternatives to the ΛCDM model in describing the evolution of the Universe. Among the models tested, the Power Law and Linder models (including the variant of the Linder Model), as well as a variant of the Linder model, performed particularly well, closely replicating the predictions of the ΛCDM model, especially at low redshifts. These models showed good agreement with the CC and PN observations, suggesting that they can effectively describe the late-time accelerated expansion of the Universe.

Conversely, the Logarithmic and Hyperbolic tangent models exhibited a notable distinction in that they do not possess a ΛCDM limit. The previous models all had a ΛCDM limit for specific values of their parameters, namely $p_1$, $\frac{1}{p_2}$, and $\frac{1}{p_3}$. While these last two models diverged slightly from the ΛCDM limit, the divergence was not pronounced. Their behaviour at different epochs of cosmic history could provide insights into how $f(T)$ might influence the Universe's expansion and structure formation over time.

In addition to the CC, PN, and BAO datasets, priors were incorporated in this chapter, specifically the R19, HW, and TRGB priors, to demonstrate the impact of these priors on $f(T)$ cosmological models and their parameters. A summary of these findings is presented in Fig. 5.7, where the influence of each prior on different parameters is immediately observable, along with the impact of each dataset used.

The statistical indicators carried out using the AIC and the BIC enabled a quantitative comparison between these $f(T)$ models and ΛCDM. Most $f(T)$ models performed comparably well with ΛCDM, as quantified using the Jeffreys' scale, while the last two models without a ΛCDM limit demonstrated slight discrepancies, particularly with the inclusion of additional priors, and therefore the focus shifts mainly to the first three models.

Given the relationship between the torsion scalar and the Ricci scalar, it was logical to extend $f(T)$ gravity to include $f(T, B)$. Chapter 6 explored the performance of $f(T, B)$ gravity models in comparison to the ΛCDM model, focusing on three specific models: the Power Law Model, Square-Root Exponential Model, and Logarithmic Model. The analysis, conducted using the MCMC algorithm, was applied to baseline datasets such as CC and PN, later supplemented with BAO data to incorporate early Universe effects. Additionally, priors from R21 (SH0ES) and F21 (TRGB Calibration), summarised in Table 3.1, were applied to assess their impact on key cosmological parameters, including the Hubble constant, matter density, and the model parameters $p_i$.

The results were visualised through the whisker plot, illustrating the influence of different datasets and priors on the models' performance in Fig. 6.5. While the R21 prior slightly elevated $H_0$ values, the F21 prior brought values closer to the prior's range. In general, the models closely aligned with ΛCDM, especially for the first two models when specific values of $p_i$ reduced to the ΛCDM limit, whereas the Logarithmic Model presented an intriguing alternative, deviating more from the ΛCDM framework. However, $f(T, B)$ models exhib-

ited limitations in comparison to the $f(T)$ framework, evidenced by higher BIC values and less well-defined joint probability regions, indicating a stronger preference for ΛCDM.

Therefore, the analysis of the $f(T, B)$ models has highlighted both their potential and limitations. While this framework offers intriguing alternative to the ΛCDM framework, these $f(T, B)$ cosmological models consistently exhibit weaker statistical performance compared to $f(T)$ models. The $f(T)$ framework emerges as a more robust alternative to ΛCDM, characterised by better-defined probability regions and more favourable statistical indicators. As a result, subsequent investigations prioritised the $f(T)$ models, extending the explored redshift range and incorporating additional observational datasets to further constrain the model parameters.

As time progresses, datasets undergo regular revisions, which necessitated a thorough analysis of the PN and PN+& SH0ES datasets within the $f(T)$ framework, as discussed in Chapter 7. These two datasets were compared and three $f(T)$ gravity models—Power Law, Square-root Exponential, and Exponential were evaluated using MCMC analysis. This analysis revealed that the PN+& SH0ES dataset provided tighter constraints on model parameters and consistently yielded higher $H_0$ values than the PN dataset, corroborating previous results from the SH0es Collaboration. Additionally, the inclusion of complementary datasets, such as CC and BAO, further refined the constraints and enabled a more detailed examination of the $H_0$ tension. Importantly, the incorporation of the BAO dataset effectively broke the degeneracy between $H_0$ and $\Omega_{m,0}$, revealing a correlation between these parameters.

While the $f(T)$ models demonstrated a general agreement with the ΛCDM model, the analysis indicated that the PN+& SH0ES dataset slightly weakened support for ΛCDM in favour of $f(T)$ models, as quantified by the AIC and BIC. This study continues to underscore the potential of $f(T)$ gravity as a viable alternative framework to address the $H_0$ tension. The capability of the PN+& SH0ES dataset to produce tighter constraints and elevated $H_0$ values suggests that integrating diverse datasets enhances the accuracy and reliability of cosmological models. Furthermore, the incorporation of late-time datasets significantly impacted parameter degeneracies, emphasising their importance for extending the redshift range under scrutiny and future investigations.

In addressing the extension of the redshift range, Chapter 8 introduced the inclusion of RSD datasets, which are particularly sensitive to the growth of structure formation. This analysis allowed for a comprehensive exploration of $S_{8,0}$ alongside constraints on cosmological parameters such as $H_0$, $\Omega_{m,0}$, and $\sigma_{8,0}$. The role of the PN+& SH0ES dataset, being the largest collection of supernovae, proved crucial in constraining the Hubble constant and addressing late-time cosmic tensions. An extensive MCMC analysis was performed to evaluate the Power Law, the Square-Exponential and the Exponential models and dataset

combination (that include CC, PN+& SH0ES, BAO, RSD), with results compared against the ΛCDM model using statistical indicators. The findings showed that while ΛCDM remains largely consistent with most datasets, certain $f(T)$ gravity models, such as the power law model, exhibited marginally superior performance in the presence of RSD data, indicating a potential preference for these models. Notably, the PN+& SH0ES dataset proved effective in sharpening constraints, especially for $H_0$, aligning values more closely with higher estimates, such as those from R22.

Additionally, the $S_{8,0}$ values obtained were consistent with current findings in the literature, including results from P18 and KiDS-1000. The radar plots in Fig. 8.13, demonstrate the differences in $\sigma$ units between the models' $H_0$ values and those from early-time P18 compared to late-time KiDS-1000 values, revealing a slight diminution in the $\sigma$ values for the models.

Thus, it can be seen that certain $f(T)$ models can closely replicate the performance of ΛCDM while offering insights into resolving cosmological tensions. The findings indicate that incorporating RSD data and other late-time datasets, such as PN+& SH0ES, enhances the constraints on cosmological parameters, which could potentially address the $H_0$ and $S_{8,0}$ tensions. These models may serve as promising frameworks for tackling ongoing discrepancies in cosmological observations. The importance of comprehensive dataset combinations to reduce uncertainties and provide more precise cosmological constraints is further emphasised.

Consequently, a more in-depth analysis was warranted to ensure that $f(T)$ gravity is not constrained solely to late-times but also incorporates modifications to include the CMB B-mode spectrum for constraining gravitational wave parameters and examining their effects on $f(T)$ parameters, particularly the Power Law model. Thus, Chapter 9 presents an in-depth investigation into primordial GWs within the $f(T)$ gravity framework, utilising both early- and late-time cosmological datasets. This chapter focused on confronting theoretical predictions of $f(T)$ gravity with observational data, by using HiCLASS Boltzmann code to model both background evolution and linear perturbations, which was modified for $f(T)$ gravity.

The study incorporated revisions to key late-time datasets, including the CC and BAO datasets, enhanced by the DESI likelihood, to improve constraints on cosmological parameters. The analysis utilised the BICEP/Keck Array (BK14) dataset alongside late-time datasets to not only constrain the standard previous parameters but also to introduce additional parameters that characterise B-mode polarisation, specifically the tensor-to-scalar ratio $r$ and the tensor spectral index $n_t$. Two case studies were conducted: one in which $n_t$ was fixed at zero, and another where $n_t$ was treated as a free parameter, thereby allowing for a more comprehensive exploration of its influence on the model.

Using MontePython as the MCMC tool, robust constraints on cosmological parameters, such as $r$, $n_t$, $H_0$, and $\Omega_{m,0}$, were obtained. The results indicated that the inclusion of updated datasets, particularly DESI, played a critical role in refining the bounds on $\Omega_{m,0}$ and improving overall parameter constraints.

When $n_t$ was fixed to zero, the BK14 dataset constrained $r$ to be less than 0.11 at a 95% confidence level, aligning with previous results. When $n_t$ was allowed to vary, the analysis provided meaningful constraints on both $r$ and $n_t$, and also had consistent results with previous results in literature, although with a broader range.

This chapter underscores the importance of combining early- and late-time datasets to achieve more precise constraints on cosmological parameters. While the DESI dataset did not directly impact $r$ and $n_t$, it significantly improved the constraints on $\Omega_{m,0}$, influencing the overall model compatibility within the $f(T)$ framework. The analysis demonstrated that the $f(T)$ gravity model remained consistent with current observational data, particularly in constraining primordial GWs, thus offering a valuable framework for future studies.

Therefore, the analysis conducted in this work spans both early and late-time cosmology, aiming to bridge the gap between these two epochs and uncover their interconnected physical implications. At early times, the focus was primarily on the inflationary phase, utilizing datasets from primordial GW signals to probe the underlying physics of the early Universe. In contrast, late-time analyses shifted attention to cosmic acceleration, leveraging datasets like CC, PN+& SH0ES, BAO, and RSD to investigate the present expansion rate and the growth of large-scale structures.

The combination of early and late-time cosmological analyses highlights the promise of $f(T)$ gravity in resolving current tensions in cosmological data. This framework not only offers a compelling alternative to $\Lambda$CDM but also provides deeper insights into the Universe's evolution from its earliest moments to the present day. By connecting these early and late-time analyses, this work provides a unified view of how modifications to gravity influence the entire cosmic history.

The physical implications of this work lie in the ability of the Power Law model within $f(T)$ to consistently describe gravitational phenomena across both early and late times, matching well with observational data throughout cosmic history. In particular, the Power Law model showcases the flexibility and predictive power of $f(T)$ gravity in capturing both inflationary phenomena and late-time cosmic acceleration, providing a consistent explanation that aligns with a broad range of observational constraints.

In conclusion, the results of this study highlight $f(T)$ gravity as a promising and viable alternative to $\Lambda$CDM, with significant potential to address key cosmological tensions. The persistent discrepancies, such as the $H_0$ and $S_{8,0}$ tensions, suggest that $f(T)$ models could provide a more comprehensive explanation for late-time cosmic acceleration, the growth of

cosmic structures, and the amplitude of matter fluctuations. This study has demonstrated that $f(T)$ gravity is not merely a theoretical framework; it provides concrete, observationally consistent solutions, including predictions for primordial GWs. By integrating datasets such as CC, PN+& SH0ES, DESI, and BK14, the models have shown a remarkable ability to accurately capture both early- and late-time cosmic phenomena. These findings underscore the necessity for further investigation into $f(T)$ gravity, as it presents a compelling alternative to ΛCDM as discussed in the next points.

## 10.1 | Future works

As highlighted above this study opens several avenues for future research and exploration in the realm of $f(T)$ gravity. The following points highlight key areas for further investigation:

- **Improving Cosmological Analysis Through Dataset Expansion**

  In this work, the impact of various datasets has been explored, including measurements from CC, PN+& SH0ES, and BAO. Additionally, density fluctuation data from RSD and tensor sector data from the BK14 dataset have been incorporated. However, to enhance the extensiveness and completeness of the research on tensor perturbations, further extension of the dataset is deemed essential.

  Future studies are expected to benefit from the inclusion of data from the Planck Release 3 (PR3) [316], which provides comprehensive CMB data, including high-resolution temperature and polarisation maps, as well as a variety of likelihood functions crucial for constraining cosmological parameters. Recently, the Planck Collaboration has released Planck Release 4 (PR4) [317, 318, 319], which includes updated CMB maps with improved calibrations and noise reductions, along with new analyses from the HiLLiPOP and LoLLiPoP projects [320, 321]. Notably, the LoLLiPoP dataset contains significant information regarding B-modes, which are pivotal for understanding the tensor modes of primordial gravitational waves.

  Another critical aspect of future work is expanding the observational datasets to include next-generation surveys like Euclid [304] and the JWST [322], which will provide unprecedented precision in measuring cosmic parameters at both low and high redshifts.

  By expanding the dataset to include these new releases, refinements in the constraints on both background and tensor perturbations are anticipated, allowing for the assessment of the viability of the $f(T)$ gravity model in comparison to the standard ΛCDM

model. This comprehensive approach will enable a critical evaluation of the effectiveness of TG in describing cosmic phenomena and provide a more extensive understanding of the underlying physics governing the Universe's evolution. Ultimately, the integration of these datasets will facilitate a more rigorous analysis of the tension between different cosmological observations and contribute to ongoing efforts to reconcile them within the framework of modified gravity.

- **Integrating Scalar Perturbation Frameworks in HiClass for Improved Cosmological Constraints**

  Another extension of the current work involves the adaptation of HiCLASS to incorporate modifications to the scalar perturbations. This approach necessitates a thorough examination of all modes from the PR3 and PR4 datasets, specifically focusing on the temperature-temperature ($TT$), temperature-polarisation ($TE$), and electric polarisation-electric polarisation ($EE$) spectra. Such an integration is expected to yield stronger constraints on critical cosmological parameters, particularly the current rate of expansion of the Universe, as derived from the $TT$ spectrum, as well as the total matter density.

  In addition to these parameters, this modified analysis will facilitate the extraction of primordial power spectrum parameters, including the spectral index ($n_s$), and provide stronger constraints on the tensor-to-scalar ratio ($r$). Furthermore, the overall shape and amplitude of the primordial power spectrum can be analysed, leading to a more comprehensive understanding of the initial conditions of the Universe.

  To achieve these advancements, the necessary adaptations to HiCLASS must first be implemented. This development will allow for a complete understanding of the early Universe, encompassing both the inflationary phase and the late-time evolution within the framework of $f(T)$ gravity, particularly in the context of the power law model. By systematically integrating these scalar perturbation modifications, the insights gained will contribute significantly to our understanding of cosmological dynamics and the underlying physics governing the Universe's expansion.

- **A Broader Look at $f(T)$ Gravity and Teleparallel Horndeski Models**

  The preceding chapter primarily focused on the $f(T)$ power law model. However, for a more detailed analysis of $f(T)$ gravity, the investigation can be extended to encompass other models, integrating the insights discussed in the previous two points. This extension will necessitate further adaptations to HiCLASS to accommodate the specific characteristics and requirements of the models under consideration.

Additionally, this analysis can be generalised through the incorporation of Teleparallel Horndeski models, which represent the teleparallel analogue of Horndeski theories, which is the most general scalar-tensor theory of gravity. In this framework, $f(T)$ gravity is situated within a broader context. The exploration of Teleparallel Horndeski models will not only enhance our understanding of $f(T)$ gravity but also facilitate a deeper investigation into the diverse behaviours of modified gravity theories.

By expanding the scope of the analysis in this manner, a richer and more nuanced understanding of the gravitational dynamics in cosmology can be achieved, contributing to the ongoing discussion on the implications of modified gravity in the evolution of the Universe.

In closing, this study has established $f(T)$ gravity as a formidable contender to the conventional $\Lambda$CDM model, adeptly addressing significant cosmological tensions such as the $H_0$ and $S_{8,0}$ discrepancies. By leveraging diverse observational datasets, including supernovae, baryon acoustic oscillations, and gravitational wave data, this research not only highlights the model's observational consistency but also its potential to offer deeper insights into the universe's evolution and the nature of gravity itself. As new astronomical discoveries are anticipated, the framework of $f(T)$ gravity is seen to pave the way for innovative explorations into the cosmos, encouraging the scientific community to deepen their understanding of fundamental physics in the pursuit of unlocking the universe's mysteries. Future work will involve the exploration of additional datasets and refined modelling techniques to further validate the implications of $f(T)$ gravity and to investigate its impact on galaxy formation and large-scale structure. Through these efforts, a more comprehensive understanding of the cosmos may be achieved, encouraging continued investigation into modified gravity theories.

# A

# Gaussian Process reconstruction of $w(z)$, $\mathcal{O}_m^{(1)}(z)$, $\mathcal{L}_m^{(1)}(z)$ and $q(z)$

In this appendix, the GP reconstructions of the dark energy equation of state, the $\mathcal{O}_m^{(1)}(z)$, $\mathcal{L}_m^{(1)}(z)$ and the deceleration parameter are shown. First the GP reconstructions of the $w(z)$ are shown based on Eq. 4.3.

The next two reconstructions ($\mathcal{O}_m^{(1)}(z)$, $\mathcal{L}_m^{(1)}(z)$) are related with each other as $\mathcal{L}_m^{(1)}(z)$ is the derivative of $\mathcal{O}_m^{(1)}(z)$ and thus, they have the same general behaviour. At lower redshifts there is a strong agreement with the $\Lambda$CDM scenario, however the situation changes for higher redshift where a considerable divergence is featured. An exception to this, are the R19 and HW priors as some deviation also exists at low redshift.

The last reconstruction includes the deceleration parameter which are based on Eq. 4.6. This reconstruction provides a good indication for the transition redshift as it is denoted by the point where the $q(z)$ curve goes from a positive value to a negative one. The corresponding transition redshifts are shown in Table 4.5. It is clear that when the BAO data set is included, $q(z)$ evolves similarly to $\Lambda$CDM. This is mostly due to its influence from the early Universe.

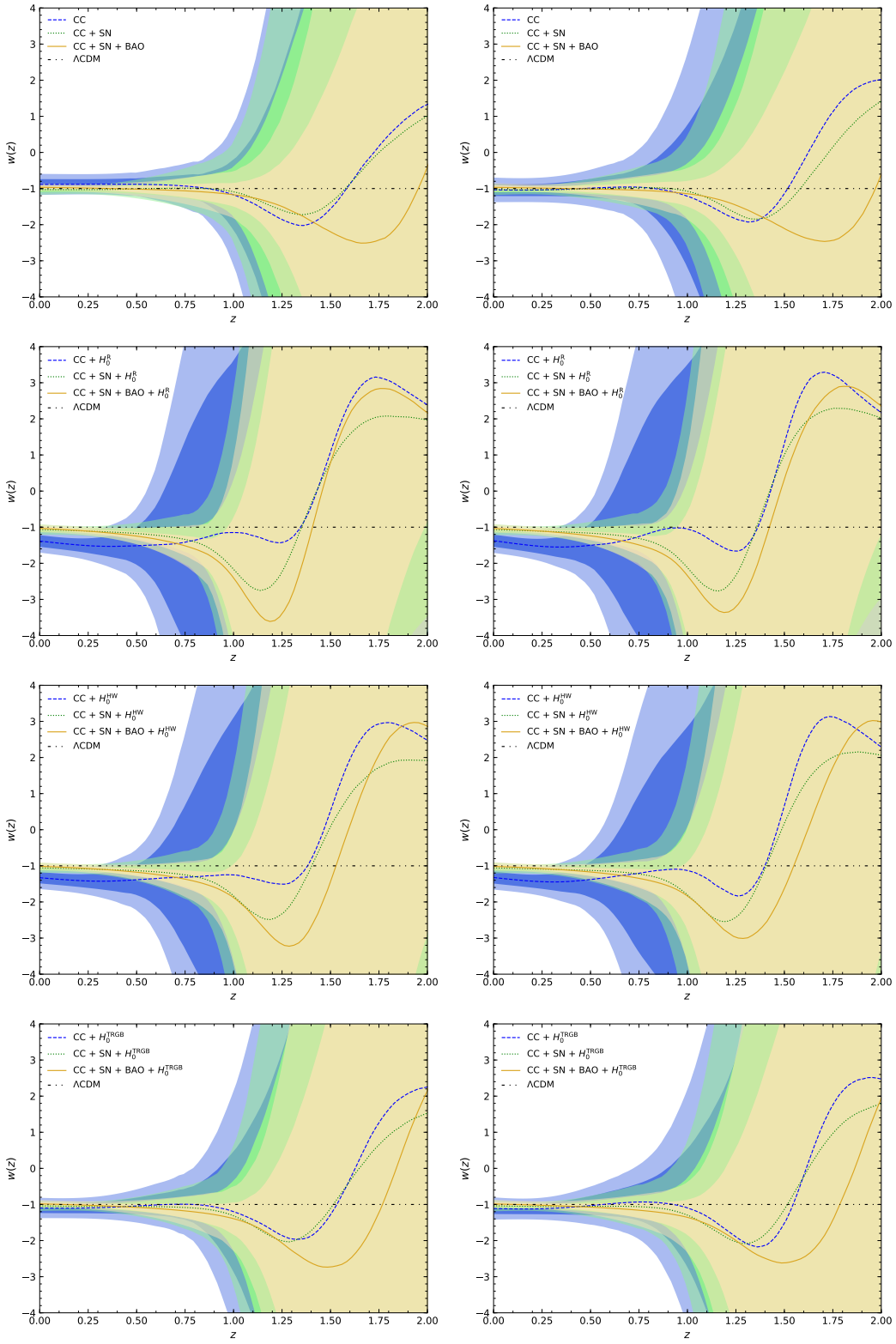


Figure A.1: GP reconstructions of $w(z)$ with the squared exponential (left) and Cauchy (right) kernel functions, along with the ΛCDM prediction.

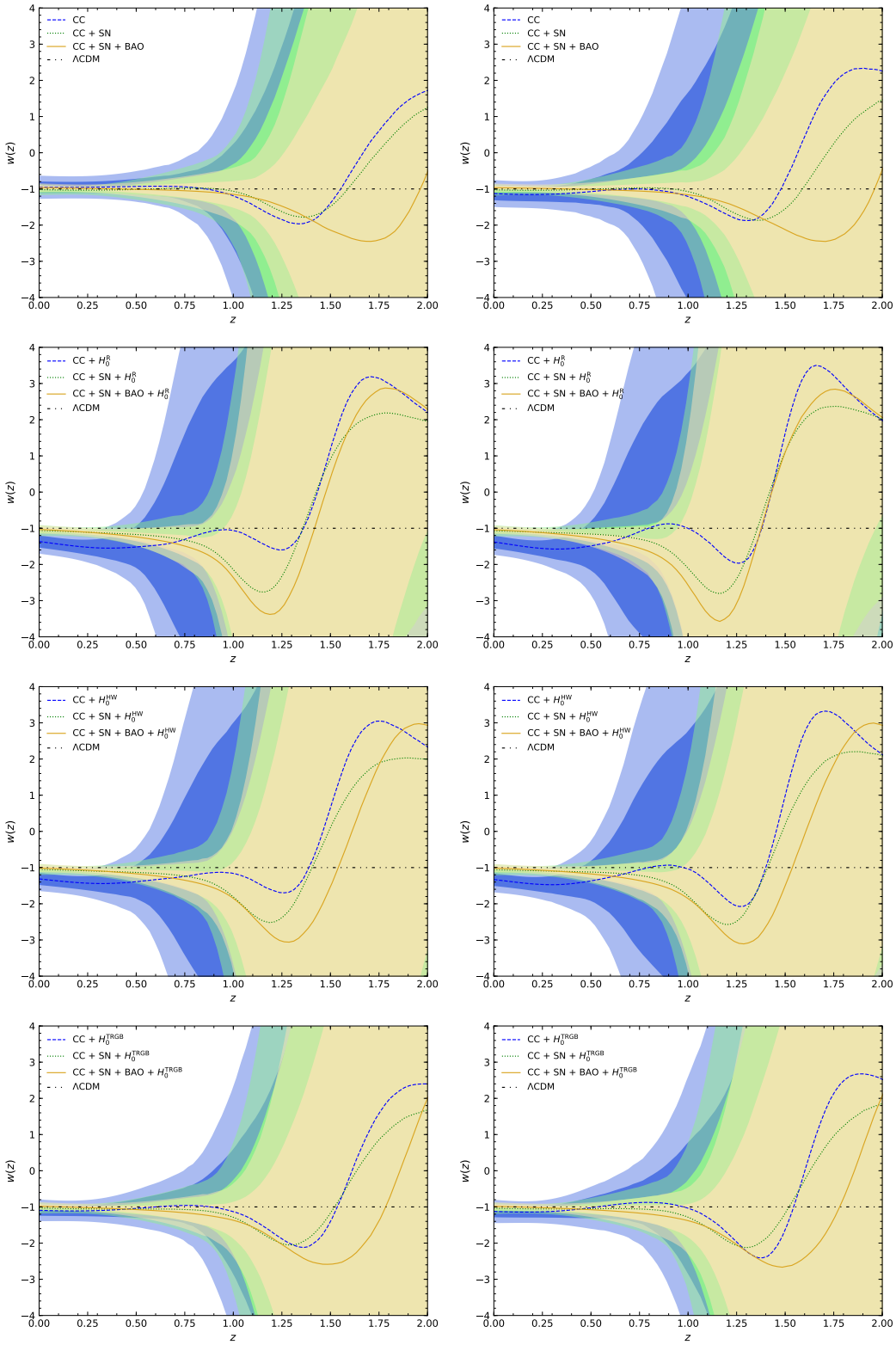


Figure A.2: GP reconstructions of $w(z)$ with the Matérn (left) and rational quadratic (right) kernel functions, along with the ΛCDM prediction.

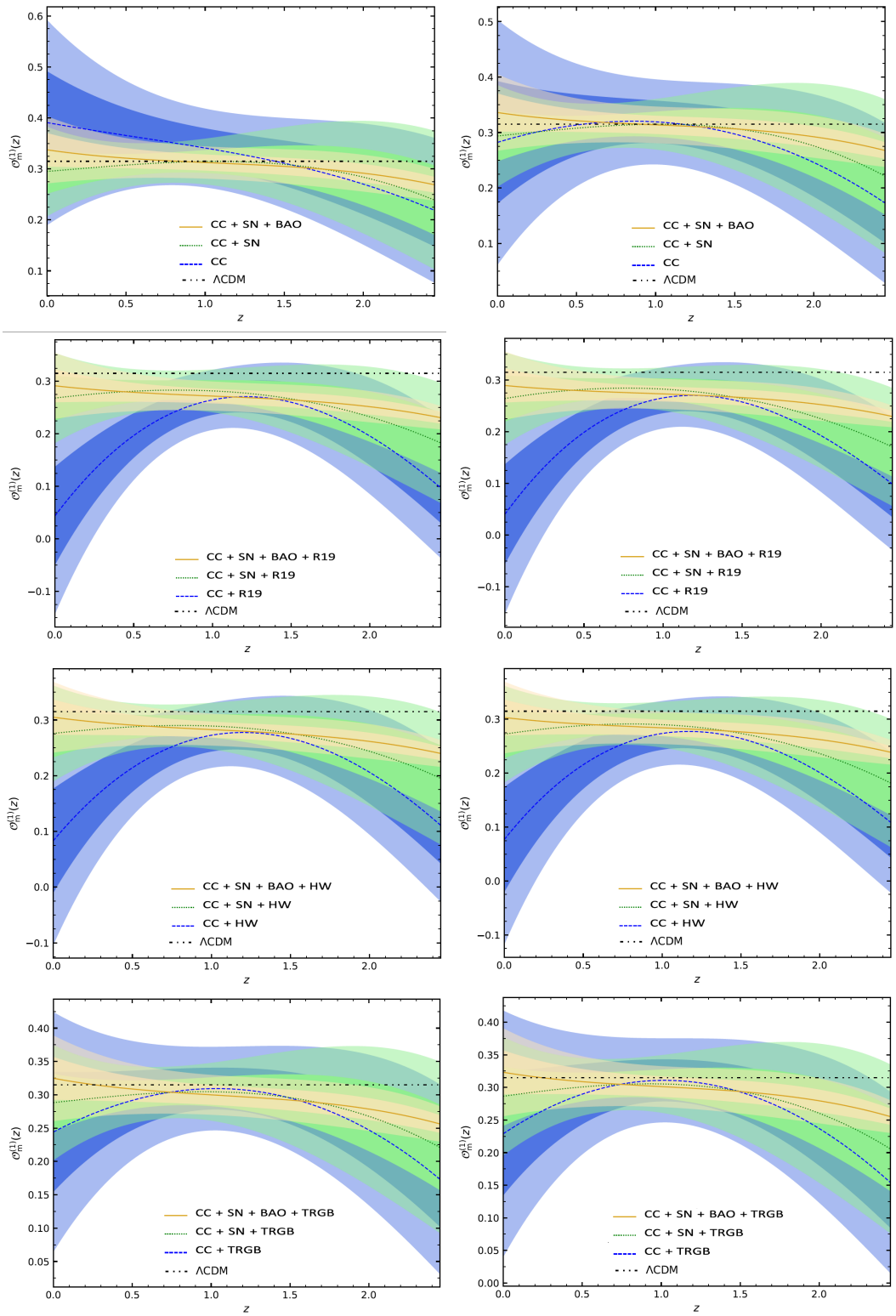


Figure A.3: GP reconstructions of $\mathcal{O}_m^{(1)}(z)$. *Left:* using the squared exponential kernel; *Right:* using the Cauchy kernel. The reconstructions are complemented with the ΛCDM prediction.

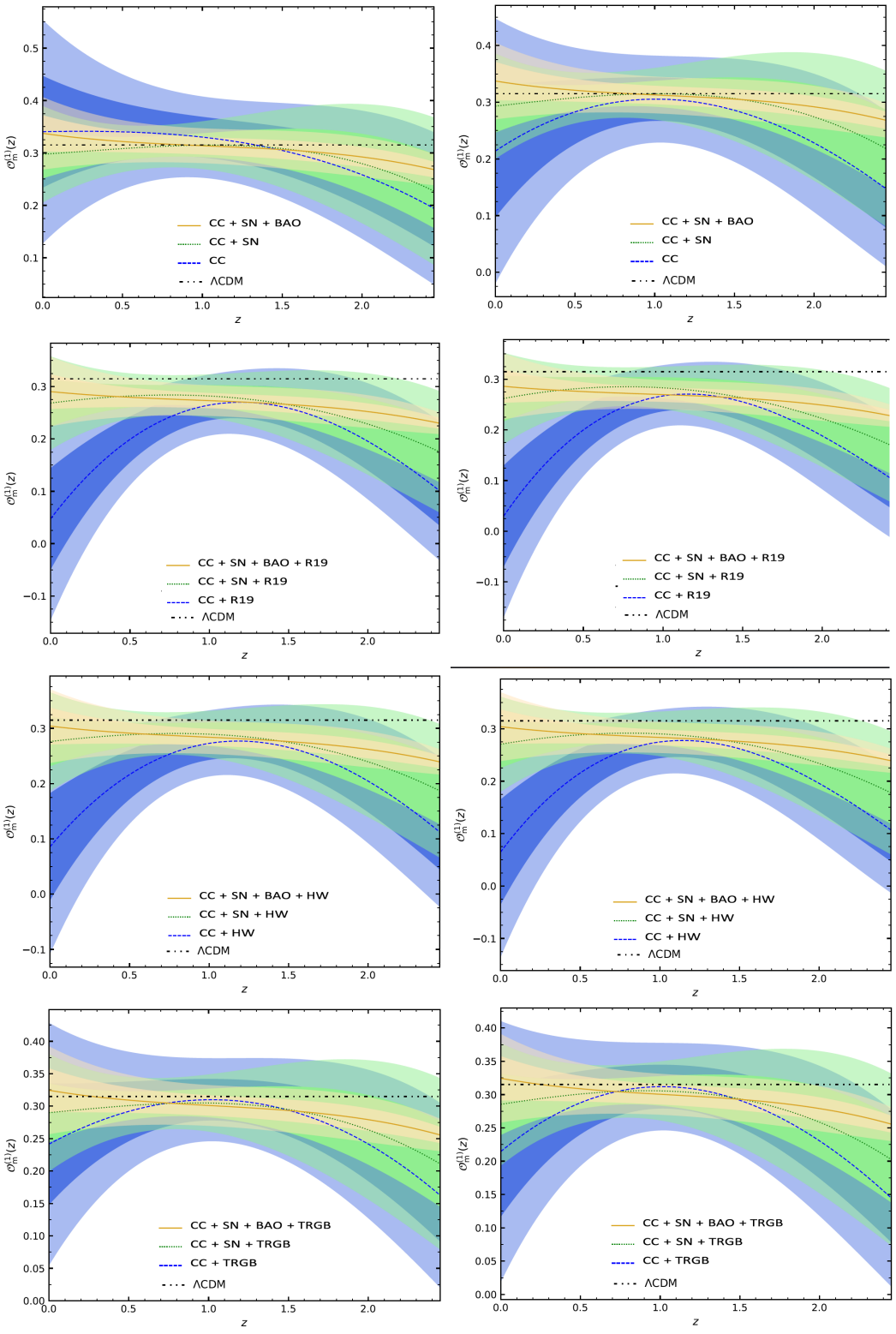


Figure A.4: GP reconstructions of $\mathcal{O}_m^{(1)}(z)$. *Left:* using the Matérn kernel; *Right:* using the rational quadratic kernel. The reconstructions are complemented with the ΛCDM prediction.

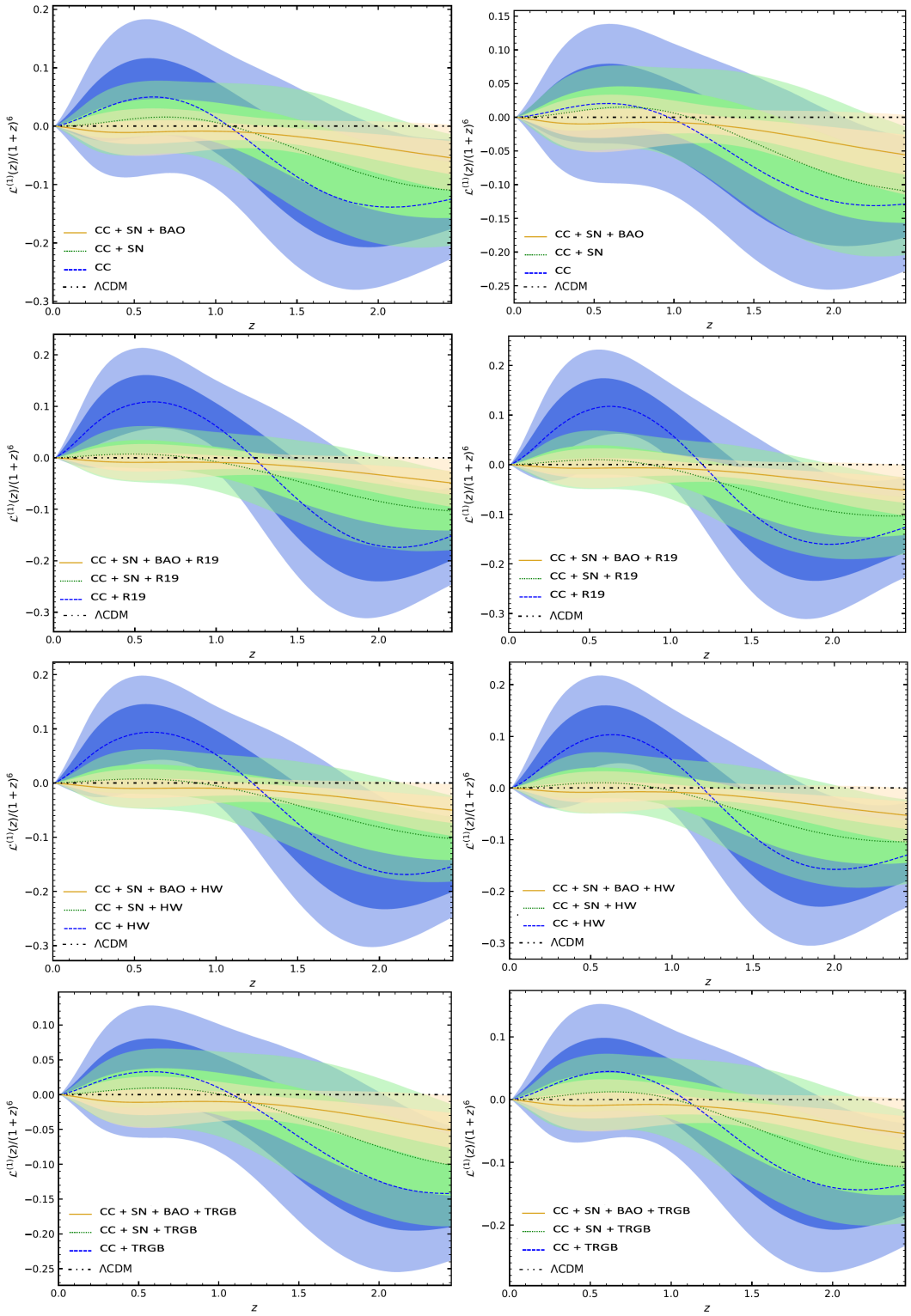


Figure A.5: GP reconstructions of $\mathcal{L}_m^{(1)}(z)$. *Left:* using the squared exponential kernel; *Right:* using the Cauchy kernel. The reconstructions are complemented with the ΛCDM prediction.

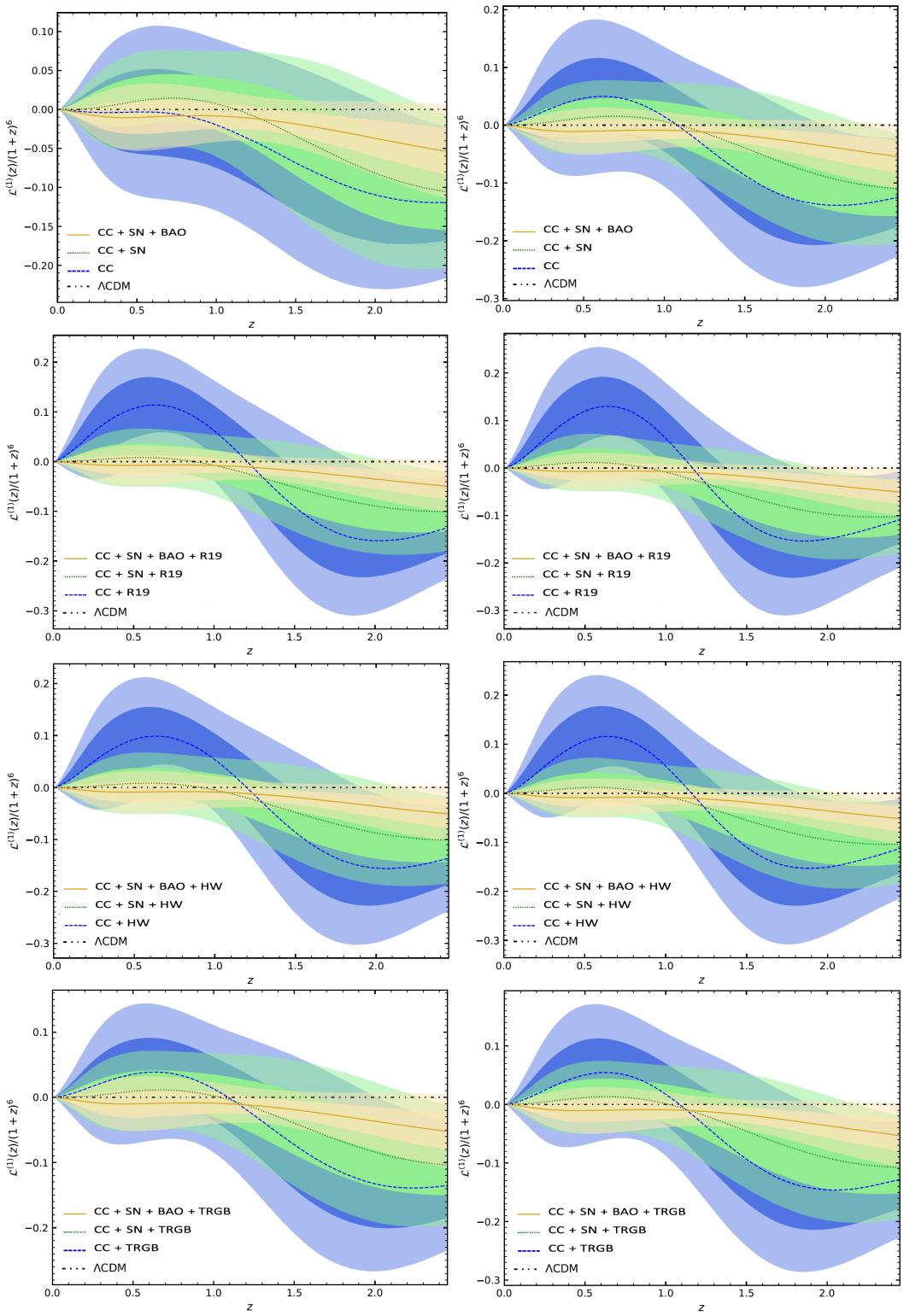


Figure A.6: GP reconstructions of $\mathcal{L}_m^{(1)}(z)$. *Left:* using the Matérn kernel; *Right:* using the rational quadratic kernel. The reconstructions are complemented with the ΛCDM prediction.

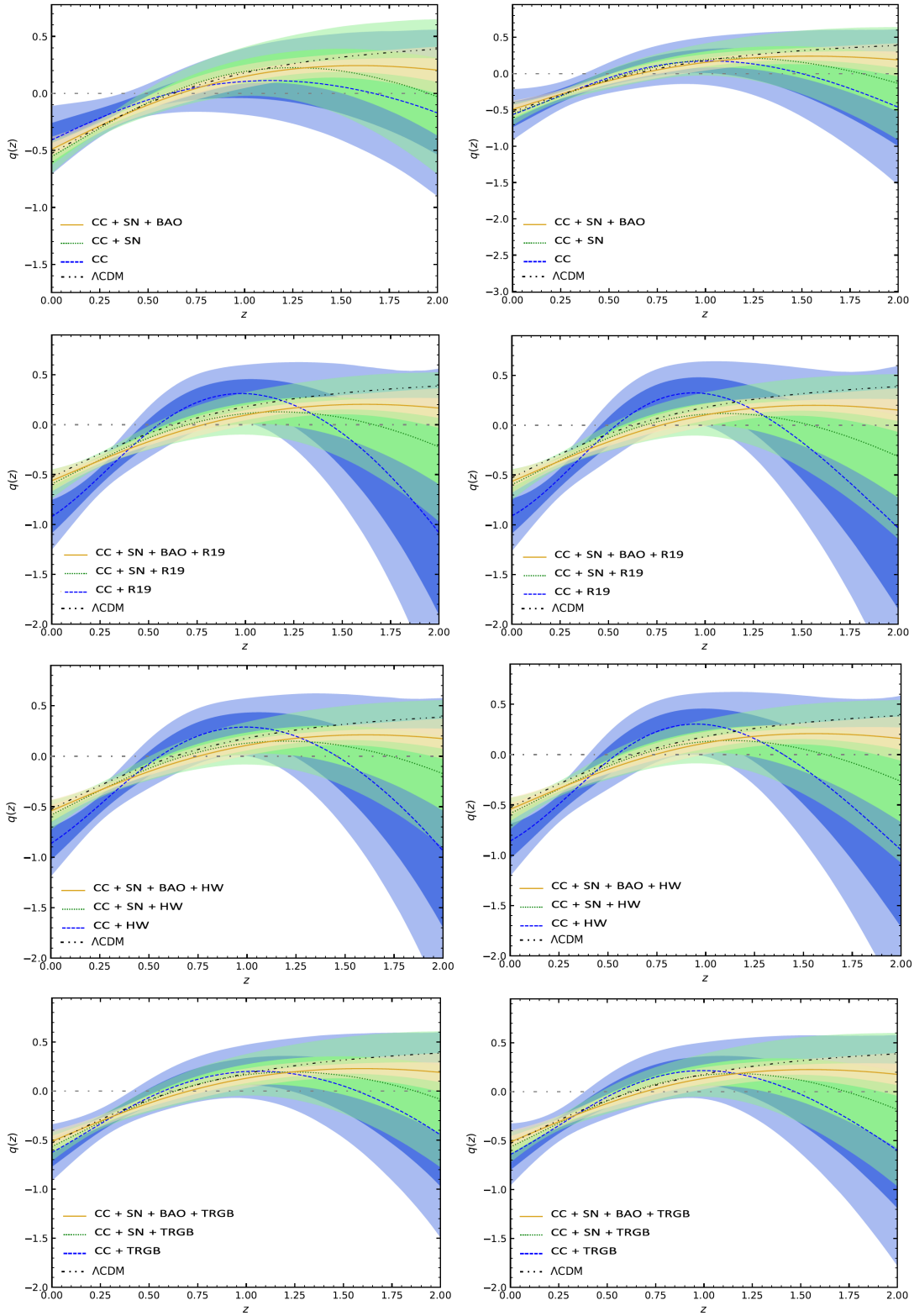


Figure A.7: GP reconstructions of the deceleration parameter, $q(z)$. *Left:* using the square exponential kernel; *Right:* using the Cauchy kernel. The reconstructions are complemented with the ΛCDM prediction and $q(z) = 0$.

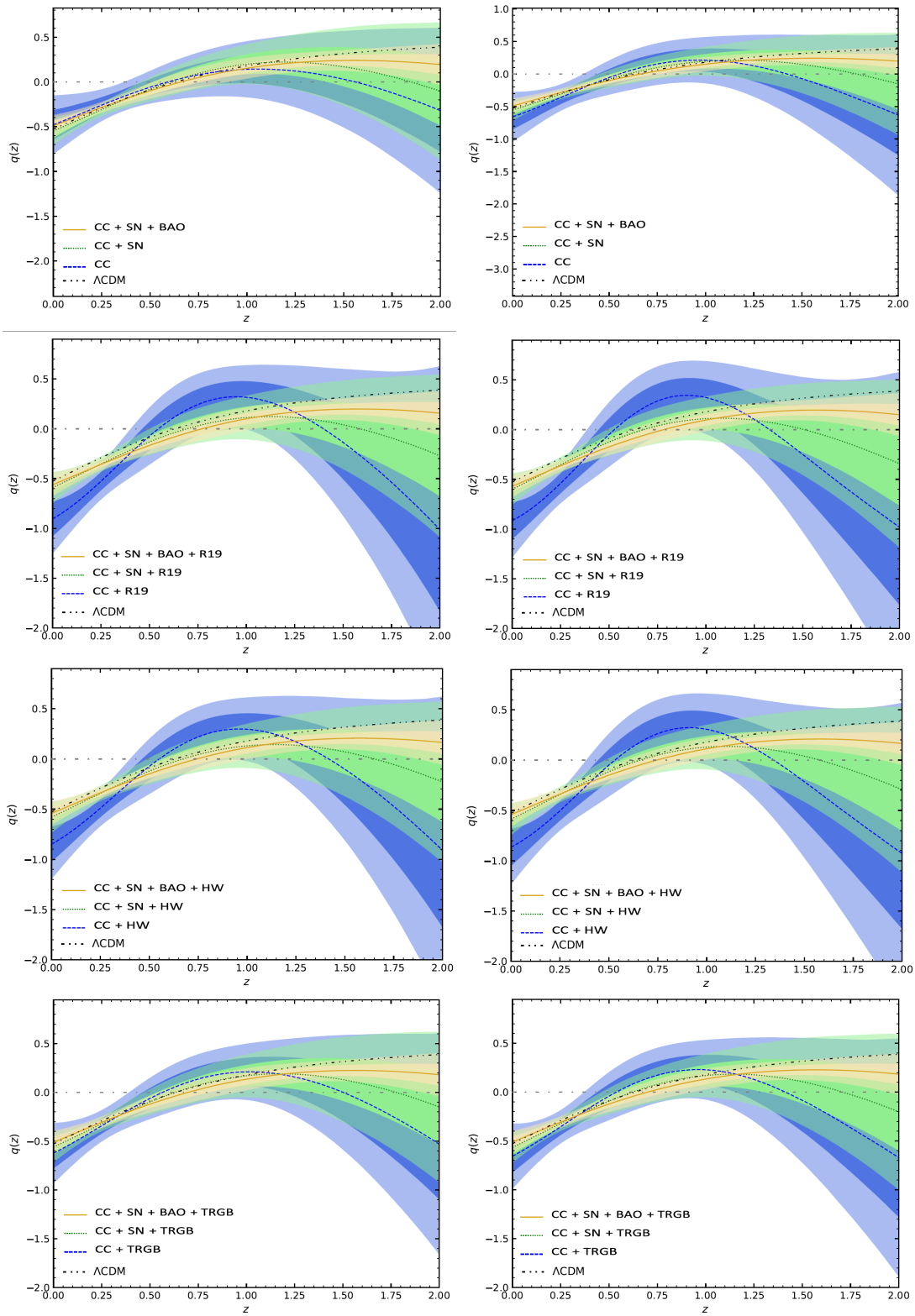


Figure A.8: GP reconstructions of the deceleration parameter, $q(z)$. *Left:* using the Matérn kernel; *Right:* using the rational quadratic kernel. The reconstructions are complemented with the ΛCDM prediction and $q(z) = 0$.

# B

# PN+& SH0ES Results

This section presents the results obtained for the PN+& SH0ES data set, which enriches the comparative analysis between PN and PN+. This investigation assesses the impact of different data set combinations on the $H_0$ tension and allows for the deviation in units of $\sigma$ between the resulting $H_0$ values for each model and each data set combination, compared to the P18 value using only the PN+& SH0ES data set, as depicted in Fig. 7.6. The constrained parameter values for each model, derived from the MCMC analysis, are detailed in the table below.

| Model | $H_0$ [km s$^{-1}$ Mpc$^{-1}$] | $\Omega_{m,0}$ | $p_i$ | $M$ |
|---|---|---|---|---|
| $\Lambda$CDM | $73.4 \pm 1.1$ | $0.334^{+0.021}_{-0.020}$ | – | $-19.247 \pm 0.033$ |
| $f_1$CDM | $73.3 \pm 1.0$ | $0.331^{+0.044}_{-0.070}$ | $0.28^{+0.22}_{-0.37}$ | $-19.248^{+0.030}_{-0.029}$ |
| $f_2$CDM | $73.2^{+1.1}_{-1.0}$ | $0.318^{+0.023}_{-0.102}$ | $0.33^{+0.32}_{-0.26}$ | $-19.259^{+0.044}_{-0.021}$ |
| $f_3$CDM | $73.2 \pm 1.1$ | $0.308^{+0.032}_{-0.099}$ | $0.33^{+0.34}_{-0.24}$ | $-19.225^{+0.040}_{-0.085}$ |

Table B.1: Results for the constrained parameters using the PN$^+$ & SH0ES data set for each model considered in the analysis section.

# C

# Model parameter $p_i$ versus $S_{8,0}$ plots

In this section, the posteriors together with their confidence regions of the $p_i$ and $S_{8,0}$ parameters are presented in order to investigate the correlation between the two.

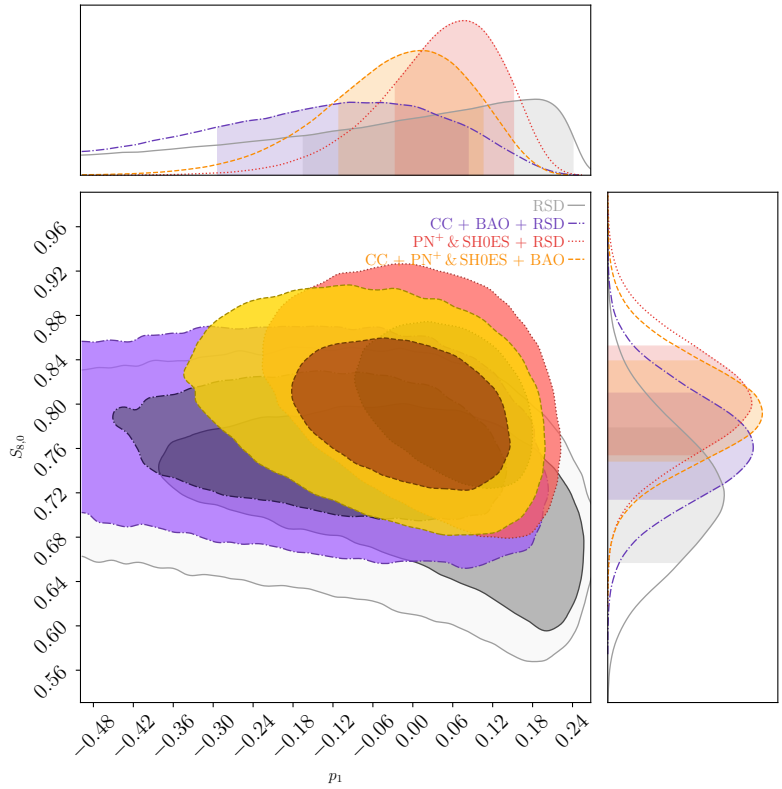


Figure C.1: Contour plots showing the relationship between the $p_1$ parameter and the $S_{8,0}$ parameter for the $f_1$CDM model (Power Law Model).

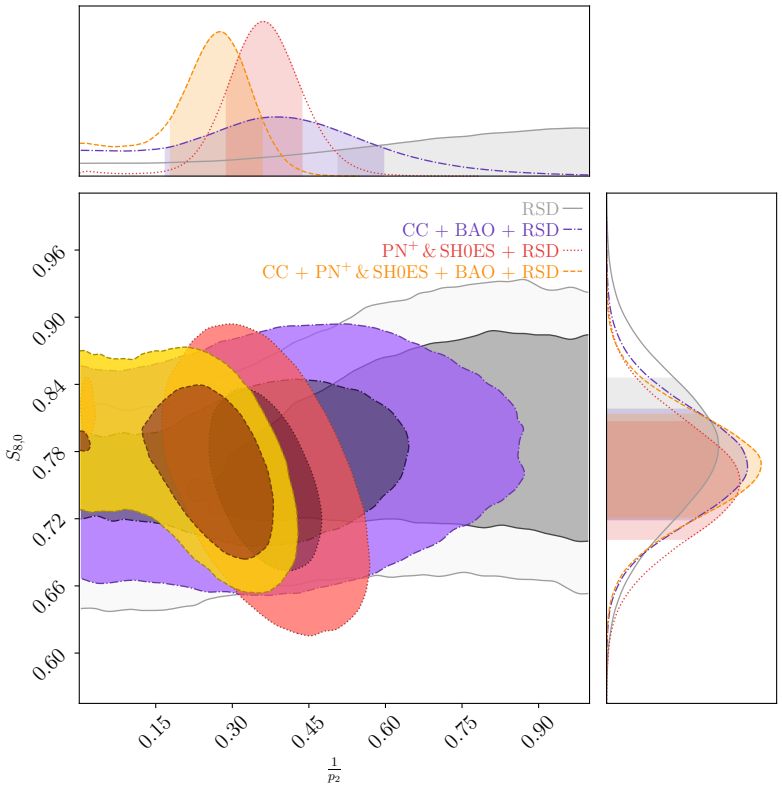


Figure C.2: Contour plots showing the relationship between the $\frac{1}{p_2}$ parameter and the $S_{8,0}$ parameter for the $f_2$CDM model (Linder Model).

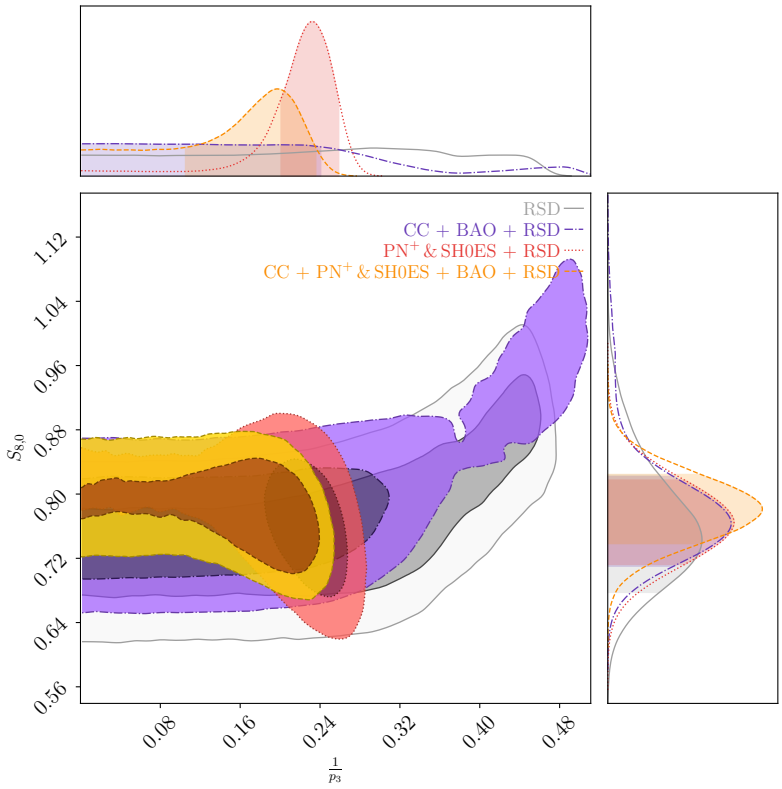


Figure C.3: Contour plots showing the relationship between the $\frac{1}{p_3}$ parameter and the $S_{8,0}$ parameter for the $f_4$CDM model (Exponential Model).

# References


[1] A. G. Riess et al. New Parallaxes of Galactic Cepheids from Spatially Scanning the Hubble Space Telescope: Implications for the Hubble Constant. *Astrophys. J.*, 855(2):136, March 2018. doi: 10.3847/1538-4357/aaadb7.

[2] A. G. Riess, S. Casertano, W. Yuan, L. M. Macri, and D. Scolnic. Large Magellanic Cloud Cepheid Standards Provide a 1% Foundation for the Determination of the Hubble Constant and Stronger Evidence for Physics beyond ΛCDM. *Astrophys. J.*, 876(1):85, 2019. doi: 10.3847/1538-4357/ab1422.

[3] A. G. Riess, S. Casertano, W. Yuan, J. B. Bowers, L. Macri, J. C. Zinn, and D. Scolnic. Cosmic Distances Calibrated to 1% Precision with Gaia EDR3 Parallaxes and Hubble Space Telescope Photometry of 75 Milky Way Cepheids Confirm Tension with ΛCDM. *Astrophys. J. Lett.*, 908(1):L6, 2021. doi: 10.3847/2041-8213/abdbaf.

[4] A. G. Riess et al. A Comprehensive Measurement of the Local Value of the Hubble Constant with 1 km $s^{-1}Mpc^{-1}$ Uncertainty from the Hubble Space Telescope and the SH0ES Team. *Astrophys. J. Lett.*, 934 (1):L7, 2022. doi: 10.3847/2041-8213/ac5c5b.

[5] A. G. Riess et al. A 2.4% Determination of the Local Value of the Hubble Constant. *Astrophys. J.*, 826(1): 56, 2016. doi: 10.3847/0004-637X/826/1/56.

[6] A. G. Riess et al. A Redetermination of the Hubble Constant with the Hubble Space Telescope from a Differential Distance Ladder. *Astrophys. J.*, 699(1):539–563, July 2009. doi: 10.1088/0004-637X/699/1/539.

[7] A. G. Riess et al. A 3% Solution: Determination of the Hubble Constant with the Hubble Space Telescope and Wide Field Camera 3. *Astrophys. J.*, 730(2):119, April 2011. doi: 10.1088/0004-637X/730/2/119.

[8] W. L. Freedman, B. F. Madore, V. Scowcroft, C. Burns, A. Monson, S. E. Persson, M. Seibert, and J. Rigby. Carnegie Hubble Program: A Mid-infrared Calibration of the Hubble Constant. *Astrophysical Journal*, 758 (1):24, October 2012. doi: 10.1088/0004-637X/758/1/24.

[9] D. N. Spergel et al. First year Wilkinson Microwave Anisotropy Probe (WMAP) observations: Determination of cosmological parameters. *Astrophys. J. Suppl.*, 148:175–194, 2003. doi: 10.1086/377226.

[10] L. Verde et al. First year Wilkinson Microwave Anisotropy Probe (WMAP) observations: Parameter estimation methodology. *Astrophys. J. Suppl.*, 148:195, 2003. doi: 10.1086/377335.

[11] D. N. Spergel et al. Wilkinson Microwave Anisotropy Probe (WMAP) three year results: implications for cosmology. *Astrophys. J. Suppl.*, 170:377, 2007. doi: 10.1086/513700.

[12] E. Komatsu et al. Five-Year Wilkinson Microwave Anisotropy Probe (WMAP) Observations: Cosmological Interpretation. *Astrophys. J. Suppl.*, 180:330–376, 2009. doi: 10.1088/0067-0049/180/2/330.

[13] C. L. and Bennett. Nine-year Wilkinson Microwave Anisotropy Probe (WMAP) Observations: Final Maps and Results. *Astrophysical Journal, Supplement*, 208(2):20, October 2013. doi: 10.1088/0067-0049/208/2/20.

[14] P. A. R. Ade et al. Planck 2013 results. XVI. Cosmological parameters. *Astron. Astrophys.*, 571:A16, 2014. doi: 10.1051/0004-6361/201321591.

[15] P. A. R. Ade et al. Planck 2015 results. XIII. Cosmological parameters. *Astron. Astrophys.*, 594:A13, 2016. doi: 10.1051/0004-6361/201525830.

[16] N. Aghanim et al. Planck 2018 results. VI. Cosmological parameters. *Astron. Astrophys.*, 641:A6, 2020. doi: 10.1051/0004-6361/201833910. [Erratum: Astron.Astrophys. 652, C4 (2021)].

[17] G. E. Addison, D. J. Watts, C. L. Bennett, M. Halpern, G. Hinshaw, and J. L. Weiland. Elucidating ΛCDM: Impact of Baryon Acoustic Oscillation Measurements on the Hubble Constant Discrepancy. *Astrophys. J.*, 853(2):119, 2018. doi: 10.3847/1538-4357/aaa1ed.

[18] L. Perivolaropoulos and F. Skara. Challenges for ΛCDM: An update. *New Astron. Rev.*, 95:101659, 2022. doi: 10.1016/j.newar.2022.101659.

[19] S. Carroll, S.M. Carroll, and Addison-Wesley. *Spacetime and Geometry: An Introduction to General Relativity*. Addison Wesley, 2004. ISBN 9780805387322. URL `https://books.google.com.mt/books?id=1SKFQgAACAAJ`.

[20] R.J. Lambourne. *Relativity, gravitation and cosmology*. Cambridge University Press, 2010.

[21] J. Beltrán J., L. Heisenberg, and T. S. Koivisto. The Geometrical Trinity of Gravity. *Universe*, 5(7):173, 2019. doi: 10.3390/universe5070173.

[22] E. Abdalla et al. Cosmology intertwined: A review of the particle physics, astrophysics, and cosmology associated with the cosmological tensions and anomalies. *JHEAp*, 34:49–211, 2022. doi: 10.1016/j.jheap.2022.04.002.

[23] I. Newton. *Philosophiae naturalis principia mathematica*. J. Societatis Regiae ac Typis J. Streater, 1687. URL `https://books.google.com.mt/books?id=-dVKAQAAIAAJ`.

[24] A. Einstein. Explanation of the Perihelion Motion of Mercury from the General Theory of Relativity. *Sitzungsber. Preuss. Akad. Wiss. Berlin (Math. Phys. )*, 1915:831–839, 1915.

[25] F. W. Dyson, A. S. Eddington, and C. Davidson. A Determination of the Deflection of Light by the Sun's Gravitational Field, from Observations Made at the Total Eclipse of May 29, 1919. *Phil. Trans. Roy. Soc. Lond. A*, 220:291–333, 1920. doi: 10.1098/rsta.1920.0009.

[26] A. Einstein. Erklärung der Perihelbewegung des Merkur aus der allgemeinen Relativitätstheorie. *Sitzungsberichte der Königlich Preussischen Akademie der Wissenschaften*, pages 831–839, January 1915.

[27] A. Friedmann. Über die Krügmmung des Raumes. *Zeitschrift fur Physik*, 10(1):377–386, 1922. doi: 10.1007/BF01332580.

[28] H. P. Robertson. Kinematics and World-Structure. *Astrophys. J.*, 82:284, Nov 1935. doi: 10.1086/143681.

[29] G. Lemaître. Expansion of the universe, A homogeneous universe of constant mass and increasing radius accounting for the radial velocity of extra-galactic nebulae. *Mon. Not. Roy. Astron. Soc.*, 91:483–490, Mar 1931. doi: 10.1093/mnras/91.5.483.

[30] A. G. Walker. On Milne's Theory of World-Structure. *Proceedings of the London Mathematical Society*, 42: 90–127, Jan 1937. doi: 10.1112/plms/s2-42.1.90.

[31] W. Rindler. *Relativity: Special, General, and Cosmological*. OUP Oxford, 2006. ISBN 9780198567325. URL `https://books.google.com.mt/books?id=LkEhsgmP4vEC`.

[32] E. Hubble. A Relation between Distance and Radial Velocity among Extra-Galactic Nebulae. *Proceedings of the National Academy of Science*, 15(3):168–173, March 1929. doi: 10.1073/pnas.15.3.168.

[33] S. Perlmutter et al. Measurements of $\Omega$ and $\Lambda$ from 42 high redshift supernovae. *Astrophys. J.*, 517:565–586, 1999. doi: 10.1086/307221.

[34] A. G. Riess et al. Observational evidence from supernovae for an accelerating universe and a cosmological constant. *Astron. J.*, 116:1009–1038, 1998. doi: 10.1086/300499.

[35] L. Amendola and S. Tsujikawa. *Dark Energy: Theory and Observations*. Cambridge University Press, 2010. ISBN 9781139488570. URL `https://books.google.com.mt/books?id=Xge0hg_AIIYC`.

[36] O. F. Piattella. *Lecture Notes in Cosmology*. UNITEXT for Physics. Springer, Cham, 2018. doi: 10.1007/978-3-319-95570-4.

[37] A. H. G. Peter. Dark Matter: A Brief Review. *arXiv e-prints*, art. arXiv:1201.3942, January 2012.

[38] D. Scott. The standard model of cosmology: A skeptic's guide. *Proc. Int. Sch. Phys. Fermi*, 200:133–153, 2020. doi: 10.3254/ENFI200007.

[39] S. Capozziello, G. Sarracino, and G. De Somma. A Critical Discussion on the $H_0$ Tension †. *Universe*, 10 (3):140, 2024. doi: 10.3390/universe10030140.

[40] L. Perivolaropoulos. Hubble Tension or Distance Ladder Crisis? *arXiv e-prints*, 8 2024.

[41] T. Cheng. *Relativity, gravitation and cosmology: a basic introduction*, volume 11. Oxford University Press, 2009.

[42] Alan H. Guth. Inflationary universe: A possible solution to the horizon and flatness problems. *Phys. Rev. D*, 23:347–356, Jan 1981. doi: 10.1103/PhysRevD.23.347. URL `https://link.aps.org/doi/10.1103/PhysRevD.23.347`.

[43] D.H. Lyth. *The History of the Universe*. Astronomers' Universe. Springer International Publishing, 2015. ISBN 9783319227436. URL `https://books.google.com.mt/books?id=M4bPsgEACAAJ`.

[44] K. A. Olive et al. Review of Particle Physics. *Chin. Phys. C*, 38:090001, 2014. doi: 10.1088/1674-1137/38/9/090001.

[45] A. A. Penzias and R. W. Wilson. A Measurement of Excess Antenna Temperature at 4080 Mc/s. *Astrophysical Journal*, 142:419–421, July 1965. doi: 10.1086/148307.

[46] R. H. Dicke, P. J. E. Peebles, P. G. Roll, and D. T. Wilkinson. Cosmic Black-Body Radiation. *Astrophysical Journal*, 142:414–419, July 1965. doi: 10.1086/148306.

[47] N. W. Boggess et al. The COBE Mission: Its Design and Performance Two Years after Launch. *Astrophysical Journal*, 397:420, October 1992. doi: 10.1086/171797.

[48] Benjamin P. Abbott et al. Upper Limits on the Stochastic Gravitational-Wave Background from Advanced LIGO's First Observing Run. *Phys. Rev. Lett.*, 118(12):121101, 2017. doi: 10.1103/PhysRevLett.118.121101. [Erratum: Phys.Rev.Lett. 119, 029901 (2017)].

[49] P. A. R. Ade et al. Detection of *B*-Mode Polarization at Degree Angular Scales by BICEP2. *Phys. Rev. Lett.*, 112(24):241101, 2014. doi: 10.1103/PhysRevLett.112.241101.

[50] P. A. R. Ade et al. Improved Constraints on Cosmology and Foregrounds from BICEP2 and Keck Array Cosmic Microwave Background Data with Inclusion of 95 GHz Band. *Phys. Rev. Lett.*, 116:031302, 2016. doi: 10.1103/PhysRevLett.116.031302.

[51] P. A. R. Ade et al. Improved Constraints on Primordial Gravitational Waves using Planck, WMAP, and BICEP/Keck Observations through the 2018 Observing Season. *Phys. Rev. Lett.*, 127(15):151301, 2021. doi: 10.1103/PhysRevLett.127.151301.

[52] P. Salucci et al. Einstein, Planck and Vera Rubin: Relevant Encounters Between the Cosmological and the Quantum Worlds. *Front. in Phys.*, 8:603190, 2021. doi: 10.3389/fphy.2020.603190.

[53] V. A. Mitsou. Overview of searches for dark matter at the LHC. *J. Phys. Conf. Ser.*, 651(1):012023, 2015. doi: 10.1088/1742-6596/651/1/012023.

[54] R. W. Schnee. Introduction to dark matter experiments. In *Theoretical Advanced Study Institute in Elementary Particle Physics: Physics of the Large and the Small*, pages 775–829, 2011. doi: 10.1142/9789814327183_0014.

[55] E. Aprile et al. The XENON1T Dark Matter Experiment. *Eur. Phys. J. C*, 77(12):881, 2017. doi: 10.1140/epjc/s10052-017-5326-3.

[56] E. Di Valentino, O. Mena, S. Pan, L. Visinelli, W. Yang, A. Melchiorri, D. F. Mota, A. G. Riess, and J. Silk. In the realm of the Hubble tension—a review of solutions. *Class. Quant. Grav.*, 38(15):153001, 2021. doi: 10.1088/1361-6382/ac086d.

[57] E. Di Valentino et al. Snowmass2021 - Letter of interest cosmology intertwined II: The hubble constant tension. *Astropart. Phys.*, 131:102605, 2021. doi: 10.1016/j.astropartphys.2021.102605.

[58] J. Hu and F. Wang. Hubble Tension: The Evidence of New Physics. *Universe*, 9(2):94, 2023. doi: 10.3390/universe9020094.

[59] W. L. Freedman, B. F. Madore, T. Hoyt, I. S. Jang, R. Beaton, M. G. Lee, A. Monson, J. Neeley, and J. Rich. Calibration of the Tip of the Red Giant Branch (TRGB). *Astrophys. J.*, 2 2020. doi: 10.3847/1538-4357/ab7339.

[60] W. L. Freedman. Measurements of the Hubble Constant: Tensions in Perspective. *Astrophys. J.*, 919(1):16, 2021. doi: 10.3847/1538-4357/ac0e95.

[61] S. Joudaki et al. KiDS+VIKING-450 and DES-Y1 combined: Cosmology with cosmic shear. *Astron. Astrophys.*, 638:L1, 2020. doi: 10.1051/0004-6361/201936154.

[62] T. M. C. Abbott et al. Dark Energy Survey Year 1 Results: A Precise H0 Estimate from DES Y1, BAO, and D/H Data. *Mon. Not. Roy. Astron. Soc.*, 480(3):3879–3888, 2018. doi: 10.1093/mnras/sty1939.

[63] E. Di Valentino et al. Cosmology Intertwined III: $f\sigma_8$ and $S_8$. *Astropart. Phys.*, 131:102604, 2021. doi: 10.1016/j.astropartphys.2021.102604.

[64] M. Asgari et al. KiDS+VIKING-450 and DES-Y1 combined: Mitigating baryon feedback uncertainty with COSEBIs. *Astron. Astrophys.*, 634:A127, 2020. doi: 10.1051/0004-6361/201936512.

[65] N. Saridakis, E et al. Modified Gravity and Cosmology: An Update by the CANTATA Network. *arXiv e-prints*, 5 2021.

[66] S. Bahamonde, K. F. Dialektopoulos, C. Escamilla-Rivera, G.l Farrugia, V. Gakis, M. Hendry, M. Hohmann, J. Levi Said, J. Mifsud, and E. Di Valentino. Teleparallel Gravity: From Theory to Cosmology. *Reports on Progress in Physics*, 6 2021.

[67] A. G. Riess et al. JWST Validates HST Distance Measurements: Selection of Supernova Subsample Explains Differences in JWST Estimates of Local H0. *arXiv e-prints*, 8 2024.

[68] W. L. Freedman, B. F. Madore, I. S. Jang, T. J. Hoyt, A. J. Lee, and K. A. Owens. Status Report on the Chicago-Carnegie Hubble Program (CCHP): Three Independent Astrophysical Determinations of the Hubble Constant Using the James Webb Space Telescope. *arXiv e-prints*, 8 2024.

[69] T. Clifton, Pedro G. Ferreira, A. Padilla, and C. Skordis. Modified Gravity and Cosmology. *Phys. Rept.*, 513:1–189, 2012. doi: 10.1016/j.physrep.2012.01.001.

[70] T. P. Sotiriou and V. Faraoni. f(R) Theories Of Gravity. *Rev. Mod. Phys.*, 82:451–497, 2010. doi: 10.1103/RevModPhys.82.451.

[71] G. Nordström. On the possibility of unifying the electromagnetic and the gravitational fields. *arXiv preprint physics/0702221*, 2007.

[72] R. Aldrovandi and J.G. Pereira. *Teleparallel Gravity: An Introduction*. Fundamental Theories of Physics. Springer Netherlands, 2012. ISBN 9789400751439. URL `https://books.google.com.mt/books?id=2dZ5zuKe_fUC`.

[73] Y. Cai, S. Capozziello, M. De Laurentis, and E. N. Saridakis. f(T) teleparallel gravity and cosmology. *Rept. Prog. Phys.*, 79(10):106901, 2016. doi: 10.1088/0034-4885/79/10/106901.

[74] M. Krssak, R. J. van den Hoogen, J. G. Pereira, C. G. Böhmer, and A. A. Coley. Teleparallel theories of gravity: illuminating a fully invariant approach. *Class. Quant. Grav.*, 36(18):183001, 2019. doi: 10.1088/1361-6382/ab2e1f.

[75] G. Farrugia and J. Levi Said. Growth factor in $f(T, \mathcal{T})$ gravity. *Phys. Rev. D*, 94(12):124004, 2016. doi: 10.1103/PhysRevD.94.124004.

[76] S. Bahamonde, K. Flathmann, and C. Pfeifer. Photon sphere and perihelion shift in weak $f(T)$ gravity. *Phys. Rev. D*, 100(8):084064, 2019. doi: 10.1103/PhysRevD.100.084064.

[77] S. Chen, J. B. Dent, S. Dutta, and E. N. Saridakis. Cosmological perturbations in f(T) gravity. *Phys. Rev. D*, 83:023508, 2011. doi: 10.1103/PhysRevD.83.023508.

[78] E. V. Linder. Einstein's Other Gravity and the Acceleration of the Universe. *Phys. Rev. D*, 81:127301, 2010. doi: 10.1103/PhysRevD.81.127301. [Erratum: Phys.Rev.D 82, 109902 (2010)].

[79] R. Ferraro and F. Fiorini. Born-infeld gravity in weitzenböck spacetime. *Phys. Rev. D*, 78:124019, Dec 2008. doi: 10.1103/PhysRevD.78.124019. URL `https://link.aps.org/doi/10.1103/PhysRevD.78.124019`.

[80] C. Escamilla-Rivera and J. Levi Said. Cosmological viable models in $f(T, B)$ theory as solutions to the $H_0$ tension. *Class. Quant. Grav.*, 37(16):165002, 2020. doi: 10.1088/1361-6382/ab939c.

[81] S. Bahamonde, K. F. Dialektopoulos, and J. Levi Said. Can Horndeski Theory be recast using Teleparallel Gravity? *Phys. Rev. D*, 100(6):064018, 2019. doi: 10.1103/PhysRevD.100.064018.

[82] S. Bahamonde, M. Zubair, and G. Abbas. Thermodynamics and cosmological reconstruction in $f(T, B)$ gravity. *Phys. Dark Univ.*, 19:78–90, 2018. doi: 10.1016/j.dark.2017.12.005.

[83] G. Farrugia, J. Levi Said, V. Gakis, and E. N. Saridakis. Gravitational Waves in Modified Teleparallel Theories. *Phys. Rev. D*, 97(12):124064, 2018. doi: 10.1103/PhysRevD.97.124064.

[84] S. Bahamonde and S. Capozziello. Noether Symmetry Approach in $f(T, B)$ teleparallel cosmology. *Eur. Phys. J. C*, 77(2):107, 2017. doi: 10.1140/epjc/s10052-017-4677-0.

[85] H. C. Ohanian and R. Ruffini. *Gravitation and spacetime*. Cambridge University Press, 2013.

[86] S. Dodelson. *Modern cosmology*. Elsevier, 2003.

[87] J.A. Peacock. *Cosmological physics*. Cambridge university press, 1999.

[88] S. Capozziello, V. De Falco, and C. Ferrara. Comparing equivalent gravities: common features and differences. *Eur. Phys. J. C*, 82(10):865, 2022. doi: 10.1140/epjc/s10052-022-10823-x.

[89] D.D. Baumann. Cosmology: Part iii mathematical tripos. `http://theory.uchicago.edu/~liantaow/my-teaching/dark-matter-472/lectures.pdf`, 2015. [Accessed 18-08-2024].

[90] C.W. Misner, K.S. Thorne, K.S. Thorne, J.A. Wheeler, W.H. Freeman, and Company. *Gravitation*. Number pt. 3 in Gravitation. W. H. Freeman, 1973. ISBN 9780716703440. URL `https://books.google.com.mt/books?id=ExAbAQAAIAAJ`.

[91] J. Plebanski and A. Krasinski. *An Introduction to General Relativity and Cosmology*. Cambridge University Press, 2 edition, 2024.

[92] S. Weinberg and W. Steven. *Gravitation and Cosmology: Principles and Applications of the General Theory of Relativity*. Wiley, 1972. ISBN 9780471925675. URL https://books.google.com.mt/books?id=XLbvAAAAMAAJ.

[93] R. Weitzenböck. *Invariantentheorie*. P. Noordhoff, Groningen, 1923.

[94] D. Hilbert. Die Grundlagen der Physik. 1. *Gott. Nachr.*, 27:395–407, 1915.

[95] D. H. Weinberg, M. J. Mortonson, D. J. Eisenstein, C. Hirata, A. G. Riess, and E. Rozo. Observational Probes of Cosmic Acceleration. *Phys. Rept.*, 530:87–255, 2013. doi: 10.1016/j.physrep.2013.05.001.

[96] G. Brown and H. A. Bethe. How a supernova explodes. *Scientific American*, 252:60–68, May 1985. doi: 10.1038/scientificamerican0585-60.

[97] J.A. Wheeler and K. Ford. *Geons, Black Holes, and Quantum Foam: A Life in Physics*. W. W. Norton, 2010. ISBN 9780393079487. URL https://books.google.com.mt/books?id=zGFkK2tTXPsC.

[98] A. Liddle. *An introduction to modern cosmology; 2nd ed.* Wiley, Chichester, 2003. URL https://cds.cern.ch/record/1010476.

[99] S. Bahamonde. *Modified teleparallel theories of gravity*. PhD thesis, U. Coll. London, 2018.

[100] E. N. Saridakis. Introduction to teleparallel and f(T) gravity and cosmology. In Massimo Bianchi, Robert T. Jansen, and Remo Ruffini, editors, *Fourteenth Marcel Grossmann Meeting - MG14*, pages 1135–1140, January 2018. doi: 10.1142/9789813226609_0074.

[101] B. Li, T. P. Sotiriou, and J. D. Barrow. $f(T)$ gravity and local Lorentz invariance. *Phys. Rev. D*, 83:064035, 2011. doi: 10.1103/PhysRevD.83.064035.

[102] K. Bamba, S. D. Odintsov, and D. Sáez-Gómez. Conformal symmetry and accelerating cosmology in teleparallel gravity. *Phys. Rev. D*, 88:084042, 2013. doi: 10.1103/PhysRevD.88.084042.

[103] J B Hartle. *Gravity: An introduction to Einstein's general relativity*. Addison-Wesley, 2003. ISBN 0805386629; 9780805386622. URL libgen.li/file.php?md5=cc85733161f8dce2a5ef1f510549aeb8.

[104] S. Weinberg. *Cosmology*. Cosmology. OUP Oxford, 2008. ISBN 9780191523601. URL https://books.google.com.mt/books?id=nqQZdg020fsC.

[105] B. W. Carroll and D. A. Ostlie. *An introduction to modern astrophysics*. Cambridge University Press, 2017.

[106] M. Ishak. Testing General Relativity in Cosmology. *Living Rev. Rel.*, 22(1):1, 2019. doi: 10.1007/s41114-018-0017-4.

[107] L. R. Abramo, R. C. Batista, L. Liberato, and R. Rosenfeld. Structure formation in the presence of dark energy perturbations. *JCAP*, 11:012, 2007. doi: 10.1088/1475-7516/2007/11/012.

[108] S. Nesseris and L. Perivolaropoulos. Testing Lambda CDM with the Growth Function delta(a): Current Constraints. *Phys. Rev. D*, 77:023504, 2008. doi: 10.1103/PhysRevD.77.023504.

[109] L. Kazantzidis and L. Perivolaropoulos. $\sigma$ 8 tension. is gravity getting weaker at low z? observational evidence and theoretical implications. In *Modified Gravity and Cosmology: An Update by the CANTATA Network*, pages 507–537. Springer, 2021.

[110] G. Panotopoulos and Á. Rincón. Growth of structures and redshift-space distortion data in scale-dependent gravity. *Eur. Phys. J. Plus*, 136(6):622, 2021. doi: 10.1140/epjp/s13360-021-01583-w.

[111] S. Nesseris, G. Pantazis, and L. Perivolaropoulos. Tension and constraints on modified gravity parametrizations of $G_{\rm eff}(z)$ from growth rate and Planck data. *Phys. Rev. D*, 96(2):023542, 2017. doi: 10.1103/PhysRevD.96.023542.

[112] L. Kazantzidis and L. Perivolaropoulos. Evolution of the $f\sigma_8$ tension with the Planck15/$\Lambda$CDM determination and implications for modified gravity theories. *Phys. Rev. D*, 97(10):103503, 2018. doi: 10.1103/PhysRevD.97.103503.

[113] M. Kamionkowski and E. D. Kovetz. The Quest for B Modes from Inflationary Gravitational Waves. *Ann. Rev. Astron. Astrophys.*, 54:227–269, 2016. doi: 10.1146/annurev-astro-081915-023433.

[114] N. N Gandilo et al. The primordial inflation polarization explorer (piper). In *Millimeter, Submillimeter, and Far-Infrared Detectors and Instrumentation for Astronomy VIII*, volume 9914, pages 372–379. SPIE, 2016.

[115] L. Krauss, S. Dodelson, and S. Meyer. Primordial Gravitational Waves and Cosmology. *Science*, 328: 989–992, 2010. doi: 10.1126/science.1179541.

[116] J. M. Ezquiaga and M. Zumalacárregui. Dark Energy in light of Multi-Messenger Gravitational-Wave astronomy. *Front. Astron. Space Sci.*, 5:44, 2018. doi: 10.3389/fspas.2018.00044.

[117] C. Caprini and D. G. Figueroa. Cosmological Backgrounds of Gravitational Waves. *Class. Quant. Grav.*, 35 (16):163001, 2018. doi: 10.1088/1361-6382/aac608.

[118] M. Zaldarriaga and U. Seljak. An all sky analysis of polarization in the microwave background. *Phys. Rev. D*, 55:1830–1840, 1997. doi: 10.1103/PhysRevD.55.1830.

[119] L. M. Krauss and M. White. Grand unification, gravitational waves, and the cosmic microwave background anisotropy. *Phys. Rev. Lett.*, 69:869–872, Aug 1992. doi: 10.1103/PhysRevLett.69.869. URL `https://link.aps.org/doi/10.1103/PhysRevLett.69.869`.

[120] Y. Akrami et al. Planck 2018 results. X. Constraints on inflation. *Astron. Astrophys.*, 641:A10, 2020. doi: 10.1051/0004-6361/201833887.

[121] Y. Inoue et al. POLARBEAR-2: an instrument for CMB polarization measurements. *Proc. SPIE Int. Soc. Opt. Eng.*, 9914:99141I, 2016. doi: 10.1117/12.2231961.

[122] P. Ade et al. The Simons Observatory: Science goals and forecasts. *JCAP*, 02:056, 2019. doi: 10.1088/1475-7516/2019/02/056.

[123] E. Hertig et al. The Simons Observatory: Combining cross-spectral foreground cleaning with multitracer B-mode delensing for improved constraints on inflation. *Phys. Rev. D*, 110(4):043532, 2024. doi: 10.1103/PhysRevD.110.043532.

[124] S. Weinberg. The cosmological constant problem. *Rev. Mod. Phys.*, 61:1–23, Jan 1989. doi: 10.1103/RevModPhys.61.1. URL `https://link.aps.org/doi/10.1103/RevModPhys.61.1`.

[125] A. Einstein. Die Grundlage der allgemeinen Relativitätstheorie. *Annalen der Physik*, 354(7):769–822, January 1916. doi: 10.1002/andp.19163540702.

[126] F. Bernardeau, S. Colombi, E. Gaztanaga, and R. Scoccimarro. Large scale structure of the universe and cosmological perturbation theory. *Phys. Rept.*, 367:1–248, 2002. doi: 10.1016/S0370-1573(02)00135-7.

[127] P. Bull et al. Beyond ΛCDM: Problems, solutions, and the road ahead. *Phys. Dark Univ.*, 12:56–99, 2016. doi: 10.1016/j.dark.2016.02.001.

[128] S. Cole et al. The 2dF Galaxy Redshift Survey: Power-spectrum analysis of the final dataset and cosmological implications. *Mon. Not. Roy. Astron. Soc.*, 362:505–534, 2005. doi: 10.1111/j.1365-2966.2005.09318.x.

[129] D. J. Eisenstein et al. Detection of the Baryon Acoustic Peak in the Large-Scale Correlation Function of SDSS Luminous Red Galaxies. *Astrophys. J.*, 633:560–574, 2005. doi: 10.1086/466512.

[130] T. Buchert, A. A. Coley, H. Kleinert, B. F. Roukema, and D. L. Wiltshire. Observational Challenges for the Standard FLRW Model. *Int. J. Mod. Phys. D*, 25(03):1630007, 2016. doi: 10.1142/S021827181630007X.

[131] Joan Sola. Cosmological constant and vacuum energy: old and new ideas. *J. Phys. Conf. Ser.*, 453:012015, 2013. doi: 10.1088/1742-6596/453/1/012015.

[132] E. J. Copeland, M. Sami, and S. Tsujikawa. Dynamics of dark energy. *Int. J. Mod. Phys. D*, 15:1753–1936, 2006. doi: 10.1142/S021827180600942X.

[133] H. E. S. Velten, R. F. vom Marttens, and W. Zimdahl. Aspects of the cosmological "coincidence problem". *Eur. Phys. J. C*, 74(11):3160, 2014. doi: 10.1140/epjc/s10052-014-3160-4.

[134] M. Moresco et al. Unveiling the Universe with emerging cosmological probes. *Living Rev. Rel.*, 25(1):6, 2022. doi: 10.1007/s41114-022-00040-z.

[135] W. L. Freedman et al. The Carnegie-Chicago Hubble Program. VIII. An Independent Determination of the Hubble Constant Based on the Tip of the Red Giant Branch. *Astrophys. J.*, 882:34, 2019. doi: 10.3847/1538-4357/ab2f73.

[136] K. C. Wong et al. H0LiCOW – XIII. A 2.4 per cent measurement of H0 from lensed quasars: 5.3$\sigma$ tension between early- and late-Universe probes. *Mon. Not. Roy. Astron. Soc.*, 498(1):1420–1439, 2020. doi: 10.1093/mnras/stz3094.

[137] M. Millon et al. TDCOSMO. I. An exploration of systematic uncertainties in the inference of $H_0$ from time-delay cosmography. *Astron. Astrophys.*, 639:A101, 2020. doi: 10.1051/0004-6361/201937351.

[138] R. Jimenez and A. Loeb. Constraining cosmological parameters based on relative galaxy ages. *Astrophys. J.*, 573:37–42, 2002. doi: 10.1086/340549.

[139] M. Moresco, L.a Pozzetti, A. Cimatti, R. Jimenez, C. Maraston, L. Verde, D. Thomas, Annalisa Citro, Rita Tojeiro, and David Wilkinson. A 6% measurement of the Hubble parameter at $z \sim 0.45$: direct evidence of the epoch of cosmic re-acceleration. *JCAP*, 05:014, 2016. doi: 10.1088/1475-7516/2016/05/014.

[140] D. Watson, K. D. Denney, M. Vestergaard, and T. M. Davis. A new cosmological distance measure using active galactic nuclei. *The Astrophysical Journal*, 740(2):L49, October 2011. ISSN 2041-8213. doi: 10.1088/2041-8205/740/2/l49. URL http://dx.doi.org/10.1088/2041-8205/740/2/L49.

[141] B. Czerny, K. Hryniewicz, I. Maity, A. Schwarzenberg-Czerny, P. T. Życki, and M. Bilicki. Towards equation of state of dark energy from quasar monitoring: Reverberation strategy. *Astronomy &; Astrophysics*, 556:A97, August 2013. ISSN 1432-0746. doi: 10.1051/0004-6361/201220832. URL http://dx.doi.org/10.1051/0004-6361/201220832.

[142] M. Asgari et al. KiDS-1000 Cosmology: Cosmic shear constraints and comparison between two point statistics. *Astron. Astrophys.*, 645:A104, 2021. doi: 10.1051/0004-6361/202039070.

[143] T. M. C. Abbott et al. Dark Energy Survey Year 3 results: Cosmological constraints from galaxy clustering and weak lensing. *Phys. Rev. D*, 105(2):023520, 2022. doi: 10.1103/PhysRevD.105.023520.

[144] F. Skara and L. Perivolaropoulos. Tension of the $E_G$ statistic and redshift space distortion data with the Planck - $\Lambda CDM$ model and implications for weakening gravity. *Phys. Rev. D*, 101(6):063521, 2020. doi: 10.1103/PhysRevD.101.063521.

[145] A. Amon et al. Dark Energy Survey Year 3 results: Cosmology from cosmic shear and robustness to data calibration. *Phys. Rev. D*, 105(2):023514, 2022. doi: 10.1103/PhysRevD.105.023514.

[146] C. Krishnan, R. Mohayaee, E. Ó. Colgáin, M. M. Sheikh-Jabbari, and L. Yin. Hints of FLRW breakdown from supernovae. *Phys. Rev. D*, 105(6):063514, 2022. doi: 10.1103/PhysRevD.105.063514.

[147] C. Krishnan, R. Mohayaee, E. Ó. Colgáin, M. M. Sheikh-Jabbari, and Lu Yin. Does Hubble tension signal a breakdown in FLRW cosmology? *Class. Quant. Grav.*, 38(18):184001, 2021. doi: 10.1088/1361-6382/ac1a81.

[148] V. Poulin, T. L. Smith, and T. Karwal. The Ups and Downs of Early Dark Energy solutions to the Hubble tension: A review of models, hints and constraints circa 2023. *Phys. Dark Univ.*, 42:101348, 2023. doi: 10.1016/j.dark.2023.101348.

[149] M. Kamionkowski and A. G. Riess. The Hubble Tension and Early Dark Energy. *Ann. Rev. Nucl. Part. Sci.*, 73:153–180, 2023. doi: 10.1146/annurev-nucl-111422-024107.

[150] E. Di Valentino and A. Melchiorri. Neutrino Mass Bounds in the Era of Tension Cosmology. *Astrophys. J. Lett.*, 931(2):L18, 2022. doi: 10.3847/2041-8213/ac6ef5.

[151] E. Di Valentino, S. Gariazzo, C. Giunti, O. Mena, S. Pan, and W. Yang. Minimal dark energy: Key to sterile neutrino and Hubble constant tensions? *Phys. Rev. D*, 105(10):103511, 2022. doi: 10.1103/PhysRevD.105.103511.

[152] F. W. Hehl, J. D. McCrea, E. W. Mielke, and Y. Ne'eman. Metric affine gauge theory of gravity: Field equations, Noether identities, world spinors, and breaking of dilation invariance. *Phys. Rept.*, 258:1–171, 1995. doi: 10.1016/0370-1573(94)00111-F.

[153] A. De Felice and S. Tsujikawa. f(R) theories. *Living Rev. Rel.*, 13:3, 2010. doi: 10.12942/lrr-2010-3.

[154] S. Nojiri and S. D. Odintsov. Unified cosmic history in modified gravity: from F(R) theory to Lorentz non-invariant models. *Phys. Rept.*, 505:59–144, 2011. doi: 10.1016/j.physrep.2011.04.001.

[155] S. Bahamonde, C. G. Böhmer, and M. Wright. Modified teleparallel theories of gravity. *Phys. Rev. D*, 92 (10):104042, 2015. doi: 10.1103/PhysRevD.92.104042.

[156] Gabriel Farrugia, Carlos Gafa', and Jackson Levi Said. White Dwarf envelops and temperature corrections in exponential f(T) gravity. *Gen. Rel. Grav.*, 57(1):5, 2025. doi: 10.1007/s10714-024-03341-6.

[157] G. R. Bengochea and R. Ferraro. Dark torsion as the cosmic speed-up. *Phys. Rev. D*, 79:124019, 2009. doi: 10.1103/PhysRevD.79.124019.

[158] R. Ferraro and F. Fiorini. Non trivial frames for f(T) theories of gravity and beyond. *Phys. Lett. B*, 702: 75–80, 2011. doi: 10.1016/j.physletb.2011.06.049.

[159] M. Krššák and E. N. Saridakis. The covariant formulation of f(T) gravity. *Class. Quant. Grav.*, 33(11): 115009, 2016. doi: 10.1088/0264-9381/33/11/115009.

[160] N. Tamanini and C. G. Boehmer. Good and bad tetrads in f(T) gravity. *Phys. Rev. D*, 86:044009, 2012. doi: 10.1103/PhysRevD.86.044009.

[161] R. Briffa, S. Capozziello, J. Levi Said, J. Mifsud, and E. N. Saridakis. Constraining teleparallel gravity through Gaussian processes. *Class. Quant. Grav.*, 38(5):055007, 2020. doi: 10.1088/1361-6382/abd4f5.

[162] R. Zheng and Q. Huang. Growth factor in $f(T)$ gravity. *JCAP*, 03:002, 2011. doi: 10.1088/1475-7516/2011/03/002.

[163] O. F. Hernández. Neutrino Masses, Scale-Dependent Growth, and Redshift-Space Distortions. *JCAP*, 06: 018, 2017. doi: 10.1088/1475-7516/2017/06/018.

[164] R. C. Nunes. Structure formation in $f(T)$ gravity and a solution for $H_0$ tension. *JCAP*, 05:052, 2018. doi: 10.1088/1475-7516/2018/05/052.

[165] I. D. Saltas, I. Sawicki, L. Amendola, and M. Kunz. Anisotropic Stress as a Signature of Nonstandard Propagation of Gravitational Waves. *Phys. Rev. Lett.*, 113(19):191101, 2014. doi: 10.1103/PhysRevLett.113.191101.

[166] A. Riazuelo and J. Uzan. Quintessence and gravitational waves. *Phys. Rev. D*, 62:083506, Sep 2000. doi: 10.1103/PhysRevD.62.083506. URL `https://link.aps.org/doi/10.1103/PhysRevD.62.083506`.

[167] E. J. Copeland, M. Kopp, A. Padilla, P. M. Saffin, and C. Skordis. Dark energy after GW170817 revisited. *Phys. Rev. Lett.*, 122(6):061301, 2019. doi: 10.1103/PhysRevLett.122.061301.

[168] Q. Wu, T. Zhu, R. Niu, W. Zhao, and A. Wang. Constraints on the Nieh-Yan modified teleparallel gravity with gravitational waves. *Phys. Rev. D*, 105(2):024035, 2022. doi: 10.1103/PhysRevD.105.024035.

[169] J. M. Ezquiaga and M. Zumalacárregui. Dark energy after gw170817: Dead ends and the road ahead. *Phys. Rev. Lett.*, 119:251304, Dec 2017. doi: 10.1103/PhysRevLett.119.251304. URL `https://link.aps.org/doi/10.1103/PhysRevLett.119.251304`.

[170] F.M. Dekking. *A Modern Introduction to Probability and Statistics: Understanding Why and How*. Springer Texts in Statistics. Springer, 2005. ISBN 9781852338961. URL `https://books.google.com.mt/books?id=XLUMIlombgQC`.

[171] C. E. Rasmussen and C. K. I. Williams. *Gaussian Processes for Machine Learning*. MIT Press, 2006.

[172] M. Seikel and C. Clarkson. Optimising Gaussian processes for reconstructing dark energy dynamics from supernovae. 11 2013.

[173] M. Seikel, C. Clarkson, and M. Smith. Reconstruction of dark energy and expansion dynamics using Gaussian processes. *JCAP*, 06:036, 2012. doi: 10.1088/1475-7516/2012/06/036.

[174] H. Zhang, Y. Wang, T. Zhang, and T. Zhang. Kernel Selection for Gaussian Process in Cosmology: With Approximate Bayesian Computation Rejection and Nested Sampling. *Astrophys. J. Suppl.*, 266(2):27, 2023. doi: 10.3847/1538-4365/accb92.

[175] D. Duvenaud. *Automatic model construction with Gaussian processes*. PhD thesis, Apollo - University of Cambridge Repository, 2014. URL `https://www.repository.cam.ac.uk/handle/1810/247281`.

[176] A. Gómez-Valent and L. Amendola. H0from cosmic chronometers and type ia supernovae, with gaussian processes and the novel weighted polynomial regression method. *Journal of Cosmology and Astroparticle Physics*, 2018(04):051–051, Apr 2018. ISSN 1475-7516. doi: 10.1088/1475-7516/2018/04/051. URL `http://dx.doi.org/10.1088/1475-7516/2018/04/051`.

[177] E. Elizalde, M. Khurshudyan, K. Myrzakulov, and S. Bekov. Reconstruction of the Quintessence Dark Energy Potential from a Gaussian Process. *Astrophysics*, 67(2):192–214, 2024. doi: 10.1007/s10511-024-09828-z.

[178] M. Ebden. Gaussian processes: A quick introduction. *arXiv preprint arXiv:1505.02965*, 2015.

[179] M. Zhang and H. Li. Gaussian processes reconstruction of dark energy from observational data. *Eur. Phys. J. C*, 78(6):460, 2018. doi: 10.1140/epjc/s10052-018-5953-3.

[180] A. Gómez-Valent and L. Amendola. $H_0$ from cosmic chronometers and Type Ia supernovae, with Gaussian Processes and the novel Weighted Polynomial Regression method. *JCAP*, 04:051, 2018. doi: 10.1088/1475-7516/2018/04/051.

[181] A. Mehrabi and S. Basilakos. Does $\Lambda$CDM really be in tension with the Hubble diagram data? *Eur. Phys. J. C*, 80(7):632, 2020. doi: 10.1140/epjc/s10052-020-8221-2.

[182] P. Mukherjee and N. Banerjee. Non-parametric reconstruction of the cosmological *jerk* parameter. *Eur. Phys. J. C*, 81(1):36, 2021. doi: 10.1140/epjc/s10052-021-08830-5.

[183] N. Metropolis, A. W. Rosenbluth, M. N. Rosenbluth, A. H. Teller, and E. Teller. Equation of state calculations by fast computing machines. *The journal of chemical physics*, 21(6):1087–1092, 1953.

[184] W. R Gilks, S. Richardson, and D. Spiegelhalter. *Markov chain Monte Carlo in practice*. CRC press, 1995.

[185] R. M Neal. Probabilistic inference using markov chain monte carlo methods. *Technical Report CRG-TR-93-1*, 1993.

[186] A. Lewis and S. Bridle. Cosmological parameters from CMB and other data: A Monte Carlo approach. *Phys. Rev. D*, 66:103511, 2002. doi: 10.1103/PhysRevD.66.103511.

[187] R. Briffa, C. Escamilla-Rivera, J. Said Levi, J. Mifsud, and N. L. Pullicino. Impact of $H_0$ priors on $f(T)$ late time cosmology. *Eur. Phys. J. Plus*, 137(5):532, 2022. doi: 10.1140/epjp/s13360-022-02725-4.

[188] R. Briffa, C. Escamilla-Rivera, J. Levi Said, and Jurgen Mifsud. f(T,B) Gravity in the late Universe in the context of local measurements. *Phys. Dark Univ.*, 39:101153, 2023. doi: 10.1016/j.dark.2022.101153.

[189] R. Briffa, C. Escamilla-Rivera, J. Levi Said, and Jurgen Mifsud. Constraints on f(T) cosmology with Pantheon+. *Mon. Not. Roy. Astron. Soc.*, 522(4):6024–6034, 2023. doi: 10.1093/mnras/stad1384.

[190] R. Briffa, C. Escamilla-Rivera, J. Levi Said, and Jurgen Mifsud. Growth of structures using redshift space distortion in f(T) cosmology. *Mon. Not. Roy. Astron. Soc.*, 528(2):2711–2727, 2024. doi: 10.1093/mnras/stae103.

[191] D. JC. MacKay et al. *Information theory, inference and learning algorithms*. Cambridge university press, 2003.

[192] D. Gamerman and H. F Lopes. *Markov Chain Monte Carlo: Stochastic Simulation for Bayesian Inference*. CRC Press, 2006.

[193] W. H Press, S. A. Teukolsky, W.T. Vetterling, and B. P. Flannery. *Numerical recipes 3rd edition: The art of scientific computing*. Cambridge university press, 2007.

[194] J. S. Speagle. A conceptual introduction to markov chain monte carlo methods. *arXiv preprint arXiv:1909.12313*, 2019.

[195] L. E. Padilla, L. O. Tellez, L. A. Escamilla, and J. A. Vazquez. Cosmological Parameter Inference with Bayesian Statistics. *Universe*, 7(7):213, 2021. doi: 10.3390/universe7070213.

[196] J. Dunkley, M. Bucher, P. G. Ferreira, K. Moodley, and C. Skordis. Fast and reliable mcmc for cosmological parameter estimation. *Mon. Not. Roy. Astron. Soc.*, 356:925–936, 2005. doi: 10.1111/j.1365-2966.2004.08464.x.

[197] W. K. Hastings. Monte Carlo sampling methods using Markov chains and their applications. *Biometrika*, 57:97–109, 1970. ISSN 0006-3444. doi: 10.1093/biomet/57.1.97. URL `semanticscholar.org/paper/143d2e02ab91ae6259576ac50b664b8647af8988`.

[198] J. Akeret, S. Seehars, A. Amara, A. Refregier, and A. Csillaghy. Cosmohammer: Cosmological parameter estimation with the mcmc hammer. *Astronomy and Computing*, 2:27–39, 2013.

[199] D. Foreman-Mackey, D. W Hogg, D. Lang, and J. Goodman. emcee: the mcmc hammer. *Publications of the Astronomical Society of the Pacific*, 125(925):306, 2013.

[200] S. R. Hinton. ChainConsumer. *The Journal of Open Source Software*, 1:00045, August 2016. doi: 10.21105/joss.00045.

[201] D. Huterer and D. L. Shafer. Dark energy two decades after: Observables, probes, consistency tests. *Rept. Prog. Phys.*, 81(1):016901, 2018. doi: 10.1088/1361-6633/aa997e.

[202] L. Perivolaropoulos. Accelerating universe: observational status and theoretical implications. *AIP Conf. Proc.*, 848(1):698–712, 2006. doi: 10.1063/1.2348048.

[203] J. E. Bautista et al. Measurement of baryon acoustic oscillation correlations at $z = 2.3$ with SDSS DR12 Ly$\alpha$-Forests. *Astron. Astrophys.*, 603:A12, 2017. doi: 10.1051/0004-6361/201730533.

[204] S. Alam et al. The clustering of galaxies in the completed SDSS-III Baryon Oscillation Spectroscopic Survey: cosmological analysis of the DR12 galaxy sample. *Mon. Not. Roy. Astron. Soc.*, 470(3):2617–2652, 2017. doi: 10.1093/mnras/stx721.

[205] A. J. Ross et al. The Completed SDSS-IV extended Baryon Oscillation Spectroscopic Survey: Large-scale structure catalogues for cosmological analysis. *Mon. Not. Roy. Astron. Soc.*, 498(2):2354–2371, 2020. doi: 10.1093/mnras/staa2416.

[206] F. Melia and M. K. Yennapureddy. Model Selection Using Cosmic Chronometers with Gaussian Processes. *JCAP*, 02:034, 2018. doi: 10.1088/1475-7516/2018/02/034.

[207] F. Melia and R. S. Maier. Cosmic Chronometers in the R_h=ct Universe. *Mon. Not. Roy. Astron. Soc.*, 432: 2669–2675, 2013. doi: 10.1093/mnras/stt596.

[208] M. Moresco, R. Jimenez, L. Verde, A. Cimatti, and L. Pozzetti. Setting the Stage for Cosmic Chronometers. II. Impact of Stellar Population Synthesis Models Systematics and Full Covariance Matrix. *Astrophys. J.*, 898(1):82, 2020. doi: 10.3847/1538-4357/ab9eb0.

[209] M. Moresco, R. Jimenez, A. Cimatti, and L. Pozzetti. Constraining the expansion rate of the Universe using low-redshift ellipticals as cosmic chronometers. *JCAP*, 03:045, 2011. doi: 10.1088/1475-7516/2011/03/045.

[210] M. Moresco et al. Improved constraints on the expansion rate of the Universe up to z~1.1 from the spectroscopic evolution of cosmic chronometers. *JCAP*, 08:006, 2012. doi: 10.1088/1475-7516/2012/08/006.

[211] C. Zhang, H. Zhang, S. Yuan, S. Liu, T. Zhang, and Y. Sun. Four new observational H(z) data from luminous red galaxies in the Sloan Digital Sky Survey data release seven. *Research in Astronomy and Astrophysics*, 14(10):1221-1233, 2014. doi: 10.1088/1674-4527/14/10/002.

[212] R. Jimenez, L. Verde, T. Treu, and D. Stern. Constraints on the equation of state of dark energy and the Hubble constant from stellar ages and the CMB. *Astrophys. J.*, 593:622–629, 2003. doi: 10.1086/376595.

[213] J. Simon, L. Verde, and R. Jimenez. Constraints on the redshift dependence of the dark energy potential. *Phys. Rev. D*, 71:123001, 2005. doi: 10.1103/PhysRevD.71.123001.

[214] M. Moresco et al. Improved constraints on the expansion rate of the Universe up to z $\sim$1.1 from the spectroscopic evolution of cosmic chronometers. *JCAP*, 2012(8):006, 2012. doi: 10.1088/1475-7516/2012/08/006.

[215] D. Stern, R. Jimenez, L. Verde, M. Kamionkowski, and S. A. Stanford. Cosmic chronometers: constraining the equation of state of dark energy. I: H(z) measurements. *JCAP*, 2010(2):008, 2010. doi: 10.1088/1475-7516/2010/02/008.

[216] M. Moresco. Raising the bar: new constraints on the Hubble parameter with cosmic chronometers at z $\sim$ 2. *Mon. Not. Roy. Astron. Soc.*, 450(1):L16–L20, 2015. doi: 10.1093/mnrasl/slv037.

[217] B. Xu, H.i Yu, and P. Wu. Testing Viable f(T) Models with Current Observations. *Astrophys. J.*, 855(2):89, 2018. doi: 10.3847/1538-4357/aaad12.

[218] P. Murdin and L. Murdin. *Supernovae*. Cambridge University Press, 1985. ISBN 9780521300384. URL `https://books.google.com.mt/books?id=2zTnw4fR17YC`.

[219] A. V. Filippenko. Optical spectra of supernovae. *Annual Review of Astronomy and Astrophysics*, 35(1): 309–355, 1997. doi: 10.1146/annurev.astro.35.1.309.

[220] C. T. Kowal. Absolute magnitudes of supernovae. *Astrophy. J.*, 73:1021–1024, December 1968. doi: 10.1086/110763.

[221] W. L. Freedman. Determination of cosmological parameters. *Phys. Scripta T*, 85:37–46, 2000. doi: 10.1238/Physica.Topical.085a00037.

[222] D. M. Scolnic et al. The Complete Light-curve Sample of Spectroscopically Confirmed SNe Ia from Pan-STARRS1 and Cosmological Constraints from the Combined Pantheon Sample. *Astrophys. J.*, 859(2):101, 2018. doi: 10.3847/1538-4357/aab9bb.

[223] A. Conley, J. Guy, M Sullivan, N. Regnault, P. Astier, C. Balland, S. Basa, R.G. Carlberg, D. Fouchez, and D .and others Hardin. Supernova constraints and systematic uncertainties from the first three years of the supernova legacy survey. *The Astrophysical Journal Supplement Series*, 192(1):1, 2010.

[224] B. Y. D. V. Mazo, A. E. Romano, and M. A. C. Quintero. $H_0$ tension or $M$ overestimation? *Eur. Phys. J. C*, 82(7):610, 2022. doi: 10.1140/epjc/s10052-022-10526-3.

[225] D. Scolnic et al. Pantheon. `https://github.com/dscolnic/Pantheon.git`, 2018.

[226] P. J. E. Peebles. Recombination of the Primeval Plasma. *Astrophysical Journal*, 153:1, July 1968. doi: 10.1086/149628.

[227] A. D. Sakharov. The Initial Stage of an Expanding Universe and the Appearance of a Nonuniform Distribution of Matter. *Soviet Journal of Experimental and Theoretical Physics*, 22:241, January 1966.

[228] R. A. Sunyaev and Ya. B. Zeldovich. Small scale fluctuations of relic radiation. *Astrophys. Space Sci.*, 7: 3–19, 1970.

[229] C. Blake and K. Glazebrook. Probing dark energy using baryonic oscillations in the galaxy power spectrum as a cosmological ruler. *Astrophys. J.*, 594:665–673, 2003. doi: 10.1086/376983.

[230] H. Seo and D. J. Eisenstein. Probing dark energy with baryonic acoustic oscillations from future large galaxy redshift surveys. *Astrophys. J.*, 598:720–740, 2003. doi: 10.1086/379122.

[231] W. J. Percival. Baryon acoustic oscillations: a cosmological ruler. *Physics Today*, 70(12):32–38, December 2017. ISSN 0031-9228. doi: 10.1063/PT.3.3789.

[232] G. Zhao et al. The clustering of the SDSS-IV extended Baryon Oscillation Spectroscopic Survey DR14 quasar sample: a tomographic measurement of cosmic structure growth and expansion rate based on optimal redshift weights. *Mon. Not. Roy. Astron. Soc.*, 482(3):3497–3513, 2019. doi: 10.1093/mnras/sty2845.

[233] F. Beutler, C. Blake, M. Colless, D. H. Jones, L. Staveley-Smith, L. Campbell, Q. Parker, W. Saunders, and F. Watson. The 6dF Galaxy Survey: Baryon Acoustic Oscillations and the Local Hubble Constant. *Mon. Not. Roy. Astron. Soc.*, 416:3017–3032, 2011. doi: 10.1111/j.1365-2966.2011.19250.x.

[234] A. J. Ross, L. Samushia, C. Howlett, W. J. Percival, A. Burden, and M. Manera. The clustering of the SDSS DR7 main Galaxy sample – I. A 4 per cent distance measure at $z = 0.15$. *Mon. Not. Roy. Astron. Soc.*, 449 (1):835–847, 2015. doi: 10.1093/mnras/stv154.

[235] H. du Mas des Bourboux et al. Baryon acoustic oscillations from the complete SDSS-III Ly$\alpha$-quasar cross-correlation function at $z = 2.4$. *Astron. Astrophys.*, 608:A130, 2017. doi: 10.1051/0004-6361/201731731.

[236] E. V. Linder. Exponential Gravity. *Phys. Rev. D*, 80:123528, 2009. doi: 10.1103/PhysRevD.80.123528.

[237] S. Nesseris, S. Basilakos, E. N. Saridakis, and L. Perivolaropoulos. Viable $f(T)$ models are practically indistinguishable from $\Lambda$CDM. *Phys. Rev.*, D88:103010, 2013. doi: 10.1103/PhysRevD.88.103010.

[238] K. Bamba, C. Geng, C. Lee, and L. Luo. Equation of state for dark energy in $f(T)$ gravity. *JCAP*, 01:021, 2011. doi: 10.1088/1475-7516/2011/01/021.

[239] P. Wu and H.W. Yu. $f(T)$ models with phantom divide line crossing. *Eur. Phys. J. C*, 71:1552, 2011. doi: 10.1140/epjc/s10052-011-1552-2.

[240] H. Akaike. A new look at the statistical model identification. *IEEE Transactions on Automatic Control*, 19 (6):716–723, 1974. doi: 10.1109/TAC.1974.1100705.

[241] S. Konishi and G. Kitagawa. *Information Criteria and Statistical Modeling*. Springer Series in Statistics. Springer, 2008. ISBN 9780387718866. URL `https://books.google.com.mt/books?id=3I9ZJusaYh0C`.

[242] A. R. Liddle. How many cosmological parameters? *Mon. Not. Roy. Astron. Soc.*, 351:L49–L53, 2004. doi: 10.1111/j.1365-2966.2004.08033.x.

[243] Gideon S. Estimating the Dimension of a Model. *The Annals of Statistics*, 6(2):461 – 464, 1978. doi: 10.1214/aos/1176344136. URL `https://doi.org/10.1214/aos/1176344136`.

[244] H. Jeffreys. *Theory of Probability*. International series of monographs on physics. Clarendon Press, 1998. ISBN 9780198503682. URL `https://books.google.com.mt/books?id=_PuRmAEACAAJ`.

[245] Harold J. *Theory of Probability*. Clarendon Press, Oxford, England, 1939.

[246] R. Easther and H. V. Peiris. Bayesian Analysis of Inflation II: Model Selection and Constraints on Reheating. *Phys. Rev. D*, 85:103533, 2012. doi: 10.1103/PhysRevD.85.103533.

[247] A. R Liddle. Information criteria for astrophysical model selection. *Mon. Not. Roy. Astron. Soc.*, 377:L74–L78, 2007. doi: 10.1111/j.1745-3933.2007.00306.x.

[248] G. Farrugia and J. Levi Said. Stability of the flat FLRW metric in $f(T)$ gravity. *Phys. Rev.*, D94(12):124054, 2016. doi: 10.1103/PhysRevD.94.124054.

[249] A. Finch and J. Levi Said. Galactic Rotation Dynamics in f(T) gravity. *Eur. Phys. J. C*, 78(7):560, 2018. doi: 10.1140/epjc/s10052-018-6028-1.

[250] G. Farrugia, J. Levi Said, and M. L. Ruggiero. Solar System tests in f(T) gravity. *Phys. Rev.*, D93(10):104034, 2016. doi: 10.1103/PhysRevD.93.104034.

[251] L. Iorio and E. N. Saridakis. Solar system constraints on f(T) gravity. *Mon. Not. Roy. Astron. Soc.*, 427:1555, 2012. doi: 10.1111/j.1365-2966.2012.21995.x.

[252] X. Ren, S. Yan, Y. Zhao, Y. Cai, and E. N. Saridakis. Gaussian processes and effective field theory of $f(T)$ gravity under the $H_0$ tension. *Astrophys. J.*, 932:2, 2022. doi: 10.3847/1538-4357/ac6ba5.

[253] Y.F. Cai, M. Khurshudyan, and E. N. Saridakis. Model-independent reconstruction of $f(T)$ gravity from Gaussian Processes. *Astrophys. J.*, 888:62, 2020. doi: 10.3847/1538-4357/ab5a7f.

[254] M. Zhang and J. Xia. Test of the cosmic evolution using Gaussian processes. *JCAP*, 12:005, 2016. doi: 10.1088/1475-7516/2016/12/005.

[255] A. Shafieloo, A. G. Kim, and E. V. Linder. Gaussian process cosmography. *Physical Review D*, 85(12), June 2012. ISSN 1550-2368. doi: 10.1103/physrevd.85.123530. URL `http://dx.doi.org/10.1103/PhysRevD.85.123530`.

[256] M. Seikel, C. Clarkson, and M. Smith. Reconstruction of dark energy and expansion dynamics using Gaussian processes. *JCAP*, 2012(6):036, June 2012. doi: 10.1088/1475-7516/2012/06/036.

[257] T. Holsclaw, U. Alam, B. Sansó, H. Lee, K. Heitmann, S. Habib, and D. Higdon. Nonparametric dark energy reconstruction from supernova data. *Phys. Rev. Lett.*, 105:241302, Dec 2010. doi: 10.1103/PhysRevLett.105.241302. URL `https://link.aps.org/doi/10.1103/PhysRevLett.105.241302`.

[258] T. Holsclaw, U. Alam, B. Sansó, H. Lee, K. Heitmann, S. Habib, and D. Higdon. Nonparametric reconstruction of the dark energy equation of state. *Physical Review D*, 82(10), November 2010. ISSN 1550-2368. doi: 10.1103/physrevd.82.103502. URL `http://dx.doi.org/10.1103/PhysRevD.82.103502`.

[259] S. Yahya, M. Seikel, C. Clarkson, R. Maartens, and M. Smith. Null tests of the cosmological constant using supernovae. *Phys. Rev. D*, 89:023503, Jan 2014. doi: 10.1103/PhysRevD.89.023503. URL `https://link.aps.org/doi/10.1103/PhysRevD.89.023503`.

[260] A. G. Riess et al. Type Ia Supernova Distances at Redshift $> 1.5$ from the Hubble Space Telescope Multi-cycle Treasury Programs: The Early Expansion Rate. *Astrophys. J.*, 853(2):126, 2018. doi: 10.3847/1538-4357/aaa5a9.

[261] S. Yahya, M. Seikel, C. Clarkson, R. Maartens, and M. Smith. Null tests of the cosmological constant using supernovae. *Phys. Rev. D*, 89(2):023503, 2014. doi: 10.1103/PhysRevD.89.023503.

[262] C. Zunckel and C. Clarkson. Consistency Tests for the Cosmological Constant. *Phys. Rev. Lett.*, 101:181301, 2008. doi: 10.1103/PhysRevLett.101.181301.

[263] P. J. E. Peebles and Bharat Ratra. The Cosmological Constant and Dark Energy. *Rev. Mod. Phys.*, 75: 559–606, 2003. doi: 10.1103/RevModPhys.75.559.

[264] S. Capozziello, O. Luongo, and E. N. Saridakis. Transition redshift in $f(T)$ cosmology and observational constraints. *Phys. Rev. D*, 91(12):124037, 2015. doi: 10.1103/PhysRevD.91.124037.

[265] P. J. E. Peebles. *Principles of physical cosmology*, volume 27. Princeton university press, 1993.

[266] Georgios Kofinas and Emmanuel N. Saridakis. Teleparallel equivalent of Gauss-Bonnet gravity and its modifications. *Phys. Rev. D*, 90:084044, 2014. doi: 10.1103/PhysRevD.90.084044.

[267] K F Riley, S J Bence, and M P Hobson. *Mathematical methods for physics and engineering: a comprehensive guide*. Cambridge Univ. Press, Cambridge, 1997. URL `https://cds.cern.ch/record/345425`.

[268] P. Wu and H. W. Yu. Observational constraints on $f(T)$ theory. *Phys. Lett. B*, 693:415–420, 2010. doi: 10.1016/j.physletb.2010.08.073.

[269] D. Wang and D. Mota. Can $f(T)$ gravity resolve the $H_0$ tension? *Phys. Rev. D*, 102(6):063530, 2020. doi: 10.1103/PhysRevD.102.063530.

[270] R.l Ferraro and F. Fiorini. Modified teleparallel gravity: Inflation without inflaton. *Phys. Rev. D*, 75:084031, 2007. doi: 10.1103/PhysRevD.75.084031.

[271] D. A. Gomes, R. Briffa, A. Kozak, J. Levi Said, M. Saal, and A. Wojnar. Cosmological constraints of Palatini f(R) gravity. *JCAP*, 01:011, 2024. doi: 10.1088/1475-7516/2024/01/011.

[272] Z. Li, Y. P. Jing, P.e Zhang, and D. Cheng. Measurement of Redshift-Space Power Spectrum for BOSS galaxies and the Growth Rate at redshift 0.57. *Astrophys. J.*, 833(2):287, 2016. doi: 10.3847/1538-4357/833/2/287.

[273] H. Gil-Marín, W. J. Percival, L. Verde, J. R. Brownstein, C. Chuang, F. Kitaura, S. A. Rodríguez-Torres, and M. D. Olmstead. The clustering of galaxies in the SDSS-III Baryon Oscillation Spectroscopic Survey: RSD measurement from the power spectrum and bispectrum of the DR12 BOSS galaxies. *Mon. Not. Roy. Astron. Soc.*, 465(2):1757–1788, 2017. doi: 10.1093/mnras/stw2679.

[274] L. Perivolaropoulos and L. Kazantzidis. Hints of modified gravity in cosmos and in the lab? *Int. J. Mod. Phys. D*, 28(05):1942001, 2019. doi: 10.1142/S021827181942001X.

[275] F. Shi et al. Mapping the Real Space Distributions of Galaxies in SDSS DR7: II. Measuring the growth rate, clustering amplitude of matter and biases of galaxies at redshift 0.1. *Astrophys. J.*, 861(2):137, 2018. doi: 10.3847/1538-4357/aacb20.

[276] N. Kaiser. Clustering in real space and in redshift space. *Monthly Notices of the Royal Astronomical Society*, 227(1):1–21, 07 1987. ISSN 0035-8711. doi: 10.1093/mnras/227.1.1. URL `https://doi.org/10.1093/mnras/227.1.1`.

[277] A. J. S. Hamilton. Linear redshift distortions: A Review. In *Ringberg Workshop on Large Scale Structure*, 8 1997. doi: 10.1007/978-94-011-4960-0_17.

[278] G. Lambiase, S. Mohanty, A. Narang, and P. Parashari. Testing dark energy models in the light of $\sigma_8$ tension. *Eur. Phys. J. C*, 79(2):141, 2019. doi: 10.1140/epjc/s10052-019-6634-6.

[279] J. E. Gonzalez, J. S. Alcaniz, and J. C. Carvalho. Non-parametric reconstruction of cosmological matter perturbations. *JCAP*, 04:016, 2016. doi: 10.1088/1475-7516/2016/04/016.

[280] G. Gupta, S. Sen, and A. A Sen. GCG Parametrization for Growth Function and Current Constraints. *JCAP*, 04:028, 2012. doi: 10.1088/1475-7516/2012/04/028.

[281] Y. Song and W. J. Percival. Reconstructing the history of structure formation using Redshift Distortions. *JCAP*, 10:004, 2009. doi: 10.1088/1475-7516/2009/10/004.

[282] S. Alam et al. Completed SDSS-IV extended Baryon Oscillation Spectroscopic Survey: Cosmological implications from two decades of spectroscopic surveys at the Apache Point Observatory. *Phys. Rev. D*, 103(8):083533, 2021. doi: 10.1103/PhysRevD.103.083533.

[283] C. Blake et al. The WiggleZ Dark Energy Survey: joint measurements of the expansion and growth history at z < 1. *Mon. Not. Roy. Astron. Soc.*, 425(1):405–414, September 2012. doi: 10.1111/j.1365-2966.2012.21473.x.

[284] C. Alcock and B. Paczynski. An evolution free test for non-zero cosmological constant. *Sci. Rep.*, 281:358, October 1979. doi: 10.1038/281358a0.

[285] J. Levi Said, J. Mifsud, J. Sultana, and K. Zarb Adami. Reconstructing teleparallel gravity with cosmic structure growth and expansion rate data. *JCAP*, 06:015, 2021. doi: 10.1088/1475-7516/2021/06/015.

[286] G. Alestas, L. Kazantzidis, and S. Nesseris. Machine learning constraints on deviations from general relativity from the large scale structure of the Universe. *Phys. Rev. D*, 106(10):103519, 2022. doi: 10.1103/PhysRevD.106.103519.

[287] C. Blake et al. The WiggleZ Dark Energy Survey: Joint measurements of the expansion and growth history at $z < 1$. *Mon. Not. Roy. Astron. Soc.*, 425:405–414, 2012. doi: 10.1111/j.1365-2966.2012.21473.x.

[288] C. Preston, A. Amon, and G. Efstathiou. A non-linear solution to the S8 tension – II. Analysis of DES Year 3 cosmic shear. *Mon. Not. Roy. Astron. Soc.*, 525(4):5554–5564, 2023. doi: 10.1093/mnras/stad2573.

[289] D. Benisty. Quantifying the $S_8$ tension with the Redshift Space Distortion data set. *Phys. Dark Univ.*, 31: 100766, 2021. doi: 10.1016/j.dark.2020.100766.

[290] S. Brieden, H. Gil-Marín, and L. Verde. A tale of two (or more) h's. *JCAP*, 04:023, 2023. doi: 10.1088/1475-7516/2023/04/023.

[291] H. Rubira, A. Mazoun, and M. Garny. Full-shape BOSS constraints on dark matter interacting with dark radiation and lifting the S8 tension. *JCAP*, 01:034, 2023. doi: 10.1088/1475-7516/2023/01/034.

[292] S. J. Clark, K. Vattis, J. Fan, and S. M. Koushiappas. H0 and S8 tensions necessitate early and late time changes to ΛCDM. *Phys. Rev. D*, 107(8):083527, 2023. doi: 10.1103/PhysRevD.107.083527.

[293] L. A. Anchordoqui, E. Di Valentino, S. Pan, and W. Yang. Dissecting the H0 and S8 tensions with Planck + BAO + supernova type Ia in multi-parameter cosmologies. *JHEAp*, 32:28–64, 2021. doi: 10.1016/j.jheap.2021.08.001.

[294] J. Beltrán Jiménez, D. Bettoni, D. Figueruelo, Florencia A. Teppa P., and S. Tsujikawa. Probing elastic interactions in the dark sector and the role of S8. *Phys. Rev. D*, 104(10):103503, 2021. doi: 10.1103/PhysRevD.104.103503.

[295] R. C. Nunes and S. Vagnozzi. Arbitrating the S8 discrepancy with growth rate measurements from redshift-space distortions. *Mon. Not. Roy. Astron. Soc.*, 505(4):5427–5437, 2021. doi: 10.1093/mnras/stab1613.

[296] A. G. Polnarev. Polarization and Anisotropy Induced in the Microwave Background by Cosmological Gravitational Waves. *Soviet Astronomy*, 29:607–613, December 1985.

[297] M. C. Guzzetti, N. Bartolo, M. Liguori, and S. Matarrese. Gravitational waves from inflation. *Riv. Nuovo Cim.*, 39(9):399–495, 2016. doi: 10.1393/ncr/i2016-10127-1.

[298] G. Galloni, N. Bartolo, S. Matarrese, M. Migliaccio, A. Ricciardone, and N. Vittorio. Updated constraints on amplitude and tilt of the tensor primordial spectrum. *JCAP*, 04:062, 2023. doi: 10.1088/1475-7516/2023/04/062.

[299] D.H. Lyth and A.R. Liddle. *The Primordial Density Perturbation: Cosmology, Inflation and the Origin of Structure*. Cambridge University Press, 2009. ISBN 9780521828499. URL `https://books.google.com.mt/books?id=Mor_ehlYc4QC`.

[300] G. Galloni, S. Henrot-Versillé, and M. Tristram. Robust constraints on tensor perturbations from cosmological data: A comparative analysis from Bayesian and frequentist perspectives. *Phys. Rev. D*, 110(6):063511, 2024. doi: 10.1103/PhysRevD.110.063511.

[301] R. Calderon et al. DESI 2024: Reconstructing Dark Energy using Crossing Statistics with DESI DR1 BAO data. *arXiv e-prints*, 5 2024.

[302] K. Lodha et al. DESI 2024: Constraints on Physics-Focused Aspects of Dark Energy using DESI DR1 BAO Data. *arXiv e-prints*, 5 2024.

[303] A. G. Adame et al. DESI 2024 VI: Cosmological Constraints from the Measurements of Baryon Acoustic Oscillations. *arXiv e-prints*, 4 2024.

[304] Y. Mellier et al. Euclid. I. Overview of the Euclid mission. *arXiv e-prints*, 5 2024.

[305] M. H. Abitbol, S. Adachi, P. Ade, J. Aguirre, Z. Ahmed, S. Aiola, A. Ali, D. Alonso, M. A Alvarez, K. Arnold, et al. The simons observatory: Astro2020 decadal project whitepaper. *arXiv preprint arXiv:1907.08284*, 2019.

[306] K. Abazajian et al. Snowmass 2021 CMB-S4 White Paper. *arXiv e-prints*, 3 2022.

[307] J. Lesgourgues. The Cosmic Linear Anisotropy Solving System (CLASS) I: Overview. *arXiv e-prints*, 4 2011.

[308] D. Blas, J. Lesgourgues, and T. Tram. The Cosmic Linear Anisotropy Solving System (CLASS) II: Approximation schemes. *JCAP*, 07:034, 2011. doi: 10.1088/1475-7516/2011/07/034.

[309] J. Lesgourgues. The Cosmic Linear Anisotropy Solving System (CLASS) III: Comparision with CAMB for LambdaCDM. *arXiv e-prints*, 4 2011.

[310] J. Lesgourgues and T. Tram. The Cosmic Linear Anisotropy Solving System (CLASS) IV: efficient implementation of non-cold relics. *JCAP*, 09:032, 2011. doi: 10.1088/1475-7516/2011/09/032.

[311] M. Zumalacárregui, E. Bellini, I. Sawicki, J. Lesgourgues, and P. G. Ferreira. hi_class: Horndeski in the Cosmic Linear Anisotropy Solving System. *JCAP*, 08:019, 2017. doi: 10.1088/1475-7516/2017/08/019.

[312] E. Bellini, I. Sawicki, and M. Zumalacárregui. hi_class: Background Evolution, Initial Conditions and Approximation Schemes. *JCAP*, 02:008, 2020. doi: 10.1088/1475-7516/2020/02/008.

[313] M. Moresco. Addressing the hubble tension with cosmic chronometers. In *The Hubble Constant Tension*, pages 277–293. Springer, 2024.

[314] A. Gelman and D. B. Rubin. Inference from Iterative Simulation Using Multiple Sequences. *Statistical Science*, 7(4):457 – 472, 1992. doi: 10.1214/ss/1177011136. URL `https://doi.org/10.1214/ss/1177011136`.

[315] A. Lewis. GetDist: a Python package for analysing Monte Carlo samples. *arXiv e-prints*, 10 2019.

[316] N. Aghanim et al. Planck 2018 results. V. CMB power spectra and likelihoods. *Astron. Astrophys.*, 641:A5, 2020. doi: 10.1051/0004-6361/201936386.

[317] F. Couchot, S. Henrot-Versillé, O. Perdereau, S. Plaszczynski, B. Rouillé d'Orfeuil, M. Spinelli, and M. Tristram. Relieving tensions related to the lensing of the cosmic microwave background temperature power spectra. *Astron. Astrophys.*, 597:A126, 2017. doi: 10.1051/0004-6361/201527740.

[318] F. Couchot, S. Henrot-Versillé, O. Perdereau, S. Plaszczynski, B. Rouillé d'Orfeuil, M. Spinelli, and M. Tristram. Cosmology with the cosmic microwave background temperature-polarization correlation. *Astron. Astrophys.*, 602:A41, 2017. doi: 10.1051/0004-6361/201629815.

[319] A. Mangilli, S. Plaszczynski, and M. Tristram. Large-scale cosmic microwave background temperature and polarization cross-spectra likelihoods. *Mon. Not. Roy. Astron. Soc.*, 453(3):3174–3189, 2015. doi: 10.1093/mnras/stv1733.

[320] M. Tristram et al. Planck constraints on the tensor-to-scalar ratio. *Astron. Astrophys.*, 647:A128, 2021. doi: 10.1051/0004-6361/202039585.

[321] M. Tristram et al. Improved limits on the tensor-to-scalar ratio using BICEP and Planck data. *Phys. Rev. D*, 105(8):083524, 2022. doi: 10.1103/PhysRevD.105.083524.

[322] J. P. Gardner et al. The James Webb Space Telescope Mission. *Publications of the ASP*, 135(1048):068001, June 2023. doi: 10.1088/1538-3873/acd1b5.